Universiteit Gent
Faculteit Toegepaste Wetenschappen
Vakgroep Informatietechnologie

Design and fabrication of a highly efficient light-emitting diode: the Grating-Assisted Resonant-Cavity Light-Emitting Diode

Ontwerp en realisatie van een hoogefficiënte lichtemitterende diode: de resonantecaviteitsdiode met diffractief rooster

Danaë Delbeke

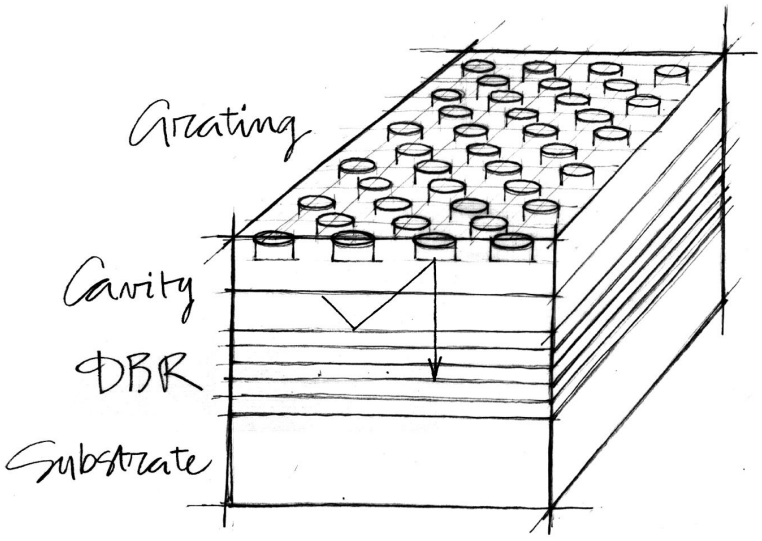

Proefschrift tot het bekomen van de graad van
Doctor in de Toegepaste Wetenschappen: Elektrotechniek
Academiejaar 2002-2003

Promotor:

Prof. dr. ir. R. Baets	INTEC, Universiteit Gent, België

Examencommissie:

Prof. dr. ir. J. Van Campenhout (voorzitter)	ELIS, Universiteit Gent, België
Prof. dr. ir. H. Benisty (leescommissie)	Ecole Polytechnique, Paris, France
Prof. dr. ir. P. Heremans (leescommissie)	IMEC vzw, Leuven, België
Prof. dr. ir. K. Neyts (leescommissie)	ELIS, Universiteit Gent, België
Prof. dr. ir. P. Van Daele (leescommissie)	INTEC, Universiteit Gent, België
Prof. dr. ir. B. Dhoedt	INTEC, Universiteit Gent, België
Prof. dr. ir. I. Moerman	INTEC, Universiteit Gent, België
Prof. dr. ir. P. Lagasse	INTEC, Universiteit Gent, België
dr. ir. P. Bienstman	INTEC, Universiteit Gent, België

Universiteit Gent
Faculteit Toegepaste Wetenschappen

Vakgroep Informatietechnologie (INTEC)
Sint-Pietersnieuwstraat 41
B-9000 Gent
België

Tel.: +32-9-264.33.16
Fax.: +32-9-264.35.93

Dit werk kwam tot stand in het kader van een specialisatiebeurs toegekend door het IWT (Vlaams Instituut voor de bevordering van het Wetenschappelijk-Technologisch Onderzoek in de Industrie).

Voor Albert Vansteenkiste

Dankwoord

Onze Westerse maatschappij plaatst het individu omwille van zijn creativiteit, originaliteit en onderscheid op een voetstuk. Nochtans is elke individuele prestatie – hoe klein ook – het resultaat van ontelbare prikkels van de groep waarin je mag vertoeven. De lezer krijgt hier met andere woorden geen allerindividueelste expressie van de allerindividueelste gedachte, maar het resultaat van talloze expressies en heel veel gedachten van velen. Dit proefschrift is een bundeling van krachten. Ook al hadden sommigen niet het flauwste idee dat hun opmerking, kwinkslag of steun tot dit werk heeft bijgedragen. Vandaar dat ik ze er hier graag op wijs en tegelijkertijd voor dank, met de vrees dat ik enkelen zal vergeten.

Eerst en vooral wil ik het Vlaams Instituut voor de bevordering van het Wetenschappelijk-Technologisch Onderzoek in de Industrie (IWT) danken voor de specialisatiebeurs die dit doctoraatsproject heeft gefinancierd.

Maar zonder de deskundigheid, de steun, de stimuli, geduld en spitante creativiteit van Prof. Roel Baets, tevens promotor van dit werk, was dit resultaat ondenkbaar. Mijn oprechte dank gaat eveneens uit naar Prof. Paul Lagasse die de structuur en het kader waarbinnen dit onderzoek werd gevoerd, heeft mogelijk gemaakt.

Bedankt Ronny Bockstaele voor de vele tips en verhelderende gesprekken over de RCLED en het kritisch nalezen van dit werk; Peter Bienstman voor de hulp bij het programmeren zonder de welke ik nu nog zat te debuggen en de opmerkzaamheden bij hoofdstuk 4; Stefan Goeman voor de LaTeX-tips, de inspirerende discussies over diffractieve structuren en het nalezen van enkele hoofdstukken; bedankt Koen Vandeputte voor de initiatie in het holografische procédé; bedankt Jan De Merlier voor de vele kleine dingen; Dirk Taillaert voor de CAMFR simulaties; Kurt De Mesel voor zijn medeleven in de mathlab-problematiek; Stefaan Vanhastel die C-- kan ombuigen in C++; thanks to Thomas Krauss for his persistent faith in the GA-RCLED expressed by several e-beam runs; thanks to the partners of the European ESPRIT project SMILED for the inspiring discussions and the sharing of their knowledge in the WP3-4 meetings; bedankt Prof. Bart Dhoedt voor het ter beschikking stellen van het programma RODIS dat de basis vormt van het in dit werk ontwikkelde softwarepakket en de stimulerende tips die een startende doctoranda nodig heeft; bedankt Steven Verstuyft, Liesbet Van Landschoot, Peter Geerinck, Wim Woittiez, Carl Sys, Yu Zong-Qiang, Steven Van Put, Prof. Ingrid Moerman en Prof. Peter Van Daele zonder wie de eerste GA-RCLED nooit het daglicht had gezien.
En Ides, voor alles.

Danaë Delbeke, Gent, 14 juni 2002

Contents

Dankwoord **i**

Nederlandstalige samenvatting **1**
1 Inleiding . . . 1
2 Hoogefficiënte Licht-Emitterende Diodes . . . 6
3 Diffractieve nanostructuren . . . 13
4 GA-RCLED: theorie en analyse . . . 18
5 Realisatie van een GA-RCLED . . . 24
6 GA-RCLED met een 1D rooster . . . 28
7 GA-RCLED met een 2D rooster . . . 34
8 Conclusie en toekomstperspectieven . . . 39
Bibliografie . . . 41

1 Introduction **1-1**
1.1 Context . . . 1-2
1.1.1 High efficiency and high brightness Light Emitting Diodes . 1-2
1.1.2 Nanostructures . . . 1-4
1.2 High brightness LEDs and nanostructures meet in the Grating-Assisted Resonant-Cavity Light-Emitting Diode: research objectives 1-6
1.3 Outline of the manuscript . . . 1-7
1.4 Publications . . . 1-8
References . . . 1-10

2 Highly Efficient Light-Emitting Diodes **2-1**
2.1 Introduction . . . 2-2
2.1.1 Short history of Light-Emitting Diodes . . . 2-2
2.1.2 Outline of this chapter . . . 2-3
2.2 Basic principles of semiconductor LEDs . . . 2-4
2.2.1 Recombination in active regions . . . 2-4
2.2.2 p-n junction . . . 2-7
2.2.3 Highly efficient LEDs or how to outsmart Snell's Law . . . 2-8
2.2.3.1 Extraction efficiency of LED . . . 2-8
2.2.3.2 Multiple side extraction . . . 2-11
2.2.3.3 Tapered LEDs . . . 2-12
2.2.3.4 Surface roughened LED . . . 2-12
2.2.3.5 Resonant-Cavity LED . . . 2-14
2.2.3.6 Applications of high efficiency LEDs . . . 2-14

2.3 The Resonant-Cavity Light-Emitting Diode 2-14
2.3.1 Basics of spontaneous emission in a layered medium 2-14
2.3.1.1 Modification of emission pattern: theoretical treatment 2-14
2.3.1.2 Total emission enhancement or *Purcell*-factor . . . 2-16
2.3.2 Design rules 2-17
2.3.2.1 Finesse, Quality factor and (effective) Cavity order 2-18
2.3.2.2 Dipole in semiconductor slab cavity: effect of cavity thickness and position of active layer 2-20
2.3.2.3 Cavity with DBR mirror(s): effect of mirror reflectivity 2-23
2.3.2.4 Temperature influence and saturation 2-26
2.3.2.5 Large diameter RCLEDs and photon-recycling . . 2-28
2.3.2.6 Modulation bandwidth of RCLEDs 2-29
2.3.3 State of the art 2-30
2.3.3.1 980-nm RCLEDs 2-30
2.3.3.2 650-nm RCLEDs 2-31
2.3.3.3 850-880-nm RCLEDs 2-32
2.3.3.4 1300-nm and 1550-nm RCLEDs 2-33
2.3.4 Advanced techniques 2-34
2.3.4.1 RC2LED 2-34
2.3.4.2 Photonic Crystal Assisted RCLED 2-35
2.3.5 Future prospects of RCLEDs 2-37
2.4 Conclusion 2-38
References 2-42

3 Diffractive Nanostructures **3-1**
3.1 Diffractive nanostructures 3-2
3.1.1 Isotropic media 3-2
3.1.2 Periodic Corrugated media 3-4
3.2 Modelling of diffractive structures 3-8
3.2.1 General grating diffraction problem 3-8
3.2.2 Overview of diffraction modelling tools 3-13
3.2.2.1 Integral or differential method? 3-13
3.2.2.2 Rigorous coupled wave or modal approach? . . . 3-13
3.2.2.3 Approximate diffraction theories 3-14
3.3 Rigorous Coupled Wave Analysis 3-15
3.3.1 Slicing of the two-dimensional periodic structure 3-15
3.3.2 Construction of the coupled-wave equations 3-16
3.3.3 Truncation 3-18
3.3.4 Solution of coupled-wave equations 3-21
3.3.5 Electromagnetic boundary conditions 3-21
3.3.6 Enhanced transmittance approach for multi-layer gratings . 3-23
3.3.7 Diffraction efficiency 3-25
3.3.8 Convergence 3-26
3.4 Conclusions 3-28

References 3-30

4 GA-RCLED: theory and analysis 4-1
4.1 Introduction 4-2
4.2 Qualitative analysis with Wave-Vector Diagram 4-3
4.2.1 Dipole emission in a planar cavity 4-3
4.2.2 Extraction of in-plane propagating waves by means of a grating 4-5
4.2.3 Grating-Assisted RCLED 4-8
4.3 Rigorous Analysis 4-9
4.3.1 Electric dipole transition 4-9
4.3.2 Unperturbed electric dipole radiation pattern 4-12
4.3.3 Dipoles in periodically modulated stratified medium 4-15
4.3.3.1 Bragg-coupled set of plane waves 4-15
4.3.3.2 External field and intensity of a single dipole at (x_d, y_d, z_d)=(0, 0, 0) 4-18
4.3.3.3 Dependence of reflection and transmission matrices on position of source 4-19
4.3.3.4 External field and intensity of a dipole at an arbitrary in-plane location $(x_d, y_d, 0)$ 4-20
4.3.3.5 Intensity of an in-plane distribution of mutually incoherent dipoles with identical orientation . . . 4-21
4.3.3.6 Intensity of mutually incoherent dipoles with isotropic orientation (θ_d,φ_d) 4-24
4.3.3.7 Extraction Efficiency 4-26
4.3.4 Implementation aspects 4-29
4.3.4.1 Infinitely thin active layer: absorbing active layers and evanescent coupling 4-29
4.3.4.2 Finite spectral width 4-30
4.3.5 External Efficiency 4-31
4.4 Conclusions 4-32
References 4-33

5 Fabrication of GA-RCLED 5-1
5.1 Introduction 5-2
5.2 Grating fabrication 5-3
5.2.1 Introduction 5-3
5.2.2 Holographic definition 5-5
5.2.2.1 Holographic illumination 5-7
5.2.2.2 Ti evaporation 5-11
5.2.2.3 Reactive Ion Etching 5-12
5.2.2.4 Possibilities and limitations 5-14
5.3 Processing of LED 5-15
5.4 Conclusion 5-16
References 5-18

6 GA-RCLED with 1-D grating **6-1**
6.1 Introduction . . . 6-2
6.2 Structure of the GA-RCLED . . . 6-2
6.2.1 Top- or bottom-emitting? . . . 6-2
6.2.2 Grating location . . . 6-5
6.2.3 Material system . . . 6-5
6.3 Design of GA-RCLED with 1-D grating . . . 6-6
6.3.1 2-D behavior . . . 6-7
6.3.1.1 The period of the grating . . . 6-8
6.3.1.2 The cavity thickness . . . 6-10
6.3.1.3 The depth of the grating . . . 6-11
6.3.1.4 Wavelength of monochromatic dipole . . . 6-12
6.3.2 3-D behavior . . . 6-14
6.3.3 Design rules . . . 6-15
6.4 Characterisation of GA-RCLED with 1-D grating . . . 6-16
6.4.1 Realisation of GA-RCLEDs with 1-D grating . . . 6-16
6.4.2 Spectral behavior . . . 6-16
6.4.3 Farfield . . . 6-20
6.4.4 Efficiency . . . 6-20
6.4.5 Roughening . . . 6-22
6.5 Conclusion . . . 6-22
References . . . 6-24

7 GA-RCLED with 2-D grating **7-1**
7.1 Introduction . . . 7-2
7.2 GA-RCLED with holographically defined square lattice grating . . . 7-2
7.2.1 Design of GA-RCLED with square lattice grating . . . 7-2
7.2.1.1 First order square lattice grating . . . 7-2
7.2.1.2 Second order square lattice grating . . . 7-7
7.2.1.3 Absorption versus diffraction . . . 7-9
7.2.2 Realisation of GA-RCLED with holographically defined square lattice grating . . . 7-9
7.2.3 Characterisation of GA-RCLED with holographically defined square lattice grating . . . 7-10
7.3 GA-RCLED with e-beam defined triangular lattice grating . . . 7-15
7.3.1 Design of GA-RCLED with triangular lattice grating . . . 7-15
7.3.2 Realisation of GA-RCLED with e-beam defined triangular lattice grating . . . 7-17
7.3.3 Characterisation of GA-RCLED with e-beam defined triangular lattice grating . . . 7-17
7.4 Thin film GA-RCLED . . . 7-23
7.5 Conclusion . . . 7-25
References . . . 7-26

8 Conclusion and Perspectives **8-1**
8.1 Evolution of (extraction) efficiency of LEDs (1998-2001) 8-2
8.2 Overview of the accomplished work and conclusion 8-3
8.2.1 GA-RCLED: Novel design idea for high-efficiency LED. Principle and main assets 8-3
8.2.2 Numerical rigorous analysis tool and computer modelling . 8-4
8.2.3 Prototyping 8-4
8.2.4 Conclusion 8-5
8.3 Perspectives 8-5
References 8-6

Nederlandstalige Samenvatting

Nederlandstalige samenvatting

OP de volgende bladzijden wordt een beknopte samenvatting gegeven van de Engelstalige tekst van het proefschrift. Verwijzing naar vergelijkingen en figuren gebeurt door middel van de nummering gevolgd in de Engelstalige tekst. Voor verdere details en achtergrondinformatie verwijzen we eveneens naar de Engelstalige tekst.

1 Inleiding

1.1 Context

1.1.1 Hoogefficiënte en heldere lichtemitterende diodes

De inefficiëntie van de hedendaagse verlichtingseenheden vormt één van 's werelds belangrijkste en vervelendste energieproblemen. De vereiste hoeveelheid elektriciteit die door deze inefficiëntie surplus geproduceerd wordt, veroorzaakt onnodige uitgaven en belast het milieu.

Recente doorbraken in de LED-technologie laten ons geloven dat de introductie van LEDs voor verlichting tegen 2020 de hoeveelheid geproduceerde elektriciteit voor verlichting met 35% kan laten afnemen. Voordat deze veronderstelling waarheid wordt, dient de efficiëntie van de LED tot minimum 50% verhoogd te worden en dient de kost onder 0.5 euro/klm gedrukt te worden.

Uiteenlopende kwaliteiten versterken de concurrentiële positie van de LED tegenover andere lichtbronnen. Door deze vele kwaliteiten zijn LEDs nu reeds in tal van commerciële toepassingen de standaard lichtbron. De directionele emissie van een LED maakt deze bron uitermate geschikt voor optische communicatietoepassingen. Zowel draadloze infraroodtoepassingen als POF-systemen maken gebruik van een LED als lichtbron. Verschillende toepassingen benutten nu reeds de monochromatische emissie van de LED. Een wel gekend voorbeeld is het verkeerslicht. Andere eigenschappen zijn modulatiesnelheid, lange levensduur, interessante ontwerpmogelijkheden, etc..

Dat er een hele reeks uiteenlopende toepassingsmogelijkheden bestaan voor LEDs, en meer in het bijzonder voor heldere LEDs, is duidelijk. Indien de efficiëntie nog verder verhoogd kan worden, kunnen LEDs ten volle de markt van nichetoepassingen en zelfs algemene verlichting betreden.

1.1.2 Nanostructuren

Nano-elektronica is gelijkaardig aan micro-elektronica, maar dan duizend keer kleiner. De laatste decennia verdubbelde de dichtheid van transistoren op een geïntegreerd circuit (IC) iedere achttien maanden, terwijl de opslagcapaciteit van DRAM chips iedere drie jaar verviervoudigde. Deze trend van exponentiële miniaturisatie is gekend als de wet van Moore. Vóór het jaar 2006 zal de massaproductie van ICs dan ook de wereld van de nanotechnologie betreden. Deze nano-elektronica, waarvan de marktwaarde honderden miljarden euros zal beslaan, is de drijvende kracht achter de ontwikkeling van de nanotechnologie. Deze groeiende technologie maakt het mogelijk materialen te structureren met resoluties op nanoschaal. Ze tast de grenzen af van de standaard optische lithografie en ontwikkelt parallel alternatieve technologieën. Door de markt gedreven blijft de micro-elektronicaindustrie het onderzoek naar nanotechnologie stimuleren. Deze ontwikkeling naar een commercieel toepasbare technologie creëert opportuniteiten voor toepassingen in andere onderzoeks- en toepassingsgebieden, zo ook in de optica en opto-elektronica. De vereiste resolutie, gaande van 1 μm tot 50 nm, is niet langer de onoverbrugbare drempel om optische nanostructuren in tal van toepassingen te commercialiseren. Inderdaad, acousto-optica, holografie, geïntegreerde optica, quantum-elektronica en spectrale analyseermethodes zijn alle reeds doorspekt met roosterdiffractietoepassingen. De opvallendste ontwikkeling situeert zich in de fotonische kristallen. Het eigen optisch gedrag van deze diffractieve structuren met een multidimensionale periodiciteit in de orde van de golflengte en een grote brekingsindexmodulatie krijgt een toenemende aandacht vooral met het oog op fotonische geïntegreerde circuits.

Hoewel diffractieve optica veel genoten heeft van en schuldig is aan de nanotechnologie – ontwikkeld ter ondersteuning van de micro-elektronica – moeten we de aandacht vestigen op het feit dat optische holografie de moderne diffractietechnologieën voorging. Verscheidene applicaties worden nog steeds met deze technologie – al dan niet in combinatie met andere – gefabriceerd.

1.2 Heldere LEDs en nanostructuren komen samen in de GA-RCLED: doel van het onderzoek

Helderheid of hoge radiantie gaat samen met een planaire geometrie en een enkelzijdige extractie. Door het hoge brekingsindexcontrast tussen het bronmateriaal en de omgeving wordt extractie echter beperkt tot een tweetal percent, gedicteerd door Snellius' wet. Er zijn verscheiden succesvolle technieken om deze wet te omzeilen. Eén ervan is de ResonananteCaviteits-LED (RCLED). In deze LEDs wordt de actieve laag in een resonante caviteit geplaatst waarvan tenminste één dimensie in de orde van de golflengte. Op die manier beïnvloed je het spontane emissieproces en verliest het zijn isotrope karakter. Efficiënties tot 28% kunnen op die manier bereikt worden. De rest van het vermogen gaat vooral verloren in lekkende DBR modi of lateraal propagerende geleide modi. Het gebruik van een 2D-periodiek rooster met een periode in de orde van de golflengte kan een oplossing zijn voor het verlies van vermogen in de lateraal propagerende geleide mode. De

diffractieve eigenschappen van het rooster, geïntegreerd in één of beide spiegels van de caviteit, kunnen de geleide mode afbuigen naar een extraheerbare richting. Door de grote vermogenfractie in die mode kan het gebruik van een rooster in een RCLED resulteren in een hogere efficiëntie en radiantie. Dit veronderstelt de beschikbaarheid van een mature nanotechnologie ter definiëring van het rooster. We noemen de component de RCLED met diffractief rooster (GA-RCLED). De GA-RCLED is het onderwerp van deze thesis.

1.3 Structuur van dit werk

In Hoofdstuk 2 recapituleren we kort spontane emissie in gelaagde media. We passen de wet van Snellius toe en we stellen technieken voor om deze te omzeilen. We behandelen één van de technieken in groter detail, namelijk de RCLED. De RCLED is één van de basiselementen van de GA-RCLED.

Hoofdstuk 3 behandelt diffractieve structuren, het tweede basiselement van de GA-RCLED. We bekijken het golfvectordiagram (WVD) van naderbij en gebruiken dit voor een kwalitatieve analyse van diffractie van de geleide mode. Verschillende diffractiemodellen worden voorgesteld en vergeleken. De RCWA lijkt hierbij het meest aangeschreven voor de roosters in dit proefschrift en wordt dan ook uitgewerkt voor 2D roosters.

In Hoofdstuk 4 nemen we de GA-RCLED onder de loep. Het concept wordt toegelicht en door middel van het WVD kwalitatief bestudeerd. De elektromagnetische analyse van dipoolemissie in een roosterstructuur wordt besproken. Deze methode werd in C++ geïmplementeerd.

Het fabricageproces wordt in Hoofdstuk 5 voorgesteld. Voor de productie van 2D roosters werd een holografisch proces ontwikkeld. Het fabricageproces van de GA-RCLED is hierdoor simpel en standaard en kan gemakkelijk dienen voor massafabricatie.

In Hoofdstuk 6 bespreken we het ontwerp, de fabricage en karakterisatie van GA-RCLEDs met een 1D rooster. Simulatieresultaten worden vergeleken met experimentele data. De data tonen aan dat de geleide mode geëxtraheerd wordt.

Ontwerp, fabricage en karakterisatie van GA-RCLEDs met een 2D rooster worden in Hoofdstuk 7 behandeld. Zowel e-beam als holografie werden gebruikt om het rooster te definiëren. Analyses van de experimentele data tonen extractie van de geleide mode aan. Een verhoogde extractie-efficiëntie wordt waargenomen.

De voornaamste verwezenlijkingen en conclusies vatten we samen in Hoofdstuk 8. tevens reiken we enkele perspectieven aan voor toekomstig onderzoek naar de GA-RCLED.

1.4 Publicaties

De resultaten die we tijdens de loop van dit werk behaalden, werden in tal van tijdschriften en conferenties voorgesteld.

(1) D. Delbeke, P. Bienstman, R. Bockstaele and R. Baets, "Rigorous Electromagnetic Analysis of Dipole Emission in Periodically Corrugated Layers: the Grating-Assisted Resonant-Cavity Light-Emitting Diode", *J. Opt. Soc. Am. A*, vol. 11(5), pp. 871-880, 2002.

(2) D. Delbeke, R. Bockstaele, P. Bienstman, R. Baets and H. Benisty, "High-efficiency semiconductor resonant-cavity light-emitting diodes: a review", *IEEE J. Sel. Top. Quantum Electron.*, vol. 8(2), pp. 189-206, 2002 (invited paper).

(3) P. Modak, D. Delbeke, I. Moerman, R. Baets, P. Van Daele and P.Demeester, "InAlGaP microcavity LEDs on Ge-substrates", *J. of Crystal Growth*, vol. 221, pp. 668-673, 2000.

(4) P. Modak, M. D'Hondt, D. Delbeke, I. Moerman, P. Van Daele, R. Baets, P. Demeester and P.Mijlemans, "AlGaInP microcavity light-emitting diodes at 650 nm on Ge substrates", *IEEE Phot. Tech. Lett.*, vol. 12(8), pp. 957-959, 2000.

(5) K. Ghawana, D. Delbeke, I. Christiaens, S. Verstuyft and R. Baets, "Heterogenous integration with BCB applied to GA-RCLEDs," in *Optoelectronic devices and heterogenous integration, Proc. SPIE*, vol. 4947, Brugge, Belgium, 2002.

(6) R. Baets, D. Delbeke, P. Bienstman, W. Bogaerts, D. Taillaert and B. Luyssaert, "Photonic crystal materials and light extraction enhancement possibilities," in *11th International workshop on Inorganic and Organic Electroluminescence and 2002 International Conference on the Science and Technology of Emissive Displays and Lighting*, Gent, Belgium, 2002.

(7) D. Delbeke, B. Dhoedt, R. Bockstaele, I. Moerman, P. Van Daele, T.F. Krauss and R. Baets,"Electrically Pumped Grating-Assisted Resonant-Cavity Light-Emitting Diodes", in *Light-Emitting Diodes: Research, Manufacturing and Applications VI, Proc. SPIE*, vol. 4641, San Jose, California, pp. 42-49, 2002.

(8) P. Modak, M. D'Hondt, D. Delbeke, P. Mijlemans, I. Moerman, R. Baets, P. Van Daele and P. Demeester, "InAIGaP microcavity LEDs on Ge-substrates", *The Tenth International Conference on Metal Organic Vapor Phase Epitaxy (IC MOVPE-X)*, Sapporo, Japan, pp. 319-320, 2000.

(9) P. Modak, M. D'Hondt, D. Delbeke, I. Moerman, P. Van Daele, R. Baets, P. Demeester and P.Mijlemans, "High efficiency InAlGaP microcavity LEDs on Ge substrates", *Proc. LEOS Benelux Symposium*, Delft, Netherlands, pp. 59-62, 2000.

(10) D. Delbeke, K. Vandeputte, R. Baets, R. Bockstaele, B. Dhoedt, I. Moerman, P. Van Daele, and S. Verstuyft, "Holograpgically defined Grating-Assisted Micro-Cavity Light Emitting Diodes", *Proc. LEOS Benelux Symposium*, Mons, Belgium, pp. 159-162, 1999.

(11) D. Delbeke, B. Dhoedt, R. Bockstaele, I. Moerman, P. Van Daele, T.F. Krauss and R. Baets, "Electrically Pumped Photonic Crystal Micro-Cavity Light

Emitting Diodes", *Proc. LEOS Summer Topical Meetings*, San Diego, USA, pp. 71-72, 1999.

(12) M. D'Hondt, P. Modak, D. Delbeke, I. Moerman, P. Van Daele. R. Baets, P. Demeester and P. Mijlemans, "4 mW micro cavity LED at 650 nm on germanium substrates", *Light-Emitting Diodes: Research, Manufacturing, and Applications IV, Proc. SPIE*, vol. 3938, San Jose, California, pp. 196-204, 1999.

(13) D. Delbeke, I. Moerman, P. Van Daele and R. Baets, "Grating-Assisted Resonant-Cavity Light-Emitting Diodes for High Brightness", *Second PhD Symposium*, Gent, Belgium, 2001.

(14) D. Delbeke, R. Baets, I. Moerman, P. Van Daele and S. Verstuyft, "High Efficiency Grating Assisted MC-LEDs", *Summer School and EOS Topical Meeting on Semiconductor Microcavity Photonics*, Monte Verita, Switserland, 2000.

(15) P. Bienstman, W. Bogaerts, R. Bockstaele, D. Delbeke, S. Goeman, B. Depreter, J. Derluyn, C. Sys, L. Vanwassenhove, B. Dhoedt, I. Moerman, P. Van Daele and R. Baets, "Microcavity and PBG-related work at the University of Ghent", *COST 268 Workshop*, Stockholm, Sweden, 1999.

(16) D. Delbeke, R. Baets, "High Efficiency Grating Assisted MC-LEDs", *Summer School on Confined Photon Systems: Fundamentals and Applications*, Cargèse, France, 1998.

2 Hoogefficiënte Licht-Emitterende Diodes

2.1 Inleiding

De prestatie van hoogefficiënte LEDs wordt door middel van de externe quantum-efficiëntie uitgedrukt (Vgl.(2.1)):

$$\eta_{ext} = \frac{P_{opt}/\hbar\omega}{I/q} = \eta_{inj}\eta_{int}\eta_{extr}$$

De injectie-efficiëntie η_{inj} (fractie van de elektronen geïnjecteerd in de nuttige actieve laag) en de inwendige efficiëntie η_{int} (fractie van de spontane emissie die radiatief is) naderen in vele gevallen tot 1.

De extractie-efficiëntie η_{extr} van de gegenereerde fotonen is echter veel lager. Door de hoge brekingsindex van het materiaal waarin de spontane emissie plaatsvindt, kan in een standaard LED slechts 2 à 3% geëxtraheerd worden. De resterende fractie kan door totaal inwendige reflectie de halfgeleider niet verlaten en wordt geabsorbeerd. Verscheidene technieken werden ontwikkeld om deze wet van Snellius te omzeilen. De Resonantecaviteits-LED gebruikt interferentie van de spontane emissie in een caviteit om de propagatierichting van de fotonen de controleren en naar de extractieconus te dirigeren. Componenten met een $\eta_{ext} = 28\%$ worden in de literatuur vermeld [1].

Naast deze "lichtgolf-optica" die interferentie benut, werden ook technieken ontwikkeld die door middel van geometrische knepen η_{extr} verhogen, of dus "lichtstraal-optica". Voorbeelden zijn piramidaal gevormde LEDs, LEDs met een verruwd oppervlak, etc. [2]- [4].

Dit hoofdstuk geeft een overzicht van de RLCED. De basisprincipes van spontane emissie worden kort gerecapituleerd. De lage η_{extr} wordt verklaard en de technieken om deze te verhogen worden behandeld. Een theoretische klassieke behandeling van spontane emissie bij zwakke koppeling in gelaagde structuren wordt besproken. Daaruit worden enkele regels voor het ontwerpen van een RCLED met hoge η_{extr} afgeleid. We lichten de state-of-the-art planaire RCLEDs voor verschillende golflengtebereiken toe. Enkele geavanceerde technieken om de η_{extr} nog verder te verhogen, waaronder de GA-RCLED, sluiten dit hoofdstuk af. In de appendix worden richtlijnen aangereikt die de lezer moet toelaten om de performantie van hoogefficiënte LEDs met elkaar te vergelijken.

2.2 Basisprincipes van halfgeleider-LEDs

2.2.1 Recombinatie in actieve gebieden

We kunnen drie mechanismen van atoom-veldinteractie onderscheiden: spontane emissie, gestimuleerde emissie en absorptie. De waarschijnlijkheid dat een elektron in de conductieband recombineert naar de valentieband met vrijlating van een foton met een energie per volume-eenheid $\hbar\omega$ wordt door Fermi's gouden regel gegeven (Vgl.(2.2)).

Door middel van deze regel kunnen we de breedte van het intrinsieke emissiespectrum – veroorzaakt door inhomogene verbreding – berekenen. We vinden voor

GaAs (bij een lage stroomdichtheid en een emissiegolflengte 980 nm) een inhomogene verbreding van ±32 nm. Deze spectrale breedte neemt met toenemende stroom toe en is breder dan de homogene verbreding, typisch enkele tientallen pm.

2.2.2 p-n junctie

Bij spontane emissie relaxeert een elektron vanuit de conductieband naar de valentieband en recombineert er met een gat. Injectie van minoritairen in een gedopeerde halfgeleider kan door middel van een voorwaarts gepolariseerde p-n junctie gebeuren. Een p-i-n junctie, waarbij een intrinsiek laag met kleinere bandafstand omvat wordt door een n- en p-gedopeerde laag, is echter beter geschikt voor lichtemitterende componenten: door de lagere bandafstand van de emitterende laag worden de uitgezonden fotonen niet in de omliggende lagen geabsorbeerd en de plaats waar de emissie gebeurt, is beter gecontroleerd. Het gebruik van QW's verschaft daarenboven controle op de emissiegolflengte en verhoogt de ladingsdragersdichtheid. In dit werk gebruiken we de actieve laag die in Tabel 2.1 gegeven wordt.

2.2.3 Hoogefficiënte LEDs of hoe we Snellius' wet omzeilen

Extractie-efficiëntie van een LED
We hebben reeds in de introductie opgemerkt dat de extractie-efficiëntie in standaard LEDs door Snellius' wet beperkt wordt. Deze wet dicteert de transmissiehoek θ_2 van licht dat vanuit een medium met brekingsindex n_1 invalt op een medium met brekingsindex n_2 onder een hoek θ_1 (Vgl.(2.16)):

$$n_1 \sin\theta_1 = n_2 \sin\theta_2$$

Wanneer $\theta_1 > \arcsin(n_2/n_1) = \theta_c$, is het licht in medium 2 evanescent. De reflectiecoëfficiënt is 1 en het regime wordt Totaal Inwendige Reflectie (TIR) genoemd. Bij een hoog brekingsindexverschil is de kritische hoek θ_c klein. De enkelzijdige η_{extr} van een standaard LED met een interne isotrope velddistributie kan ruwweg geschat worden of 1%, waarbij rekening wordt gehouden met de Fresnelverliezen. Bij encapsulatie van de component in een epoxy omhulsel met ronde kop, kan η_{extr} tot 4% gebracht worden door de hogere brekingsindex $n_2 = 1.5$ van de epoxy. Om deze η_{extr} drastisch te verhogen worden in de literatuur meerdere technieken beschreven. De voornaamste technieken, compatibel met de planaire technologie, worden hier besproken.

Extractie via meerdere facetten
Een hogere η_{extr} kan men behalen door het licht via meerdere facetten uit te koppelen. Bij gebruik van een transparant super- en substraat kan een $\eta_{ext} = 32\%$ gerealiseerd worden [5] . Het licht wordt er via de zes facetten van de cubusvormige LED geëxtraheerd. Hewlett Packard, de aanvoerder van dit onderzoek, vervolgde zijn weg naar hogere efficiënties. In 1999 bracht HP een geïnverteerde piramide op de markt met een $\eta_{ext} = 60.9\%$, een wereldrecord [2] . Door de piramidale vorm wordt het pad van de fotonen na meervoudige reflecties dusdanig veranderd dat ze niet gevangen blijven in het regime van TIR. Doordat de extractie via meerdere

facetten gebeurt, is deze component niet geschikt voor toepassingen die een hoge radiantie vragen.

Tapse LEDs
W. Schmid *et al.* gebruikt een planaire getaperde LED om de η_{extr} te verhogen via één extractiefacet. Opnieuw wordt het pad van de fotonen door meervoudige reflecties aan de hellende vlakken van de taper gewijzigd. De verhoogde kans tot extractie leidt tot $\eta_{ext} = 30\%$ [3]. Het oppervlak wordt echter niet efficiënt gebruikt: het injectie-oppervlak beslaat slechts 2% van het extractie-oppervlak, wat nefast is voor het schalen van de component en voor de radiantie.

LEDs met een verruwd oppervlak
Windisch *et al.* toonden aan dat door verstrooiing van fotonen aan een verruwd oppervlak van de LED een $\eta_{ext} \approx 50\%$ kan behaald worden. Het geïnjecteerde gebied beslaat ongeveer 10% van het extractie-oppervlak [4].

Resonantecaviteits-LEDs
Het mechanisme waarop de RCLED steunt om de η_{extr} te verhogen, is volledig anders dan de vorige technieken. Hier wordt door interferentie het emissiepatroon veranderd. Deze component is een basiselement van de GA-RCLED – de component bestudeerd in dit werk – en zal dan ook in een aparte paragraaf gedetailleerder behandeld worden.

Toepassingen van hoogefficiënte LEDs
Volgens een recent gepubliceerd rapport, wordt de wereldmarkt voor hoogefficiënte LEDs geschat op 3.4 miljard euro in 2005. Hoogefficiënte LEDs dienen een brede waaier van toepassingen (lees hieromtrent in Hoofdstuk 1).

2.3 De RCLED

2.3.1 Basisprincipes van spontane emissie in een gelaagd medium

Modificatie van het emissiepatroon: theoretische benadering
In een RCLED wordt de spontane emissie in een meerlagige Fabry-Pérotresonator gegenereerd. Interferentie zorgt ervoor dat het inwendige emissiepatroon niet langer isotroop is. Een goed ontworpen caviteit zorgt voor een toegenomen emissie in de richting van de extractieconus, en verhoogt aldus η_{extr}.

De hoekafhankelijke inwendige intensiteit wordt gegeven door Vgl.(2.21):

$$I_{dip}^{pol}(\theta) = \frac{|A_{\uparrow}^{pol} + A_{\downarrow}^{pol}|r_2|e^{-j2\phi_{2\,eff}}|^2}{|1 - |r_1 r_2|e^{-j2\phi_{eff}}|^2}$$

De teller noemen we de staande-golffactor $\zeta(\phi_{2\,eff})$ en is verantwoordelijk voor de afhankelijkheid van de geëmitteerde intensiteit van de plaats van de dipool in de caviteit. De noemer is de caviteitsversterkingsfactor of de Airyfactor $\Gamma(\phi_{eff})$. De Airyfactor is periodiek in ϕ_{eff} met een periode π, en bij een maximum wordt de caviteit "resonant" genoemd. Resonanties waarvoor $\theta < \theta_c$ zijn Fabry-Pérotmodes

en kunnen de caviteit verlaten. Is $\theta > \theta_c$, dan spreken we van geleide modi die lateraal in de caviteit propageren.

Versterking van de totale emissie of de Purcell-factor
De impact die de caviteit heeft op het totale vermogen dat uitgezonden wordt door een dipool, wordt uitgedrukt als de verandering van de leeftijd van het elektron-gat recombinatieproces in de caviteit ten opzichte van emissie in bulkmateriaal. Deze verhouding is de Purcell-factor. De Purcell-factor van praktische RCLEDs nadert 1 (caviteit in slechts 1 dimensie en spiegels met eerder lage reflectiecoëfficiënten).

2.3.2 Ontwerpregels

Een kwantitatief accuraat ontwerp van een RCLED vereist een numerieke analyse op basis van Vgl.(2.21). Er kunnen echter in het eerste stadium van het ontwerp enkele vuistregels aangewend worden.

Finesse, kwaliteitsfactor en (effectieve) caviteitsorde
We definiëren de finesse F, de (effectieve) caviteitsorde $m_{c(eff)}$ en de kwaliteitsfactor Q. m_{ceff}, die evenredig is met de effectieve caviteitsdikte, is een maat voor het aantal resonante modes in de caviteit. Het is belangrijk m_{ceff} zo laag mogelijk te houden aangezien de η_{extr} – in het geval slechts één mode de caviteit kan verlaten – benaderend gegeven wordt door Vgl.(2.36):

$$\eta_{extr} \cong 1/(\lfloor m_{c\,eff,\theta} \rfloor/2)$$

Dipool in een halfgeleiderslabcaviteit: invloed van caviteitsdikte en positie van de actieve laag
De η_{extr} is evenredig met de verhouding van de oppervlakte onder de Airyfunctie in de extractieconus met de totale oppervlakte onder de Airyfunctie. De Fabry-Pérotresonantie heeft bijgevolg een optimale angulaire positie die door de caviteitsdikte bepaald wordt. De optimale positie (grootste verhouding van respectieve oppervlaktes) is deze waarbij de Airypiek van de Fabry-Pérotresonantie overeenkomt met een uitwendige hoek $\theta_0^{ext} = 45°$. Het verreveldprofiel van een RCLED met een hoge totale η_{extr} is dus meerlobbig.

De staande-golffactor $\zeta(\phi_{2\,eff})$ drukt de koppelingssterkte van de dipool met de optische modi uit. Deze sterkte is afhankelijk van de dipoolpositie ten opzichte van het staande-golfpatroon van de modi: is de dipool geplaatst in een knoop van de mode dan is de koppelingssterkte minimaal. In een buik geplaatst is de koppeling maximaal. Het interferentie-effect wordt uitgemiddeld wanneer een dikke actieve laag (minstens $\lambda_0/2n_s$) wordt gebruikt. De totale versterking wordt in dat geval gehalveerd ten opzichte van een caviteit met een dunne actieve laag in een buik geplaatst.

Wordt de caviteitsdikte (en dus ook de caviteitsorde m_{ceff}) drastisch verhoogd, dan neemt het aantal resonanties toe. Er werd reeds gezegd dat dit nefast is voor η_{extr}.

Caviteit met DBR spiegel(s): invloed van de spiegelreflectiviteit
Via m_{ceff} beïnvloedt de fase van de reflectiecoëfficiënten van de spiegels de η_{extr}. De hoekafhankelijkheid van die fase wordt uitgedrukt in een penetratiediepte waarmee de caviteitsdikte vermeerderd wordt voor het bepalen van m_{ceff}. Metalen spiegels hebben een kleine penetratiediepte, maar kunnen grote verliezen veroorzaken, vooral wanneer die als uitkoppelspiegel worden gebruikt. DBR spiegels hebben een grotere penetratiediepte, maar lagere absorptieverliezen. Hoe hoger het brekingsindexverschil tussen de lagen van de DBR, hoe lager die penetratiediepte. Tevens wordt dan het angulaire gebied met hoge reflectiecoëfficiënten groter.

De amplitude van de reflectiecoëfficiënt optimaliseren we door die waarde te kiezen die de Fabry-Pérotmode een optimale finesse F geeft, die de verliezen aanneembaar houdt en rekening houdt met de intrinsieke spectrale bandbreedte van de spontane emissie. Het aantal lagen in een DBR kan de reflectiecoëfficiënt over een breed bereik bepalen. De hoekafhankelijke reflectie laat echter ruimte voor lekkende DBR modi.

Invloed van temperatuur en het saturatiefenomeen
In praktijk worden RCLEDs elektrisch gepompt. Bij hoge stroomdichtheden treedt saturatie van het optisch vermogen op. Typische waarden zijn enkele $\mu W/\mu m^2$. Verschillende redenen liggen aan de basis: een hogere stroomdichtheid veroorzaakt een breder intrinsiek spectrum en zorgt voor opwarming van de actieve laag. Deze opwarming gaat samen met een afname van de interne efficiëntie en een verschuiving tussen de resonantiepiekgolflengte en de intrinsieke centrale golflengte.

RCLEDs met een grote diameter en fotonrecyclage
De fotonen van de geleide mode kunnen geabsorbeerd worden in de actieve laag en geheremitteerd worden. Hierdoor krijgt een foton een grotere kans om uitgekoppeld te worden. De η_{int} en bijgevolg de η_{ext} nemen toe. Een belangrijke factor die de toenamen van η_{int} bepaalt, is de absorptielengte van de geleide mode. Deze is meestal echter laag: ongeveer 100 μm, en dus groter dan de typische afmetingen van de gebruikte componenten. Fotonrecyclage nemen we vooral waar in RLCEDs met een grote diameter.

Modulatiebandbreedte van RCLEDs
De invloed van de caviteit op de modulatiesnelheid van de RCLED gebeurt via de bimoleculaire recombinatiecoëfficiënt. Deze is een maat voor de stralende recombinatiesnelheid. De verandering van de recombinatiesnelheid door de dipool in een caviteit te plaatsen, wordt weergegeven door de Purcell-factor. We hebben al gewezen op het feit dat in praktische, hoogefficiënte RCLEDs deze Purcell-factor slechts een weinig groter is dan één. De toename van de modulatiebandbreedte van RCLEDs is dus in vergelijking met conventionele LEDs eerder klein.

2.3.3 State-of-the-art

980-nm RCLEDs
Ondanks het ontbreken van een brede waaier aan toepassingsmogelijkheden voor

componenten met een emissiegolflengte van 980 nm, maakt het kwaliteitsvolle GaAs/Al(Ga)As systeem met InGaAs QW's deze componenten ideaal als "proof of principle". Een topemitterende caviteit met geoxideerde DBR onderspiegel toont de mogelijkheid aan om extractie-efficiënties van 30% ($\eta_{ext} = 28\%$) te realiseren [1].

650-nm RCLEDs
Componenten met een emissiegolflengte van 650 nm zijn commercieel belangrijk voor POF-communicatiesystemen. De golflengte 650 nm valt in het zichtbare spectrumgebied. De componenten kunnen dus tevens een brede waaier van niet-communicatiegerichte toepassingen dienen. Het GaAsP materiaal systeem wordt meer en meer vervangen door het hoogkwalitatieve AlGaInP. R. Wirth *et al.* rapporteren een topemitterende geëncapsuleerde component, dimensies 300 μm x 300 μm, met een $\eta_{wp} = 10.2\%$ [6].

850-880-nm RCLEDs
Naast (Fast-)Ethernet LAN datalinks, is de voornaamste toepassing van 850-880-nm emitterende componenten afstandsbediening en infraroodcommunicatie zoals gereguleerd door de IrDA. R. Bockstaele *et al.* vermelden een AlGaAs 850 nm topemitterende component met 2 DBR spiegels die een $\eta_{ext} = 14.6\%$ vertoont [7].

1300-nm en 1500-nm RCLEDs
Het voornaamste materiaalsysteem voor de componenten -die met hun golflengte bij uitstek geschikt zijn voor telecommunicatietoepassingen- is InP. Bovenop het bredere intrinsieke spectrum inherent aan de langere golflengte, begrenzen de beperkte haalbare brekingsindexcontrasten de maximaal te realiseren extractie-efficiëntie. Efficiënties van 9% en 6.8% worden voor respectievelijk 1300 nm en 1550 nm in de literatuur gevonden [8], [9].

2.3.4 Geavanceerde technieken

RC2LED
De RC2LED verhoogt de η_{extr} voor kleine numerieke apertuur. Door een DBR te vervangen door een resonantecaviteitsreflector wordt de penetratiediepte negatief [10].

RCLEDs met fotonische kristallen
De efficiëntie van planaire RCLEDs wordt beperkt door het verlies van het vermogen dat gekoppeld wordt naar de lateraal propagerende geleide modi. Wanneer we de homogeniteit in het vlak van de RCLED opheffen, krijgen we controle over het gedrag in deze dimensie. Dit kan gebeuren door middel van fotonische kristallen of periodieke roosters. Twee principes kunnen we onderscheiden: roosters die propagatie van de geleide mode verhinderen en roosters die de geleide mode diffracteren naar de extractieconus. De eerste zorgen voor een verboden gebied in de dispersierelatie van de geleide mode bij de emissiegolflengte. Dit vereist diepe roosters, geëtst door de actieve laag. Naast moeilijke stroominjectie worden dergelijke componenten gekweld door hoge oppervlakterecombinaties. Om deze laatste tegen

te gaan kunnen ondiepe roosters gebruikt worden, of een structuur waarbij een caviteit gecreëerd wordt in het vlak. De dimensies van de caviteit zijn meestal kleiner dan de diffusielengte van de ladingsdragers, zodat oppervlakterecombinatie niet volledig vermeden wordt.

Veel praktischer zijn de structuren die de geleide mode uitkoppelen door diffractie. Een ondiep rooster boven de actieve laag verandert het moment van de geleide fotonen zodat die geëxtraheerd kunnen worden. De GA-RCLED, de component die wij in dit werk bestuderen, is gebaseerd op dit principe en komt verder in dit werk uitgebreid aan bod. Een variant op de laatste is een structuur waarbij het rooster en de actieve laag niet samenvallen. Het homogene centrale stuk extraheert de Fabry-Pérotmode, het rooster aan de periferie extraheert de geleide mode. Rattier *et al.* verwachten een supplementaire extractie van 10% [1]. De GA-RCLED is complexer aangezien het verticale en horizontale optisch gedrag gekoppeld zijn. Slecht ontwerp of realisatie kunnen ertoe leiden dat de efficiëntie van de GA-RCLED slechter is dan de respectieve RCLED zonder rooster. De GA-RCLED is daarentegen meer flexibel wat betreft de mogelijke dimensies.

2.3.5 Vooruitzichten van de RCLED

RCLEDs zijn niet de enige kandidaten die in communicatie- en non-communicatietoepassingen als hoogefficiënte bronnen gebruikt kunnen worden. Ze concurreren met andere hoogefficiënte LEDs en VCSELs.

Ten opzichte van vele andere hoogefficiënte LEDs is het voornaamste voordeel van de RCLED zijn planaire vorm en hoge radiantie. Bovendien is de fabricage standaard.

Het fabricageproces is ook eenvoudiger en goedkoper dan dat van VCLSELs. RCLEDs presteren beter dan VCSELs wanneer de applicatie een hoogefficiënte bron nodig heeft bij een laag-vermogenwerkingspunt, zoals in dichtgestapelde matrices.

2.4 Conclusies

De RCLED is de geprefereerde lichtbron wanneer een combinatie van hoge efficiëntie en radiantie gevraagd is. Deze kunnen nog verder verhoogd worden door middel van een periodiek rooster in de spiegels van de caviteit. Dit principe wordt in dit werk besproken.

3 Diffractieve nanostructuren

3.1 Diffractieve nanostructuren

3.1.1 Isotrope media

Het golfvectordiagram (WVD) is een grafische voorstelling van de mogelijke golfvectoren **k** voor een specifieke optische frequentie in de k-ruimte. Het Brillouindiagram (BD) stelt de dispersierelatie tussen de optische frequentie ω en k grafisch voor.

Voor een isotroop medium met brekingsindex n_1, liggen de mogelijke golfvectoren op het boloppervlak $k_0 n_1$. De dispersierelatie van een meerlagige structuur wordt gevonden door de resonante conditie voor consistentie op te leggen (Vgl.(3.3)).

3.1.2 Periodiek gemoduleerde media

Door middel van de Floquetstelling kunnen we aantonen dat de dispersierelatie van een periodieke (langs x-as) structuur eveneens periodiek is, maar dan in k_x met periode $2\pi/\Lambda$. Dit duidt de aanwezigheid van hogere-ordeharmonischen naast de fundamentele orde aan. Contra-directioneel propagerende hogere-ordeharmonischen geven aanleiding tot een verboden gebied in de dispersierelatie. Hogere-ordeharmonischen die grafisch in het BD boven de lichtlijn vallen, kunnen vermogen koppelen naar de buitenwereld.

Ook het WVD toont de aanwezigheid van een verboden gebied en lekkende hogere-ordeharmonischen aan. Bij zwakke periodieke modulaties wordt de propagatieconstante β van de respectieve niet-gemoduleerde structuur slechts weinig veranderd. Het WVD van de periodieke structuur vinden we dan door projectie van die propagatieconstante volgens de respectieve Braggvectoren. Het WVD is een ideaal grafisch hulpmiddel om het gedrag van diffractieve structuren kwalitatief te analyseren.

3.2 Modellering van diffractieve structuren

3.2.1 Algemeen diffractieprobleem aan een rooster

Het algemeen 3D diffractieprobleem staat geschetst in Fig. 1. Een lineair gepolariseerde elektromagnetische golf valt in onder een willekeurige hoek θ en met azimuthale hoek ϕ op een gelaagd periodiek medium. De roosterperiode is in het algemeen samengesteld uit een aantal gebieden met verschillende brekingsindex. Het rooster is begrensd met twee half-oneindige ruimtes 1 en 2 met brekingsindex n_1 en n_2. De Floquet-Blochstelling stelt dat de veldoplossingen in de homogene media 1 en 2 te schrijven zijn als (Vgl.(3.16)):

$$\mathbf{E}_1 = \mathbf{E}_{inc} + \sum_{m,n} \mathbf{R}_{mn} e^{-j\mathbf{k}_{1mn}\cdot\mathbf{r}}$$

$$\mathbf{E}_2 = \sum_{m,n} \mathbf{T}_{mn} e^{-j\mathbf{k}_{2mn}\cdot(\mathbf{r}-\mathbf{d})}$$

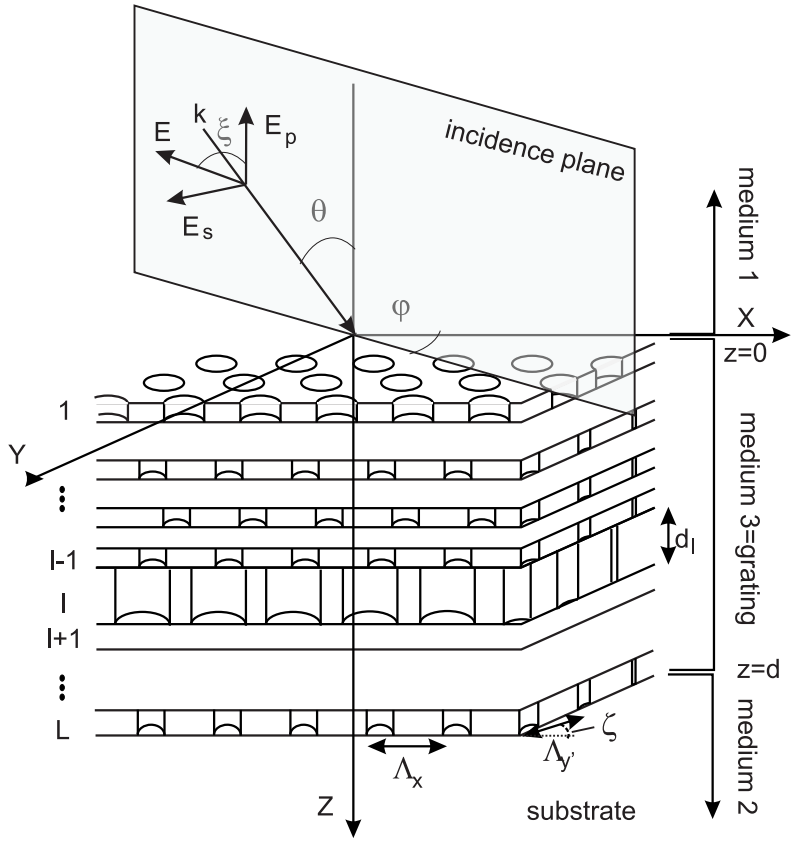

Figuur 1: 3D diffractieprobleem.

Het diffractieprobleem oplossen betekent dat we de complexe amplitudes van de reflectie- en transmissiecoëfficiënten $\mathbf{R}_{mn}$ en $\mathbf{T}_{mn}$ van de diffractieordes dienen te bepalen. Die unieke oplossing vinden we door Maxwells randvoorwaarden op te leggen aan de randen van het rooster en de half-oneindige ruimtes. Verschillende modellen, met elk hun eigen voorstelling van veldoplossing in het rooster, worden in de literatuur gevonden. Wij hebben gekozen om de rigoureuze gekoppeldegolfanalyse (RCWA) uit te werken voor diffractie aan 2D roosters. De GA-RCLED vereist een nauwkeurige berekening van de complexe $\mathbf{R}_{mn}$ en $\mathbf{T}_{mn}$. Bovendien was reeds een programma RODIS beschikbaar dat diffractie aan 1D roosters simuleert.

3.2.2 Overzicht van de verschillende diffractiemodellen

Integraal- of differentiaalmethode?
We kiezen een differentiaalmethode boven een integraalmethode aangezien deze beter geschikt is voor het simuleren van het diffractief gedrag van roosters met een discontinu (gekanteeld) profiel.

Rigoureuze gekoppeldegolf- of modale methode?
De gekoppeldegolf- en modale methode hebben elk hun eigen voorstelling van het veld in het roostergebied. Hun naam verraadt hun vooropstelling van veldoplossing in het roostergebied. Beide methodes zijn duaal, maar numerieke methodes om het randvoorwaardenprobleem op te lossen dat via de modale methode tot stand komt, zijn slechts voor een aantal specifieke periodieke modulaties gekend. De toepassingsmogelijkheden van de modale methode zijn dan ook beperkter.

Benaderende diffractietheorieën?
De computationele complexiteit van rigoureuze methodes kan efficiënt ontwerp van roosters en hun toepassingen in de weg staan. Afhankelijk van de roosterparameters kunnen benaderende theorieën gebruikt worden. De roosterparameters van de GA-RCLED vallen echter buiten de geldigheidsgebieden van de gangbare benaderende diffractietheorieën.

3.3 De rigoureuze gekoppeldegolftheorie

De RCWA werd door Moharam en Gaylord gedefinieerd voor planaire en conische diffractie aan 1D roosters [11]- [15]. Li [16] en Lalanne [17] verhoogden de convergentiesnelheid van de oplossing voor het geval TM-gepolariseerd licht invalt op een geleidend rooster.

Deze methode die diffractie analyseert aan 1D roosters, werd door Dhoedt geïmplementeerd [18]. Wij breiden de methode uit tot planaire en conische diffractie aan 2D roosters.

3.3.1 Opdeling van 2D-periodiek profiel in lagen

Diffractieroosters met een willekeurig profiel kunnen benaderd worden door dat profiel op te delen in verschillende lagen. De periodieke brekingsindex in iedere laag is dan onafhankelijk van z. Dit geldt ook voor de Fouriercomponenten van de brekingsindex van de respectieve lagen (Vgl.(3.21)).

3.3.2 Constructie van de gekoppeldegolfvergelijkingen

De eerste stap is het opstellen van de gekoppeldegolfvergelijkingen. Hierbij wordt de oplossing van het veld in iedere laag van het rooster geschreven als een Fourierexpansie van de ruimtelijke harmonischen, waarbij de Fouriercomponenten een z-afhankelijkheid vertonen. Deze z-afhankelijkheid wijst op de koppeling tussen de verschillende harmonischen. Substitueren we de Fourierontwikkeling voor de permittiviteit van het rooster en de Fourierontwikkeling voor de velden in het roostergebied in de vergelijkingen van Maxwell, dan verkrijgen we de gekoppeldegolfvergelijkingen. Deze kunnen in matrixvorm worden geschreven (Vgl.(3.27)).

3.3.3 Beperken van het aantal diffractieordes

De matrices in Vgl.(3.27) hebben oneindige dimensies. Een numerieke implementatie zal deze matrices afbreken tot matrices met een eindige dimensie. Hierbij hebben we gekozen om deze diffractieordes te weerhouden die in een parallellogram rond de nulde diffractieorde liggen. Met M de hoogste orde weerhouden in de positieve x-richting, en N analoog in de y'-richting, is het totaal aantal ordes $n = (2M + 1)(2N + 1)$. De nauwkeurigheid van de oplossing wordt bepaald door het aantal ordes die in de berekening weerhouden wordt.

Wannneer we het aantal ordes in de berekening beperken, worden de vergelijkingen Vgl.(3.27) slecht geconditioneerd. De afgeknotte vergelijkingen voldoen ter hoogte van de discontinuïteiten van de relatieve permittiviteit immers niet langer aan de continuïteitseis van het desbetreffende veld. Li herdefinieert Laurents factorisatieregel voor afgeknotte discontinue reeksen. Deze nieuwe regels passen we toe voor 2D roosters. Vgl.(3.27) wordt hiermee vervangen door Vgl.(3.37).

3.3.4 Oplossing van de gekoppeldegolfvergelijking

Vgl.(3.37) wordt uitgewerkt tot een eigenwaardenvergelijking. Door deze eigenwaardenvergelijking op te lossen verkrijgen we een uitdrukking voor de ruimtelijke harmonische componenten in de verschillende lagen van het roostergebied in functie van de eigenwaarden en eigenvectoren (Vgln.(3.40) en (3.41)).

3.3.5 Elektromagnetische randvoorwaarden

De ongekende constanten in Vgln.(3.40) en (3.41) en $R_{s(p),mn}$ en $T_{s(p),mn}$ – allen samen $4n(L+1)$ onbekenden – kunnen door het opleggen van de randvoorwaarden gevonden worden.

3.3.6 Transmissiematrixalgoritme voor meerlagige structuren

Het oplossen van de $4n(L+1)$ vergelijkingen waartoe de randvoorwaarden leidden, gebeurt met een ingenieus transmissiematrixalgoritme voorgesteld door Moharam *et al.*. Door dit algoritme worden matrixinversies vermeden die tot numerieke instabiliteiten kunnen leiden. Een oplossing voor $R_{s(p),mn}$ en $T_{s(p),mn}$ wordt gevonden op het einde van de toepassing van dit algoritme.

3.3.7 Diffractie-efficiëntie

De diffractie-efficiëntie van de mn^{de} orde wordt gedefinieerd als de verhouding van het vermogen in deze orde tot het invallend vermogen. We vinden voor de diffractie-efficiëntie in de mn^{de} gereflecteerde orde en getransmitteerde orde respectievelijk (Vgl.(3.60)):

$$\mathrm{DE}_{R,mn} = \mathrm{Re}\left(\frac{-k_{1,z,mn}}{k_{inc,z}}\right)|R_{s,mn}|^2 + \mathrm{Re}\left(\frac{-k_{1,z,mn}/n_1^2}{k_{inc,z}}\right)|R_{p,mn}|^2$$

$$\mathrm{DE}_{T,mn} = \mathrm{Re}\left(\frac{k_{2,z,mn}}{k_{inc,z}}\right)|T_{s,mn}|^2 + \mathrm{Re}\left(\frac{k_{2,z,mn}/n_2^2}{k_{inc,z}}\right)|T_{p,mn}|^2$$

3.3.8 Convergentie

De implementatie van de RCWA is stabiel en convergeert voor een toenemend aantal diffractieordes. De nauwkeurigheid van de berekening zal enkel afhangen van het aantal ordes in de expansie van de ruimtelijke harmonischen in de roostergebieden. De convergentiesnelheid in functie van het aantal ordes wordt voor een diëlektrisch en een metallisch rooster in Fig. 3.9 getoond. De convergentiesnelheid van diffractie aan een metallisch rooster is trager door de grotere spatiale variaties in de velden aan de randen van de metaaltanden. De waarden komen overeen met data gepubliceerd in de literatuur.

De absorptie van de roosters die gebruikt zullen worden in de GA-RCLED wordt gesimuleerd, zowel voor normale als schuine inval, corresponderend met respectievelijk de Fabry-Pérotmode en de geleide mode. Het metallische rooster vertoont een significant grotere absorptie dan het partieel met metaal bedekte rooster.

Deze berekeningen worden behaald door het oplossen van een eigenwaardenprobleem. Het oplossen van het eigenwaardenprobleem is evenredig met n^3, waarbij n de dimensie van de op te lossen matrix is. Het is meteen duidelijk dat het simuleren van diffractie aan een 2D rooster tijdrovend is. Immers vereist een nauwkeurig resultaat een groot aantal ordes in de berekening.

3.4 Conclusies

Diffractieve nanostructuren kunnen door middel van het WVD kwalitatief bestudeerd worden.

Een kwantitatieve analyse wordt aangeboden door de RCWA. De RCWA werd voor diffractie aan 2D roosters uitgewerkt. De implementatie, in C++ in een Unix-omgeving, levert accurate waarden voor diffractie aan verliesloze en verlieshebbende 2D roosters. Dit blijkt uit een vergelijking met data uit de literatuur.

Een simulatieprogramma is nu beschikbaar om accuraat diffractie aan 2D roosters te berekenen. Door de numerieke complexiteit blijken de berekeningen echter tijdrovend te zijn. De verschillende matrixalgoritmes zijn nog vatbaar voor optimalisatie van de computationele snelheid.

4 GA-RCLED: theorie en analyse

4.1 Inleiding

De externe efficiëntie van standaard LEDs wordt beperkt door de lage extractie-efficiëntie. Het licht wordt gegenereerd in een materiaal met een hoge brekingsindex. Totale inwendige reflectie – gedicteerd door Snellius' wet – limiteert extractie tot enkele percenten.

Het belang van hoge efficiënties werd aangehaald in de introductie. Verschillende technieken werden dan ook geïntroduceerd om Snellius' wet te omzeilen: getaperde LEDs, LEDs met geïnverteerde piramidale structuur, niet-resonante LEDs met verruwd oppervlak. Bij deze technieken wordt het pad van de fotonen door de specifieke structuur als dus danig gevarieerd zodat de kans op extractie verhoogt.

Een andere techniek, die uitgebreid aan bod kwam in Hoofdstuk 2, is de resonantecaviteits-LED. Het spontane verval vindt plaats in een caviteit. Deze optische omgeving brengt een spatiale herverdeling van het licht teweeg, door een discretisatie van propagerende optische modi. Bij een goed ontwerp wordt het licht bij voorkeur uitgezonden loodrecht op het substraat. Externe efficiënties van 28% worden gerapporteerd. Echter, de opgewekte modi die lateraal in de caviteit propageren kunnen niet geëxtraheerd worden via het extractiefacet en zijn verloren. Een oplossing voor dit verlies kan gevonden worden in een tweedimensionaal (2D) periodiek rooster geïntegreerd in één of meer facetten van de caviteit. Verschillende ontwerpopties zijn mogelijk. Het rooster, of beter fotonisch kristal, kan een verboden gebied creëren in de dispersierelatie van de geleide mode of het rooster kan de geleide mode diffracteren naar een extraheerbare richting. Wij kiezen voor de laatste optie, waarbij het diffractieve rooster of het extractiegebied samenvalt met het actieve gebied. Dit zal resulteren in een hoogefficiënte compacte planaire component met enkelzijdige extractie. We noemen deze component de Rooster-Geassisteerde RCLED (GA-RCLED). Een alternatieve configuratie bestaat erin optische extractie en elektrische injectie te scheiden door het rooster aan de periferie van de actieve laag te plaatsen.

Dit hoofdstuk brengt een kwalitatieve analyse met behulp van het WVD en een rigoureuze analyse aan.

4.2 Kwalitatieve analyse met WVD

Conceptueel wordt de GA-RCLED in drie stappen uitgelegd, overeenkomstig de basisprincipes van de component.

4.2.1 Dipoolemissie in een planaire caviteit

In een caviteit is de emissie van een dipool niet langer isotroop. Door interferentie worden de fotonen spatiaal geredistribueerd. We kunnen vier kanalen onderscheiden: (*1*) extraheerbare Fabry-Pérotmode; (*2*) geleide modi totaal intern gereflecteerd aan beide facetten van de caviteit; (*3*) lekkende modi die bij gebruik van een DBR buiten het angulair hoogreflecterende gebied vallen en in

het substraat geabsorbeerd worden; (*4*) metaalverliezen. De drie eerste kanalen kunnen door middel van hun golfgetal in de k-ruimte voorgesteld worden. Het golfvectordiagram of WVD van een planaire caviteit staat voorgesteld in Fig. 4.1.

4.2.2 Extractie van geleid licht door middel van een rooster

Het WVD kan ook gebruikt worden om een kwalitatieve analyse uit te voeren van het gedrag van een geleide mode in een passieve golfgeleider voorzien van een ondiep rooster (Fig. 4.2). Het geleide licht wordt in dit WVD voorgesteld door een cirkel met als straal de propagatieconstante $\beta = |\mathbf{k}_{\|}|$ van de geleide mode. Door het ondiepe karakter van het rooster komt deze min of meer overeen met de propagatieconstante in de respectieve onverstoorde golfgeleider. Volgens de Floquet-Blochstelling zullen golven met $\mathbf{k}_{\|} = \mathbf{k}_{0\|} n_{eff} + n\mathbf{K}_x + m\mathbf{K}_{y'}$, en m, n gehele getallen, aanwezig zijn door de periodieke corrugatie met respectieve Bragg vectoren $\mathbf{K}_x$ en $\mathbf{K}_{y'}$. Het geleide licht zal continu vermogen koppelen naar deze diffractieordes en vice versa. In het WVD wordt dit voorgesteld door een projectie volgens de Braggvectoren van de cirkel representatief voor het geleide licht. De stukken van deze projecties die met de extractieconus overlappen, kunnen geëxtraheerd worden. Zo kunnen we grafisch aantonen dat met een 1D rooster in een GaAs systeem bij een golflengte van 980 nm, 22% geëxtraheerd kan worden. Met een triangulair eerste-orderooster wordt dit 66%, een triangulair tweede-orderooster 100%. Let wel, dit is een kwalitatieve analyse die een indicatie geeft tot welke mate de geleide mode maximaal uitgekoppeld kan worden. Het stelt een bovenlimiet aan de extraheerbare fractie van de geleide mode. Kwantitatieve informatie dient door middel van een rigoureuze analyse gevonden te worden.

4.2.3 De GA-RCLED

Analoog aan extractie van een geleide mode in een passieve structuur, kan een geleide mode, opgewekt door een dipool geplaatst in een periodiek gemoduleerde structuur, geëxtraheerd worden. We spreken van een GA-RCLED (zie Fig. 4.3). Hiervoor dienen we een correcte waarde voor de caviteitsparameters (zoals caviteitsdikte, roosterdiepte, periode, vulfactor, etc.) te vinden. Dit gebeurt door middel van de rigoureuze analyse gepresenteerd in de volgende paragraaf.

4.3 Rigoureuze analyse

4.3.1 Elektrische dipooltransitie

We bestuderen spontane emissie in een niet-absorberende laag omgeven door twee periodiek gemoduleerde gelaagde media. De bron en de media zijn oneindig uitgestrekt in de x- en y-richting (zie Fig. 4.4). De luminescente punten worden verondersteld licht te emitteren in een dipooltransitie. De elektrische dipool oscilleert met een vaste frequentie ω en heeft een vast dipoolmoment met willekeurige maar vaste oriëntatie. De verandering van de radiatieve leeftijd van een elektrische dipooltransitie kan berekend worden door middel van het genormaliseerde stralingspatroon. Dit stralingspatroon wordt in de volgende paragrafen berekend.

4.3.2 Stralingsveld van een elektrische dipool in homogene laag

We ontbinden het elektrische dipoolveld in vlakke golven (Vgl.(4.16)):

$$\begin{aligned}
&\mathbf{E}_{dip}(x,y,z) \\
&= \int_{-\infty}^{+\infty}\int_{-\infty}^{+\infty} \left[\frac{jn_sk_0}{2(2\pi)^2}\mathbf{p}(k_x,k_y)\right] e^{-j\left(k_xx+k_yy+\sqrt{n^2k_0^2-k_x^2-k_y^2}|z|\right)} \left[\frac{dk_xdk_y}{n_sk_0k_z}\right] \\
&= \left(\int_0^{\pi/2} + \int_{\pi/2+j0}^{\pi/2+j\infty}\right) \int_0^{2\pi} \left[\frac{jn_sk_0}{2(2\pi)^2}\mathbf{p}(\theta,\varphi)\right] e^{-j\left(k_xx+k_yy+\sqrt{n^2k_0^2-k_x^2-k_y^2}|z|\right)} [\sin\theta d\theta d\varphi]
\end{aligned}$$

In beide uitdrukkingen is de tweede term tussen haakjes een vlakke golf, de derde term is de ruimtehoek en de eerste term stelt het vlakkegolfveld voor (per eenheid ruimtehoek). Door het vermogen, uitgestraald door de dipool in een homogeen medium, te normaliseren, krijgen we voor de vlakkegolfvelden de waarden getabuleerd in Tabel 4.1.

4.3.3 Dipolen in periodiek gemoduleerde gelaagde media

De afleiding van het stralingsveld van een planaire distributie willekeurig georiënteerde dipolen in een 2D-periodiek gemoduleerd gelaagd medium wordt in verschillende stappen opgesplitst.

Set vlakke golven gekoppeld door Braggvoorwaarde
Om het stralingspatroon te berekenen in periodiek gemoduleerde lagen, passen we het transfermatrixformalisme aan dat ontwikkeld werd voor het analyseren van dipoolemissie in homogeen gelaagde media. Het wezenlijke verschil ligt bij de aanwezigheid van Braggkoppeling tussen de vlakke golven met golfvectoren met een parallelle golfcomponent (Vgl.(4.18)):

$$\mathbf{k}_{\parallel}^{mn} = \mathbf{k}_{\parallel}^{in} + m\mathbf{K}_x + n\mathbf{K}_{y'}$$

met m, n gehele getallen. Om deze koppeling uit te drukken, definiëren we matrices. De elementen van deze matrices zijn met de respectieve gediffracteerde ordes gerelateerd. Indien we in de numerieke berekeningen het aantal gediffracteerde ordes in de respectieve periodieke richtingen beperken tot M en N, krijgen we een $MN \times 1$ veldmatrix $\overline{\mathbf{E}}$ en $MN \times MN$ reflectiematrix $\overline{\overline{\mathbf{R}}}$, transmissiematrix $\overline{\overline{\mathbf{T}}}$ en veldpropagatiematrix $\overline{\overline{\mathbf{P}}}$. De elementen van deze matrices zijn vectoren. Opsplitsing in s- en p-polarisatie resulteert in scalaire matrices van respectievelijk orde $2MN \times 1$ en $2MN \times 2MN$.

Extern veld en intensiteit van een enkele dipool met (x_d, y_d, z_d)=$(0,0,0)$
Door middel van het transfermatrixformalisme wordt het externe veld van een

enkele dipool in de oorsprong en met een vaste oriëntatie afgeleid (Vgl.(4.27)):

$$\overline{\mathrm{E}}_2^0 = \left[\overline{\mathrm{E}}_{2s}^0 \overline{\mathrm{E}}_{2p}^0\right] = \left[\overline{\overline{I}} - \overline{\overline{P}}_1\overline{\overline{R}}_1\overline{\overline{P}}_1\overline{\overline{P}}_2\overline{\overline{R}}_2\overline{\overline{P}}_2\right]^{-1}\left[\overline{\overline{P}}_1\overline{\overline{R}}_1\overline{\overline{P}}_1\overline{A}_\uparrow + \overline{A}_\downarrow\right]$$

en de intensiteit (Vgl.(4.29)):

$$P_s(\theta_d, \varphi_d, 0, 0, 0, k_x^{mn}, k_y^{mn}) = \frac{1}{2}\sqrt{\frac{\varepsilon_0\varepsilon_2}{\mu_0}}\left|\overline{\mathrm{E}}_{2ext\,s}^0[Nm+n]\right|^2$$

$$P_p(\theta_d, \varphi_d, 0, 0, 0, k_x^{mn}, k_y^{mn}) = \frac{1}{2n_2^2}\sqrt{\frac{\varepsilon_0\varepsilon_2}{\mu_0}}\left|\overline{\mathrm{E}}_{2ext\,p}^0[Nm+n]\right|^2$$

Afhankelijkheid van de reflectie- en transmissiematrix van de bronpositie
De reflectie- en transmissiematrices waren tot nu toe gedefinieerd voor een bron die zich bevindt in de oorsprong. De reflectiecoëfficiënt $r_{s(p)s(p)}^{mn,m'n'}$ van invallend licht met een parallelle k-vector $\mathbf{k}_\parallel^{m'n'}$ naar een richting met parallelle k-vector $\mathbf{k}_\parallel^{mn}$ van een dipool op een locatie $\mathbf{r}_d = (x_d, y_d, 0)$ zal in fase verschoven zijn ten opzichte van deze van een dipool in de oorsprong (Vgl.(4.31)):

$$r_{s(p)s(p)}^{mn,m'n'}(\mathbf{r}_d) = e^{j(m'-m)\mathbf{K}_x.\mathbf{r}_d}\; e^{j(n'-n)\mathbf{K}_{y'}.\mathbf{r}_d}\; r_{s(p)s(p)}^{mn,m'n'}(\mathbf{0})$$

Dit geldt ook voor de transmissiecoëfficiënt. Deze plaatsafhankelijkheid dient in de reflectie- en transmissiematrix opgenomen te worden.

Extern veld en intensiteit van dipool met willekeurige locatie $(x_d, y_d, 0)$
Deze plaatsafhankelijkheid wordt opgenomen in de formule om het elektrische veld van een set door de Braggvoorwaarde gekoppelde vlakke golven te berekenen.

Intensiteit van een in het vlak verdeelde groep onderling incoherente dipolen met zelfde oriëntatie
In de berekening van het veld van een in het vlak willekeurig gepositioneerde dipool, worden de respectieve bijdragen van de dipool tot één van de Bragggekoppelde vlakke golf richtingen (k_x^{mn}, k_y^{mn}) coherent opgeteld. We tonen aan dat bij uitmiddeling van de dipoolpositie over een periodieke eenheidscel, de bijdragen nochtans incoherent optellen. Dit is te verklaren doordat de fasesprongverandering van de reflectie- en transmissiecoëfficiënt een zelfde periodieke afhankelijkheid vertonen.

Intensiteit van een in het vlak verdeelde groep onderling incoherente dipolen met verschillende oriëntatie
De intensiteit wordt vervolgens uitgemiddeld over de mogelijke dipooloriëntaties. Uitmiddeling leidt ertoe dat de intensiteit gemiddeld over de mogelijke oriëntaties gelijk is aan de intensiteit geproduceerd door drie incoherente stralende dipolen

met hun assen respectievelijk volgens de x-, y- en z-as georiënteerd.

Extractie-efficiëntie
De extractie-efficiëntie kan nu gemakkelijk berekend worden. Het totaal genormaliseerde vermogen L_2 in medium 2 behalen we door het intensiteitsprofiel van de respectieve dipoolorientaties (x,y en z) over de ruimtehoek 4π te integreren. Door de incoherente bijdragen van de respectieve Bragggekoppelde richtingen is deze integratie gemakkelijk te berekenen. Bij gebruik van de matrixnotatie, analoog als voorheen, wordt de integratie beperkt tot de ruimtehoek corresponderend met één periodieke eenheidscel. Deze oefening wordt herhaald om het totaal genormaliseerde vermogen L_{dip} door de dipolen uitgestraald te berekenen. De extractie-efficiëntie wordt dan (Vgl.(4.58)):

$$\eta_{extr}^{n_2} = \frac{L_2}{L_{dip}}$$

Deze analyse werd in C++, in een UNIX-omgeving geïmplementeerd.

4.3.4 Implementatie-aspecten

Oneindig dunne actieve laag
Bij het uitvoeren van de analyse wordt de bron in een oneindig dunne laag met een referentiebrekingsindex geplaatst. De reden is tweevoudig.

Door de oneindige integratie van de Fouriertransformatie van het dipoolveld, wordt evanescente koppeling van dit veld naar metalen of lagen met een hogere brekingsindex dan de index van de dipoollaag meegerekend. Bij de numerieke implementatie van de analyse wordt de integratie beperkt tot $|\theta| < \pi/2$ of $|k_{\|}| < 2\pi n_s/\lambda$. Een oneindig dunne laag met willekeurige brekingsindex, zal het fysisch gedrag van de structuur niet veranderen. Indien we die brekingsindex hoog kiezen, kunnen we artificieel de integratieruimte vergroten. Aldus kan evanescente koppeling meegerekend worden.

Ten tweede is de analyse enkel geldig wanneer de dipool zich in een verliesvrije laag bevindt. De actieve laag is echter meestal absorberend. Door de dipool in een oneindig dunne laag te plaatsen met een reële brekingsindex, wordt dit euvel omzeild.

Eindige spectrale bandbreedte
De analyse behandelt monochromatische emissie van dipolen. Het intrinsieke spectrum heeft echter een eindige breedte. Een Gaussisch profiel met een FWHM dat afhangt van de ladingsdragersdichtheid, benadert het intrinsieke spectrum sterk. Een met dit spectrum gewogen integratie van het golflengte afhankelijke monochromatische vermogen levert het totale vermogen.

Externe efficiëntie
De externe efficiëntie wordt gegeven door het product van de injectie-efficiëntie η_{inj} met de interne efficiëntie η_{int} en de extractie-efficiëntie η_{extr}. Indien de kwaliteit van het actieve materiaal hoog is, kan een fotonrecyclagefactor η_{rec} toegevoegd

worden. (Vgl.(2.46)).

$$\eta_{ext} = \eta_{inj}\eta_{int}\eta_{extr}\eta_{rec}$$

4.4 Conclusies

Een nieuw concept voor hoogefficiënte LEDs werd voorgesteld: de GA-RCLED. Het betreft een RCLED met een diffractieve structuur. De diffractieve structuur breekt de propagatie van het lateraal propagerende geleid licht, en buigt het af naar een extraheerbare richting.

Het WVD werd voorgesteld als grafisch middel om de GA-RCLED kwalitatief te bestuderen. Het geeft aan tot welke mate de geleide mode maximaal uitgekoppeld kan worden.

Een rigoureuze analyse van dipoolemissie in een periodiek gemoduleerd gelaagd medium werd afgeleid. Hiermee kan de GA-RCLED kwantitatief (extractie-efficiëntie, intensiteitsdistributie, etc.) geanalyseerd worden. De belangrijkste conclusie die uit de afleiding kan worden gedestilleerd, is dat bij uitmiddeling van de dipoolpositie over een periodieke eenheidscel, de respectieve bijdragen van de willekeurig gelokaliseerde dipool tot één van de Bragggekoppelde vlakkegolfrichtingen (k_x^{mn}, k_y^{mn}) incoherent optellen.

Deze analyse werd in C++, in een UNIX-omgeving geïmplementeerd. Numerieke berekeningen van GA-RCLEDs worden in Hoofdstuk 6 en Hoofdstuk 7 voorgesteld.

5 Realisatie van een GA-RCLED

5.1 Inleiding

Het vertrekpunt van een GA-RCLED is de planaire RCLED. We hebben gekozen om als basis de structuur die getabelleerd staat in Tabel 5.1 te nemen. Het betreft een GaAs/Al(Ga)As-materiaalsysteem, met drie InGaAs QW's. De diktes van de respectieve lagen worden door middel van het simulatiepakket voorgesteld in Hoofdstuk 4 bepaald. De epilagen worden in een MOCVD-reactor gegroeid. Het is belangrijk dat de lagen zo accuraat mogelijk gegroeid worden. In realiteit zijn afwijkingen van de beoogde dikte niet te vermijden. Fouten van 3% zijn niet ondenkbaar. Tevens dient de kwaliteit van het gegroeide materiaal hoog te zijn om optische absorptieverliezen en lage interne quantumefficiënties te vermijden.

Het processchema van de GA-RCLED begint met de realisatie van het rooster in het oppervlak van de epistructuur. Vervolgens wordt de LED (mesa, contacten, etc.) gefabriceerd. Deze opeenvolgende processtappen worden in volgende paragrafen besproken. Een SEM-foto van de dwarsdoorsnede van een gefabriceerde GA-RCLED wordt in Fig. 2 getoond.

5.2 Roosterfabricage

5.2.1 Inleiding

Optische diffractieve roosters hebben periodes in de orde van de golflengte. In onze toepassing varieert de gevraagde periode van 300-600 nm, of dus kleinste afmetingen van 100-300 nm. Standaard optische lithografie vertoont niet de nodige resolutie voor dergelijke fijnstructuren. Diepe-UV-lithografie, die gebruik maakt van een golflengte van 193 nm en geavanceerde technieken, kan daarentegen resoluties tot 120 nm aan. Momenteel wordt gebruik van diepe-UV-lithografie voor optische toepassingen in een ander onderzoeksproject onderzocht. Realisatie van lagere resoluties wordt door de meer geavanceerde nodige optica steeds duurder. Dit verklaart de toegenomen interesse voor alternatieve technieken. Eén van deze technieken is e-beam. State-of-the-art fotonische kristallen worden door middel van e-beam gefabriceerd. Hoewel de haalbare resoluties vele ordes kleiner zijn dan haalbaar met standaard optische productiemiddelen, wordt e-beam door zijn seriële schrijfkarakter niet schikbaar geacht voor massafabricage. E-beam is voornamelijk een onderzoekswerkmiddel.

De hoge haalbare nauwkeurigheid en resolutie van e-beam en de opgebouwde ervaring voor de productie van fotonische kristallen hebben we aangewend voor de fabricage van het rooster in onze GA-RCLEDs. De epilagen, gegroeid door INTEC, worden door de University of Glasgow (Prof. Thomas F. Krauss and Prof. Richard De La Rue) door middel van e-beam en RIE gestructureerd. De verdere processing tot LEDs werd door INTEC verzorgd.

Er werd tevens onderzoek verricht naar de haalbaarheid van holografie ter definiëring van 2D roosters. Dit 1-stapsproces is – in tegenstelling tot de seriële e-beam – wel geschikt voor massafabricage.

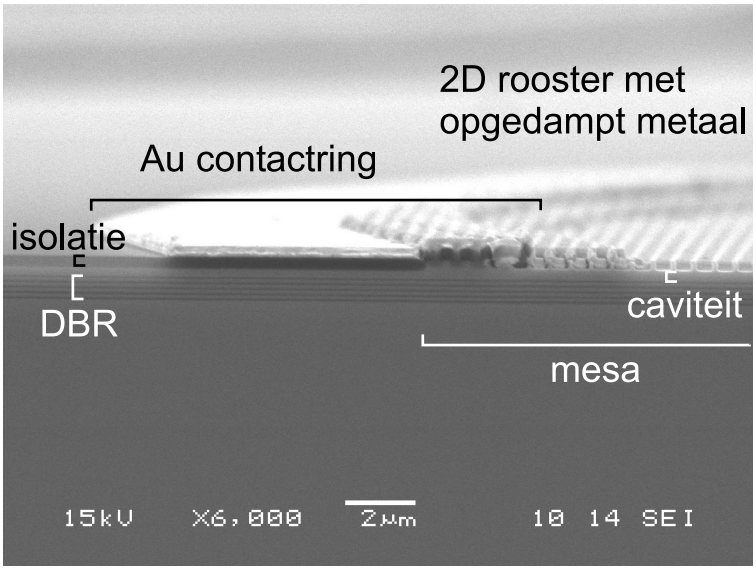

Figuur 2: SEM foto van de dwarsdoorsnede van een GA-RCLED. Enkel de helft van de circulaire mesa wordt getoond.

5.2.2 Holografische definitie van het rooster

De opeenvolgende stappen in het holografische proces worden in de volgende punten besproken. De eerste stap (schoonmaken, spinnen en bakken van ARC en fotolak) wordt niet gedetailleerd, aangezien dit basisprocesstappen zijn.

Holografische belichting
De interferentie-opstelling die we in dit onderzoek gebruikt hebben, is een interferometer gekend als Lloyds spiegel. Een lens focusseert licht van een UV-laser op een pinhole. Deze fungeert als spatiaal filter. Een quasi-Gaussische bundel verlaat de pinhole. Op een afstand die groot is ten opzichte van het te belichten oppervlak kan het licht als een vlakke golf beschouwd worden. Het sample is gemonteerd op een houder die aan een spiegel is vastgehecht. Een deel van de invallende golf belicht het sample direct, een ander deel bereikt het sample pas na reflectie op de spiegel. Deze twee bijdragen – direct en indirect – interfereren en creëren een 1D-periodiek intensiteitsprofiel waarvan de periode door Vgl.(5.1) gegeven wordt:

$$\Lambda = \frac{\lambda_{UV}}{2 \sin \alpha \sin \beta}$$

Dit is de klassieke set-up voor 1D roosters. De 2D-periodieke structuren kunnen door middel van verschillende technieken gerealiseerd worden. Bij een eerste techniek interfereren drie coherente bundels. Deze drie bundels kunnen verkregen worden door gebruik te maken van verschillende stralendelers, van een diffractief-roostermasker of van een uitgebreide Lloydsspiegelopstelling.

Een andere techniek realiseert een 2D rooster door meervoudige belichting in een 2-straleninterferometer. Deze techniek is recht toe recht aan en minder complex dan de vorige technieken. Voor een triangulair rooster wordt het sample 60° gedraaid tussen de twee opeenvolgende belichtingen. Voor een vierkant rooster draaien we het sample 90°. De belichtingsenergie van elke belichting is de helft zo sterk als de belichtingsenergie gebruikt bij de definiëring van 1D roosters. Visuele karakterisatie van de gerealiseerde roosters laat blijken dat deze techniek afdoende is.

Na de holografische belichting wordt het sample ontwikkeld in een verdunde KOH-oplossing. Het ontwikkelingsproces is zeer kort (enkele seconden) en gebeurt manueel. Door deze zeer korte ontwikkelingstijd en het manuele karakter wordt deze processtap niet ten volle gecontroleerd. De dikte van het fotolakprofiel is niet precies te voorspellen. Dit is nochtans een belangrijke parameter bij het bepalen van de vulfactor door middel van schuin opdampen van Ti. De reproduceerbaarheid van het holografische proces wordt hierdoor beperkt.

Schuin opdampen van Ti
Het fotolakpatroon wordt door middel van RIE omgezet naar de halfgeleider. RIE etst – weliswaar met een verschillende snelheid – zowel de fotolak als de halfgeleider. Hierdoor wordt de haalbare verhouding van de diepte op de periode beperkt, en worden geen verticale wanden verkregen. Daarenboven is het belangrijk dat de vulfactor van het rooster gecontroleerd wordt, wat niet het geval is met een dergelijk fotolakmasker.

Een hoge verhouding van de diepte op de periode en controle over de vulfactor verkrijgen we door Ti schuin op de fotolak te dampen onder een gecontroleerde hoek. Dit proces staat geschetst in Fig. 5.7. Door schaduweffect van het sinusoïdaal profiel zal de fotolak slechts gedeeltelijk met Ti bedekt worden. Dit Ti vormt dan het masker voor de hierop volgende RIE stap. Door de grote weerstand van Ti kan met RIE een grote verhouding van de diepte op de periode gerealiseerd worden. Door accurate regeling van de opdamphoek met de oppervlaknormale en de azimuthale opdamphoek kunnen de vulfactor en vorm van de geëtste stukken gecontroleerd worden. De fout op de vulfactor is te verklaren door de irreproduceerbaarheid van de dikte van het fotolakpatroon door de manuele ontwikkelingstijd.

RIE
Twee opeenvolgende RIE-stappen worden uitgevoerd. In beide etsstappen dient het Ti als masker. Onbedekt fotolak en ARC worden door middel van een O_2-plasma verwijderd. Vervolgens wordt $SiCl_4$-gas geïoniseerd om het GaAs-sample te etsen. Het anisotrope karakter van RIE resulteert in een gekanteeld roosterprofiel.

Mogelijkheden en beperkingen
We hebben aangetoond dat 2D roosters, zowel triangulaire als vierkante, door middel van holografie gedefinieerd kunnen worden. Hoewel het mogelijk is om dergelijke structuren via e-beam of diepe-UV-lithografie te realiseren, staat holo-

grafie voor een goedkoop en veelzijdig alternatief dat het gebruik van maskers overbodig maakt. Toch zijn er enkele beperkingen mee verbonden.

Enkel 1D, vierkante en triangulaire 2D roosters kunnen met het proces vervaardigd worden. Geavanceerde roosterstructuren met verhoogde rotationele symmetrie in het vlak van het rooster zijn niet met deze techniek te realiseren.

Het ontwikkelingsproces wordt niet accuraat gecontroleerd waardoor het fotolakpatroon irreproduceerbaar is. Dit heeft invloed op de gerealiseerde vulfactor. Deze stap is echter vatbaar voor verdere optimalisatie.

SEM foto's tonen aan de etsranden een zekere ruwheid. Deze ruwheid kan verstrooiingsverliezen veroorzaken en aldus de efficiëntie beïnvloeden. De ruwheid wordt aan de Ti-opdampstap gerelateerd en kan eventueel verder geoptimaliseerd worden.

5.3 RCLED-fabricage

Eens het rooster in het oppervlak van de epilaag gedefinieerd staat, kan de LED-definitie het processchema afronden.

De eerste stap definieert de mesa. Deze dient om stroomspreiding tegen te gaan. Om oppervlakrecombinatie te vermijden, mag de mesa echter niet door de QW's geëtst worden.

Ten tweede definieert men door middel van optische lithografie het p-contact. Twee mogelijkheden doen zich voor. Een vol metallisch contact wordt behaald door een dikke laag ($>$ 200 nm) Au op de mesa te dampen. Een halfgeleiderluchtrooster, op de tanden bedekt met metaal, wordt door een gecontroleerd schuinopdampproces verkregen, analoog aan het eerder besproken Ti opdampproces.

120 nm Al_2O_3 wordt gedeponeerd, en hierop de contactringen en -paden. Het sample wordt verdund en de n-contacten worden op de achterkant van het sample aangebracht.

5.4 Conclusies

We hebben het fabricageproces van de GA-RCLED voorgesteld. Met uitzondering van de roosterdefinitie en de metallisatie van dit rooster is het processchema identiek aan dat van een standaard RCLED: simpel en goedkoop. Bij gebruik van het ontwikkelde holografisch proces, waarmee 1D en 2D roosters kunnen worden gefabriceerd, verandert dit niet en blijft het proces geschikt voor massafabricage.

6 GA-RCLED met een 1D rooster

6.1 Inleiding

In Hoofdstuk 4 toonden we aan dat de rotationele symmetrie in het vlak van de geleide mode de zelfde symmetrie vereist van het rooster. Van de 2D Bravais-roosters vertoont de triangulaire de hoogste rotationele symmetrie. GA-RCLEDs met 2D roosters worden in Hoofdstuk 7 beschreven.

In dit hoofdstuk raken we vertrouwd met de GA-RCLEDs door hun gedrag te bestuderen in het geval ze van een 1D rooster worden voorzien.

Eerst en vooral kiezen we een basisstructuur. Deze structuur wordt ook de basisstructuur van de componenten met een 2D rooster.

6.2 Structuur van de GA-RCLED

6.2.1 Top- of bodememitterend?

Een GA-RCLED is in essentie een verticaalstralende bron: het licht wordt geëmitteerd in de groeirichting van de meerlagige structuur. De richting kan nog vrij gekozen worden: top- of bodememitterend. Deze keuze heeft consequenties bij het kiezen van de ideale spiegels: hoogreflectief metaal met kleine indringdiepte maar hoge absorptie; optisch transparante halfgeleider-DBR met beperkt angulair reflectief bereik en hogere indringdiepte; elektrisch isolerende diëlektrische DBR met verbeterde reflectie-eigenschappen.

We kiezen een bodememitterende structuur, en meer bepaald de RCLED configuratie die in ons lab werd ontwikkeld en geoptimaliseerd door H. De Neve [19]. Deze 980-nm bodememitterende GaAs-LED heeft een simpel elektronisch ontwerp en een voor de hand liggende processing. Dit inspireerde ons deze structuur te gebruiken om extractieverhoging aan te tonen door incorporatie van een rooster. Het principe is echter uitbreidbaar naar andere ontwerpstructuren.

6.2.2 Plaats van het rooster

De ervaring op het lab heeft ons ook op dit punt ertoe aangezet ons te beperken tot structuren met een rooster geëtst in de bovenste lagen van de epistructuur.

Het epitaxiaal deponeren van materiaal op gestructureerde oppervlakken verhoogt de ontwerpflexibiliteit, maar is gevoelig aan ongecontroleerde variaties in de lokale compositie tijdens de groei. Deze kunnen tot sterk gelokaliseerde kristallografische schade leiden. Dit proces vereist dan ook de nodige ervaring.

6.2.3 Materiaalsysteem

We gebruiken het hoogkwalitatief GaAs/Al(Ga)As-materiaalsysteem met InGaAs-QW's. Het GaAs-substraat is transparant voor 980 nm, de emissiegolflengte van de LED, zodat de keuze compatibel is met de bodememitterende structuur.

6.3 Ontwerp van een GA-RCLED met een 1D rooster

Optimalisatie van een GA-RCLED houdt in dat optimale waarden voor de verschillende rooster- en caviteitsparameters (Fig. 6.3) dienen bepaald te worden. Dit optimalisatieproces maakt gebruik van het model voorgesteld in Hoofdstuk 4. Door de numerieke complexiteit van een 3D simulatie (de rekentijd is evenredig met LN^3, L het aantal lagen en N het aantal ordes), wordt de structuur eerst geoptimaliseerd in een vlak (2D gedrag). Daarna wordt deze optimalisatie verfijnd door 3D berekeningen.

6.3.1 2D gedrag

Het interne intensiteitsprofiel voorziet ons van fysisch inzicht in het gedrag van GA-RCLEDs.

De periode van het rooster
Indien een rooster geïntegreerd wordt in de topspiegel van een RCLED, wordt – volgens de Braggconditie – de geleide mode gediffracteerd (Vgl.(6.1)):

$$\mathbf{k}_{\parallel}^{m} = \mathbf{k}_{\parallel}^{gm} - m\mathbf{K}_x$$

De minimumvereiste voor efficiëntieverhoging is dat tenminste één van de diffractieordes samenvalt met de extractieconus, zodat vermogen naar de omgeving kan lekken. De periode van het rooster bepaalt de diffractierichting van de verscheidene diffractieordes, en is dus de eerste parameter die we dienen te bepalen.

Indien de geleide mode via een eerste diffractieorde koppelt met de buitenwereld, spreken we van een eerste-orderooster. De interne netto vermogenflux wordt weergegeven in Fig. 6.5. De gediffracteerde geleide mode – een piek ter hoogte van $\theta_{diff} = 0°$ – is als het ware gesuperponeerd op de Fabry-Pérotmode, met (Vgl.(6.2)):

$$\theta_{diff} = \arcsin\left(\sin\theta_{gm} - \frac{\lambda/n_s}{\Lambda}\right)$$

De extractie-efficiëntie η_{extr} in het 2D vlak bedraagt 46.8%. Door de lage rotationele symmetrie van de GA-RCLED is dit cijfer niet representatief voor de totale η_{extr}, wel tendentieus.

Wanneer we de periode variëren, verschuift de piek van de gediffracteerde geleide mode (Fig. 6.6).

Koppelen we de geleide mode uit via de tweede diffractieorde, dan spreken we van een tweede-orderooster. Fig. 6.8 toont dat met een tweede-orderooster vermogen van de geleide mode gekoppeld wordt naar de omgeving via de tweede diffractieorde, en naar het substraat via de eerste diffractieorde. Deze laatste is een extra verliesterm en kan geminimaliseerd worden door een extra DBR die een hoge reflectie vertoont voor de hoek corresponderend met de eerste diffractieorde. Dit wordt in Hoofdstuk 7 besproken.

De caviteitsdikte
Een verandering van de caviteitsdikte wordt in de eerste plaats vertaald in een

verschuiving van de Fabry-Pérotresonantie. De koppelingssterkte is maximaal wanneer de hoek van de gediffracteerde mode samenvalt met van de Fabry-Pérot-resonantie. Dit wordt duidelijk in Fig. 6.9.

De diepte van het rooster
De diepte van het rooster bepaalt de reflectie- en transmissiecoëfficiënten en de absorptie van invallend licht op het rooster.

De fase van de nulde-ordereflectiecoëfficiënt van het (quasi-)loodrecht invallende licht bepaalt de reonantieconditie van de Fabry-Pérotmode. Een toename van de diepte van het rooster resulteert in een kleinere effectieve caviteitsdikte, en het effect op de η_{extr} is dezelfde als wanneer de caviteitsdikte wordt gevarieerd.

De amplitude van de reflectiecoëfficiënten hebben een invloed op de η_{extr} via de gerelateerde diffractie-efficiëntie van het rooster. Zo zal een dieper metallisch rooster een grotere absorptie vertonen. De twee effecten kunnen afzonderlijk bestudeerd worden door de roosterdiepte te laten toenemen bij gelijkblijvende effectieve caviteitsdikte (Fig. 6.11).

De golflengte van de monochromatische dipool
De voorgaande simulaties veronderstellen een monochromatische dipoolemissie. Nochtans heeft het intrinsieke spectrum van de spontane emissie een FWHM van $\pm$20 nm. Fig. 6.12 toont aan dat de efficiëntie voor een golflengtebereik van 20 nm rond 980 nm hoog blijft.

6.3.2 3D gedrag

De η_{extr} kan enkel berekend worden door middel van een 3D simulatie van de netto vermogenflux. Fig. 3 toont de netto vermogenflux per eenheid spatiale frequentie in het $k_x - k_y$-vlak voor een GA-RCLED met respectievelijk een eerste-orderooster en een tweede-orderooster. De η_{extr} is 23% en 14.7%. De hogere absorptieverliezen – in vergelijking met deze van een vlakke metalen spiegel – en de lage rotationele symmetrie dragen ertoe bij dat de η_{extr} lager is dan van een standaard RCLED.

6.4 Karakterisatie van GA-RCLEDs met een 1D rooster

6.4.1 Realisatie van GA-RCLEDs met een 1D rooster

Visuele karakterisatie van de dwarsdoorsnede van GA-RCLEDs door middel van SEM-foto's, toont aan dat het holografisch proces adequaat is voor het definiëren van 1D roosters met periodes gaande tot 300 nm.

6.4.2 Spectraal gedrag

Het spectrale gedrag van de GA-RCLED uit Fig. 6.16 wordt weergegeven in Fig. 4-6. De grafieken aan de linkerkant tonen experimentele data, de grafieken aan de rechterkant de respectieve simulatie. Naast de opvallende overeenkomst tussen de experimentele en berekende data, zijn enkele specifieke fenomenen waar te nemen.

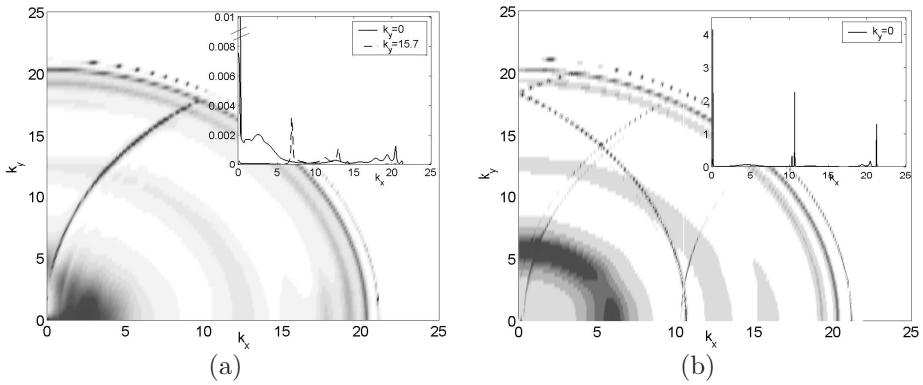

Figuur 3: 2D plot van de s-gepolariseerde interne netto vermogenflux per eenheid spatiale frequentie in een GA-RCLED (a) met een eerste-orderooster (cfr. Fig. 6.4); (b) met een tweede-orderooster (cfr. Fig. 6.8).

Fig. 4 toont het polarisatieselectief gedrag van de GA-RCLED. Enkel wanneer de E-component evenwijdig met de roosterkam ligt krijgen we een verhoogde η_{extr}.

Wanneer het spectrum opgemeten wordt voor verschillende hoeken in het vlak gespannen door de Braggvector en de oppervlaknormale, wordt de symmetrie van de Braggconditie verbroken (Fig. 5). Voor een bepaalde hoek wordt de bijdrage tot het vermogen geleverd door gediffracteerde geleide modi met verschillende propagatierichting en verschillende golflengte. Dit resulteert in een splitsing van het spectrum wanneer de hoek van de observatierichting toeneemt. Fig. 6 toont dat dit niet het geval is wanneer men observeert in het vlak gespannen door de kam van het rooster en de oppervlaknormale. Dit is evident, gezien het 1D karakter van het rooster.

6.4.3 Verreveld

Het asymmetrische verreveld wordt opnieuw veroorzaakt door het 1D karakter van het rooster. In het vlak gespannen door de Braggvector en de oppervlaknormale wordt de geleide mode naar een beperkt angulair bereik gekoppeld (zie Fig. 6.24).

6.4.4 Efficiëntie

Spectrale metingen en verreveldmetingen tonen extractie van de geleide mode aan. De η_{extr} is echter laag: 4.1%. De reden is meervoudig: tijdens de experimenten was het simulatiepakket nog niet beschikbaar. De optimalisatie in niet maximaal: de caviteit is slecht afgestemd. De metingen tonen de afwezigheid van de Fabry-Pérotmode aan. Bovendien is de η_{extr} beperkt door de lage rotationele symmetrie en de hoge absorptieverliezen.

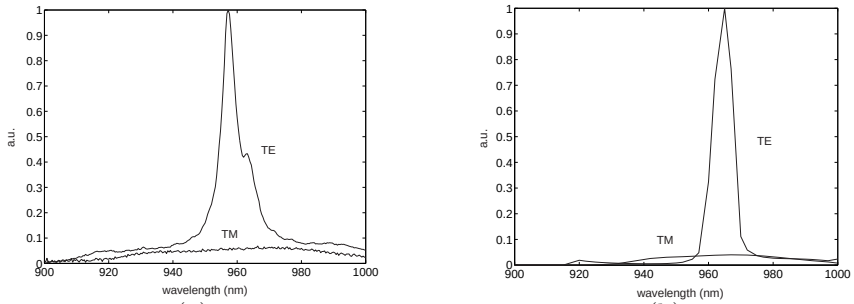

Figuur 4: Polarisatieselectieve emissie van een GA-RCLED met een 1D tweede-orderooster (zie Fig. 6.16) (a) experimentele data; (b) metingen.

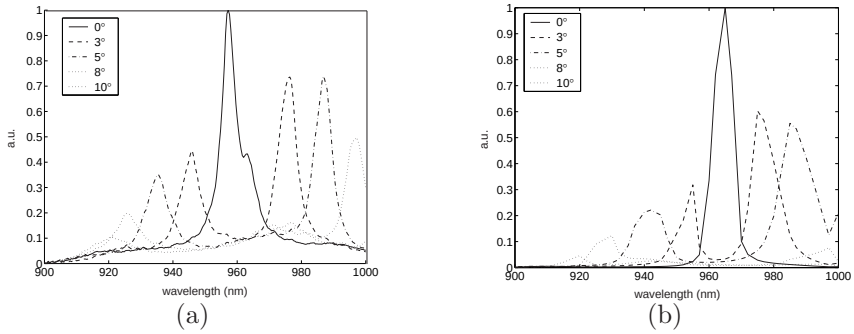

Figuur 5: Hoekgeresolveerde spectrum in het vlak gespannen door de Braggvector en de oppervlaknormale van een GA-RCLED met een 1D tweede-orderooster (zie Fig. 6.16) (a) experimentele data; (b) metingen.

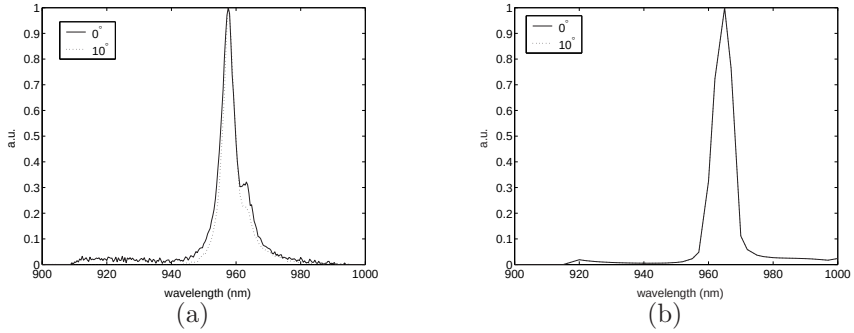

Figuur 6: Hoekgeresolveerd spectrum in het vlak gespannen door de kam van het rooster en de oppervlaknormale van een GA-RCLED met een 1D tweede-orderooster (zie Fig. 6.16) (a) experimentele data; (b) metingen.

6.4.5 Verruwing

Niet-succesvolle experimenten kunnen tot leuke resultaten leiden. Fig. 6.26 toont het oppervlak van een GA-RCLED na een mislukte holografische definitie van het rooster. Eerder dan een gekanteeld profiel, zien we een verruwd oppervlak. Verhoging van de efficiëntie van LEDs door middel van het verruwen van het oppervlak werd succesvol toegepast door Windisch *et al.* [4]. De η_{ext} van onze LEDs is 22%, bij een diameter van 72 μm. He substraat is verdund en een ARC beperkt de Fresnelverliezen.

6.5 Conclusies

Alhoewel incorporatie van een 1D rooster de efficiëntie niet zal opdrijven, verhogen ze wel fysisch inzicht in het gedrag van de GA-RCLED. De GA-RCLED met een 1D rooster is de ideale "proof of principle". De invloed van de verschillende rooster- en caviteitsparameters werd door middel van het simulatiepakket bestudeerd. De consistente berekende en gemeten waarden tonen een polarisatieselectief gedrag van de LED, bepaald door het 1D karakter van rooster.

7 GA-RCLED met een 2D rooster

7.1 Inleiding

Om een verhoogde extractie-efficiëntie te realiseren, dient het rooster dezelfde rotationele symmetrie in het vlak te vertonen als de geleide mode. Van de 2D Bravaisroosters, vertonen de triangulaire roosters de hoogste rotationele symmetrie en een Brillouinzone die het dichtst nadert tot een cirkel. Deze structuur en vierkante roosters worden in dit hoofdstuk besproken.

7.2 GA-RCLED met een holografisch gedefinieerd vierkant rooster

7.2.1 Ontwerp van een GA-RCLED met vierkant rooster

Vierkante roosters vertonen niet dezelfde rotationele symmetrie als triangulaire roosters. Door middel van het WVD kunnen we nochtans aantonen dat een vierkant tweede-orderooster in staat is de volledige in het vlak propagerende geleide mode te diffracteren naar de extractieconus. Het WVD toont echter ook de onvermijdelijke eerste diffractieordes die lekken naar het substraat.

Vierkant eerste-orderooster
Een GA-RCLED met een vierkant rooster wordt op dezelfde manier ontworpen als de GA-RCLED met een 1D rooster. Het gedrag wordt eerst geanalyseerd in een vlak gespannen door de oppervlaknormale en een Braggvector. Daarna wordt de optimalisatie door middel van 3D simulaties verfijnd.

Fig. 7.2 toont een 2D simulatie van de interne netto vermogenflux in functie van enkele rooster- en caviteitsparameters. De invloed van deze parameters op het gedrag van de GA-RCLED is analoog als besproken in Hoofdstuk 6. Het voornaamste verschil met de roosters uit het vorige hoofdstuk is, buiten hun periodieke dimensionaliteit, hun metallisatie. Om de absorptieverliezen te beperken, werd geopteerd voor halfgeleiderluchtroosters die op de top van hun tanden bedekt worden door metaal. Deze configuratie behoudt een hoge oppervlaknormale reflectie en een homogene stroominjectie, terwijl de absorptieverliezen sterk verminderd zijn: van $\pm 25\%$ naar $\pm 10\%$.

3D simulaties verfijnen de optimalisatie. 3D plots van de interne vermogenflux per eenheid spatiale frequentie van de geoptimaliseerde structuren staan geschetst in Fig. 7.4. De extractie-efficiëntie van het licht van een monochromatische parallelle dipool in de geoptimaliseerde structuur is 34%. De extractie-efficiëntie blijft hoog voor een golflengtebereik overeenkomend met de spectrale breedte van het intrinsieke spectrum. De extractie-efficiëntie blijkt wel gevoelig aan caviteitsdiktevariaties.

Vierkant tweede-orderooster
Vierkante tweede-orderoosters zijn in staat geleide modes te diffracteren naar de extractieconus, ongeacht hun propagatierichting. Eerste diffractieordes zijn echter onontkoombaar. Om het verlies van vermogen te minimaliseren dat via deze ordes

lekt naar het substraat, kan een extra DBR onder de al aanwezige DBR geplaatst worden. Deze extra DBR vertoont een hoge reflectie voor licht met een invalshoek = $\pm 27°$, overeenkomstig de eerste diffractieorde. Fig. 7.7 toont de verminderde netto vermogenflux naar het substraat van een GA-RCLED met extra DBR.

Door het hoge aantal spatiale harmonischen dat in de numerieke berekening dient meegenomen te worden om een nauwkeurig resultaat te behalen in het geval van een 2D tweede-orderooster, kan de beschikbare processor de analyse niet in een redelijke termijn uitvoeren. Optimalisatie van GA-RCLEDs met een 2D tweede-orderooster valt terug op 2D simulaties.

Absorptie versus diffractie
Twee concurrerende processen bepalen de propagatielengte van de geleide mode: de diffractie-efficiëntie van het rooster en de absorptie van de geleide mode in de actieve laag. Bovenstaande simulaties tonen reeds aan dat de diffractie-efficiëntie sterker is dan de absorptie. Hier wordt een grootteorde van beide fenomenen gegeven.

Absorptie in de actieve laag is afhankelijk van de overlap van het profiel van de geleide mode met de actieve laag en de absorptiecoëfficiënt van de actieve laag. Deze laatste wordt tevens door de stroomdichtheid beïnvloed. Een waarde van ± 100 dB/mm wordt met de absorptie van de geleide mode in de actieve laag geassocieerd.

De diffractie-efficiëntie wordt door middel van CAMFR berekend. De verzwakkingscoëfficiënt van de geoptimaliseerde structuur met een eerste-orderooster is 718 dB/mm, met een tweede-orderooster 407 dB/mm. Aangezien dit softwarepakket tot nu toe enkel 2D berekeningen aankan, is het getal eerder indicatief dan kwantitatief accuraat. Toch blijkt duidelijk dat de diffractie-efficiëntie grootteordes groter is dan de absorptie in de actieve laag.

7.2.2 Realisatie van GA-RCLEDs met holografisch gedefinieerde vierkante roosters

De geoptimaliseerde ontwerpen werden geïmplementeerd volgens het processchema besproken in Hoofdstuk 5. SEM foto's van de gerealiseerde structuren worden in Fig. 7.8 getoond. Het schuin opdampen van metaal op de holografisch gedefinieerde vierkante roosters blijkt visueel geslaagd, onafhankelijk van de vulfactor.

7.2.3 Karakterisatie van GA-RCLEDs met holografisch gedefinieerde vierkante roosters

Tijdens dit onderzoek, kregen we de opportuniteit drie reeksen experimenten met GA-RCLEDs met 2D holografisch gedefinieerde roosters uit te voeren.

Tijdens de eerste reeks werden de mogelijkheden van de verschillende metallisaties van het rooster getest: gevulde metallische roosters en halfgeleiderluchtroosters die enkel op de tanden met metaal bedekt zijn. Analyse van hun spectraal gedrag laat blijken dat in beide gevallen de geleide mode uitgekoppeld wordt. Echter bij de volle metallische roosters is duidelijk te zien dat de absorptie van de

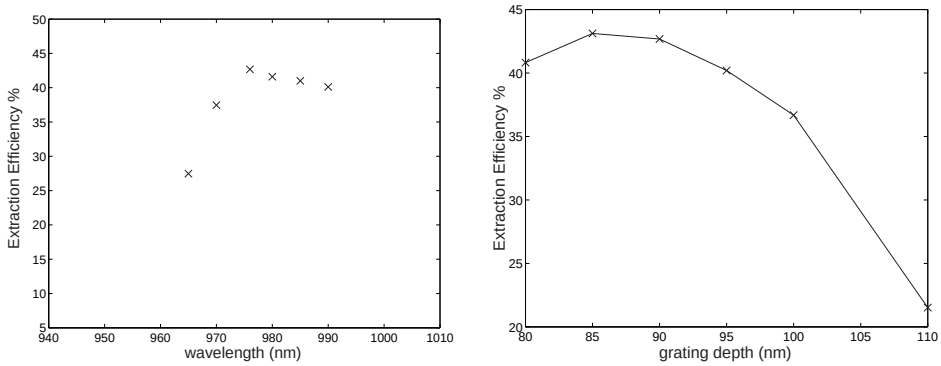

(a) (b)

Figuur 7: Gesimuleerde extractie-efficiëntie van het licht van een horizontale dipool in een GA-RCLED met een triangulair eerste-orderooster (a) voor verschillende golflengtes; (b) verschillende roosterdieptes.

geleide mode hoger is. De IV-curves representeren in beide gevallen een aardige diodekarakteristiek met een lage seriële weerstand (Fig. 7.9).

De tweede reeks experimenten toont het belang van een correct afgestemde caviteit aan. Het opgemeten hoekgeresolveerde spectrum van een uit de gegroeide epistructuur gefabriceerde RCLED toont aan dat een fout op de laagdiktes -3.5% is. Het opgemeten spectrum van de GA-RCLEDs toont aan dat de geleide mode uitgekoppeld wordt, maar met een matige $\eta_{ext} = 5\%$ tot gevolg (Fig. 7.12).

SEM foto's van de holografisch gedefinieerde roosters van de derde reeks worden in Fig. 7.13 gegeven. Een residu van fotolak en ARC is duidelijk zichtbaar. De spiegelkwaliteit van het opgedampte metaal zal bijgevolg laag zijn en resulteren in verstrooiingsverliezen van de geleide mode. Zwakke extractie is zichtbaar in het spectrum, het verreveld vertoont een verhoogde radiantie, $\eta_{ext} = 12.5\%$, waarbij het substraat nog niet verdund is en geen ARC werd voorzien (Fig. 7.14).

7.3 GA-RCLEDs met e-beam gedefinieerde triangulaire roosters

7.3.1 Ontwerp van GA-RCLED met triangulair rooster

Het ontwerp van een GA-RCLED met een triangulair rooster is analoog aan dat van een GA-RCLED met een vierkant rooster, en wordt daarom niet herhaald. Het belangrijkste resultaat staat samengevat in Fig. 7.15: $\eta_{extr} = 43\%$ voor monochromatisch licht uitgezonden door een horizontale dipool. De η_{extr} blijft hoog ($> 40\%$) voor een golflengtebereik overeenkomstig de intrinsieke spectrale breedte van de spontane emissie. De performantie is echter sterk afhankelijk van de caviteitsparameters (Fig. 7).

7.3.2 Realisatie van GA-RCLED met e-beam gedefinieerd triangulair rooster

Het roosterpatroon werd door middel van e-beam in fotolak gedefinieerd. RIE vertaalt dit fotolakpatroon naar een halfgeleiderpatroon. Deze beide stappen werden uitgevoerd in de University of Glasgow. De samples werden nadien door INTEC verder gefabriceerd tot LEDs.

7.3.3 Karakterisatie van GA-RCLED met e-beam gedefinieerd triangulair rooster

Van de vier reeksen e-beamexperimenten, waren slechts de eerste en de derde bruikbaar. Het belang van de extra DBR wordt bij vergelijking van de experimentele data van beide reeksen duidelijk. Spectrale metingen vertonen in beide gevallen extractie van de geleide mode. De efficiëntie van de eerste reeks is eerder laag. De tweede reeks heeft componenten met een $\eta_{ext} = 15.1\%$ (Fig. 8). Door parameterextractie kunnen we de η_{int} schatten op 79%. De substraatabsorptie zorgt voor een verlies van 22%, de fresnelreflecties voor 30%. Indien we rekening houden met deze waarden, komen we aan een $\eta_{extr} = 35\%$. Deze waarde ligt dicht bij de theoretisch voorspelde 40%. De afwijking ligt bij een kleine detuning van de caviteit.

7.4 Dunnefilm-GA-RCLED

In de vorige paragrafen werd een bodememitterende GA-RCLED, met periodiek gemoduleerde topspiegel en DBR onderspiegel, bestudeerd. Sinds kort startte onderzoek naar dunnefilm-GA-RCLEDs. Deze substaatloze LED gebruikt het GaAs-substraat voor de kristalgroei, waarvan het achteraf ontdaan wordt. SEM foto's van de eerste dunnefilm-GA-RCLED met een triangulair holografisch gedefinieerd rooster worden in Fig. 7.19 gegeven. Eerste numerieke simulaties tonen aan dat door het ontbreken van lekkende DBR modi en hoge metaalabsorptieverliezen de η_{extr} hoog is (50 à 60%).

7.5 Conclusies

Bodememitterende GA-RCLEDs met een 2D-periodiek gemoduleerde topspiegel en DBR bodemspiegel werden ontworpen en geoptimaliseerd. Een $\eta_{extr} = 40\%$ wordt gesimuleerd voor een triangulair eerste-orderooster.

De experimenteel waargenomen $\eta_{ext} = 15.1\%$, wat overeenkomt met een $\eta_{extr} = 35\%$. Interpretatie van de verschillende meetresultaten legt tevens de achilleshiel van de GA-RCLED bloot: de performantie van de component is sterk afhankelijk van de correcte afstemming van de caviteit. Dit vereist een accurate controle over de gebruikte technologische processen.

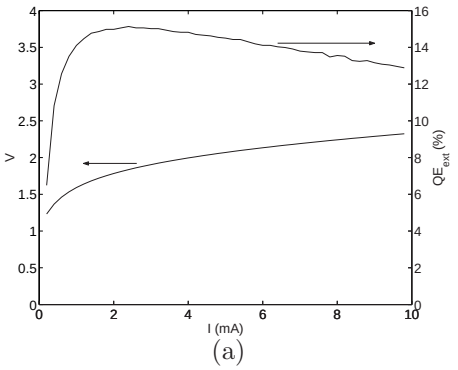

(a)

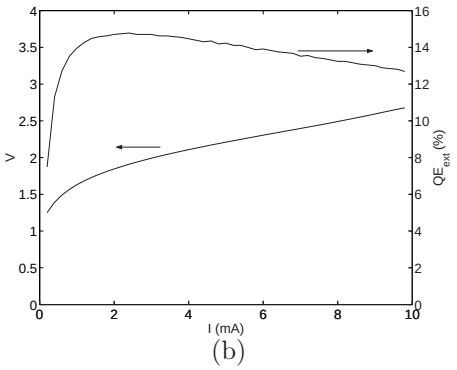

(b)

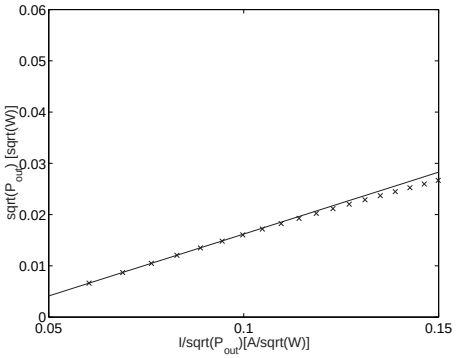

(c)

param.	value
Λ	598/298 nm
d_{gr}	$\pm$50 nm
d_1	$\pm$85 nm
d_2	79 nm
hole diam.	$\pm$149/221 nm
X	5(0°)+8(30°)
cont.	t

(d)

Figuur 8: Gemeten IV en QE van een GA-RCLED met (a) triangulair tweede-orderooster; (b) triangulair eerste-orderooster; (c) gemeten en gefitte curve van het optisch vermogen in overeenstemming met Vgl.(7.5) *voor de component uit (a); (d) GA-RCLED parameterwaarden. De diameter van de component is 115 μm, het substraat is niet verdund en niet voorzien van een ARC.*

8 Conclusie en toekomstperspectieven

De belangrijkste resultaten en opportuniteiten die dit werk biedt worden samengevat. Eerst vermelden we enkele mijlpalen in de (r)evolutie van de extractie-efficiëntie van LEDs die andere onderzoeksgroepen realiseerden gedurende de periode van dit werk.

8.1 Evolutie van (extractie-)efficiëntie van de LED (1998-2001)

Bij aanvang van dit werk werd de hoogste efficiëntie verwezenlijkt door grote diameter RCLEDs: 22.4% [19]. In 1999 en 2002 leidde verdere uitwerking van het concept tot $\eta_{ext} = 27\%$ [20] en $\eta_{ext} = 28\%$ [1].

Extractie via meerdere zijden in een piramidale LED leidden in 1999 tot een wereldrecord $\eta_{ext} = 60.9\%$ [2].

Enkelzijdige extractie door middel van tapse LED toonde een $\eta_{wp} = 30\%$ in 2000 [3], door middel van een LED met verruwd oppervlak $\eta_{ext} = 46\%$ in 2000 [4].

Bij deze laatste drie componenten wordt een deel van het licht geëxtraheerd in niet-gepompte gebieden.

8.2 Overzicht van belangrijkste resultaten en algemene conclusie

8.2.1 GA-RCLED: nieuw conceptueel ontwerp van een hoogefficiënte LED. Principe en voornaamste kwaliteiten

De GA-RCLED is een nieuwe component, voor het eerst gerapporteerd in dit werk. Rigneault *et al.* publiceerden onafhankelijk een analoog conceptueel idee met speciale aandacht voor dunnefilmcomponenten, in 1999 [21].

Simplistisch voorgesteld, bestaat de idee van de GA-RCLED erin de emissie te laten gebeuren in een caviteit. Hierdoor wordt het licht geconcentreerd in een aantal discrete modi. Modi met een propagatieconstante die groter is dan de vacuümgolfvector kunnen de caviteit enkel lateraal verlaten en zijn dus verloren tenzij het moment van de fotonen kan worden veranderd. Dit kan tot stand gebracht worden door middel van een ondiep rooster geïntegreerd in een van de spiegels van de caviteit. De Braggvector van het rooster dient zodanig gekozen te worden dat het licht gediffracteerd wordt naar de omgeving of naar extraheerbare richtingen.

De component is planair, de extractie is enkelzijdig en door het samenvallen van extractie- en injectieoppervlak wordt de beschikbare oppervlakte efficiënt gebruikt. Extractie van de geleide mode versterkt de emissie in een beperkte NA (15°) rond de oppervlaknormale, wat de radiantie van de component ten goede komt.

8.2.2 Numerieke rigoureuze analyse

Een elektromagnetische analyse van dipoolemissie in een periodiek gelaagd medium werd opgesteld. Het model werd geïmplementeerd. De reflectie- en transmissie-

coëfficiënten worden door middel van de rigoureuze gekoppeldegolftheorie berekend.

Dit model werd gebruikt om het optisch gedrag van een GA-RCLED met een rooster als topspiegel en een DBR als bodemspiegel te bestuderen. Een $\eta_{extr} = 40\%$ wordt voorspeld. Dit bevestigt de verhoogde efficiëntie die verwacht wordt met het nieuwe concept van de GA-RCLED.

8.2.3 Prototype

Het model werd gebruikt om de optimale caviteits- en roosterparameters te bepalen. GA-RCLEDs werden in overeenstemming met deze ontwerpen gefabriceerd.

Een holografisch procedure werd ontwikkeld en geoptimaliseerd ter definitie van 2D roosters. In tegenstelling tot de sequentiële e-beamprocedure, definieert het holografische proces de roosters in één enkele stap. Hierdoor blijft het fabricageproces van de GA-RCLED simpel en goedkoop, geschikt voor massafabricage.

Karakterisatie van de gefabriceerde GA-RCLED toont aan dat de geleide mode geëxtraheerd wordt. Met een triangulair tweede-orderooster wordt een $\eta_{ext} = 15.1\%$. Indien rekening wordt gehouden met $\eta_{int} = 79\%$, de propagatieverliezen in het 500 μm dikke substraat en de fresnelverliezen, komt dit overeen met een $\eta_{extr} = 35\%$.

De metingen tonen tegelijkertijd aan dat prestaties van de GA-RCLED sterk afhangen van de correcte afstemming van de caviteit. Deze wordt zowel door rooster- als door caviteitsparameters bepaald, en vereist dus een doorgedreven accuraatheid van de verschillende processtappen.

8.3 Perspectieven

Het concept van dipoolstraling in een roosterstructuur werd in detail besproken. Een verhoogde η_{extr}, en meer in het bijzonder een verhoogde radiantie, in vergelijking met dipoolemissie in homogeen gelaagde media, wordt voorspeld. We hebben onze aandacht vooral gericht op bodememitterende GA-RCLEDs met een periodiek gemoduleerde topspiegel en een DBR bodemspiegel. Het concept is echter toepasbaar voor andere GA-RCLED structuren.

Zo kan een topemitterende RCLED met een geoxideerde DBR als bodemspiegel van een periodiek gemoduleerde topspiegel voorzien worden. Door de geoxideerde spiegel worden daarenboven de lekkende DBR modi geminimaliseerd. Onlangs startte onderzoek naar dunnefilm-GA-RCLEDs. Eerste simulaties tonen een $\eta_{extr} > 50\%$. Dit is hoger dan de η_{extr} van de in dit werk bestudeerde GA-RCLED door de afwezigheid van lekkende DBR modi en lagere metaalabsorpties.

Het concept en simulatiepakket voor dipoolstraling in roosterstructuren werd uitgewerkt. Deze algemene bevindingen kunnen geconcretiseerd worden in hoogefficiënte componenten met verschillende structuren. De componenten zijn in essentie planair met een enkelzijdige extractie, de beschikbare oppervlakte wordt efficiënt gebruikt. Mede door de verhoogde radiantie is de GA-RCLED een ideale kandidaat in toepassingen waar het licht gefocusseerd dient te worden tot een kleine spot of in 2D reeksen met een hoge dichtheid.

Bibliografie

[1] M. Rattier, H. Benisty, R.P. Stanley, J.F. Carlin, R. Houdré, U. Oesterle, C.J.M. Smith, C. Weisbuch and T.F. Krauss, "Toward ultrahigh-efficiency aluminum oxide microcavity light-emitting diodes: guided mode extraction by photonic crystals", *IEEE J. Sel. Top. Quantum Electron.,* vol. 8(2), pp. 238-247, 2002.

[2] M.O. Holcomb, M.R. Krames, G.E. Hofler, C. Carter-Coman, E. Chen, P. Grillot, K. Park, N.F. Gardner, J.-W. Huang, J. Posselt, D. Collins, S.A. Stockman, G. M. Craford, F.A. Kish, I.-H. Tan, T.S. Tan, C.P. Kocot and M. Hueschen, "High-power truncated-inverted-pyramid $(Al_xGa_{1-x})_{0.5}In_{0.5}P$ light-emitting diodes exhibiting $> 50\%$ external quantum efficiency," *Appl. Phys. Lett.,* vol. 75(16), pp. 2365-2367, 1999.

[3] W. Schmid, M. Scherer, C. Karnutsch, A. Ploessl, W. Wegleiter, S. Schad, B. Neubert and K. Streubel, "High efficiency, red and infrared light-emitting diodes using radial outcoupling taper", *IEEE J. Sel. Top. Quantum Electron.,* vol. 8(2), pp. 256-263, 2002.

[4] R. Windisch, C. Rooman, S Meinlschmidt, P. Kiesel, D. Zipperer, G. H. Doehler, B. Dutta, M. Kuijk, G. Borghs, and P. Heremans, "Impact of texture-enhanced transmission on high-efficiency surface-textured light-emitting diodes", *Appl. Phys. Lett.,* vol. 79(15), pp. 2315-2317, 2001.

[5] N.F. Gardner, H.C. Chui, E.I. Chen,M.R. Krames, J.W. Huang, F.A. Kish, S.A. Stockman, C.P. Kocot, T.S. Tan, N. Moll, "1.4x efficiency improvement in transparent-substrate $(Al_xGa_{1-x})_{0.5}In_{0.5}P$ light-emitting diodes with thin (<= 2000 angstrom) active regions", *Appl. Phys. Lett.,* vol. 74(15), pp. 2230-2232, 1999.

[6] R. Wirth, C. Karnutsch, S. Kugler and K. Streubel "High efficiency resonant cavity LEDs emitting at 650 nm", *IEEE Phot. Tech. Lett.,* vol. 13(5), pp. 421-423, 2001.

[7] R. Bockstaele, J. Derluyn, C. Sys, S. Verstuyft, I. Moerman, P. Van Daele and R. Baets "Realisation of highly efficient 850nm top emitting resonant-cavity light-emitting diodes", *Electron. Lett.,* vol. 35(18), pp. 1564-1565, 1999.

[8] B. Depreter, I. Moerman, R. Baets, P. Van Daele and P. Demeester, "InP based 1300 nm microcavity LEDs with 9% quantum efficiency", *Electron. Lett.,* vol. 36(15), pp. 1303-1304, 2000.

[9] B. Depreter, S. Verstuyft, I. Moerman, R. Baets and P. Van Daele "InP-based microcavity light emitting diodes emitting at 1.3μm and 1.55 μm", in *Proc. of the 11th International Conference on InP and related materials (IPRM)*, Davos, Switserland 16-20 may, 1999, pp. 227-230 , 1999.

[10] P. Bienstman and R. Baets, "The RC2LED: an novel Resonant-Cavity LED design using a symmetric resonant cavity in the outcoupling reflector", *IEEE J. Quantum Electron.*, vol. 36(6), pp. 669-673, 2000.

[11] M.G. Moharam, D.A. Pommet, E.B. Grann and T.K. Gaylord, "Stable implementation of the rigorous coupled-wave analysis for surface-relief gratings: enhanced transmittance matrix approach", *J. Opt. Soc. Am. A,* vol. 12, pp. 1077-1086, 1995.

[12] M.G. Moharam and T.K. Gaylord, "Rigorous Coupled-Wave analysis of planar-grating diffraction", *J. Opt. Soc. Am. A,* vol. 71, pp. 811-818, 1981.

[13] M.G. Moharam and T.K. Gaylord, "Three dimensional Coupled-Wave analysis of planar-grating diffraction", *J. Opt. Soc. Am. A,* vol. 73, pp. 1105-112, 1983.

[14] M.G. Moharam and T.K. Gaylord, "Diffraction analysis of dielectric surface-relief gratings", *J. Opt. Soc. Am. A,* vol. 72, pp. 1385-10392, 1982.

[15] M.G. Moharam, E.B. Grann, D.A. Pommet and T.K. Gaylord, "Formulation of stable and efficient implementation of the rigorous coupled-wave analysis of binary gratings", *J. Opt. Soc. Am. A,* vol. 12, pp. 1068-1076, 1995.

[16] Lifeng Li, "Use of Fourier series in the analysis of discontinuous periodic structures", *J. Opt. Soc. Am. A,* vol. 13, pp. 1870-1876, 1996.

[17] P. Lalanne, "Effective properties and band structures of lamellar subwavelength crystals: Plane-wave method revisited", *Phys. Rev. B,* vol. 58, pp. 9801-9807, 1998.

[18] B. Dhoedt, *"Theoretical and Experimental Study of Free Space Optical Interconnections Based on Diffractive Lens Arrays"* , Ph. D. Thesis, Ghent University, Ghent, 1995.

[19] H. De Neve, *Design and Fabrication of Light Emitting Diodes based on the MicroCavity Effect,* Ph. D. dissertation, Ghent University, Ghent, Belgium, 1997.

[20] J.J. Wierer, D.A. Kellogg and N. Holonyak, "Tunnel contact junction native-oxide aperture and mirror vertical-cavity surface-emitting lasers and resonant-cavity light-emitting diodes", *Appl. Phys. Lett.,* vol. 74(7), pp. 926-928, 1999.

[21] H. Rigneault, F. Lemarchand, A. Sentenac and H. Giovannini, "Extraction of light from source located inside waveguide grating structures", *Opt. Lett.,* vol. 24(3), pp. 148-150, 1999.

English Text

1 Introduction

THIS research project combines the world of optoelectronics and nanostructures. In search for high efficiency, the Light-Emitting Diode meets the versatility of periodically corrugated diffractive structures with sub-wavelength scaled dimensions in the Grating-Assisted Resonant-Cavity Light-Emitting Diode.

This introductory chapter presents the opportunities and challenges of nowadays high efficiency LEDs and points out the importance of a further increase in efficiency.

The possibilities of state-of-the-art nanotechnologies are discussed. Nanotechnology, driven by microelectronics, is increasingly applied in photonics. Fabrication of structures with sub-wavelength scaled dimensions is not insurmountable.

The subject of this research, the Grating-Assisted Resonant-Cavity Light Emitting Diode, applies nanotechnology to enhance the efficiency of photon extraction. It is a new but realistic concept, presented for the first time in this research work. The concept will be detailed in this thesis. A rigorous analysis tool, developed to simulate its optical behavior, will be discussed as well as prototyping. The outline of the thesis is given in this introductory chapter.

1.1 Context

1.1.1 High efficiency and high brightness Light Emitting Diodes

In Western society, 16 to 20% of the electricity production is consumed to produce artificial light. Most of the electricity comes from burning combustible fossil fuels (71% of the total electricity production in the US, 51% in the EU, both in 2001) and nuclear power (20% in the US, 34% in the EU, both in 2001) [1]. The environmental cost of smog and carbon dioxide pollution and nuclear waste disposal must be added to the economical cost of producing the electricity used for lighting. Reduction of energy consumption will thus create both environmental and economical savings. Solid State Lighting (SSL), specifically Light Emitting Diodes[1], have the potential to offer these substantial energy savings in general lighting. Major breakthroughs in LED technology during the last decade led us to believe that by 2020, LEDs could reduce the global amount of electricity used for lighting by 35 % or expressed in terms of costs: by the year 2020, the US and the EU could spare 6.5 billion euro a year on electricity generation costs, the atmosphere would be spared some 200 million tonnes of carbon emission annually. No other electricity consumer has such a large energy-savings potential [2], [3].

However, the feasibility of this estimation on potential energy-savings by 2020 depends on how quickly and to what extent the technological developments of the last decade will evolve and occur. Particularly the price, expressed in euro/klm, [2] and the wall-plug efficiency, expressed in lm/W, of the LED need to outperform conventional light sources. Today's average first cost price for incandescent and fluorescent technologies is approximately 0.52 euro/klm. The efficiency of incandescent light sources and fluorescent lighting is about 14 lm/W and 60 lm/W, respectively. There is little room left for these conventional lighting sources for cost improvement without sacrificing performance[3]. As they have competed against each other for a while, cost efficiency has already been driven to the edge, and these values will remain more or less unchanged by the year 2020.

Nowadays LEDs show an average first cost price of 150-500 euro/klm and an efficiency of 10-40lm/W. Since the first commercial LED introduced in 1968 with an efficiency of about 0.01 lm/W, the breakthrough in efficiency is mainly situated in the last decade and is due to the rapid enhancement in the development

[1] A semiconductor Light Emitting Diode (LED) consists essentially of an electron-carrying n-doped layer and a hole-carrying p-doped layer. When a forward voltage is applied to the structure, electrons are injected from the n-layer and holes from the p-layer. Electrons and holes can radiatively recombine, emitting a photon. The wavelength (color) of the emitted light is determined by the difference in energy levels of the electrons and holes.

[2] kilo lumen. A lumen is the SI unit of luminous flux.

[3] Exceptions confirm the rule, and must be welcomed. Researchers from Sandia National Laboratories and Iowa State University have found very recently a way to structure a tungsten filament with a microscopic lattice so that, instead of emitting radiation made up of a broad mix of light and heat wavelengths, it emits 60 percent of the energy it receives in a relatively narrow band of wavelengths. The lattice structure appears thus to be able to modify the range of wavelengths emitted by the filament.This would raise the efficiency of an incandescent electric bulb from 5 percent to greater than 60 percent. It is the first application of photonic crystals to the energy industry [4].

of the AlGaInP material system, producing red and amber LEDs (led by Hewlett-Packard [5] and Toshiba [6]) and of the AlGaInN material system, spanning near ultraviolet to the deep green (led by Nichia Chemical [7] and the Nagoya University [8]) [9]. The broad range in cost and price of nowadays LEDs are due to the large differences in performance and technology capabilities of the different material systems, associated with a specific wavelength range. If by the year 2020, the efficiency of the LED amounts to 120 lm/W (or a power conversion efficiency of about 50%), showing a first cost price of about 0.5 euro/klm, the LED can achieve full market penetration in almost all lighting applications. To realise this future, enormous challenges lie ahead among which improved light extraction from the high refractive index LED material is of utmost importance. An extraction efficiency, and specifically a single facet extraction efficiency, of over 50% for LEDs can have tremendous economical and environmental implications.

LED's ability for directional emission, modulation speed, exceptional longevity (50-100 khrs), interesting design possibilities (e.g. flatness, dimensions, color and intensity control) and vibration and shock resistance reinforce their competitive position towards conventional lighting. Moreover, thanks to these assets, LEDs have these days already commercial entry points in special niche applications.

Specifically their ability for directional emission makes them particularly well suited for optical communications. High directionality, expressed by the label "high brightness" for visible light or "high radiance" (radiance is the output power per unit of solid angle, per unit of emitting area), is needed however for a broad range of applications.
The radiance is a quantity that -at best- is conserved in an imaging system: the radiance of the image cannot be higher than that of the object. Therefore high radiance is important in any application where light needs to be focused to a small spot or where light needs to be coupled into a fiber with small core size and numerical aperture, which is a primary issue in telecommunications. With the ever increasing demand for bandwidth beyond what can be achieved with copper, optical communication is being used for shorter and shorter links than ever before. However, the difficulty and expense of properly terminating glass fibres is causing a number of industries to look at Plastic Optical Fibers (POF) as the low cost, flexible and rugged alternative. Automotive, telecommunications and consumer electronics industry groups have all recently drawn up standards based on POF in combination with high radiance LEDs (RCLED (see beyond)). These markets are now growing very rapidly, and the growth is expected to become explosive as digital TV becomes commonplace. Besides optical fiber telecommunication, brightness and radiance are indispensable in wireless short-range communication, i.e. remote control, infrared data communication (with standards set by the Infrared Data Association IrDA), LCD backlights, displays, automotive applications (today over 50% of European-made cars are using blue, green, white and amber high-brightness LEDs for interior instrument panel illumination), signage, etc..

Already, LED devices are viable choices for a variety of jobs requiring saturated colors. LED traffic signals have experienced dramatic market growth thanks to using 80% less electricity than incandescent lamps. The energy crisis in California

has caused the California Department of Transportation (Caltrans) to retrofit more than 200,000 traffic signals with LEDs. High-brightness LEDs in automobile center high-mounted stop lamps have made significant inroads in the U.S., Europe and Japan [9] .

Their interesting design possibilities made large, full-color outdoor LED signs become ubiquitous. Thanks to high-brightness LEDs, colorful advertising signs adorn Times Square, the NASDAQ building, and major city centers around the world with full video displays.

Robustness and long lifetime is of utmost importance in applications where maintenance and replacement costs exceed the installation cost.

The existence of a broad range of applications for high efficiency, and more specifically high brightness LEDs, is clear. If the efficiency can be further increased to 50% and more and if the cost per lumen of an LED can be further decreased, the LED could fully penetrate the market of commercial niche applications and even general illumination.

1.1.2 Nanostructures

Nanoelectronics[4] is similar to microelectronics, but a thousand times smaller. In order to produce more powerful computers, the density of transistors on a manufactured integrated circuit has roughly doubled every eighteen months over the last decades, storage capacity of dynamic random access memory (DRAM) chips has increased with a factor of four every three years. This trend of exponential miniaturisation is known as Moore's Law. Mass production of integrated circuits is therefore expected to enter the area of nanotechnology before the year 2006[5].

The more powerful electronic processors and memories to be integrated in computers, telephones, cars etc. amount to a world market of hundreds of billions of euros, which makes nanoelectronics the driving force behind the current development of nanotechnology [10]. This emerging field of research and development dedicated to increasing the control over material structures of nanoscale size in at least one dimension, is exploring the edges of optical lithography and, parallel, is searching for alternatives for this standard optical lithography used to produce microchips.

At the borderline of optical lithography, there is deep-ultraviolet lithography using a krypton-fluoride laser ($\lambda = 248$ nm), applied for the current generation of chips. Further gain is possible by utilizing an argon fluoride excimer laser operating at 193 nm with additional resolution enhancement techniques based on the use of the phase of the light. Further evolution in the optical lithography is increasingly less evident. The new International Technology Roadmap for Semiconductors (ITRS) reveals that keeping up with Moore's law will be a progressively

[4]Nano, inspired by the ancient Greek word 'nanos' for dwarf, is a standard prefix in the list of physical units, meaning 1/1000 000 000.

[5]However, even the experts don't know if miniaturisation will progress according to Moore's Law. Various factors, such as increased costs of miniaturisation and decreasing added value, may well slow down the current descent into the nanoworld. Ultimately the miniaturisation is limited by the size of the atom.

more expensive proposition. For the 157 nm optical lithography generation, new materials need to be explored and developed for lenses, coatings, resists, masks, etc.. For wavelengths below 120 nm, no optical materials are transparent and the development of diffraction limited lenses is improbable.

Until about 2007, the ITRS sees a continued evolution of traditional optical lithography as the most likely lithography solution, in spite of growing costs, to provide the 60 nm resolution. However, as 157-nm lithography won't be ready for volume productions [11], alternative technologies are considered, especially in view of small production run applications. Viable successors for deep-ultraviolet lithography are still in lab phase, but are emerging to be applicable for commercial use: extreme-ultraviolet lithography ($<$ 100 nm), ion-beam projection lithography ($<$ 100 nm), atom lithography (80 nm), electron-beam (e-beam) lithography (5 nm), x-ray proximity (30 nm), etc..

This market-driven pull inducing the microelectronics industry to continue the current trend of miniaturisation and to develop nanotechnology towards commercially applicable techniques, creates opportunities for new devices in areas other than electronics: medicine, cosmetics, etc.. Particularly, in opto-electronics and optics, nanotechnology can create properties otherwise unattainable, with greater complexity, homogeneity and density. This legitimises the research into the suitability of nanostructures for photonic devices. Nanostructures for optical applications are characterised by a periodicity or pitch of the order of the wavelength. As the application area is mostly situated in the visible light or near-infra red, including the telecommunication wavelengths, the required resolution ranges from 1 μm down to 50 nm. This is feasible on lab level, but especially more and more on a commercial level. The required resolutions of optical nanostructures is no longer the insurmountable threshold towards commercialisation. Indeed, periodically modulated nanostructures or diffractive gratings are well spread in modern optical technology. The broad areas of acousto-optics, holography, integrated optics, quantum-electronics and spectral analysis are inherently interwoven with grating diffraction. Without going in to great detail, we mention some possible applications.

In the field of spectral analysis, diffraction gratings are often used in monochromators. A monochromator is a wavelength tunable narrowband optical filter. The light incident on the grating is reflected with a wavelength dependent angle. Rotating the grating, one can fine tune the wavelength that exits the monochromator via the exit-slit. The tuning, accomplished by the rotation of the grating is typically large (800 nm). The spectral resolution is, among others, defined by the exit-slit (typically 0.05 nm).

Well-known applications of diffraction gratings integrated with opto-electronic devices are the *Distributed Feedback Laser* (DFB) and *Distributed Bragg Reflector* (DBR) Laser. The required feedback for laser action in these lasers is accomplished by a reflection grating. The spectral selectivity of the grating results in a higher modal purity [12], [13]. Integration of a surface relief grating with a *Vertical Cavity Surface Emitting Laser* (VCSEL) can exploit the polarisation selective nature of linear diffraction gratings. It has been shown that polarisation instability typical for rotational symmetric VCSELs is counteracted with a grating [14].

The peculiar optical behavior of diffractive structures with a multi-dimensional periodicity in the order of the wavelength of the light and large modulation depth of the refractive index has retrieved attention. When the structure is designed appropriately, a *Photonic Band Gap* (PBG) or a range of optical frequencies that can not exist in the structure can appear. This "*Photonic Crystal*" (PC) -by analogy with the electron states in crystals- can exhibit a full PBG when the refractive index is strongly modulated in the 3 dimensions [15]. Although they do not exhibit a complete PBG, 1-dimensional PCs (DBR mirror) and 2-dimensional PCs (gratings) are common due to their far less complex fabrication process. Their anomalous and intriguing effects expected around Bragg-condition are fully exploited. 2-dimensional PCs can for example be used to increase the level of integration in *Photonic Integrated Circuits* (PICs). The PCs are used to scale down the area required for waveguiding: removing a (some) rows of holes, an "impurity" is introduced in the periodic PC, and light can be guided along this impurity [16]. In this way, extremely short bends, filters, combiners, etc. can be made. In combination with a vertical/horizontal coupler, dense PICs can be realised [17].

Diffractive optics and micro-optics have benefited from and owe much of their rapid growth to precision micro-machining and high-resolution pattern generation techniques developed originally to support micro-electronics. However, it is worth emphasizing that optical holography preceded the modern era of diffractive technology, and, in fact, some novel diffractive devices are being fabricated by this technique or a combination of techniques of both fields.

1.2 High brightness LEDs and nanostructures meet in the Grating-Assisted Resonant-Cavity Light-Emitting Diode: research objectives

High brightness[6] or high radiance is in general associated with a planar geometry and a single side surface extraction. Intrinsically, due to the high refractive index contrast between the source material and surrounding medium, Snell's law limits the single side extraction efficiency of a standard planar LED to $\pm 2\%$.

There are several successful approaches to increase the efficiency of LEDs. One of them is the resonant cavity LED (RCLED). In these LEDs the active layer is embedded in a resonant cavity with at least one dimension of the order of the wavelength of the emitted light. Under these circumstances the spontaneous emission process itself is modified, such that the internal emission is no longer isotropic. A single side external efficiency up to 28% has been demonstrated [19]. However, again, Snell's law limits the extraction to the resonant power emitted in the limited numerical aperture around the direction perpendicular to the substrate, corresponding to the critical angle θ_c. The optical power coupled to the so-called leaky DBR modes, which are total internally reflected at the semiconductor-air

[6] The commercial labelling "High Brightness" LEDs is strongly linked with "High Efficiency" as the saturation level of a device at high pumping levels can only be increased when efficiency is increased.

interface and the power coupled to the laterally propagating or guided modes, which are total internally reflected at the DBR mirror are lost (except through partial photon recycling by reabsorption). These losses cause the external extraction efficiency to be substantially lower than 100%.

A solution to this loss of power in the unextractable guided modes can be found in a two-dimensional periodic wavelength-scaled nanostructure or grating integrated into one or more of the mirrors of the resonant cavity. The grating is used for purely optical "photon recycling": the diffractive properties of the periodic grating redirect the laterally propagating resonant guided mode to an extractable direction in the extraction cone. Because of the high power fraction in these guided modes, the use of such gratings, fabricated with a mature nanostructure technology, will then result in a higher external extraction efficiency and radiance. We will hereafter call these devices *Grating-Assisted Resonant-Cavity LEDs* (GA-RCLEDs). This conceptually new device is the subject of this thesis.

1.3 Outline of the manuscript

In Chapter 2, we shortly review the physics of light emission in stratified semiconductors. Snell's law is applied on a LED and techniques to outsmart this law are presented. We take a closer look to one of these techniques: the RCLED. The RCLED is the basic element of the GA-RCLED.

Chapter 3 focuses on diffractive nanostructures, the second basic element of the GA-RCLED. The *Wavevector diagram* (WVD) is presented as a tool to analyse gratings qualitatively. An overview of diffraction modelling tools is given. Comparison of their optimal working field results in the choice of the *RCWA (Rigorous Coupled Wave Theory)* to be used in this work. This model will be detailed as it has been implemented to simulate diffraction of 2-dimensional gratings.

Chapter 4 touches upon the GA-RCLED. Firstly, the device concept is described in greater detail. Using the WVD, the possibilities of the GA-RCLED are qualitatively analysed. Secondly, we describe the electromagnetic analysis on which the numerical calculations used to simulate dipole emission inside periodically corrugated layer structures is based. This tool will be used in further chapters to analyse the GA-RCLED quantitatively.

The fabrication process of the GA-RCLED is presented in Chapter 5. Alternatively to the more standard e-beam technology to define 2-dimensional gratings, a holographical technique has been developed and is discussed in this chapter. It is found that the GA-RCLED has a standard processing scheme that can easily serve mass-fabrication.

Chapter 6 discusses the design, realisation and characterisation of a GA-RCLED with a 1-dimensional grating. Numerical simulations based on the tool presented in Chapter 4 are compared to experimental data. Evidence of guided mode extraction is given.

The design, realisation and characterisation of GA-RCLEDs with a 2-dimensional grating are detailed in Chapter 7. Two fabrication technologies have been applied to define the grating. Holography was used to generate mainly square lattice

gratings. E-beam was employed to define triangular lattice gratings. Spectral measurements and farfield data reveal guided mode extraction. An enhanced extraction efficiency is achieved.

Finally, in Chapter 8 we present our main conclusions and perspectives for future work.

1.4 Publications

The results obtained in this work have been published in various papers and presented at various conferences. This paragraph gives an overview of the publications.

Journal papers published:

(1) D. Delbeke, P. Bienstman, R. Bockstaele and R. Baets, "Rigorous Electromagnetic Analysis of Dipole Emission in Periodically Corrugated Layers: the Grating-Assisted Resonant-Cavity Light-Emitting Diode", *J. Opt. Soc. Am. A*, vol. 11(5), pp. 871-880, 2002.

(2) D. Delbeke, R. Bockstaele, P. Bienstman, R. Baets and H. Benisty, "High-efficiency semiconductor resonant-cavity light-emitting diodes: a review", *IEEE J. Sel. Top. Quantum Electron.*, vol. 8(2), pp. 189-206, 2002 (invited paper).

(3) P. Modak, D. Delbeke, I. Moerman, R. Baets, P. Van Daele and P.Demeester, "InAlGaP microcavity LEDs on Ge-substrates", *J. of Crystal Growth*, vol. 221, pp. 668-673, 2000.

(4) P. Modak, M. D'Hondt, D. Delbeke, I. Moerman, P. Van Daele, R. Baets, P. Demeester and P.Mijlemans, "AlGaInP microcavity light-emitting diodes at 650 nm on Ge substrates", *IEEE Phot. Tech. Lett.*, vol. 12(8), pp. 957-959, 2000.

Papers presented at international conferences with publication in proceedings:

(5) K. Ghawana, D. Delbeke, I. Christiaens, S. Verstuyft and R. Baets, "Heterogenous integration with BCB applied to GA-RCLEDs," in *Optoelectronic devices and heterogenous integration, Proc. SPIE*, vol. 4947, Brugge, Belgium, 2002.

(6) R. Baets, D. Delbeke, P. Bienstman, W. Bogaerts, D. Taillaert and B. Luyssaert, "Photonic crystal materials and light extraction enhancement possibilities," in *11th International workshop on Inorganic and Organic Electroluminescence and 2002 International Conference on the Science and Technology of Emissive Displays and Lighting*, Gent, Belgium, 2002.

(7) D. Delbeke, B. Dhoedt, R. Bockstaele, I. Moerman, P. Van Daele, T.F. Krauss and R. Baets, "Electrically Pumped Grating-Assisted Resonant-Cavity Light-Emitting Diodes", in *Light-Emitting Diodes: Research, Manufacturing and Applications VI, Proc. SPIE*, vol. 4641, San Jose, California, pp. 42-49, 2002.

(8) P. Modak, M. D'Hondt, D. Delbeke, P. Mijlemans, I. Moerman, R. Baets, P. Van Daele and P. Demeester, "InAIGaP microcavity LEDs on Ge-substrates", *The Tenth International Conference on Metal Organic Vapor Phase Epitaxy (IC MOVPE-X)*, Sapporo, Japan, pp. 319-320, 2000.

(9) P. Modak, M. D'Hondt, D. Delbeke, I. Moerman, P. Van Daele, R. Baets, P. Demeester and P.Mijlemans, "High efficiency InAlGaP microcavity LEDs on Ge substrates", *Proc. LEOS Benelux Symposium*, Delft, Netherlands, pp. 59-62, 2000.

(10) D. Delbeke, K. Vandeputte, R. Baets, R. Bockstaele, B. Dhoedt, I. Moerman, P. Van Daele, and S. Verstuyft, "Holograpgically defined Grating-Assisted Micro-Cavity Light Emitting Diodes", *Proc. LEOS Benelux Symposium*, Mons, Belgium, pp. 159-162, 1999.

(11) D. Delbeke, B. Dhoedt, R. Bockstaele, I. Moerman, P. Van Daele, T.F. Krauss and R. Baets, "Electrically Pumped Photonic Crystal Micro-Cavity Light Emitting Diodes", *Proc. LEOS Summer Topical Meetings*, San Diego, USA, pp. 71-72, 1999.

(12) M. D'Hondt, P. Modak, D. Delbeke, I. Moerman, P. Van Daele. R. Baets, P. Demeester and P. Mijlemans, "4 mW micro cavity LED at 650 nm on germanium substrates", *Light-Emitting Diodes: Research, Manufacturing, and Applications IV, Proc. SPIE*, vol. 3938, San Jose, California, pp. 196-204, 1999.

Presentations at symposia without proceedings:

(13) D. Delbeke, I. Moerman, P. Van Daele and R. Baets, "Grating-Assisted Resonant-Cavity Light-Emitting Diodes for High Brightness," *Second PhD Symposium*, Gent, Belgium, 2001.

(14) D. Delbeke, R. Baets, I. Moerman, P. Van Daele and S. Verstuyft, "High Efficiency Grating Assisted MC-LEDs", *Summer School and EOS Topical Meeting on Semiconductor Microcavity Photonics*, Monte Verita, Switserland, 2000.

(15) P. Bienstman, W. Bogaerts, R. Bockstaele, D. Delbeke, S. Goeman, B. Depreter, J. Derluyn, C. Sys, L. Vanwassenhove, B. Dhoedt, I. Moerman, P. Van Daele and R. Baets, "Microcavity and PBG-related work at the University of Ghent", *COST 268 Workshop*, Stockholm, Sweden, 1999.

(16) D. Delbeke, R. Baets, "High Efficiency Grating Assisted MC-LEDs", *Summer School on Confined Photon Systems: Fundamentals and Applications*, Cargèse, France, 1998.

References

[1] The International Energy Agency, *"Monthly Electricity Survey, February 2002"*, www.iea.org.

[2] M. Kendall, M. Scholand, *"Energy Savings Potential of Solid State Lighting in General Lighting Applications"*, US Department of Energy, Washington DC, April 2001.

[3] The European Environment Agency, *"Energy and environment in the Europian Union"*, www.eea.eu.int.

[4] K. Patch, *"Crystal turns heat to light"*, Technology Research News, www.trnmag.com/Stories/2002/052902.

[5] C. P. Kuo, R. M. Fletcher, T. D. Osentowski, M. C. Lardizabal, M. G. Craford and V. M. Robbins, "High-performance AlGaInP visible light-emtting-diodes", *Appl. Phys. Lett.,* vol. 57(27), pp. 2937-2939, 1990.

[6] H. Sugawara, M. Ishikawa and G. Hatakoshi, "High-efficiency InGaAlP/GaAs visible light-emtting-diodes", *Appl. Phys. Lett.,* vol. 58(10), pp. 1010-1012, 1991.

[7] S. Nakamura, M. Senoh, N. Iwasa, S. Nagahama, T. Yamaka and T. Mukai, "Superbright green InGaN single-quantum-well-structure light-emitting diode", *Jpn. J. Appl. Phys.,* vol. 2 34(10B), pp. L1332-L1335, 1995.

[8] H. Amano, N. Sawaki, I. Akasaki and Y.Toyoda, "Metalorganic vapor phase epitaxial growth of a high quality GaN film using an AlN buffer layer", *Appl. Phys. Lett.,* vol. 48(5), pp. 353-355, 1986.

[9] A. Bergh, G. Craford, A. Duggal and R. Haitz, "The Promise and Challenge of Solid-State Lighting", *Physics Today,* vol. 54(12), pp. 42, 2001.

[10] A. Ten Wolde, *Nanotechnology*, Netherlands Study Centre for Technology Trends, The Netherlands, 1998.

[11] P. Ware, "Removing the mask", *SPIE's OEmagazine*, vol. 3, pp.26-27, 2002.

[12] T. Erdogan and D.G. Hall, "Circularly symmetrical Distributed Feedback Semiconductor-laser-an analysis", *J. Appl. Phys.,* vol. 68(4), pp. 1435-1444, 1990.

[13] M. Fallahi, K.J. Kasunic, S. Penner, O. Nordman and N. Peyghambarian, "Design and fabrication of circular grating coupled distributed Bragg reflector lasers," *Opt. Eng.,* vol. 37(4), pp. 1169-1174, 1998.

[14] S. Goeman, *"Integration of surface relief structures with vertical cavity surface emitting lasers for polarisation and mode control",* Ph. D. Thesis, Ghent University, Ghent, Belgium, 2001.

[15] J. D. Joannopoulos, R. D. Meade, J. N. Winn, *Photonic crystals : molding the flow of light*, Princeton university press, Princeton, N.J., 1995.

[16] European IST project: *"Photonic Integrated Circuits using photonic Crystal Optics"*, 1/3/2000-28/2/2003.

[17] D. Taillaert, W. Bogaerts, P. Bienstman, T. F. Krauss, I. Moerman, P. Van Daele and R. Baets, "A high-efficiency out-of-plane fibre coupler for coupling to high index contrast waveguides", *ECOC Proceedings 01*, Amsterdam, The Netherlands, pp.30-31, 2001.

[18] http://www.strategies-u.com.

[19] M. Rattier, H. Benisty, R.P. Stanley, J.F. Carlin, R. Houdré, U. Oesterle, C.J.M. Smith, C. Weisbuch and T.F. Krauss, "Toward ultrahigh-efficiency aluminum oxide microcavity light-emitting diodes: guided mode extraction by photonic crystals", *IEEE J. Sel. Top. Quantum Electron.,* vol. 8(2), pp. 238-247, 2002.

2

Highly Efficient Light-Emitting Diodes

THE physics of spontaneous emission is shortly recapitulated. Snell's law, limiting efficiency to several percents, is presented together with some successful techniques to outsmart this limitation. One of these techniques, the highly efficient resonant-cavity light-emitting diode (RCLED), is enlightened in greater detail. The basics of dipole emission in planar cavities are reviewed. From these, a number of design rules to design RCLEDs are derived. A short list of state-of-the-art devices in different material systems and at different wavelengths is given. We finally discuss some advanced techniques based on gratings or photonic crystals to improve the efficiency of these devices. This technique will be studied in the rest of this work, both theoretically and experimentally.

[D. Delbeke, R. Bockstaele, P. Bienstman, R. Baets and H. Benisty, "High-efficiency semiconductor resonant-cavity light-emitting diodes: a review", *IEEE J. Sel. Top. Quantum Electron.,* vol. 8(2), pp. 189-206, 2002.]

2.1 Introduction

2.1.1 Short history of Light-Emitting Diodes

The exploratory development of the *Light-Emitting Diode* (LED) started with first reports of electroluminescence by Round (1907) and Losev (1923), and continued with the understanding of recombination phenomena by Lehovec (1951) and the first fabrication of an infrared LED at MIT (1960). During the mid sixties or the early handheld calculator epoch, research accelerated [1]. Since then, the development of the cold light sources has been characterised by a race for high efficiency. This optimisation towards a higher efficiency took more or less place in three stages, reflected by a change in focus to increase the efficiency.

The external quantum efficiency η_{ext} is the key performance figure for high efficiency LEDs and stands for the number of photons generated per injected electron:

$$\eta_{ext} = \frac{P_{opt}/\hbar\omega}{I/q} = \eta_{inj}\eta_{int}\eta_{extr} \tag{2.1}$$

with P_{opt} the emitted optical power (W), I the injection current (A), q the elementary electron charge (C) and $\hbar\omega$ the energy per emitted photon (eV). The η_{ext} depends on the fraction of carriers injected in the useful active region (η_{inj} or injection efficiency), the fraction of spontaneous recombination that is radiative (η_{int} or internal efficiency) and the extraction efficiency of the generated photons (η_{extr}). These three contributions are representative for the more or less successive introductions of optimisation. Firstly, exhaustive study of semiconductor electronic band structures in the early sixties led to a better control of carrier injection. Accordingly, η_{inj} could be raised, reaching unity (1963 [2]) by the introduction of heterostructures and *Quantum Wells* (QWs). The introduction of *Liquid Phase Epitaxy* (LPE) (1967), *Metal-Organic Chemical Vapor Deposition*(MOCVD) and *Molecular Beam Epitaxy* (MBE) (1980) overcame the moderate η_{int}-values. Non-radiative recombination at low current densities mainly originates from defects in the crystal. Successive improvement of epitaxial fabrication techniques resulted in the availability of high-quality crystals. Nowadays, the quality of the crystal measured by the density of defects, can be very high for a broad range of material systems. For AlInGaAs on GaAs substrates for example, this results in an η_{int} reaching unity. However, even today the internal efficiency remains a major issue for some material systems, e.g. in AlInGaP LEDs and in LED structures in which substantial reabsorption occurs.

It is at this stage ($\eta_{inj}\eta_{int} \approx 1$) that it is appropriate to optimise η_{extr} which is limited to 2-4% by Snell's law for conventional planar LEDs due to the high refractive index contrast between the source material and the surrounding medium. Improvement of the extraction efficiency happened in the early nineties, when cavity optics entered the world of LEDs with the *Resonant-Cavity LED* (RCLED). In these devices the active layer is embedded in a cavity with at least one dimension of the order of the wavelength of the emitted light. Under those circumstances the spontaneous emission process itself is modified, such that the internal emission is no longer isotropic. In spite of earlier work by Lukosz on emission in multi-layers

in 1980 [3]- [6], experimental evidence has only been introduced in 1990-1992 by the work of Yokoyama, Björk, Yamamoto, Deppe, Hunt *et al.* [7]- [13], Schubert *et al.* presented the RCLED as a conceptual novel LED in 1992 [14]. In 1994 a communication application design has been proposed by the same group [15]. However the overall external efficiency remained low. The first highly efficient RCLED was made by De Neve *et al.* in 1995 obtaining $\eta_{ext} \approx 23\%$ [16]- [18], and has been further optimised in 1999 by Wierer *et al.* (differential $\eta_{ext} \approx 27\%$) [19] and in 2002 by R. Stanley *et al.* $\eta_{ext} \approx 28\%$ [20]. Parallel with this "wave" optics based technique exploiting cavity interference effects, "ray" optics based techniques oriented towards geometrical light collection were introduced. In 1992 Hewlett-Packard produced its first LED with transparent superstrate ($\eta_{ext} \approx 6\%$). Elaboration of the principle and geometrical optimisation resulted in 1999 in a pyramidal shaped device with world record efficiencies of 60% [21]. In 1993 Schnitzer and Yablonovitch [22] proposed the idea of random surface texturing to enhance escape probability by scattering of the photons, a principle resumed in 1998 by Windisch *et al.* giving rise to thin film devices with $\eta_{ext} \approx 50\%$ [23]. The LED with a radial outcoupling taper [24] is another successful technique which tilts the path of the photon inside the semiconductor until it reaches the semiconductor-air interface within the extraction cone.

2.1.2 Outline of this chapter

This chapter will give a review of the Resonant-Cavity LED. This high efficient light emitter is no longer just an object of research. It has been launched commercially in 1999 by Mitel Corp. (now Zarlink Semiconductors) for *Plastic Optical Fibre* (POF) communication applications. The market for LEDs for communications is increasing, for instance the newly approved standard for 100BASE-SX (Fast Ethernet) is based on 850nm LEDs [25]. RCLEDs are benefitting from this evolution: recently, RCLEDs emitting red light in combination with POF is proposed as the standard for FireWire or i.Link (IEEE1394b) [26]. This standard covers broadband service applications such as digital TV, DVD, etc. Several companies do participate in this commercialisation of the RCLED for communication applications and some extend this activity towards non-communication applications.

First, some basic principles of LEDs and spontaneous emission are discussed in section 2.2. The modest extraction efficiency of a basic LED is explained and some solutions to this drawback are presented. A theoretical investigation of the planar RCLED is summarised in section 2.3. Theoretical models to analyse spontaneous emission can mainly be subdivided in two major approaches. The first series is a quantum-mechanical description based on quantisation of the electromagnetic field and mode density. These methods can become complex and their application is restricted to simple, ideal media [9], [28] (see also section 2.2.1). The second series is based on a classical approach valid in the so-called weak-coupling regime, which is the working regime of practical planar RCLEDs. Spontaneous emission is modelled as an electric dipole. To calculate the far field emission, a transfer matrix formalism is implemented for the plane wave components of the dipole field. This

numerical method is described in detail in a series articles by H. Benisty *et al.* [29]-[31] and in [32]- [33]. For the sake of physical insight, this numerically solvable analysis is summarised in section 2.3.1. The different parameters influencing η_{extr} are then presented in section 2.3.2. Section 2.3.3 reviews the state-of-the-art of high efficiency RCLEDs. Although planar RCLEDs have been optimised thoroughly, advanced techniques to improve η_{extr} even further are nevertheless still welcome. Some of these techniques are presented in section 2.3.4. A vision of the future ends this chapter. Appendix A discusses some guidelines and figures of merit for comparison of high efficiency LEDs.

Although the principle is extendable to all sorts of material, the given examples and general trends are limited to semiconductor devices.

2.2 Basic principles of semiconductor LEDs

Basically a *Light-Emitting diode* (*LED*) consists of a p-n direct semiconductor junction. Under forward bias, holes diffuse from the p-doped semiconductor to the n-doped region and vice-versa. Once the depletion region, in which there are no free carriers, besides the ones that are diffusing, is crossed, the minority carrier will recombine with a majority carrier. The excess of energy can be converted into light. This is called *cold light emission*, in contrast with incandescent lamps.

In practice, the LED takes the form of a p-n *double heterostructure* in order to improve electron-hole injection, to reduce the absorption of recombination radiation and -in combination with proper geometry design- to improve photon escape. The region where recombining carriers contribute to useful photon emission is called the active region [34]. The quantum-mechanical description of spontaneous emission in bulk media will shortly be described, to deep physical insight [27], [34]-[36]. In this scope, the approach is limited to one-electron ions and discrete level transitions. Homo- and hetero-junction characteristics will shortly be discussed. Spontaneous emission in stratified media will be discussed using a semiclassical approach in 2.3.

2.2.1 Recombination in active regions

An atomic or nuclear system can interact with electromagnetic radiation in different ways. To understand the physics of light generation in semiconductors, we consider three basic processes of interaction of photons with electrons [36]. First the atomic or nuclear systems can make spontaneous transitions from an excited state to a state of lower energy with the emission of a photon. This process is called spontaneous emission and can take place in absence of any external field. Second, a system can emit radiation under the influence of an applied radiation field. This process is called stimulated emission and has an important practical application in lasers which produce intense beams of coherent light. Finally, a system can absorb photons from radiation making a transition from a state of lower to a state of higher energy.

The transition probability of an electron in the conduction band (initial state $|i\rangle$) to the valence band (final state $|f\rangle$) with emission of a photon with energy $\hbar\omega$

per unit volume is given by Fermi's golden rule (see [34] for derivation):

$$W_{sp}(i) = \frac{2\,\pi}{\hbar} \sum_f |\langle f|H_p|i\rangle|^2\, \delta(E_f - E_i - \hbar\omega) \tag{2.2}$$

with E_f and E_i the band edge energies of final and initial state and H_p the Hamiltonian that describes the perturbation created by the electromagnetic field, in case of weak fields, given by:

$$H_p = -\frac{q}{m_0}\mathbf{A}\cdot\mathbf{p} \tag{2.3}$$

with q and m_0 respectively the magnitude and mass of the electron charge in free space, $\mathbf{A}$ the vector potential of the electric field, $\mathbf{p}$ the momentum operator. The matrix element $|H_{f\,i}|^2 = |\langle f|H_p|i\rangle|^2$ determines the strength of interaction between the two states of the electron. The strength of this interaction depends on the wavefunction describing the two electron states[1] and the polarisation of the electromagnetic field in accordance with particular symmetries of the conduction and valence Bloch functions. The **k**-selection rule, dictating that transitions between plane wave states are forbidden unless the k-vectors of the two states are equal, is comprised in this matrix element (overlap of orthonormal set wavefunctions). This explains why direct semiconductors (e.g. GaAs) are required for efficient light-emitters. According to this selection rule, (2.2) can be reformulated:

$$W_{sp}(\mathbf{k_{el}}) = \frac{2\,\pi}{\hbar} \sum_f |\langle f|H_p|i\rangle|^2\, \delta(\hbar\omega(\mathbf{k_{el}}) - \hbar\omega) \tag{2.4}$$

with $\hbar\omega(\mathbf{k_{el}})$ the energy difference between the electron and hole level for wave vector $\mathbf{k_{el}}$:

$$\hbar\omega(\mathbf{k_{el}}) = E_f(\mathbf{k_{el}}) - E_i(\mathbf{k_{el}}) \tag{2.5}$$

The summation can be replaced by an integral for a sufficiently dense set of modes:

$$W_{sp}(\mathbf{k_{el}}) = \frac{2\,\pi}{\hbar} \int_{\mathbf{k}} |\langle f|H_p|i\rangle|^2\, \delta(\hbar\omega(\mathbf{k_{el}}) - \hbar\omega)\, \rho(\mathbf{k})\, d\mathbf{k} \tag{2.6}$$

with $\rho(\mathbf{k})$ the optical mode density in the **k**-space. Calculation of the mode density and matrix element in the case of a homogeneous bulk medium is straightforward [27]. In layered media however, the analytical treatment of the matrix element and mode density gets laborious. Theoretical analysis of spontaneous emission presented in literature are consequently limited to elementary multi-layers with constant real refractive indices [28], or Fabry-Pérot resonators with perfect mirrors [9] (see section 2.3.1.2).

Previous theory is valid for a single transition. In practice there are different transitions over different energy levels. Eq. (2.6) can be used to calculate the

[1] The wavefunction describing the two electron states corresponds with plane waves in case of an isotropic medium, for a *Quantum Well (QW)* the wavefunctions solution is a plane wave in the directions within the plane of the well, but along the confinement direction the wavefunction has a (co)sine wave distribution inside the well with exponential decay outside the well.

intrinsic emission spectrum as a result of inhomogeneous broadening caused by the difference of the emission energies of the individual transitions. This intrinsic emission spectrum will be used in the semiclassical approach of section 2.3. Summation of $W_{sp}(\mathbf{k_{el}})$ over $\mathbf{k_{el}}$, weighted with the probability to find a carrier with wave vector $\mathbf{k_{el}}$, results in $W_{sp}(\hbar\omega)$ or the spontaneous emission rate of frequency ω:

$$W_{sp}(\hbar\omega) = \sum_{\mathbf{k_{el}}} W_{sp}(\mathbf{k_{el}}) f_c(E_c(\mathbf{k_{el}}))(1 - f_v(E_v(\mathbf{k_{el}})))\delta(E_c(\mathbf{k_{el}}) - E_v(\mathbf{k_{el}}) - \hbar\omega) \tag{2.7}$$

with f_c and f_v the Fermi-Dirac distributions with quasi-Fermi level E_{fc} and E_{fv}. The probability to find an electron in the conduction band is then given by $f_c(E_c(\mathbf{k_{el}}))$ and to find a hole in the valence band by $(1 - f_v(E_v(\mathbf{k_{el}})))$. With the Boltzmann approximation for low current injection levels, the Fermi-Dirac distribution can be written as an exponential and the spontaneous emission rate gets, with a first order approximation in k of $W_{sp}(\mathbf{k_{el}}) = W_{sp}(0) = 1/\tau_0$ [2]:

$$W_{sp}(\hbar\omega) \simeq \frac{1}{\tau_0} \sum_{\mathbf{k_{el}}} e^{\frac{E_{fc} - E_c(\mathbf{k})}{k_B T}} e^{\frac{E_v(\mathbf{k}) - E_{fv}}{k_B T}} \delta(E_c(\mathbf{k_{el}}) - E_v(\mathbf{k_{el}}) - \hbar\omega) \tag{2.8}$$

This expression can be solved, approaching the summation by an integration over the electron-hole states:

$$W_{sp}(\hbar\omega) \simeq \frac{\sqrt{2} m_r^*}{\pi^2 \hbar^3} \frac{1}{\tau_0} \frac{np}{N_c N_v} \sqrt{\hbar\omega - E_g} e^{-\frac{\hbar\omega - E_g}{k_B T}} \tag{2.9}$$

with m_r^* the reduced mass of an electron-hole system, n (p) the electron (hole) concentration, N_c (N_v) the effective density of states in conduction (valence) band, E_g the energy bandgap, $k_B = 1.38 \cdot 10^{-23}\, JK^{-1}$ Boltzmann's constant, T the temperature in K. For small $(\hbar\omega - E_g)$, emission is dictated by the density of states by $\sqrt{\hbar\omega - E_g}$, the maximum is situated at $\hbar\omega = E_g + k_B T$, from which point on the emission is limited by the exponential decay of the carrier density dictated by the Fermi-dirac distribution. The *Full-Width-Half-Maximum* (FWHM) $\Delta(\hbar\omega)$ at low current injection densities approximately equals $1.8 k_B T$ or

$$\Delta(\lambda) \simeq \frac{1.8 k_B T}{hc} \lambda^2 \tag{2.10}$$

For GaAs at low injection current density, emitting at $0.98\mu m$, the inhomogeneous broadening is approximately $\Delta(\lambda) \simeq 32$ nm. Increasing the injection current drives the semiconductor further away of its thermodynamic equilibrium, resulting in an increase of np, which translates itself in a broadening of $\Delta(\lambda)$. This is in agreement with the experimental verification of the band filling effects in [37]. This inhomogeneous broadening surpasses the homogeneous broadening, typically a few tens pm, which is caused by the finite lifetime of some nanoseconds characterising spontaneous emission.

[2] This approximation is justified as the electron and hole population is concentrated in the extremes of the energy bands.

To complete this section on recombination, it is worth to mention that direct radiative recombination is in competition with mainly two other non-radiative recombination mechanisms [34]. Defect, impurity and surface recombination is the mechanism where an electron is temporarily trapped in an energy level in between the energy gap before releasing to the valence band. This two-step recombination mechanism is also called Shockley-Read-Hall recombination which states that this recombination rate is linear in n. The second type of transitions is called Auger recombination. It is a collision between two electrons which knocks one electron down to the valence band and the other to a higher energy state in the conduction band. The higher electron eventually thermalises back down to the bottom of the conduction band, releasing the excess of energy as heat to the crystal lattice. (equivalent process can happen with holes). The Auger rate will thus depend on the probability of finding the various states occupied or empty, as the case may be. Considering the Fermi-Dirac distribution under Boltzmann approximation for low carrier density, and the low dopant level in the active layer (n=p), this probability is proportional to n^3. Equation (2.9) shows that the spontaneous emission rate is proportional with n^2 (n=p in the lightly doped or intrinsic active layer). The total recombination rate can thus be written as:

$$\begin{aligned} W_{sp}^{tot} &= W_{sp}^{rad} + W_{sp}^{nrad} \\ &= Bn^2 + An + Cn^3 \end{aligned} \tag{2.11}$$

Shockley-Read-Hall recombination will be dominant at low carrier concentration, the radiative at moderate and Auger at high carrier concentration. A or the reciprocal of τ_{nrad} depends on the impurity and defects concentration, B or the bimolecular recombination coefficient can be found by integrating equation (2.9) over all photon energies $\hbar\omega > E_g$. C or the Auger recombination coefficient depends strongly on the bandgap of the material. C will be large for small bandgap or long wavelength devices [34]. The devices studied in this work are short-wavelength emitting devices working at moderate carrier concentration, Auger recombination can and will be neglected.

$$W_{sp}^{tot} \simeq Bn^2 + \frac{n}{\tau_{nrad}} \tag{2.12}$$

2.2.2 p-n junction

Spontaneous emission is the process of an electron in the conduction band that relaxes to the valence band recombining with a hole. The presence of an electron in the conduction band and a hole in the valence band is indispensable. It can be achieved injecting minorities in a doped semiconductor. This is what happens in a forward biased p-n junction[3]. The external voltage counteracts the internal field that initially prohibited diffusion of electrons to the p-doped and holes to the n-doped semiconductor. Diffusion occurs and the minorities recombine while

[3]The semiconductor can also be excited by the carriers generated from absorbed light. This work however focusses on the direct current injection technique.

diffusing towards the electrode. The voltage-current density relation of a homo-junction (the semiconductor material composition of both n and p layers is the same) is the well-known Schockley's law:

$$V(J) = \frac{k_B T}{q} \ln(\frac{J}{J_0} + 1) \simeq \frac{k_B T}{q} \ln(\frac{J}{J_0}) \tag{2.13}$$

with J_0 the saturation current density, a material characteristic quantity.

This simple pn-junction where the carriers are swept through the depletion layer with negligible recombination, to relax while diffusing in the adjoining semiconductor is not appropriate for light-emitting devices. More preferable is the double heterojunction diode where the recombination takes place in an intrinsic small-bandgap material sandwiched between a p- and a n-doped larger-bandgap semiconductor layer. The advantages are plural. The carriers are trapped in between two energy barriers, which makes it possible to obtain higher carrier densities and prohibits non-radiative defect recombination associated with large diffusion lengths. The emitted photons carrying an energy equal to the bandgap of the intrinsic material will not be absorbed in the surrounding large-bandgap material. Moreover, the better control on the location of the light generation in combination with an elaborated geometrical design of the device can ameliorate extraction of the photons.

The p-i-n junction can be further optimised: to control the emission wavelength and to obtain even higher carrier densities, the active layer can be performed as a (more) QW(s) in between large-bandgap barriers. In this work, we have used the 3-QW double hetero-junction optimised by H. De Neve in [38]. The refractive index of this structure, tabulated in Table 2.1, is sketched in Fig. 2.1. The bandgap is associated with this refractive index: a higher refractive index corresponds with a smaller bandgap. The internal field of this hetero-junction optimises carrier caption.

The voltage characteristic of a QW junction is given by [39]:

$$V(J) = m\frac{k_B T}{q} \ln(\frac{J}{J_0}) \tag{2.14}$$

with m the ideality factor, $m = 1$ for radiative recombination, $m = 2$ for non-radiative recombination. The voltage drop over the LED device is given by the sum of the junction voltage and the voltage drop over the series resistance R_s:

$$V_{LED}(J) = V(J) + R_s J * S \tag{2.15}$$

with S the diode cross-section surface.

2.2.3 Highly efficient LEDs or how to outsmart Snell's Law

2.2.3.1 Extraction efficiency of LED

In its minimal and most common appearance, an LED consists of a semiconductor p-n junction chip (side dimensions are typically 200-400μm) through which a current is injected (Fig 2.2(a)). The chip is mounted on an ideally parabolic metallic

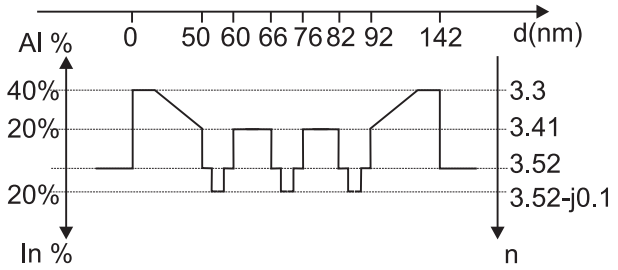

Fig. 2.1: 3-QW hetero-junction used in this work.

thickness	material	doping level	remarks
	GaAs	p-doped	
30 nm	$Al_{40}Ga_{60}As$	p-doped	GRIN spacer
20 nm	$Al_{20}Ga_{80}As$	intrinsic	GRIN spacer
2 nm	GaAs	intrinsic	barrier
6 nm	InGaAs	intrinsic	QW
2 nm	GaAs	intrinsic	barrier
6 nm	$Al_{20}Ga_{80}As$	intrinsic	barrier
2 nm	GaAs	intrinsic	barrier
6 nm	InGaAs	intrinsic	QW
2 nm	GaAs	intrinsic	barrier
6 nm	$Al_{20}Ga_{80}As$	intrinsic	barrier
2 nm	GaAs	intrinsic	barrier
6 nm	InGaAs	intrinsic	QW
2 nm	GaAs	intrinsic	barrier
20 nm	$Al_{20}Ga_{80}As$	intrinsic	GRIN spacer
30 nm	$Al_{40}Ga_{60}As$	n-doped	GRIN spacer
	GaAs	n-doped	

TABLE. 2.1: Active layer with GRIN-confinement structure used in this work. The hetero-junction contains 3 QWs.

holder. The holder serves both as electrical contact and as back reflector. The evaporated top contact is wire-bonded. The whole is encapsulated in an epoxy dome. The epoxy dome protects the chip and enhances extraction of the light. The slightly higher refractive index of the epoxy ($n_{ep} \simeq 1.5$) reduces the total internal reflection domain at the interface of the semiconductor. Due to the large dome shape, the light impinges almost perpendicular on the extraction interface when the chip is positioned centrally. The external emission is quasi-isotropic[4]. The naked chip is sketched in Fig 2.2(a), the encapsulated ensemble in Fig 2.2(b).

[4]The chip can also be placed at a distance $d = r_{ep}/n_{ep}$, with r_{ep} the radians of the dome, under the central point. This will result in a slightly lower extraction efficiency, but the light will be more directional in the chip normal direction.

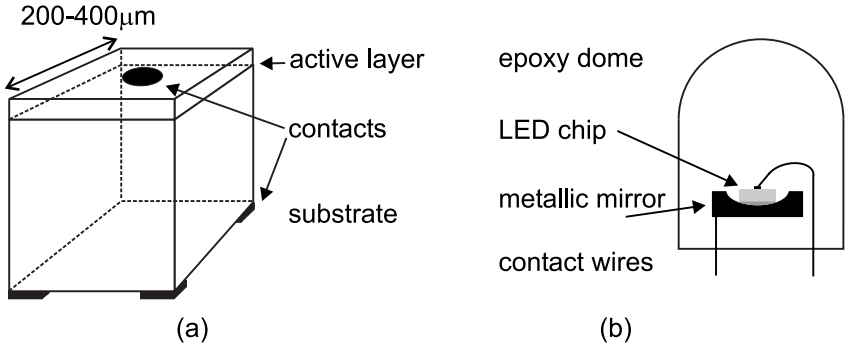

Fig. 2.2: Schematic presentation of a (a) naked LED-chip; (b) encapsulated LED-chip.

The latter is well known in several commercial applications such as remote control, stoplights, etc.. Typical used voltages are in the order of $2V$, the applied current varies form 1 to 50mA.

The main drawback of LEDs is quoted in the introduction: the extraction efficiency of light generated in high refractive index material. Snellius' law dictates the transmission angle of light in a medium with refractive index n_2 that propagates with an angle θ_1 in a material with refractive index n_1 (Fig. 2.3):

$$n_1 \sin\theta_1 = n_2 \sin\theta_2 \tag{2.16}$$

When θ_1 equals the so called critical angle θ_c, θ_2 equals 90°. θ_c is given by:

$$\theta_c = \arcsin\left(\frac{n_2}{n_1}\right) \tag{2.17}$$

The light becomes evanescent in medium 2 when θ_1 surpasses θ_c. The reflection coefficient is one and the regime is called *total internal reflection* (TIR). For $\theta_1 < \theta_c$ both a reflected and a transmitted beam appear. Considering an internal isotropic field distribution, the fraction of light in the extraction cone is given by:

$$\frac{2\pi(1-\cos\theta_c)}{4\pi} \simeq \frac{n_2^2}{4n_1^2} \tag{2.18}$$

and If we approximate the reflection coefficient by its value for normal incidence $(n_1 - n_2)/(n_1 + n_2)$, the single side extraction efficiency denotes as:

$$\eta_{extr} \simeq \frac{n_2^2}{4n_1^2}\left(1 - \left(\frac{(n_1-n_2)}{(n_1+n_2)}\right)^2\right) \tag{2.19}$$

For GaAs ($n_1 = \pm 3.52$), the naked chip has a single side extraction efficiency to vacuum $\eta_{extr} \simeq 2\% * (1 - 31\%) \simeq 1.38\%$, encapsulated this value is enhanced: $\eta_{extr} \simeq 4.5\% * (1 - 16\%) \simeq 3.8\%$. Until the early nineties, these values fixed the

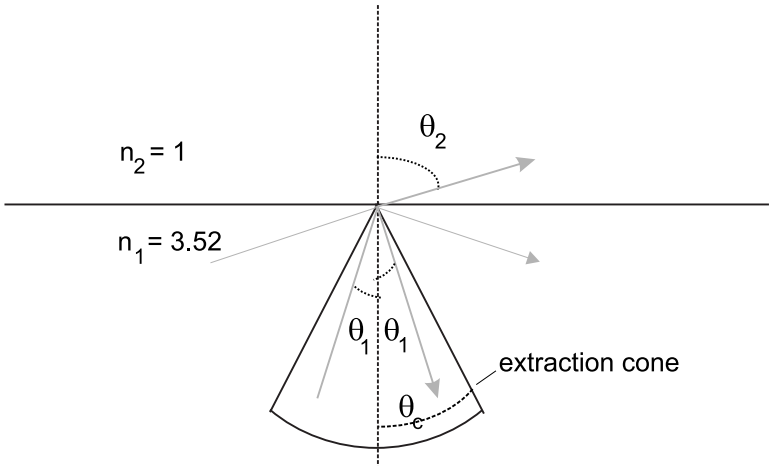

Fig. 2.3: Transmission and reflection of a light beam at a GaAs/air interface. The critical angle delimits the extractable light cone.

upper limit of efficiency of LEDs. TIR can be avoided if the source is put in the center of a semiconductor sphere. This ideal case, in that all beams impinge the interface orthogonally, however, is very difficult to realise as it is not compatible with the state of the art planar technologies. Several techniques, compatible with planar technology, to augment the efficiency have been reported. The main techniques that were already mentioned in the introduction, are detailed here.

2.2.3.2 Multiple side extraction

The extraction efficiency can be increased if the light is extracted from multiple sides. A LED with a thick transparent superstrate showed external efficiencies of 6% in epoxy [40]. A cone and 4 half cones contribute to the extraction (see Fig. 2.4(b)). Replacing the absorbing substrate by a transparent one can further enhance the extraction efficiency.

For LEDs based on the GaAs:$(Al_xGa_{1-x})_{0.5}In_{0.5}P$ material system, a 6 side extraction led to an external efficiency of 32% for the 600 nm wavelength range [41]-[43] (see Fig. 2.4(c)). After wet chemical etching of the original GaAs substrate, the thin film was wafer-bonded on the new transparent substrate GaP. Hewlett Packard, the drivers of this research, did continue their way to higher efficiencies and came up in 1999 with an inverse pyramidically shaped device showing world record external efficiencies of 60.9% for $\lambda = 650nm$. The device is encapsulated, the upper surface has a surface of approximately $1mm^2$, the junction surface equals $0.25mm^2$. The devices are sawn with a bevelled dicing blade to provide chip sidewall angles at 35° with respect to the vertical [21], [44]. Besides the 6 cones of direct extraction, the pyramidical shape can redirect the photons that are internally reflected by multiple reflection to an extraction cone. A rear mirror can be applied to reflect the downwards propagating light towards the desired direction.

It is clear that this device serves applications in which the overall optical power and low power consumption is of major concern. They are commercialised in traffic light applications (orange). The optical power is about 0.5W at an injection current of 0.5A. This corresponds with a current density of 200A.cm^{-2} for 25-30 QWs. The maximal output power is limited by thermal effects.

However, for plenty of applications, the overall optical power is a matter of little account. In telecommunication applications, for example, the coupling efficiency of the source into a fibre is directly related with the radiance of the source (see Appendix A for definition of radiance). The radiance is a quantity that -at best- is conserved in an imaging system: the radiance of the image cannot be higher than that of the object and cannot be increased by using lenses or other means. Therefore high radiance is important in any application where light needs to be focused to a small spot or where light needs to be coupled into a fiber with finite core size and numerical aperture. It is clear that extraction from multiple output planes does not benefit the radiance. Moreover, the small surface of the junction in comparison with the extraction surface indicates an inefficient use of the active surface or a small density efficiency (see Appendix A) and is baleful for scaling of high radiant sources. These characteristics do also exclude their use in high density two-dimensional arrays. Planar devices with small dimensions are needed for these applications.

2.2.3.3 Tapered LEDs

A planar device that enhances the extraction efficiency by altering the path of the photons in a controlled way is sketched in Fig. 2.5 [24]. At first sight, this tapered LED looks very similar to the inverted pyramid LED of the previous section. However, this device is planar and extraction is single sided. The light beams that are not extracted due to TIR, propagate in a lateral way. Their propagation angle increases while propagating in the thin-film tapered section which has an inclination angle of about 20°. After multiple reflections, the propagation angle becomes larger than the critical angle θ_c and the light will be extracted. Substrate-removed thin film devices, covered with metal show external efficiencies of 30% in air and 45% in epoxy for $\lambda = 980nm$ [45]. However, the taper sections need to be quiet large and the injected region (diameter 20 μm) takes up only 2% of the total extraction surface (diameter 140 μm). This small density efficiency is unfavorable for scaling and coupling.

A similar concept has been studied in the form of a top-emitting device [46]. The tapered waveguide is defined by a bottom DBR mirror. Extraction efficiencies of more than 80% are predicted. Experimental results did not yet confirm this.

2.2.3.4 Surface roughened LED

The path of the photons can also be altered in a random way by roughening an interface of the planar device. Light is scattered at the roughened surface. If the dimensions of the LED are small, absorption will be minimal and the multiply scattered photons have a statistically larger probability to escape the LED. The idea proposed in 1993 by Schnitzer and Yablonovitch [22] is picked up in 1998 by

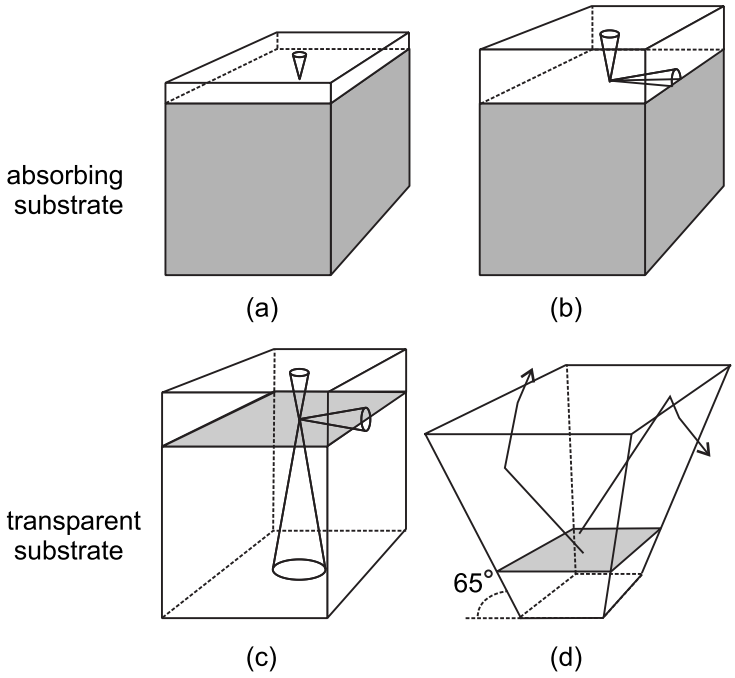

Fig. 2.4: Schematic presentation of a naked LED-chip with (a) thin transparent superstrate; (b) thick transparent superstrate; (c) transparent substrate; (d) pyramidical shape, ($\eta_{ext} \simeq 60.9\%$) [21].

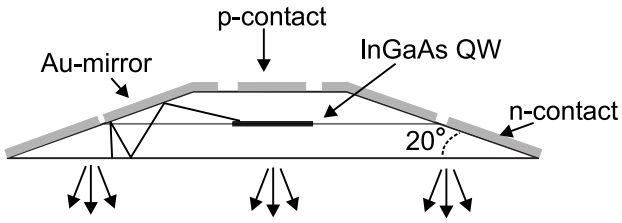

Fig. 2.5: Schematic presentation of a tapered LED ($\eta_{ext} \simeq 30\%$) [24].

Windisch *et al.* giving rise to thin film devices with $\eta_{ext} \approx 50\%$ for $\lambda = 870$ nm [23]. Measurements at a low temperature point out that the extraction efficiency can be as high as $\pm 70\%$. The surface of the LEDs is textured by dry etching with a mask of a randomly packed monolayer of polystyrene spheres. The mesa surface as well as the surface around the mesa is roughened. The obtained corrugation exists of cylindrical pillars with diameter 300 nm , spacing 400 nm and depth 170 nm [47]. Epitaxial lift-off is performed to obtain a thin film. Metal is evaporated as mirror and the whole is mounted on a glass plate (see Fig. 2.6). One third of the light is extracted in the roughened region around the mesa, while the injected area occupies only one tenth of the total emitting surface.

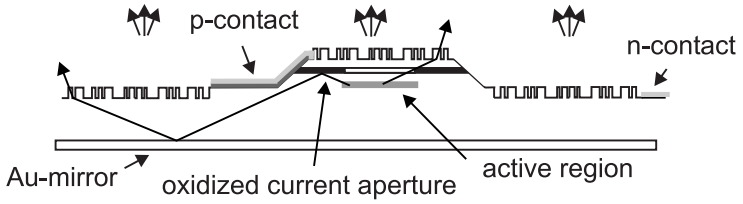

Fig. 2.6: Schematic presentation of a surface roughened non-resonant cavity LED ($\eta_{ext} \simeq 50\%$) [23].

2.2.3.5 Resonant-Cavity LED

Resonant-Cavity LEDs or Micro-Cavity LEDs do exhibit a different mechanism to enhance extraction compared to the former devices. The angular power distribution inside the device is altered by means of multiple interferences in a stratified medium. It is the basic component of the Grating-Assisted RCLED, which is studied in this work, and we will therefore enlighten the RCLED in greater detail in paragraph 2.3. Some advanced techniques that exploit the RCLED are discussed at the end of the section. It will be clear that while the radiance of a RCLED is lower than that of a laser (for a given power), it is easily orders of magnitude larger than that of an LED chip with light extraction from all chip sides or with small density efficiency. The discussed advanced techniques can even further enhance this radiance. Together with the inverted pyramidical LED, the RCLED is the only commercialised high efficiency LED so far.

2.2.3.6 Applications of high efficiency LEDs

With a growth rate exceeding 58% annually for the past five years, the worldwide market for high-brightness LEDs reached 1.2 billion euro in 2000, and accounted for 42% of the total LED market [48].

According to a recently published report by market research firm Strategies Unlimited, robust growth is projected to continue for the next three years. The market is expected to exceed 3.4 billion euro in 2005. The reader is referred to Chapter 1 to read about the broad range of applications and possibilities of high efficiency and high brightness LEDs.

2.3 The Resonant-Cavity Light-Emitting Diode

2.3.1 Basics of spontaneous emission in a layered medium

2.3.1.1 Modification of emission pattern: theoretical treatment

In a RCLED (also called *Micro-Cavity LED* (MCLED)), spontaneous emission is generated inside a multi-layer Fabry-Pérot resonator, in which interference effects alter the internal angular power distribution (Fig. 2.7). With an appropriate cavity design, the preferential propagation direction of the photons can thus be

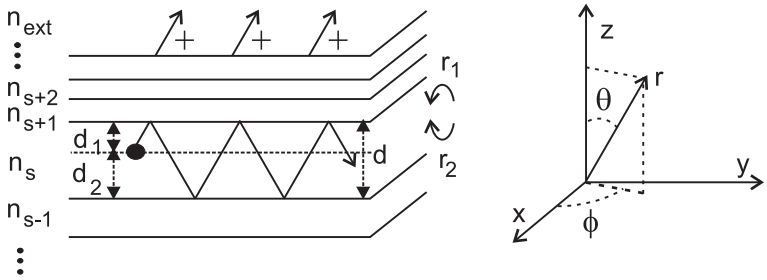

Fig. 2.7: Structure of a light-emitting multi-layer device. The emitting medium has a refractive index n_s, the intermediate layers $n_{s\pm1}, n_{s\pm2}, \ldots$, the half infinite surrounding media n_{ext}. The emitting layer has a thickness d. The dipole is located at a distance d_1 from the interface with the first layer of the upper mirror; at a distance d_2 from the interface with the first layer of the bottom mirror. The upper mirror has a reflection coefficient r_1; the bottom mirror a reflection coefficient r_2. Interference takes place when the radiation is reflected back and forth between the two interfaces of the layer. The emission angle θ and ϕ are defined in the xyz coordinate system.

forced from total internal reflection regime towards the extraction cone, benefitting to η_{extr}. Together with this increase of directivity and/or efficiency due to a redistribution of the photons, the spontaneous emission rate may be enhanced due to the *Purcell*-effect. However, because of the planar geometry and the rather small reflectivity coefficients of the cavity mirror(s) in practical applications, the Purcell-factor is close to one, resulting in a negligible spontaneous emission rate enhancement (see section 2.3.1.2).

In this so-called "weak coupling" regime the spontaneous emission of electron/hole pairs can adequately be represented by an electric dipole. The electric field of the electric dipole can be decomposed in a set of plane waves $\mathbf{A}(\mathbf{k}) = exp(-j\mathbf{k}\cdot\mathbf{r})$. This linearly polarised field can be decomposed in an s-polarised component (or Transverse Electric: the plane wave has its E-field in the (x-y)-plane and orthogonal to k) and an p-polarised component (transverse magnetic or p: has its H-field transverse to the plane of incidence). The reader is referred to Chapter 4 for more details on the electric dipole description of spontaneous emission.

Decomposition of the electromagnetic problem in purely TE and TM systems in relation with the multi-layer interfaces, transforms the *vectorial* electromagnetic problem in simple *scalar* problems. Indeed, the beauty of TE-TM decomposition lies in the polarisation maintaining reflection or refraction of TE and TM-waves upon a planar interface. Analysis of electromagnetic wave propagation in an isotropic layered structure can as such be decomposed in two uncoupled systems. From Fig. 2.7, it is clear that for the respective polarisations, the emitted intensity $I^{pol}(\theta)$, with θ the internal emission angle, caused by the source's plane wave component A^{pol} is given by ($pol = s, p$):

$$I^{pol}(\theta) = T_1\, I^{pol}_{dip}(\theta) \tag{2.20}$$

$$I_{dip}^{pol}(\theta) = |(A_{\uparrow}^{pol} + A_{\downarrow}^{pol} r_2 e^{-j2\phi_2})(1 + r_1 r_2 e^{-j2\phi} + r_1^2 r_2^2 e^{-j4\phi} + \ldots)|^2$$
$$= \frac{|A_{\uparrow}^{pol} + A_{\downarrow}^{pol}|r_2| e^{-j2\phi_{2\,eff}}|^2}{|1 - |r_1 r_2| e^{-j2\phi_{eff}}|^2} \tag{2.21}$$

with $|r_1 r_2| < 1$, r_1, r_2 the upwards and downwards amplitude reflection coefficients, T_1 the upwards power transmission coefficient, $\phi_i = k_0 n_s d_i \cos\theta$, $i = 1, 2$, $\phi = \phi_1 + \phi_2$ and $2\phi - \arg(r_1) - \arg(r_2) = 2\phi_{eff}(\theta, \lambda)$ and $2\phi_i - \arg(r_i) = 2\phi_{i\,eff}(\theta, \lambda)$ and d_1, d_2 the distances of the dipole from the interfaces of respectively the first layer of the upper mirror and the first layer of the bottom mirror. r_1, r_2, T_1 are polarisation dependent and can be calculated using a transfer matrix method [32]. The numerator is called the *standing wave factor* $\zeta(\phi_{2\,eff})$ and is responsible for the dependence of the emitted intensity on the position of the source: the radiated emission in a particular direction is high if the standing wave field strength at the source position is high. The denominator is independent of the position of the source, but depends strongly on λ and θ. The inverse of the denominator is called the *cavity enhancement factor* or *Airy factor* $\Gamma(\phi_{eff})$. The Airy function is periodic in ϕ_{eff} with a period π, and at a maximum, the cavity is said to be *resonant* [32]. These maxima define a *resonant mode* and obey the phase condition:

$$2\phi - \arg(r_1) - \arg(r_2) = 2\phi_{eff}(\theta, \lambda) = 2m\pi \tag{2.22}$$

with m a positive or negative integer. In section 2.3.2, it will be clear that these resonances account both for Fabry-Pérot ($\theta < \theta_c$) and guided modes ($\theta > \theta_c$), with $\theta_c = asin(n_{ext}/n_s)$ the critical angle for *Total Internal Reflection* (TIR), with n_{ext} the refractive index of the external surrounding medium (see Fig. 2.7). If $|r_1 r_2| = 1$, the resonator is "perfect" and the mode will never be damped after the excitation is switched off. This occurs when there are no losses, neither due to absorption nor extraction.

The extraction efficiency η_{extr} can then be defined as:

$$\eta_{extr} = \frac{2\pi \int_0^{\theta_c} I(\theta) \sin\theta d\theta}{2\pi \int_0^{\pi} I(\theta) \sin\theta d\theta} \tag{2.23}$$

Eq.(2.23) has to be solved numerically [5], approximating the integral by a discrete summation.

2.3.1.2 Total emission enhancement or *Purcell*-factor

The impact of the cavity on the total power emitted by the dipole can be expressed as the spontaneous emission (SE) lifetime alteration of the radiative electron-hole recombination process:

$$\frac{\frac{1}{\tau}}{\frac{1}{\tau_0}} = \frac{\text{emitted dipole power in cavity}}{\text{emitted dipole power in bulk}} \tag{2.24}$$

[5] Integration has to be performed with care so that evanescent coupling is taken into account (see further in Chapter 4.

where τ and τ_0 are the lifetimes with and without cavity. The change of lifetime due to the presence of a cavity is known as the *Purcell* effect [51]. The Purcell-factor expresses this lifetime change and has been derived by Purcell as $(3Q/4\pi^2)(\lambda^3/V)$. It is defined for 3-D optical cavities of volume V and mode quality factor $Q = \lambda/\delta\lambda$ with $\delta\lambda$ the narrow emission linewidth around λ [52].

The impact of a planar cavity on the change of spontaneous decay rate has been studied in detail [8], [53], [54]. In the case of a cavity with perfect (100% reflecting) mirrors an analytical expression for the SE enhancement has been derived in [54] for the case of a horizontal dipole in the middle of the cavity. The results depend on the phase of the mirror reflection coefficient. For $r = +1$ there are $\lfloor m_{c\,eff} \rfloor = \lfloor m_c \rfloor + 1$ modes but only $\lfloor m_c/2 + 1 \rfloor$ are excited ($\lfloor\rfloor$ means: largest integer smaller than the argument), with m_c the cavity order or normalised cavity length, a measure for the number of resonant modes, which is defined in section 2.3.2. The others are not excited because the dipole is located at a zero of the mode profile. The decay rate enhancement can then be expressed as:

$$\frac{\frac{1}{\tau}}{\frac{1}{\tau_0}} = \frac{6\left\lfloor \frac{m_c}{2} \right\rfloor + 3}{4m_c} + \frac{4\left\lfloor \frac{m_c}{2} \right\rfloor^3 + 6\left\lfloor \frac{m_c}{2} \right\rfloor^2 + 2\left\lfloor \frac{m_c}{2} \right\rfloor}{2m_c^3} \tag{2.25}$$

For $r = -1$ there are $\lfloor m_{c\,eff} \rfloor = \lfloor m_c \rfloor$ modes, $\lfloor (m_c + 1)/2 \rfloor$ of which are excited and the resulting decay rate enhancement is:

$$\frac{\frac{1}{\tau}}{\frac{1}{\tau_0}} = \frac{6\left\lfloor \frac{m_c+1}{2} \right\rfloor}{4m_c} + \frac{4\left\lfloor \frac{m_c+1}{2} \right\rfloor^3 - \left\lfloor \frac{m_c+1}{2} \right\rfloor}{2m_c^3} \tag{2.26}$$

The terms in $1/m_c$ in these expressions correspond to TE-waves, whereas the terms in $1/m_c^3$ correspond to TM-waves. The two expressions are shown in Fig. 2.8 as a function of m_c. One can see that apart from the singular $1/m_c$ behavior for small m_c in the $r = +1$ case, the maximum SE enhancement is 3 and is obtained in a half-wavelength thick cavity with $r = -1$ (perfect metallic mirrors). For thick cavities the Purcell effect converges to 1. In other words, thick cavities with many modes have a similar impact on the dipole as uniform space with a continuum of modes. For real metals, the phase shift lies in between these extreme cases, and can give rise to an intermediate Purcell-factor.

In 3-dimensional cavities the Purcell effect can be substantially larger than in planar cavities. In [51] a strong enhancement of the spontaneous emission rate has been observed for self-assembled InAs/GaAs quantum boxes inserted in GaAs-based pillar microcavities (x5) and microdisks (x15) using time-resolved as well as c.w. photoluminescence experiments, and in spite of various detrimental averaging effects compared to the ideal case (such as variation on dot diameter, etc.).

2.3.2 Design rules

A quantitatively accurate design of an RCLED is only possible by a numerical analysis with the methods presented in section 2.3.1.1. However, a number of approximate design rules can be used as guidelines in the first phase of a design.

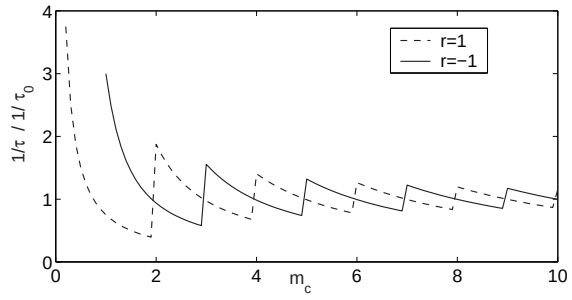

Fig. 2.8: Modification of spontaneous emission rate or the Purcell effect according to (2.25) and (2.26).

If one allows for some parameter variations in the experimental devices, it is often unnecessary to move to detailed numerical analysis, at least for simple planar RCLEDs. An RCLED can be optimised to fulfill diverse conditions. We will discuss the optimisation of overall extraction efficiency, considering several practical configurations. First, some cavity variables will be defined.

2.3.2.1 Finesse, Quality factor and (effective) Cavity order

The *Full Width Half Maximum* (FWHM) of the resonant peaks $\delta\phi_{eff}$ caused by the Airy factor $\Gamma(\phi_{eff})$, is inversely proportional to the *finesse* F:

$$F \equiv \frac{\Delta\phi_{eff}}{\delta\phi_{eff}} = \frac{\pi}{\delta\phi_{eff}} \tag{2.27}$$

with $\Delta\phi_{eff}$ the separation between two adjacent resonances. The *cavity order* m_c is defined as the normalised cavity length, when ideal mirrors are assumed $(arg(r_1) + arg(r_2) = 0)$:

$$m_c \equiv \frac{d}{\lambda_0/2n_s} \tag{2.28}$$

$$= \frac{\lambda_0}{\pi}\frac{\partial\phi}{\partial\lambda}|_{\theta\approx 0} \tag{2.29}$$

$$= \frac{1}{\pi}\frac{\partial\phi}{\partial(\cos\theta)} \tag{2.30}$$

The cavity order m_c is a measure for the number of resonant modes in the bare ideal cavity: from reformulation of the resonance condition (2.22) as $m_c \cos\theta = m$, it is clear that the number of resonances is limited to $\lfloor m_c \rfloor$. It also links F with the *Quality Factor* Q of the Fabry-Pérot mode, when small variations are considered:

$$Q \equiv \frac{\lambda_0}{\delta\lambda} = \frac{\phi_{eff}}{\delta\phi_{eff}} = \frac{\lambda_0}{\pi}\frac{\delta\phi_{eff}}{\delta\lambda}\frac{\pi}{\delta\phi_{eff}} = m_c F \tag{2.31}$$

Using the numerical analysis of section 2.3.1.1, the intensity emitted by an isotropic point source in an RCLED of cavity order $m_c = 4$ with ideal mirrors can be

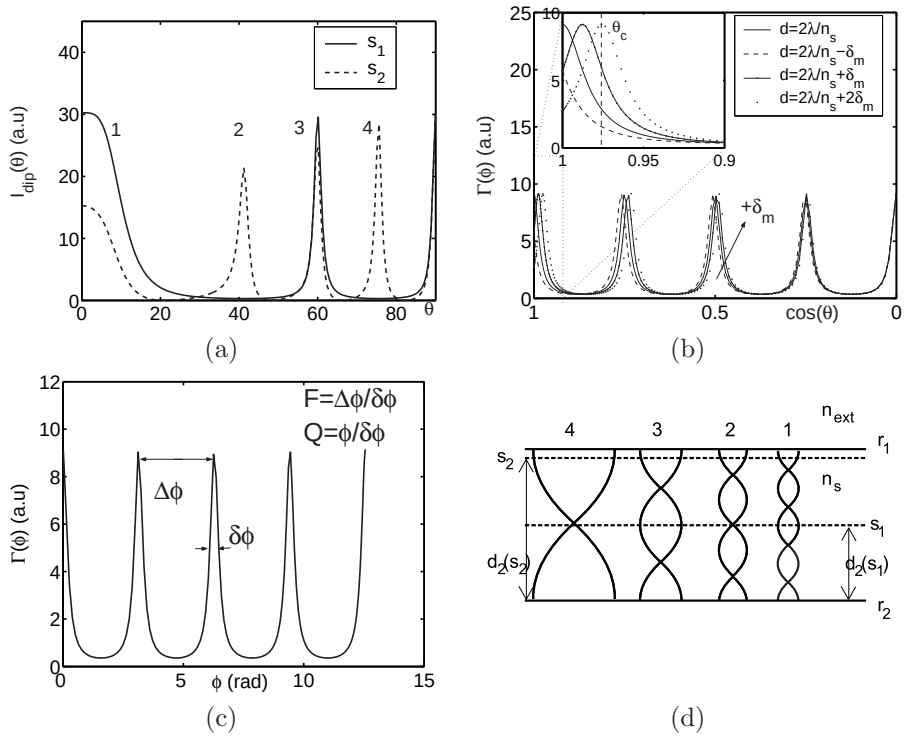

Fig. 2.9: (a) Internal angle-resolved TE intensity of an ideal (angle independent reflection coefficients r_1 and r_2) RCLED with $m_c = 4$ for respectively source location s1 and s2 (b) corresponding Airy Function of respectively a λ-, $(\lambda-\delta_m)$-, $(\lambda+\delta_m)$- and $(\lambda+2\delta_m)$-cavity for source location s1; (c) graphical definition of Q and F; (d) resonant mode distributions in RCLED and source locations s1 and s2.

calculated and is depicted in Fig. 2.9(a). The Airy function Γ is modulated with the standing wave factor ζ for respective source positions s1 and s2 placed at different distances from the bottom mirror interface d_2 as defined in Fig. 2.9(d). This coupling strength ζ is proportional to the respective mode intensity at the source position. When the source is located at a node of the standing wave pattern, no coupling occurs. This happens for the second and fourth mode when the source is located at s_1. For a dipole positioned at the height of s_2, coupling to all modes is realised. The resonant mode in the extraction cone ($\theta < \theta_c$) is called the *Fabry-Pérot mode*, the other "trapped" modes are the *guided modes*. The Airy function Γ is presented for different cavity thicknesses around $d = 2\lambda_0/n_s = 2\lambda_s$ in Fig. 2.9(b). The source is kept at the center of the cavity, leaving ζ invariable. A shift of the resonant peaks towards smaller $\cos\theta$ (larger θ) for increasing cavity thickness is observed. An optimal value for δ_m is deduced in the next paragraph. Q and F are graphically defined in Fig. 2.9(c).

In reality, the phase of the reflection coefficients r_1 and r_2 of a multi-layer depends on the wavelength and angle of incidence. Considering the Fabry-Pérot

mode, in a small range around its working point, the phase will change approximatively in a linear way. This allows to define an effective penetration depth, defined as the depth measured from the interface, where an ideal mirror interface should be positioned to give rise to the same variation of the phase. As the reflectivities of the individual interfaces have a distinct spectral and angular behavior, two penetration depths and corresponding effective cavity thicknesses can be defined using Eq.(2.22) and Eqs.(2.28)-(2.30) [55]:

$$d_{eff,\theta} = d + d_{pen,\theta} = d + \frac{\lambda_0}{2n_s} \frac{-\partial(arg(r_1) + arg(r_2))}{\partial \cos\theta} \frac{1}{2\pi} \tag{2.32}$$

$$d_{eff,\lambda}|_{\theta\approx 0} = d + d_{pen,\lambda} = d + \frac{\lambda_0}{2n_s} \frac{\partial(arg(r_1) + arg(r_2))}{\partial\lambda} \frac{\lambda_0}{2\pi} \tag{2.33}$$

$d_{eff,i}$ gives rise to an effective cavity order $m_{c\,eff,i}$, $i = \lambda, \theta$:

$$m_{c\,eff,i} = \frac{d_{eff,i}}{\lambda_0/2n_s} \tag{2.34}$$

When the resonances of the cavity are characterised by a high F, a rough estimate for η_{extr} can be obtained: the Airy function can be approximated by a Dirac distribution for which η_{extr} is translated to a ratio of discrete sums.

$$\eta_{extr} = \frac{\sum\limits_{i,\theta<\theta_c} \zeta_i}{\sum\limits_{i} \zeta_i} \tag{2.35}$$

The numerator accounts for the extractable modes and the denominator for all modes, both Fabry-Pérot and guided modes. For the RCLED of Fig. 2.9(a), with the source located in the center of the cavity (s_1), only even modes are excited with equal ζ_i. With a single mode in the extraction cone Eq.(2.35) can be written as

$$\eta_{extr} \cong 1/(\lfloor m_{c\,eff,\theta} \rfloor/2) \tag{2.36}$$

The importance of $m_{c\,eff}$ for extraction efficiency estimation is thus obvious: the extraction efficiency depends on the penetration depth of the mirror. In general the penetration depth is positive, resulting in an increase of $m_{c\,eff,\theta}$. A novel design -the RC2LED- realises a negative angular penetration depth using a non-periodic high index-contrast mirror. As a result, coupling to small NA is enhanced (see section 2.3.4) [56].

2.3.2.2 Dipole in semiconductor slab cavity: effect of cavity thickness and position of active layer

Fig. 2.10 shows a generic example of a monochromatic (λ_0) horizontal dipole (TE) and vertical dipole (TM) in the middle of a semiconductor layer, thickness $d = \lambda_s$ and refractive index n_s surrounded by air. This is a cavity with rather modest mirror reflectivity (about 30%) for normal incidence and perfect reflectivity (100%) for oblique incidence in the total internal reflection regime. Two resonances appear

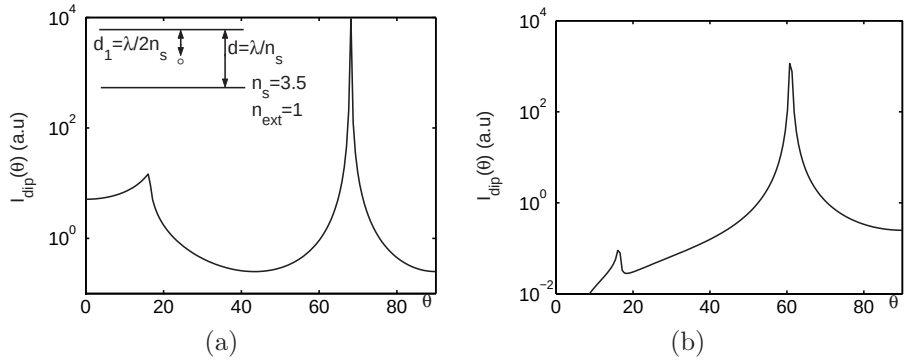

Fig. 2.10: Internal angle-resolved (a) TE intensity of horizontal dipole and (b) TM intensity of vertical dipole in a λ-cavity.

in the upwards emitted intensity through plane $z = 0$: a broad resonance from $\theta = 0°$ to $\theta = \theta_c$ corresponding with the extractable Fabry-Pérot mode and a second high Q resonance at $\theta = 68°$ for TE and $\theta = 60°$ for TM, or the guided mode trapped in the cavity. The Fabry-Pérot mode shows a peak at $\theta = \theta_c$ although the phase resonance operation point, defined by Eq.(2.22) is fulfilled for $\theta = 0°$. This is due to the higher reflectivity coefficient of slanted angles, resulting in a stronger Airy factor than at phase resonance operation point. In a lossless cavity, the guided mode corresponds with a singularity in the power flux, as can be expected from Eq.(2.21). This singularity is not unphysical: integration over a finite solid angle results in a finite value. To maximize η_{extr}, the thickness of the layer has to be optimised. The Fabry-Pérot enhancement has to be located optimally in the extraction cone to maximise its extraction: η_{extr} is proportional to the ratio of the area below the Airy function within the extraction cone to the total spanned surface. Fig. 2.9(b) shows that extraction will be maximal for the ideal cavity if the Airy-factor peak is located symmetrically in the $[\phi(0), \phi(\theta_c)]$ interval or $\phi(\theta_0) = (\phi(0) + \phi(\theta_c))/2$. With Eq.(2.22) and $\theta_c \simeq n_{ext}/n_s$, θ_0 can be deduced and is approximately given by [57]:

$$\theta_0 \simeq \frac{n_{ext}}{\sqrt{2} n_s} \tag{2.37}$$

This skew propagation direction corresponds with an optimal cavity thickness correction δ_m:

$$\delta_m \simeq \lambda_0 \frac{n_{ext}^2}{4 n_s^2} \tag{2.38}$$

With Snell's law ($n_s \sin\theta_0 = n_{ext} \sin\theta_0^{ext}$), this cavity thickness $d_m = \lambda_s + \delta_m$ results in an external angle of approximately $\theta_0^{ext} = 45°$. The detuning will influence the external emission profile strongly: the "rabbit-ears" in the emission pattern are an unavoidable property of highly efficient RCLEDs. This results in different design parameters for devices with an overall high efficiency and devices with a high efficiency towards a limited NA around the surface normal direction needed

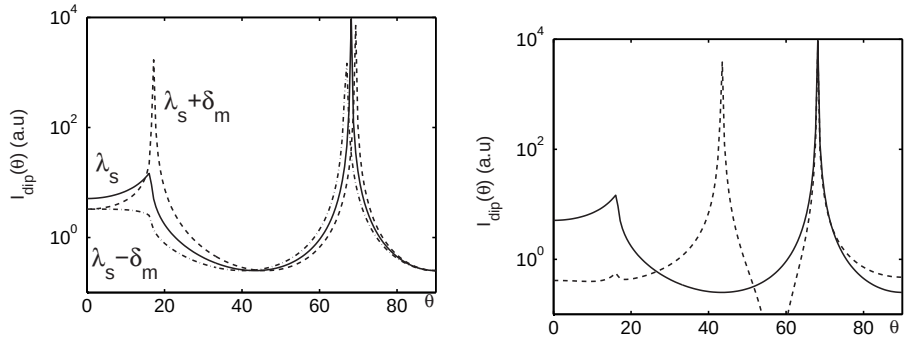

Fig. 2.11: (a) Internal angle-resolved TE intensity for λ-, $(\lambda + \delta_m)$-, $(\lambda - \delta_m)$-cavity ($\lambda_s = \lambda_0/n_s$);(b) Internal angle-resolved TE intensity in a λ-cavity for dipole at antinode position of Fabry-Pérot mode (full line) and at node position of Fabry-Pérot mode (dashed line).

in optical fiber communication applications. The internal angle-resolved intensity is depicted in Fig. 2.11(a) for varying cavity thicknesses.

The position of the dipole in reference to the standing wave pattern defines the coupling strength of the source to this optical mode. It is expressed by the standing wave factor $\zeta(\phi_{2\,eff})$. This factor reveals that the use of a thin active layer located at a standing wave node results in minimal coupling strength, while at an antinode height coupling strength is maximal. The optimal dipole position is thus at an antinode of the extractable Fabry-Pérot mode as shown in Fig. 2.11(b), where the Fabry-Pérot mode vanishes for a dipole at the level of a node. The interference effects are averaged out when a thick -at least $\lambda_0/2n_s$- bulk active layer is used, halving the overall enhancement as compared to the thin active layer placed at an antinode.

The effect of drastically increasing the cavity length is shown in Fig. 2.12 where d is changed from $1\lambda_0/n_s$ to $2\lambda_0/n_s$, while the dipole is kept in the middle of the cavity. The intensity profile clearly shows a growing number of resonances when the cavity length is increased. Eq.(2.36) can be applied to estimate the trend of η_{extr}: increasing the reduced cavity length $m_{c\,eff}$ results in a drop of η_{extr}. This explains why an RCLED needs to have a small cavity length. Ideally, the total optical power is emitted in a single extractable Fabry-Pérot mode, using a $\lambda/2$-cavity. However, λ-cavities are in generally used in practical applications for several reasons. Due to losses, finite spectral width, etc., the coupling efficiency of the optical power to a single Fabry-Pérot mode is not as efficient as Fig. 2.12 might suggest (see next section). Secondly, in case the cavity is set up by metallic mirror(s), a $\lambda/2$ cavity implies that the distance of the active layer to the metal is very small and can result in considerable losses due to nonradiative energy transfer from the dipole to the absorptive metal [58]. For a perfect mirror with phase shift π the distance is maximally $\lambda_0/4n_s$ (e.g. about 70 nm for a GaAs RCLED emitting at 980 nm). For realistic metallic mirrors, with a phase shift

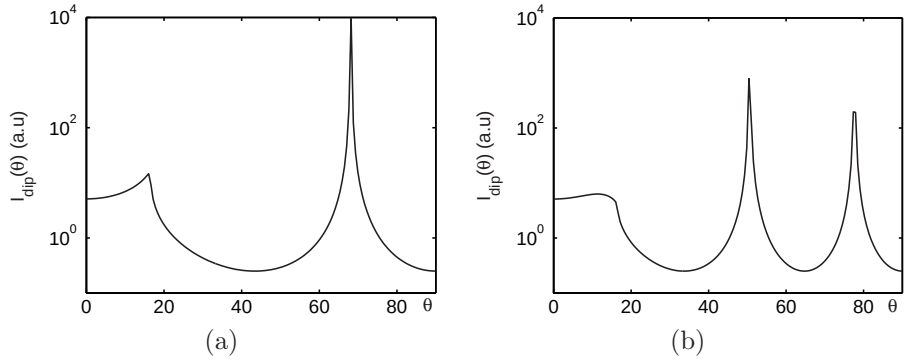

Fig. 2.12: Internal angle-resolved TE intensity for (a) λ-cavity and (b) 2λ-cavity.

different from π, this distance is even further reduced by some tens of nanometers (a reduction of about 45 nm for a GaAs RCLED emitting at 980 nm with Au-mirror). Finally, from a technological point of view, a λ-cavity is preferable to its thinner counterpart, and will in general be used in practical devices both when metallic mirrors or dielectric mirrors are used. A metallic mirror requires a heavily doped contact layer to ensure good electrical contact. Experiments evidenced that minimal thicknesses of several tens of nanometer (50 nm for a GaAs RCLED emitting at 980 nm with Au-mirror [39]) are needed for the contact layer. As this contact layer (heavily doped GaAs) extends to a distance of some 20nm from the active layer, there is not much space left for band gap engineering to optimise the device. Multiple QW layers sandwiched in a carrier confinement structure (like Graded Refractive Index (GRIN) confinement structures optimising carrier capture [59]) typically have a total thickness of about 120 nm. When dielectric mirrors are used, a sideways current supply is needed to pump the device. In this case again, a minimal thickness can be needed. To achieve proper carrier injection and low series resistance, extra layers can be added in the cavity.

2.3.2.3 Cavity with DBR mirror(s): effect of mirror reflectivity

Besides the cavity thickness tuning, the efficiency of the RCLED depends strongly on both amplitude and phase of the reflection coefficient of the cavity mirrors. Fig. 2.13 generically shows the amplitude and penetration depth of different mirrors as a function of the angle of incidence for TE and TM polarisation: a semiconductor/metal interface, a semiconductor/air interface and a *Distributed Bragg Reflector* or DBR mirror. A DBR mirror consists of a periodic quarter-wave stack of alternating high and low index material.

For both the back mirror and outcoupling mirror, the penetration depth has to be minimal to enhance the extraction efficiency $\eta_{extr} \sim 1/m_{c\,eff}$ (see Eq.(2.36)). For the outcoupling mirror, absorption losses have to be low.

The metallic mirror scores best for minimal penetration depth, but is preferably not used as an outcoupling mirror due to its high absorption losses. When metal is used as the back mirror, deposited on the semiconductor after epitaxial growth,

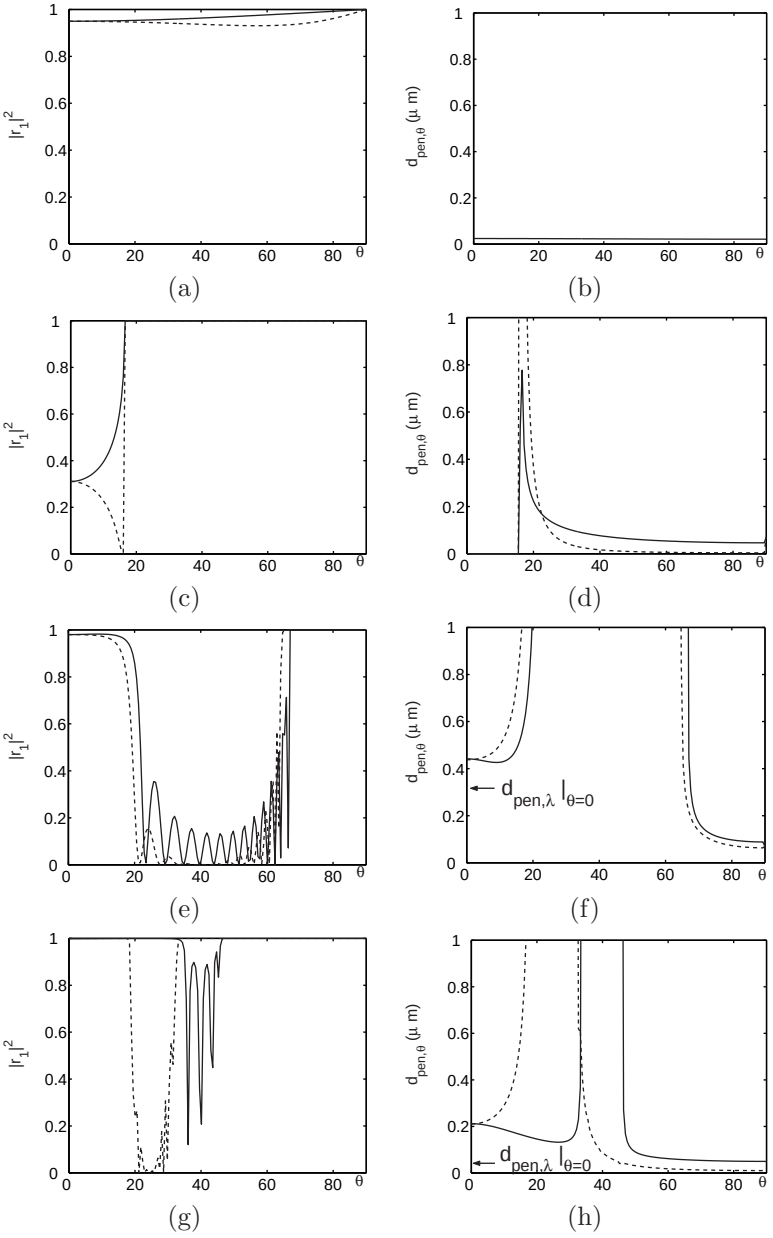

Fig. 2.13: Reflectivity and penetration depth as a function of the incident angle ($\lambda = \lambda_{DBR} = 0.98\mu m$) Full line: TE-polarisation; dashed line: TM-polarisation. (a-b) GaAs/Au interface; (c-d) GaAs/Air interface; (e-f) GaAs/(AlAs-GaAs DBR)/GaAs interface (N=30)(g-h) GaAs/(AlOx-GaAs DBR)/GaAs interface (N=10).

the device will be bottom-emitting and a transparent substrate is needed, or a substrate removal. The metal will both serve as mirror and electrical contact.

The penetration depth of a DBR decreases with increasing refractive index-contrast. Approximate expressions for the penetration depth around the working point $\lambda_0 = \lambda_{DBR}$ and $\theta = 0°$, with λ_{DBR} the Bragg wavelength, are given in [60], for a large number N of DBR pairs:

$$d_{pen,\lambda} \approx \frac{\lambda_{DBR}}{4n_s^2} \frac{n_H n_L}{n_H - n_L} \tag{2.39}$$

$$d_{pen,\theta} \approx \frac{n_s^2}{2} \left(\frac{1}{n_H^2} + \frac{1}{n_L^2} \right) d_{pen,\lambda} \tag{2.40}$$

with n_H, n_L respectively the highest and lowest refractive index of the DBR stack. The penetration depth decreases with decreasing number of DBR pairs. Eqs.(2.39) and (2.40) define an upper limit for the respective penetration depths. It is important to note that $d_{pen,\lambda} < d_{pen,\theta}$ and this for all N. With $d_{pen,\theta}$ the most significant parameter to determine $m_{c\,eff}$, the effect of high index-contrast mirrors on penetration depth will be less effective than might be expected from $d_{pen,\lambda}$, the commonly used definition for penetration depth. Not intuitive is the fact that $d_{pen,\theta}$ and hence $m_{c\,eff,\theta}$ are minimal for $n_L \approx \sqrt{n}_H$. When a transparent material set with high refractive index-contrast can be found, a DBR is suitable for both back and outcoupling mirror.

In practical applications, a single facet extraction is preferred. This requires a very high reflectivity of the back mirror (ideally 1), which can be met by both a metallic mirror or a large stack DBR. Optimising light extraction at the output facet, requires moderate reflection coefficients and corresponding finesse F_{FP} and Q_{FP} for the Fabry-Pérot mode. The reason is threefold [29]: Considering a monochromatic source in a lossless cavity, η_{extr} is proportional to the ratio of the area below the Airy function within the extraction cone to the total spanned surface (cf. Eqs.(2.23) and (2.35)). It is thus clear that the finesse of the Fabry-Pérot mode has an optimal value, such that the peak resides well in the extraction cone, and above which value η_{extr} increases only marginally. With the resonant peak given by Eq.(2.37), an approximate criterion can be deduced:

$$\frac{1}{Q_{FP}} = \frac{\delta\phi}{\phi} = \delta \cos\theta < \frac{(1 - cos\theta_c)}{3} = \frac{1}{6} \frac{n_{ext}^2}{n_s^2} \equiv \frac{1}{Q_{FP}^{crit}} \tag{2.41}$$

or $|r_1| > r_1^{crit}$, with r_1^{crit} the reflection coefficient that gives rise to a Q factor Q_{FP}^{crit} as defined in (2.41).

Secondly, practical cavities have absorption losses. A moderate $|r_1|$ prevents a large number of round-trips in the cavity, minimising the absorption losses. If such losses are low enough, the FP resonance will not be affected, and criterion (2.41) will apply. In case of large losses, the width of the FP resonance remains large for increasing $|r_1|$, and maximum efficiency is reached when the "exit losses" or extraction equal the absorption losses, corresponding with some value r_1^{loss}. The criterion becomes: $|r_1| = \min(r_1^{crit}, r_1^{loss})$.

Finally, due to the nonzero natural linewidth of the dipole source $\delta\lambda$ (the emitting material intrinsic spectrum), improving extraction efficiency at some wavelengths occurs at the expense of other wavelengths, which can cause a decrease of the spectrally integrated efficiency. If $Q_{intr} = \lambda/\delta\lambda = 1/\delta\cos\theta$ is lower than $3/(1-\cos\theta_c) = Q_{FP}^{crit}$ (see (2.41)), it is of no use to enlarge the finesse of the cavity, that is $|r_1| > r_1^{intr}$, with r_1^{intr} corresponding with Q_{intr}. In semiconductors, the relative intrinsic spectral width tends roughly to scale with the wavelength due to thermal motion of carriers:

$$Q_{intr}^{-1} = \frac{\delta\lambda}{\lambda} \sim \lambda \sim kT/\hbar\omega \tag{2.42}$$

Hence short wavelength RCLEDs (e.g. InGaP red RCLED (see section 2.3.3)) do not suffer from the linewidth penalty. In GaAs-based RCLEDs $\delta\lambda/\lambda$ is of the same order as $1/2n^2$. In long wavelength RCLEDs, the broadening $\delta\lambda/\lambda$ is larger than $1/2n^2$, which explains why it is very difficult to make 1.3-μm or 1.55-μm RCLEDs with high efficiency.

The rule of thumb for the optimal reflection of the outcoupling mirror can be summarised as:

$$|r_1| = \min(r_1^{crit}, r_1^{loss}, r_1^{intr}) \tag{2.43}$$

From Fig. 2.13, Eq.(2.36) and Eq.(2.43), it is clear that a DBR with a high refractive index contrast is a suitable outcoupling mirror. On the other hand, the angular response of a DBR (Fig. 2.13) gives evidence of a high reflectivity around $\theta = 0°$ [61]:

$$\Delta\cos\theta = \frac{\Delta\lambda}{\lambda_{DBR}} \approx \frac{2}{\pi}\frac{\Delta n}{n_s} \tag{2.44}$$

but vanishes for larger θ. Reflection rises again when TIR inside the DBR is met. The part with low reflectivity gives rise to a continuum of optical modes, called the *DBR-leaky modes*. This is comparable with emission in bulk. These modes and the guided modes in the TIR regime are lost. The limits of the stop band and of TIR are drawn in Fig. 2.14(a) as a function of the low refractive index n_L in a DBR stack when $n_H = 3.52$. A high index-contrast material suppresses the leaky modes in favor of the extraction but most of all in favor of the guided mode [62]. The angle-resolved internal intensity of a metal/DBR cavity is depicted in Fig. 2.14(b) for the respective index-contrasts marked in (a).

In a micro-cavity bound by DBR-mirror(s), the Purcell-factor for horizontal dipole is generally close to unity (between 0.8 and 1.2 typically) except if the cavity thickness goes to 0 or $m_c \to 0$. The reason for this is twofold. First of all, the DBR is leaky over a wide angular range which means that in this range the situation is little different from homogeneous material. Secondly, the penetration depth of the DBR leads to an enlarged effective cavity thickness, even with zero cavity thickness. This enlarges $m_{c\,eff}$.

2.3.2.4 Temperature influence and saturation

Injection of carriers in the active region can be performed by optical pumping or current injection. For practical use, electrically pumped devices are far more

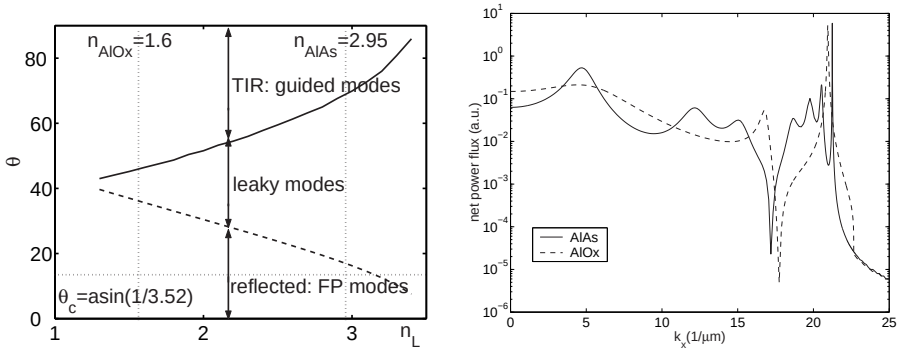

(a) (b)

Fig. 2.14: (a) Angular limits of the reflection band and of TIR band as a function of the index-contrast ($n_H = 3.52$);(b) Internal TE net power flux per unit spatial frequency for λ-cavity with Au mirror and GaAs/AlAs and GaAs/AlOx DBR respectively.

preferred. This does not only call for an electrically optimised design next to an optically optimised design, generally requiring a compromise, but can lead to detrimental temperature effects. First, the higher the current density, the broader the intrinsic emission spectrum. This results in a decreased overlap between the cavity resonance and the intrinsic spectrum, and a decreased extraction efficiency. Secondly, as the current increases, the electrical dissipation in and around the active layer, caused by the non-radiative recombination and ohmic heating by the series resistance, results in a temperature increase of the active region. The temperature increase has two consequences. First, the internal quantum efficiency decreases (with T_0 a characteristic temperature) [32]:

$$\eta_{int}(T) \approx \eta_{int,0} \exp\left(-\frac{T}{T_0}\right) \tag{2.45}$$

Second, the cavity resonance wavelength (mainly due to the temperature dependency of the refractive index, and little due to the thermal expansion of the material) and the intrinsic emission wavelength (due to the decreasing gap energy of semiconductors with increasing temperature) will shift at different rates towards longer wavelengths. The shift of the cavity resonance is much smaller than the shift of the peak wavelength emitted from the active semiconductor material. This results in a temperature dependent overlap between the intrinsic emission spectrum and the cavity enhancement, and a decreasing extraction efficiency when increasing current [63].

The decrease of efficiency as a function of the current level results in a saturation of the optical power. The decreasing efficiency at low currents is related to the increasing FWHM of the intrinsic spontaneous emission profile. At higher current levels the thermal effects become more important, and the efficiency decreases faster. At a certain current level, the optical power does not increase anymore. This maximum power is proportional to the RCLED-area. Typical values are in

the order of several $\mu W/\mu m^2$, but do strongly depend on the thermal resistance of the ambient media.

If the current density of the device is known in advance, proactive design can partially intercept the temperature effect on efficiency at the working point. A detuning has to be chosen such that the overlap between intrinsic emission spectrum and the cavity enhancement increases as function of increasing temperature and is maximal at the operating temperature. The increase should at least compensate the decrease of the internal efficiency. This implies a decreased efficiency at low temperature compared to a cavity designed for maximum efficiency at the same temperature. The performance at the working point is best expressed as a differential efficiency (see appendix A).

2.3.2.5 Large diameter RCLEDs and photon-recycling

The photons emitted in the guided wave can not escape the cavity and are -at first sight- lost. However, they can be reabsorbed in the active layer, and be re-emitted. This recycling effect increases the internal efficiency η_{int} and thus the overall external efficiency η_{ext} of the device, as an electron will have a higher probability to produce a photon that escapes from the cavity. This is expressed by an "apparent internal quantum efficiency" $\eta^{\star}_{int}$:

$$\eta^{\star}_{int} = \eta_{int} \frac{1}{1 - g\eta_{int}} \tag{2.46}$$

The reabsorption factor g is defined as the ratio of the number of recycled photons to the total number of internally generated photons. This ratio depends on two factors: the number of photons emitted into the guided mode and the number of guided photons that is reabsorbed in the active layer before they escape the cavity laterally or are absorbed in the rest of the cavity. The first depends on the layer structure (i.e. the cavity tuning). The second factor depends on the characteristic absorption length of the layer structure and the device diameter. The characteristic absorption length of a cavity is a function of the absorption coefficient of the active layer (which depends on the carrier density in the active layer) and the overlap between the internal field profile and the active layer. The guided mode is not necessarily concentrated around the active layer: the field profile can be concentrated in the DBR, resulting in a rather small overlap factor. A typical value of the absorption length is 100 μm [39]. Consequently, the recycling effect is present in large diameter devices and negligible (or even absent) in small diameter devices. Fig. 2.15 shows the calculated increase of η_{int} in case of full lateral reabsorption (i.e. device diameter much larger than reabsorption length) and assuming an internal quantum efficiency $\eta_{int} = 90\%$. The recycling increases as function of the number of DBR pairs, as this results in a more concentrated field profile around the active layer, and thus an increased overlap. The influence of a variation of the thickness of the top spacer d_1 of the cavity is less pronounced. In large devices, the recycling effect results in a 1.4 times enhancement of the overall efficiency.

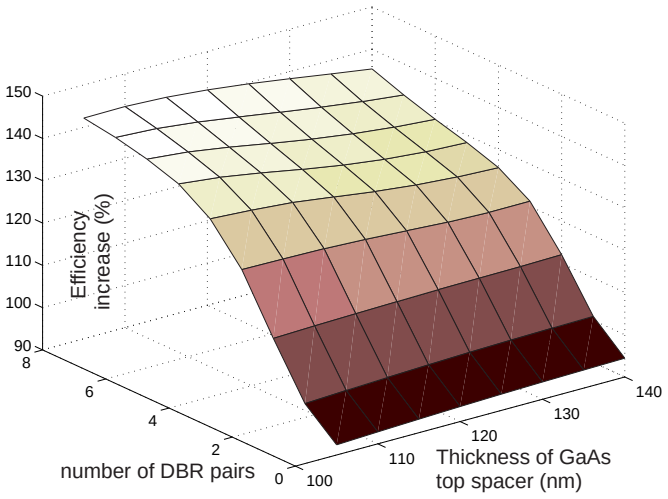

Fig. 2.15: Efficiency increase due to recycling as a function of top spacer thickness d_1 and number of GaAs/AlAs DBR pairs of GaAs λ-cavity emitting at 980 nm [39].

2.3.2.6 Modulation bandwidth of RCLEDs

Besides efficiency, the modulation bandwidth is of utmost importance in communication applications [15], [63]. The response of an LED can be described by rate equations:

$$\frac{dn}{dt} = \frac{I(t)}{qV_{act}} - \frac{n}{\tau_{nrad}} - Bn^2 \tag{2.47}$$

$$P = \hbar\omega\eta_{extr}Bn^2V_{act} \tag{2.48}$$

with $I(t)$ the injected current, V_{act} the volume of the active region, τ_{nrad} the non-radiative lifetime and n the carrier concentration. B is the bimolecular recombination coefficient, describing the radiative recombination speed. For simplicity, the Auger recombination, dominant at very high carrier concentrations is neglected (only in long wavelength devices, Auger recombination can be an important effect, and should not be neglected) [34].

The radiative recombination speed is found after averaging the recombination lifetime of an electron-hole pair in the semiconductor over all available energy levels of the electrons and holes in the active region. Therefore, it includes the Purcell effect. This implies that the micro-cavity effect which alters the optical mode density and thus the Purcell factor, will influence the dynamics of the RCLED. However, as mentioned in section 2.3.1.2, the spontaneous emission rate enhancement depends on the emission wavelength, the cavity parameters and the dipole orientation. The change in lifetime is limited for practical cavities with an AlAs/GaAs DBR [54]. Several experiments have been reported [7], [64]. The largest decrease in recombination lifetime is obtained with a high-Q cavity (corresponding to a small cavity

bandwidth), optically pumped RCLEDs and an overtuned cavity. The measured decay time was 10% shorter compared to standard LEDs.

Besides the effect of the cavity on the bimolecular recombination coefficient, the speed behavior of RCLEDs is similar to standard LEDs. Although the radiative recombination lifetime is slow, compared to stimulated emission, special enhancements can be used to speed up the devices. Examples are the use of a background doping, the use of peaking current driver circuits or voltage drivers, and the use of smaller active regions (such as quantum wells). Photon recycling (see section 2.3.2.5), based on absorption and re-emission of emitted photons affects the bandwidth of the (RC)LED. It increases the LED's response time to an electrical input signal. Photon recycling can be beneficial for high efficiency applications but undesirable for high-speed communication devices.

2.3.3 State of the art

An overview of high efficiency RCLEDs presented in literature is given. The overview is limited to electrically injected devices without epoxy encapsulation, unless explicitly mentioned.

2.3.3.1 980-nm RCLEDs

Unlike the 650-nm and 850-880-nm RCLEDs (cf. below), there is up till now no killer application for 980-nm infrared devices. Moreover, there is a strong competition of 980-nm VCSELs. Nevertheless, thorough investigation on these devices has been carried out and is still going on. The GaAs/Al(Ga)As material system is used with InGaAs high quality strained QWs for active material. Contrary to 650/850-880 nm, GaAs is transparent for 980-nm light. This makes devices emitting at 980 nm preferable for proof of principle experiments. Highly efficient bottom-emitting devices, grown by MOCVD are reported in [17]. With a Au/(GaAs/AlAs)-DBR asymmetric λ-cavity, the metal layer both serving as electrical contact and as mirror, and three InGaAs strained QWs, the overall external efficiency of 80 μm devices is up to 17%. When the diameter is larger, photon-recycling is more significant. An overall external efficiency up to 23% is obtained for large diameter ($\pm 1mm$) RCLEDs, or a 1.4 enhancement. The sensitivity of the η_{extr} to the cavity tuning and the influence of the reflectivity of the bottom DBR, expressed in number DBR pairs, is shown in Fig. 2.16. A deviation of the cavity thickness in the order of $\lambda_s/10$ from the optimal value can result in a reduction of the efficiency by a factor 3. The performance of the RCLED is in direct relation with the precision of the growth of the cavity thickness. This also accounts for devices in other wavelength ranges.

The measured eye-diagram of a voltage-driven 980-nm RCLED (diameter is 30 μm) is shown in Fig. 2.17. Sub-nanosecond rise and fall times of the optical signals and communication with open eye-diagrams at over 1 Gbps have been achieved [65]. The structure and doping profile are the same as the above-mentioned high efficiency devices, but due to the smaller diameter, the overall external efficiency drops to 11%.

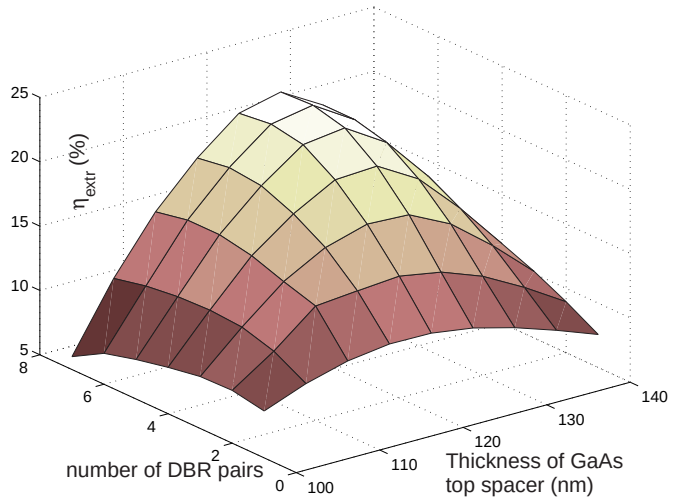

Fig. 2.16: Simulation of η_{extr} of a 980-nm RCLED as a function of top spacer thickness d_1 and number of DBR pairs [39].

Leaky DBR modes, metal mirror absorption and a trapped guided mode are the main loss channels. According to section 2.3.2, a higher index-contrast DBR could result in higher efficiencies due to the suppressed leaky modes and decreased penetration depth ($d_{pen,\theta}$). It can be achieved by laterally oxidising the Al(Ga)As layers to obtain a high index-contrast AlOx/GaAs DBR mirror ($n_{AlOx} \approx 1.6$). There are some drawbacks however. This electrically isolating material necessitates advanced techniques like intra-cavity contacts. Moreover, the use of a high contrast DBR is less appreciated in combination with a metallic top mirror: for a high contrast DBR, the reflectivity of even a single pair is comparable with the gold mirror, resulting in detrimental metal absorption losses (cf. (2.43)). The benefits of the use of a high index-contrast AlOx/GaAs DBR are thus limited to top-emitting devices not using a metallic mirror. A top-emitting device, aperture diameter 11 μm, with a lower 6.5 AlOx/GaAs DBRs and a 1-2 period upper SiO_2/ZnSe DBR on the λ-cavity, and a tunnel contact junction to confine the laterally injected current under the DBR shows external *differential* quantum efficiencies as high as 27% [19]. A laterally injected top-emitting λ-cavity with a single 3.5 pair AlOx/GaAs bottom DBR, diameter 350 μm, shows η_{ext} as high as 28% [20].

2.3.3.2 650-nm RCLEDs

650-nm emitting devices are commercially important for *Plastic Optical Fibre* (POF) based communication. Due to their visible wavelength, they can also serve a broad range of non-communication applications for which a high efficiency is important. Like in standard LEDs, the GaAsP material system is increasingly substituted by the high quality AlGaInP. Due to the absorbing substrate (GaAs

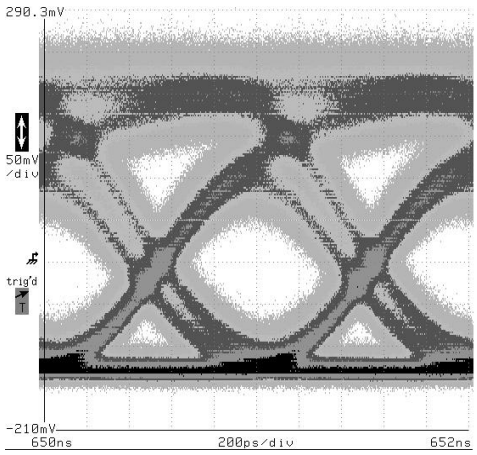

Fig. 2.17: Measured eye-diagram of voltage-driven 980-nm RCLED at 1 Gbit/s (diameter = 30 μm) [39].

or Ge), the device is preferably top-emitting with a cavity sandwiched in between two DBR mirrors and an appropriate current injection design. Devices in the 600-650 nm range are described by several research groups, showing η_{ext} ranging from some percents to 7% [66], [67], [68], [69]. A highly efficient top-emitting RCLED grown by MOCVD operating at 650 nm and having a low forward voltage is reported in [70]. A 300 μm x 300 μm encapsulated device shows a $\eta_{wp} \approx 10.2\%$. The device, a λ-cavity with GaInP active layer enclosed by 2 $Al_xGa_{1-x}As$ DBRs, is ready for large scale production.

2.3.3.3 850-880-nm RCLEDs

Apart from (Fast-)Ethernet LAN data links, the target applications of 850-880 nm devices are remote control and infrared communication as regulated by *Infrared Data Association* (IrDA) (mainly because of the availability of low-cost Si-based detectors). The demands for these applications are different from telecom applications. While brightness and bandwidth are less important, absolute power, overall efficiency and low cost are of paramount importance. The obvious material system for this wavelength range is GaAs, as its bandgap corresponds with this wavelength range. On the other hand this implies that the use of GaAs in the substrate, as part of the DBR, etc. will absorb this light, and thus its use has to be minimised. An 850-nm top-emitting device, consisting of a λ-cavity sandwiched between 2 DBRs grown by MOCVD, shows an overall efficiency η_{ext} of 14.6% [71]. The top mirror is a 1.5 pair $Al_{0.15}Ga_{0.85}As$/ AlAs DBR, the bottom mirror a 20 pairs DBR. The decreased refractive index-contrast compared with a GaAs/AlAs DBR results in the need of a thicker DBR-stack. Current injection was optimised with a selectively oxidised current window with a diameter of 180 μm.

A 880-nm monolithic top-emitting device with λ-cavity, a 20 pairs n-doped

$Al_{0.2}Ga_{0.8}As$/ $Al_{0.9}Ga_{0.1}As$ bottom DBR and a 5-7 pairs top DBR, all grown by solid-source MBE is reported in [72]. With an emission window of 80 μm and an epoxy cap, η_{ext} is 16%.

2.3.3.4 1300-nm and 1550-nm RCLEDs

The principal material system for the pre-eminently telecom-wavelength devices is InP. In addition to the broader intrinsic spectrum of long wavelength devices (see (2.42)), the restrictions of the appropriate material systems (cf. long wavelength Vertical-Cavity Surface-Emitting Lasers (VCSELs)), limits the maximal efficiency of long wavelength devices. The problem lies in the low refractive index-contrast that can be realised with InP lattice matched alloys to form the DBR, resulting in large penetration depths. Highly efficient 1300-nm large diameter devices (2 mm) with a peak quantum efficiency of 9% are reported in [73] using a monolithic cavity grown by MOCVD. The electrically pumped device is bottom-emitting, using an asymmetric Au/DBR InP λ-cavity with three 4.5 nm $InGa_{0.12}As_{0.56}P$ strained QWs . The low refractive index-contrast of the 5.5 pair $InGa_{0.23}As_{0.50}P$/InP DBR is the main drawback.

Research towards high quality epitaxial DBR mirrors is driven by VCSEL research. Contrary to RCLEDs, the need for high index-contrast mirrors in VCSELs arises from the sole need for highly reflective mirrors, whatever their penetration length, say R > 99%. A low Δn requires a large number of DBR mirror pairs in order the achieve the high reflectivity, translated into several growth-related problems. Other InP-lattice matched alloys are reported in VCSEL-literature for fabrication of high refractive index-contrast DBR mirrors: especially aluminium and antimonide containing compound semiconductors are promising candidates [74].

On the other hand, VCSEL research has an increasing interest in the development of GaAs based devices for long wavelength applications, i.e. active material compatible with GaAs. Next to the possibility of high index-contrast GaAs/AlAs Bragg mirror, this system is more temperature insensitive and cheaper. A path not yet entered by RCLEDs, is the use of GaInNAs as active material [75] to emit at 1300 nm. The use of *Quantum Dots* (QD) has been investigated in several research groups. With self-assembled InAs-InGaAs QDs emitting at 1300 nm in a single mirror (Au) cavity, grown by solid-source MBE on a GaAs substrate, an external quantum efficiency of 1% at room temperature is obtained, limited by the low radiative efficiency of 13% of the QDs.

An MOCVD InP-based RCLED of diameter 80 μm emitting at 1550 nm with a 6.8% external quantum efficiency is cited in [77]. The device is bottom-emitting, using an asymmetric Au/DBR(12 pairs $InGa_{0.38}As_{0.82}P$/InP) cavity. The active region consists of three 7.5 nm $In_{0.84}Ga_{0.16}As_{0.74}P_{0.26}$ QWs. An electrically pumped top-emitting all epitaxial InGaAsP/InP DBR/DBR RCLED is reported in [78], optimised for high coupling efficiency to fibre, the main demand for this wavelength, instead of overall efficiency.

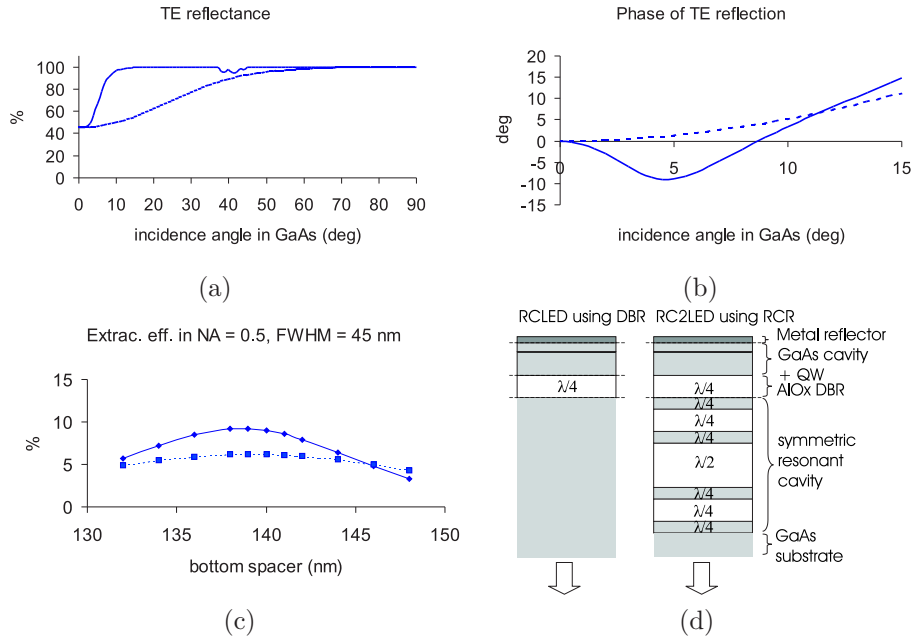

Fig. 2.18: RC2LED (a) TE reflectance for DBR and RCR, as seen from the GaAs cavity (full line: RCR, dashed line: DBR); (b) phase of TE reflection for DBR and RCR, as seen from the GaAs cavity (full line: RCR, dashed line: DBR) ; (c) simulated extraction efficiency into NA = 0.5 (full line: RCR, dashed line: DBR); (d) RC2LED [56].

2.3.4 Advanced techniques

2.3.4.1 RC2LED

In the RC2LED, a symmetric resonant cavity is added to the outcoupling mirror [56]. This novel mirror design, the *Resonant Cavity Reflector* (RCR) yields high reflectance for off-axis incidence, combined with a moderate reflectance for normal incidence. This results in a narrower radiation pattern. Also, because the angular penetration depth is negative, extra resonances are created within the extraction cone, which boosts the extraction efficiency. These TE reflection properties of the RCR are depicted in Fig. 2.18(a)-(b) and compared with the corresponding DBR, sketched in (d). These factors combine to yield an extraction efficiency to a given NA which can be 50% to 100% higher than conventional RCLEDs. The extraction efficiency in a NA=0.5, for a GaAs/AlOx RC2LED (see [56]) with Gaussian spectrum with FWHM=45 nm is shown in Fig. 2.18(c). This idea has not been verified experimentally yet.

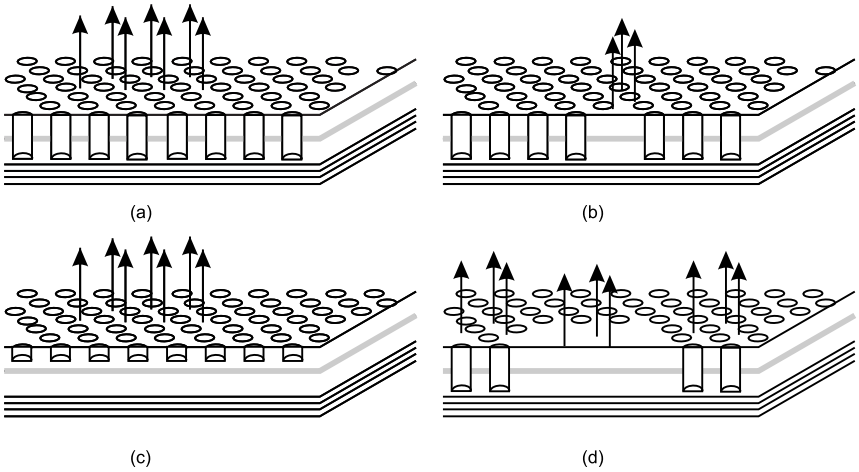

Fig. 2.19: Photonic Crystal Assisted RCLED (a) 2-D PC etched through the active layer; (b) 2-D PC to inhibit lateral emission by creating an in-plane cavity; (c) shallow 2-D PC to extract guided mode, extraction of guided mode and active region coincidence (d) 2-D PC surrounding active region to extract guided mode,extraction of guided mode and active region do not coincidence. The opposite mirror is in each case a DBR.

2.3.4.2 Photonic Crystal Assisted RCLED

The main drawback of planar RCLEDs is the distribution of the optical power over several optical modes, while only a fraction will be extracted. Leaky modes and guided modes are lost, except through partial photon-recycling by reabsorption (see section 2.3.2.5). When the planarity of the RCLED is abandoned, control on the in-plane dimensions can be obtained. The world of *Photonic Crystals* (PCs) and resonant cavities meet in the *Photonic Crystal Assisted RCLED* (PCA-RCLED). A PC is a 1-, 2- or 3-dimensional periodic corrugated medium. Its wavelength-scale period and high refractive index contrast can strongly influence the optical mode density. Apart from the 1-D PC, in the form of a DBR mirror already present in most RCLEDs, a 2-D PC can be added in the plane of the device. Different top-emitting configurations are sketched in Fig. 2.19. Configuration (a) and (b) inhibit emission in the guided mode, (c) and (d) extract the guided mode using a 2-D PC.

Inhibition of guided mode

The periodic corrugation can provide a band gap in the dispersion relation of the guided modes at the emission frequencies. Emission will then initially be prevented in the guided modes [79]. Eliminating the guided modes at the transition frequency, spontaneous emission can be enhanced to couple to the free space modes via the Fabry-Pérot mode. In the first configuration (Fig. 2.19(a)), a 2-D PC is etched through the active layer of the planar RCLED [80]. Besides troublesome current injection, etching through the active layer can cause large non-radiative

recombination rates due to induced surface states. An alternative configuration which somehow circumvents the latter problem is sketched in Fig. 2.19(b). A bare cavity is surrounded by a 2-D PC. The high reflective 2-D PC creates an in-plane cavity. To be efficient, the lateral dimensions of the micro-disk have to be of the same order as the wavelength, cf. the vertical dimensions of the planar RCLED. These dimensions are in general quite smaller than the diffusion length of carriers and thus do not fully tackle the non-radiative recombination problem at the etched surfaces. Moreover, due to the small in-plane cavity dimensions, only small saturation values can be achieved [81]. Depending on spectral width and absorption losses, the configuration of Fig. 2.19(a) or Fig. 2.19(b) is preferred [82]. Since a band gap can be opened in the guided mode spectrum with holes not etched through the active material, surface recombination can be completely avoided using shallow gratings.

Extraction of the guided mode

Far more practical than inhibition of the guided mode is its extraction. The diffractive properties of the periodic grating can redirect the laterally propagating resonant guided mode to an extractable direction in the extraction cone. Because of the high power fraction in these guided modes (see Fig. 2.14(b)), the use of such gratings can result in a higher η_{extr}. In configuration (c), the shallow PC or grating coincidences with the active layer, but is not etched through it. The 2-D grating is designed to diffract efficiently the guided mode to the extraction cone and thus to the free space optical modes. Investigation of a GaAs 980 nm cavity with GaAs/AlAs bottom DBR and metallic grating, the so called *Grating-Assisted RCLED* (GA-RCLED), has been carried out in this work and will be discussed in detail, theoretically and experimentally, in the following chapters. A 6-fold extraction enhancement is reported for an optically pumped asymmetric cavity with a DBR and a semiconductor-air grating-interface [83], but absolute efficiencies are not mentioned.

A variant on the latter can be found in a 2-D periodic corrugation surrounding the active region. In these devices, the Fabry-Pérot mode is extracted in the central part of the light source where the layers are homogeneous, the guided mode leaves the semiconductor in the surrounding periodically corrugated region (see Fig. 2.19(d)). The region of generation and extraction of the guided mode are separated. The diameter of the unpatterned light generation region has to be smaller than the reabsorption length of the guided mode. The PC has to be designed to scatter the guided mode efficiently to the free space modes lying above the light-line (see Chapter 3), this for all in-plane directions. Theoretical investigation of a top-emitting laterally current injected λ-cavity with AlO_x/GaAs DBR is promising: a supplementary extraction of 10% is predicted as worst case scenario [84]. Optically pumped thin-film devices showed a 6-fold efficiency increase compared to the unetched thin-film in an NA=0.7 [85].

Configuration (c) is technologically more tedious since the grating, and thus its deviations, influences the cavity directly (see Fig. 2.16 for sensitivity of η_{ext} to cavity tuning variation). The vertical and horizontal design issues are entangled. An ill designed GA-RCLED can affect existing extraction channels, resulting in

a decrease of efficiency in comparison with gratingless RCLEDs. On the other hand, because the extraction and generation region are not separated, it is more efficient in the use of its active layer to total emitting surface than (d), resulting in a compact device with relative better η_{dens} (see Appendix A).

2.3.5 Future prospects of RCLEDs

RCLEDs are not the only candidates that can be used as high efficiency light source in communication and non-communication applications. They compete with other high efficiency LEDs and with VCSELs.

The key merit of a RCLED (and a VCSEL) as compared to many other high efficiency LED types is that it is a planar device, allowing for 1-D and 2-D arrays. In combination with its both high efficiency and high radiance or brightness, this makes the RCLED an ideal light source for multi-mode fiber coupling in array applications and opens the possibility of massively parallel optical data communication. Non-communication applications, e.g. sensors, printers and scanners, do also require arrays of small diameter sources with high radiance.

Fabrication of a RCLED is similar to the fabrication of conventional planar LEDs: straightforward and at low cost. No advanced processing techniques are needed that can boost up costs.

In terms of modulation bandwidth, all LEDs are restricted by the same fundamental limitation, i.e. the spontaneous emission lifetime. The modulation bandwidth of RCLEDs can be relatively high without penalty on efficiency because they generally have thin active layers and a small diameter resulting in a relatively high current density. Therefore the carrier density in the active layer is relatively high leading to high modulation rates up to about 1Gbps (see section 2.3.2.6 and section 2.3.3).

While RCLEDs and LEDs both rely on spontaneous emission, VCSELs are based on stimulated emission in high Q-factor cavities. The cavity is formed by placing an active layer (QWs or Quantum Dots) between two DBRs. In contrast with the DBRs of the RCLED, both DBRs need to be highly reflecting, because the single-pass gain of these very thin active layers is rather small. This fundamentally different physical process of stimulated emission makes the VCSEL a monochromatic optical source, with a near-diffraction limited output field (single mode VCSEL). These characteristics make the VCSEL far more suitable for coupling to single mode fibers than RCLEDs. Moreover, the fast stimulated emission makes it possible to modulate a biased VCSEL up to about 10 GHz.

On the other hand, fabrication of the RCLED is simpler and at lower cost than the VCSEL. Compared to a VCSEL with its high reflective DBRs, the small total thickness of the RCLED reduces the epitaxial growth time and the incorporated strain in case of lattice mismatch, simplifying wafer handling and device processing. This is important in long-wavelength and red applications, where typically very thick DBR-mirrors are used. Uniformity will be higher because VCSEL performance is more sensitive on the device parameters (emission wavelength of

QW, thickness of cavity, etc. need to be controlled to a higher degree). For both VCSEL and RCLED, the operation principle is qualitatively suitable for all wavelengths, although quantitatively strongly depends on the appropriate material system. However the RCLED has less stringent requirements on the material system. Especially the high gain in the active region and the high quality of the optical cavity are difficult the achieve in some material systems.

Another noteworthy aspect is that VCSELs, as all lasers, have a threshold current below which the efficiency is zero. LEDs do not have a threshold current and therefore they can outperform VCSELs in situations where a high efficiency is needed at a low-power operation point. This can be the case in high density array applications, where a low power dissipation is of utmost importance.

The RCLED is an incoherent source. While this fact makes the RCLED unsuitable for coupling to single mode fibers, it should be emphasized that coherence is not necessary for coupling to multi-mode fibers. Even more, incoherence helps to reduce modal noise and speckle. Incoherence is even necessary for certain applications such as speckle-free medium-coherent sources for use in low-coherence interferometric techniques, to give one out of many possible examples.

Finally the low temperature dependence of the output power of a RCLED (see section 2.3.2.4) can be desirable in various applications that are used in extreme circumstances. However, due to the multi-facetted and complex temperature behavior of both RCLEDs and VCSELs, a comparison can not be expressed in terms of simple statements.

2.4 Conclusion

In conclusion it is clear that the RCLED can serve a broad range of low cost, high volume applications, both communication and non-communication, and this for a broad range of wavelengths. The RCLED can be a favorable choice in comparison to VCSELs and most high efficiency LEDs when: a relatively high radiance is needed, modulation bandwidth of 1GHz suffices and when the incoherent nature of the source is not a problem or is even an asset. In particular dense array applications do profit from the combination of properties of the RCLED.

The RCLED has been introduced on the market for 650-nm applications and is ready to be commercialised for a broader range of applications.

The efficiency and radiance of a RCLED can still be further increased using advanced techniques. One of these advanced designs is the grating-assisted RCLED. This device is discussed in detail in this work.

APPENDIX A: Guidelines for comparison of high efficiency LEDs

There are many ways to compare the performance of high efficiency LEDs and the preferred technique depends strongly on the application. In spite of the importance of the external efficiency η_{ext}, it has to be emphasized that an objective comparison of the different techniques to enhance η_{ext} can only be obtained when a complete analysis is done. This includes in the first place a clear indication of the definition of the indicated efficiencies and saturation values and a comparative analysis of some basic aspects. A checklist is given hereafter.

- The external performance of an LED can be expressed in different ways, making comparison of devices to be done with care. The commonly used definitions to express the efficiency and saturation values are presented in Table 2.2.

Efficiency	Saturation value
$\eta_{ext} = \dfrac{P_{opt}/\hbar\omega}{I/q}$ $[\%]$	$S^{sat}_{phot} = \dfrac{P^{max}_{opt}}{\hbar\omega}$ $\left[s^{-1}\right]$
$\eta_{wp} = \dfrac{P_{opt}}{IV}$ $[\%]$	$P^{sat} = P^{max}_{opt}$ $[W]$
$\eta_{phot} = 683\, V_{CIE}(\lambda)\, \eta_{wp}$ $[lm/W]$	$L^{sat} = 683\, V_{CIE}(\lambda)\, P^{sat}$ $[lm]$
$\eta_{dens} = \dfrac{1/A_{extr}}{1/A_{act}}$ $[\%]$	$M^{sat} = \dfrac{P^{max}_{opt}}{A_{extr}}$ $\left[W/m^2\right]$
$\eta_{rdn} = \dfrac{dP_{opt}/d\Omega\, A_{extr}}{IV}$ $\left[W/W.m^2.sr\right]$	$R^{sat} = \dfrac{dP^{max}_{opt}}{d\Omega\, A_{extr}}$ $\left[W/m^2.sr\right]$
$\eta_{lum} = 683\, V_{CIE}(\lambda)\, \eta_{rdn}$ $\left[cd/W.m^2\right]$	$B^{sat} = 683\, V_{CIE}(\lambda)\, \dfrac{dP^{max}_{opt}}{d\Omega\, A_{extr}}$ $\left[cd/m^2\right]$

TABLE. 2.2: Commonly used definitions to express efficiency and saturation values.

The *external quantum efficiency* η_{ext} is the most commonly used definition expressing the number of photons per injected electron. Either the overall

η_{ext} can be given, or the η_{ext} to a limited *Numerical Aperture* (NA). The corresponding relevant absolute value is the *maximum photon flux* S_{phot}^{sat}. These definitions allow to compare LEDs with a different emission wavelength.

The *wall plug efficiency* η_{wp} is an alternative for η_{ext}. It takes into account the series resistance of the diode, as it is defined as the ratio of the emitted optical power to supplied electrical power IV, with V the bias voltage (V). Again, an NA can be specified. The *maximal output power* P^{sat} indicates the saturated power or radiant flux.

The *photometric efficiency* η_{phot} weighs the wall plug efficiency with the relative luminosity V_{CIE} (lm/W), defined by the Commission Internationale de l'Eclairage (CIE). V_{CIE} is proportional to the effectiveness in stimulating the human visual sense. η_{phot} is thus only defined for LEDs emitting visible light. The *maximal luminous flux* L^{sat} scales the radiant flux with the relative luminosity.

The *density efficiency* η_{dens} is a measure for the efficient active use of the available surface. It is defined as the ratio of the inverse of the extraction surface A_{extr} to the inverse of the surface of the active layer A_{act}. In a RCLED $A_{act} \approx A_{extr}$ and thus very high. This parameter is important for scaling of high brightness devices. M^{sat} expresses the maximal total near-field power density or *radiant emittance*.

The *radiant efficiency* η_{rdn} defines the conversion efficiency of the electrical power to the peak radiance. R^{sat} is the saturation *radiance*. The radiance is a quantity that -at best- is conserved in an imaging system: the radiance of the image cannot be higher than that of the object. Therefore high radiance is important in any application where light needs to be focused to a small spot or where light needs to be coupled into a fiber with finite core size and numerical aperture. While the radiance of a RCLED is still orders of magnitude lower than that of a laser (for a given power), it is easily orders of magnitude larger than that of an LED chip with light extraction from all chip sides or with small density efficiency.

The *luminous efficiency* η_{lum} weighs the radiant efficiency with the relative luminosity V_{CIE}. *Brightness* is defined as the optical luminous power per unit solid angle (Ω) per unit surface (A). η_{lum} and B^{sat} are only defined for LEDs emitting visible light, due to the relative luminosity in their definition. Unlike the efficiency, the power and brightness of an LED can be augmented when the pumping level is increased. The commercial labelling "High Brightness" LEDs is strongly linked with "High Efficiency" as the saturation level of a device at high pumping levels can only be increased when efficiency is increased.

A distinction has to be made between an efficiency and a differential efficiency. The differential efficiency defined as a power increase due to an infinitesimal rise of the current, will typically be higher than the absolute efficiency. The reason can be excessive non-radiative recombination, parallel current paths, saturation effects,....

- Is the device optically or electrically pumped? Electrically pumped devices demand electrical contacts, complex doping profile, etc.. This tends to go together with geometrical issues that are not always favorable for η_{ext}.
- What is the emission wavelength? The intrinsic linewidth penalty, Eq.(2.42), scales with the wavelength. Moreover, the wavelength more or less defines the used material system. Table 2.3 summarises commonly used material systems for different wavelength ranges. The refractive index contrast that can be realised varies strongly from wavelength range to wavelength range. As mentioned in section 2.3.2, the refractive index contrast is an important figure to determine the penetration depth of the DBR and thus the extraction efficiency.

λ	high index mat.	low index mat.	Δ n
0.65μm	$Al_{0.5}Ga_{0.5}As$ n=3.47	$Al_{0.95}Ga_{0.05}As$ n=3.14	0.33
0.85μm	$Al_{0.15}Ga_{0.85}As$ n=3.5	AlAs n=2.98	0.52
0.98μm	GaAs n=3.52	AlAs n=2.95	0.57
0.98μm	GaAs n=3.52	AlOx n=1.6	1.92
1.3μm	$InGa_{0.23}As_{0.50}P$ n=3.42	InP n=3.21	0.21
1.55μm	$InGa_{0.38}As_{0.82}P$ n=3.47	InP n=3.17	0.3

TABLE. 2.3: Refractive index contrast in commonly used material systems.

- η_{extr} scales roughly spoken with $(1-\cos(\theta_c)) \approx 1/2n_s^2$. This has to be kept in mind when comparing the performance of RCLEDs with different refractive index n_s e.g. polymer RCLEDs and semiconductor RCLEDs.
- Is the device encapsulated by an epoxy dome? Embedding the semiconductor device in a transparent plastic with a dome shape, enlarges the extraction cone in the semiconductor and hence its η_{extr}. The waves impinge more or less normally on the surface of the large dome and are extracted.
- Is the device emitting through a single surface or do several surfaces contribute to the extraction? Some applications, e.g. fibre coupling and array devices do demand a single surface emitting diode. Is the diameter specified?
- The simplicity of fabrication: how easy can the production process be adopted for mass production?
- Dependent on the application, advanced characteristics -directivity, speed- can play an important role in the suitability of the device.

References

[1] E.E. Loebner, "Subhistories of the Light Emitting Diode", *IEEE Trans. Electron. Dev.*, ED-23(7), pp. 675-699, 1976.

[2] H. Krömer, "A proposed class of heterojunction injection lasers", *Proc. of IEEE*, vol. 51, pp. 1782, 1963.

[3] W. Lukosz and R. E. Kunz, "Light Emission by Magnetic and Electric Dipoles Close to a Plane Interface. I Total radiated power", *J. Opt. Soc. Am.*, vol. 67(12), pp. 1607-1615, 1977.

[4] W. Lukosz and R. E. Kunz, "Light Emission by Magnetic and Electric Dipoles Close to a Plane Interface. II Radiation Patterns of Perpendicular Oriented Dipoles", *J. Opt. Soc. Am.*, vol. 67(12), pp. 1615-1619, 1977.

[5] W. Lukosz and R. E. Kunz, "Light Emission by Magnetic and Electric Dipoles Close to a Plane Interface. III Radiation Patterns of Dipoles with Arbitrary Orientation", *J. Opt. Soc. Am.*, vol. 69(11), pp. 1495-1503, 1979.

[6] W. Lukosz, "Theory of optical-environment-dependent spontaneous-emission rates for emitters in thin layers", *Phys. Rev. B*, vol. 22(6), pp. 3030-3037, 1980.

[7] H. Yokoyama, K. Nishi, T. Anan, H. Yamada, S. D. Brorson and E. P. Ippen, "Enhanced spontaneous emission from GaAs quantum wells in monolithic microcavities", *Appl. Phys. Lett.*, vol. 57(26), pp. 2814-2816, 1990.

[8] H. Yokoyama, "Physics and Device Applications of optical Microcavities", *Science*, vol. 256, pp. 66-70, 1992.

[9] G. Bjork, S. Machida, Y. Yamamoto and K.Igeta, "Modification of spontaneous emission rate in planar dielectric micro-cavity structures", *Phys. Rev.A*, vol. 44(1), pp. 669-681, 1991.

[10] F. De Martini, M. Marrocco, P. Mataloni, L. Crescentini and R. Loudon, "Spontaneous Emission in the Optical Microscopic Cavity", *Phys. Rev. A*, vol. 43(5), pp. 2480-2497, 1991.

[11] D. G. Deppe and C. Lei, "Spontaneous emission from a dipole in a semiconductor microcavity", *J. Appl. Phys.*, vol. 70(7), pp. 3443-3448, 1991.

[12] Y. Yamamoto, S. Machida and G. Bjork, "Micro-cavity semiconductor laser with enchanced spontaneous emission", *Phys. Rev. A*, vol. 44(1), pp. 657-668, 1991.

[13] N. E. Hunt, E. F. Schubert, R. A. Logan and G. J. Zydzik, "Enhanced Spectral power density and reduced linewidth at 1.3mm in an InGAaSP quantum well resonant-cavity light-emitting diode", *Appl. Phys. Lett.*, vol. 61(19), pp. 2287-2289, 1992.

[14] E. F. Schubert, Y.-H. Wang, A. Y. Cho, L.-W. Tu and G. J. Zydzik, "Resonant Cavity light-emitting Diode", *Appl. Phys. Lett.*, vol. 60(8), pp. 921-923, 1992.

[15] E. Schubert, N. Hunt, M. Micovic, R. Malik, D. Sivco, A. Cho and G. Zydzik, "Highly Efficient Light Emitting Diodes with Microcavities", *Science*, vol. 265, pp. 943-945, 1994.

[16] J. Blondelle, H. De Neve, G. Borghs, P. Van Daele, P. Demeester and R. Baets "High Efficiency (>20%) Micro-cavity Light Emitting Diodes", in *Proc. IEE Coll. on Semiconductor Optical MicroCavity Devices and Photonic Bandgaps*, London, UK, 1996.

[17] H. De Neve, J. Blondelle, P. Van Daele, P. Demeester, R. Baets and G. Borghs, "Recycling of Guided Mode Light Emission in Planar Micro-cavity Light Emitting Diodes", *Appl. Phys.Lett.*, vol. 70(7), pp. 799-801, 1997.

[18] H. De Neve, J. Blondelle, P. Van Daele, P. Demeester, R. Baets and G. Borghs, "Planar substrate-emitting Micro-cavity Light Emitting Diodes with 20% external QE", in *Light-Emitting Diodes: Research, Manufacturing, and Applications, Proc. SPIE,* vol. 3002, pp. 74-84, 1997.

[19] J.J. Wierer, D.A. Kellogg and N. Holonyak, "Tunnel contact junction native-oxide aperture and mirror vertical-cavity surface-emitting lasers and resonant-cavity light-emitting diodes," *Appl. Phys. Lett.,* vol. 74(7), pp. 926-928, 1999.

[20] M. Rattier, H. Benisty, R.P. Stanley, J.F. Carlin, R. Houdré, U. Oesterle, C.J.M. Smith, C. Weisbuch and T.F. Krauss, "Toward ultrahigh-efficiency aluminum oxide microcavity light-emitting diodes: guided mode extraction by photonic crystals", *IEEE J. Sel. Top. Quantum Electron.,* vol. 8(2), pp. 238-247, 2002.

[21] M.O. Holcomb, M.R. Krames, G.E. Hofler, C. Carter-Coman, E. Chen, P. Grillot, K. Park, N.F. Gardner, J.-W. Huang, J. Posselt, D. Collins, S.A. Stockman, G. M. Craford, F.A. Kish, I.-H. Tan, T.S. Tan, C.P. Kocot and M. Hueschen, "High-power truncated-inverted-pyramid $(Al_xGa_{1-x})_{0.5}In_{0.5}P$ light-emitting diodes exhibiting $> 50\%$ external quantum efficiency," *Appl. Phys. Lett.,* vol. 75(16), pp. 2365-2367, 1999.

[22] I. Schnitzer, E. Yablonovitch, C. Carneau, T.J. Gmitter and A. Scherer, "30% external quantum efficiency from surface textured, thin-film light-emitting diodes", *Appl. Phys. Lett.,* vol. 63(16), pp. 2174-2176, 1993.

[23] R. Windisch, C. Rooman, S Meinlschmidt, P. Kiesel, D. Zipperer, G. H. Doehler, B. Dutta, M. Kuijk, G. Borghs, and P. Heremans, "Impact of texture-enhanced transmission on high-efficiency surface-textured light-emitting diodes", *Appl. Phys. Lett.,* vol. 79(15), pp. 2315-2317, 2001.

[24] W. Schmid, M. Scherer, C. Karnutsch, A. Ploessl, W. Wegleiter, S. Schad, B. Neubert and K. Streubel, "High efficiency, red and infrared light-emitting diodes using radial outcoupling taper", *IEEE J. Sel. Top. Quantum Electron.,* vol. 8(2), pp. 256-263, 2002.

[25] www.fols.org

[26] S. Morikura, K. Kinoshita, K. Numata and S. Furusawa, "High Speed POF Transmission technology and its Standardization", in *27th European Conference on Optical Communication 2001, Amsterdam,* vol. 1, pp. 20-21, 2001.

[27] R. Loudon, *"The quantum theory of light,"* Oxford University Press, New York, 1983.

[28] C. Hooijer, G. Li, K. Allaart and D. Lenstra, "Spontaneous emission in multilayer semiconductor structures", *IEEE J. Quantum Electron.,* vol. 37, pp. 1161-1169, 2001.

[29] H. Benisty, H. De Neve and C. Weisbuch, "Impact of Planar Microcavity Effects on Light Extraction - Part I: Basic Concepts and Analytical Trends", *IEEE J. Quantum Electron.,* vol. 34(9), pp. 1612-1631, 1998.

[30] H. Benisty, H. De Neve and C. Weisbuch, "Impact of Planar Microcavity Effects on Light Extraction - Part II: Selected Exact Simulations and Role of Photon Recycling", *IEEE J. Quantum Electron.,* vol. 34(9), pp. 1632-1643, 1998.

[31] H. Benisty, R. Stanley and M. Mayer, "Method of source terms for dipole emission modification in modes of arbitrary planar structures", *J. Opt. Soc. Am. A*, vol. 15(5), pp. 1192-1201, 1998.

[32] R. Baets, *"Micro-cavity light emitting diodes"*, in Semiconductor Quantum Optoelectronics, A. Miller, M. Ebrahimzadeh and D.M. Finlayson, eds., St.-Andrews, UK, 1998.

[33] R. Baets, P. Bienstman and R. Bockstaele, *"Basics of Dipole Emission from a Planar Cavity"*, in Confined Photon Systems, Fundamentals and applications, H. Benisty, J.-M. Gérard, R. Houdré., J.Rarity and C. Weisbuch, eds., Springer-Verlag, 1999.

[34] L.A. Coldren and S.W. Corzine, *"Diode lasers and photonic integrated circuits"*, John Wiley and Sons, New York, 1995.

[35] A. Yariv, *"Quantum Electronics"*, John Wiley and Sons, New York, 1989.

[36] P. Bhattacharya, *"Semiconductor Optoelectronic Devices"*, Prentice Hall Inc., second edition, 1997.

[37] J. Blondelle, *"Realisatie van hoogefficiente substraatemitterende InGaAs/(Al)GaAs microcaviteitsLEDs met behulp van MOCVD"*, Ph. D. Thesis, Ghent University, Ghent, Belgium, 1997.

[38] H. De Neve, *"Ontwerp en realisatie van Licht Emitterende Diodes op basis van het Microcaviteitseffect"*, Ph. D. Thesis, Ghent University, Ghent, Belgium, 1997.

[39] R. Bockstaele, *"Resonant Cavity Light Emitting Diode Based Parallel Interconnections"*, Ph. D. Thesis, Ghent University, Ghent, Belgium, 2001.

[40] K.H. Huang, J.G. Yu, C.P. Kuo, R.M. Fletcher, T.D. Osentowski, L.J. Stinson, M.g. Craford and A.S.H. Liao, "Twofold efficiency improvement in high-performance AlGaInP light-emitting-diode in the 555-620nm spectral region using a thick gap window layer", *Appl. Phys. Lett.,* vol. 61(9), pp. 1045-1047, 1992.

[41] F.A. Kish, F.M. Steranka, D.C. Defevere, D.A. Vanderwater, K.G. Park, C.P. Kuo, T.D. Osentowski, M.J. Peanasky, J.G. Yu, R.M. Fletcher, D.A. Steigerwald, M.G. Craford and V.M. Robbins, "Very high-efficiency semiconductor wafer-bonded transparant-substrate $(Al_xGa_{1-x})_{0.5}In_{0.5}P$ light-emitting-diodes", *Appl. Phys. Lett.,* vol. 64(21), pp. 2839-2841, 1994.

[42] F.A. Kish, D.A. Vanderwater, D.C. Defevere, D.A. Steigerwald, G.E. Hofler, K.G. Park and F.M. Steranka, "Highly reliable and efficient semiconductor wafer-bonded AlGaInP/GaP light-emitting diodes," *Electron. Lett.,* vol. 32(2), pp. 132-134, 1996.

[43] N.F. Gardner, H.C. Chui, E.I. Chen,M.R. Krames, J.W. Huang, F.A. Kish, S.A. Stockman, C.P. Kocot, T.S. Tan, N. Moll, "1.4x efficiency improvement in transparent-substrate $(Al_xGa_{1-x})_{0.5}In_{0.5}P$ light-emitting diodes with thin (<= 2000 angstrom) active regions", *Appl. Phys. Lett.,* vol. 74(15), pp. 2230-2232, 1999.

[44] M.O. Holcomb, M.R. Krames, G.E. Hofler, C. Carter-Coman, E. Chen, P. Grillot, K. Park, N.F. Gardner, J.-W. Huang, J. Posselt, D. Collins, S.A. Stockman, G. M. Craford, F.A. Kish, I.-H. Tan, T.S. Tan, C.P. Kocot and M. Hueschen, "High power Truncated-Inverted-Pyramid $(Al_xGa_{1-x})_{0.5}In_{0.5}P$ Light-Emitting Diodes", in *Light-Emitting Diodes: Research, Manufacturing, and Applications IV, Proc. SPIE,* vol. 3938, pp. 77-81, 2000.

[45] W. Schmid, F. Eberhard, R. Jäger, R. King, M. Miller, J. Joos and K.J. Ebeling, " 45% Quantum Efficiency Light-Emitting Diodes with Radial Outcoupling Taper", in *Light-Emitting Diodes: Research, Manufacturing, and Applications IV, Proc. SPIE,* vol. 3938, pp. 90-97, 2000.

[46] D. Ochoa, *"Diodes électroluminescentes planaires à haute extraction lumineuse"*, Ph. D. Thesis, Ecole Polytechnique Fédérale de Lausanne, Lausanne, Switzerland, 2000.

[47] R. Windisch, M. Kuijk, B. Dutta, A. Knobloch, P. Kiesel, G.H. Dölher, G. Borghs and P. Heremans, "Non-Resonant Cavity Light-Emiotting Diodes", in *Light-Emitting Diodes: Research, Manufacturing, and Applications IV, Proc. SPIE,* vol. 3938, pp. 71-76, 2000.

[48] http://www.strategies-u.com.

[49] M. Yamanishi, I. Suemune, "Comment on polarization dependent momentum matrix elements in quantum well lasers", *Jap.J. Appl. Phys.*, vol. 23, pp. L35-L36, 1984.

[50] G. Jones, A. Ghiti, M. Silver, E.P. O'Reilly and A.R. Adams, "Radiative perfomance of strained-layer lasers", *IEE Proceedings-J*, vol. 140(1), pp. 85-89, 1993.

[51] J.M. Gérard and B. Gayral, "Strong Purcell effect for InAs quantum boxes in three-dimensional solid-state microcavities", *IEEE J. Lightwave Tech.*, vol. 17(11), pp. 2089-2095, 1999.

[52] E.M. Purcell, "Spontaneous emission probabilities at Radiofrequencies", *Phys. Rev*, vol. 69, pp. 681, 1946.

[53] G.Bjork, "On the Spontaneous Lifetime Change in an Ideal Planar Micro-cavity - Transition from a Mode Continuum to Quantized Modes", *IEEE J. Quantum Electron.*, vol. 30(10), pp. 2314-2318, 1994.

[54] I. Abram, I. Robert and R. Kuszelewicz, "Spontaneous Emmission Control in Semiconductor Microcavities with Metallic or Bragg Mirrors", *IEEE J. Quantum Electron.*, vol. 34(1), pp. 71-76, 1998.

[55] K. Neyts, "Microcavities for electroluminescent devices", *Semiconductors and semimetals*, vol. 65, pp. 183-234, 2000.

[56] P. Bienstman and R. Baets, "The RC2LED: an novel Resonant-Cavity LED design using a symmetric resonant cavity in the outcoupling reflector", *IEEE J. Quantum Electron.*, vol. 36(6), pp. 669-673, 2000.

[57] D. Ochoa, R. Houdré, R.P. Stanley, U. Oesterle and M. Illegems, "Device simultaneous determination of the source and cavity parameters of a microcavity Light-Emitting diode", *J. Appl. Phys.*, vol. 85(5), pp. 2994-2996, 1999.

[58] Z. Huang, C.C. Lin, and D.G. Deppe, "Spontaneous lifetime and quantum efficiency in light emitting diodes affected by a close metal mirror", *IEEE J. Quantum Electron.*, vol. 29(12), pp. 2940-2949, 1993.

[59] C. Weisbuch and B. Vinter, "Quantum Semiconductor structures- Fundamentals and applications", Academic Press, San Diego, CA, 1991.

[60] R. Ram, D. Babic, R. York and J. Bowers, "Spontaneous emission in microcavities with distributed mirros", *IEEE J. Quantum Electron.*, vol. 31(2), pp. 399-410, 1995.

[61] P. Yeh, *"Optical waves in layered media"*, John Wiley and Sons, US, 1988.

[62] M. Rattier, H. Benisty and C. Weisbuch, "Photonic crystal extractor," in *Electromagnetic Crystal Structures: Proceedings of Workshop on Photonic and Electromagnetic Crystal Structures III (PECS3), 9-14 June 2001, St. Andrews, United Kingdom,* T.F. Krauss (Ed.), 2001.

[63] E. F. Schubert, N. E. J. Hunt, R. J. Malik, M. Micovic and D. L. Miller, "Temperature and Modulation Characteristics of Resonant-Cavity light-emitting Diodes", *IEEE J. Lightwave Tech.*, vol. 14(7), pp. 1721-1729, 1996.

[64] K. Tanaka, T. Nakamura, W. Takamatsu, M. Yamanishi, Y. Lee and T. Ishihara, "Cavity-induced Changes of Spontaneous Emission Lifetime in One-Dimensional Semiconductor Cavities", *Phys. Rev. Lett.*, vol. 74(17), pp. 3380-3386, 1995.

[65] R. Bockstaele, T. Coosemans, C. Sys, L. Vanwassenhove, A. Van Hove, B. Dhoedt, I. Moerman, P. Van Daele, R.G. Baets,R. Annen, H. Melchior, J. Hall, P.L. Heremans, M. Brunfaut and J. Van Campenhout, "Realization and characterization of 8×8 resonant cavity LED arrays mounted onto CMOS drivers for POF-based interchip interconnections", *IEEE J. Sel. Top. Quantum Electron.*, vol. 5(2), pp. 224 -235, 1999.

[66] P. Modak, M. D'Hondt, I. Moerman, P. Van Daele, P. Mijlemans and P. Demeester, "5.2% efficiency InAlGaP microcavity LEDs at 640nm on Ge substrates", *Electron. Lett.,* vol. 37(6), pp. 377-378, 2001.

[67] R. Wirth, C. Karnutsch, S. Kugler, S. Thaler and K. Streubel "Red and Orange resonant cavity LEDs", in *Light-Emitting Diodes: Research, Manufacturing, and Applications V, Proc. SPIE,* vol. 4278, 2001.

[68] S. Orsila, T. Leinonen, P. Uusimaa, M. Saarinen, M. Guina, P. Sipila, V. Vilokkinen, P. Melanen, M. Dumitrescu and M. Pessa "Resonant cavity light-emitting diodes grown by solid source MBE," *J. of Crystal Growth,* vol. 227-228, pp. 346-351, 2001.

[69] J.W. Gray, Y.S. Jalili, P.N. Stavrinou, M. Whitehead, G. Parry, A. Joel, R. Robjohn, R. Petrie, S. Hunjan, P. Gong and G. Duggan, "High-efficiency, low voltage resonant-cavity light-emitting diodes operating around 650 nm", *Electron. Lett.,* vol. 36(20), pp. 1730-1731, 2000.

[70] R. Wirth, C. Karnutsch, S. Kugler and K. Streubel "High efficiency resonant cavity LEDs emitting at 650 nm", *IEEE Phot. Tech. Lett.,* vol. 13(5), pp. 421-423, 2001.

[71] R. Bockstaele, J. Derluyn, C. Sys, S. Verstuyft, I. Moerman, P. Van Daele and R. Baets "Realisation of highly efficient 850nm top emitting resonant-cavity light-emitting diodes", *Electron. Lett.,* vol. 35(18), pp. 1564-1565, 1999.

[72] P. Sipila, M. Saarinen,V. Vilokkinen, S. Orsila,P. Melanen, P. Savolainen, M. Toivonen, M. Dumitrescu and M. Pessa "Resonant cavity LEDs at 655 and 880 nm wavelengths", in *Light-Emitting Diodes : Research, Manufacturing, and Applications IV, Proc. SPIE,* vol. 3938, pp. 82-89, 2000.

[73] B. Depreter, I. Moerman, R. Baets, P. Van Daele and P. Demeester, "InP based 1300 nm microcavity LEDs with 9% quantum efficiency", *Electron. Lett.,* vol. 36(15), pp. 1303-1304, 2000.

[74] M. Linnik and A. Christou, "High reflective Bragg Mirrors for VCSEL Application at 1.3 and 1.55 μm", in *Phys. and Sim. of Optoelectr. Devices VIII* , H. Binder, P. Blood, M. Osinski, eds., Proc. SPIE 3944, pp. 874-881, 2000.

[75] M.C.Larson, C.W. Coldren, S.G. Spruytte, H.E. Petersen and J.S. Harris, "Low-threshold oxide-confined GaInNAs long wavelength vertical cavity lasers", *IEEE Phot. Tech. Lett.*, vol. 12(12), pp.1598-1600, 2000.

[76] A. Fiore, U. Oesterle, R.P.Stanley, R. Houdre, F. Lelarge, M.Ilegems, P. Borri, W. Langbein, D.Birkedal,J.M.Hvam, M. Cantoni and F. Bobard, "Structural and electrooptical characteristics of quantum dots emitting at 1.3 μm on gallium arsenide", *IEEE J. Quantum Electron.*, vol. 37(8), pp. 1050-1058, 2001.

[77] B. Depreter, S. Verstuyft, I. Moerman, R. Baets and P. Van Daele "InP-based microcavity light emitting diodes emitting at 1.3μm and 1.55 μm", in *Proc. of the 11th International Conference on InP and related materials (IPRM)*, Davos, Switserland 16-20 may, 1999, pp. 227-230 , 1999.

[78] F. Salomonsson, S. Rapp, K. Streubel, M. Hammar and J. Daleiden, "InP-based 1.55μm Resonant Cavity Light-Emitting Diode with two Epitaxial Mirrors", *Physica Scripta*, T79, pp. 135-137, 1999.

[79] M.G. Salt, P. Andrew and W.L. Barnes, "Microcavities, texture symmetry, and photonic bandgaps", *J. Opt. Soc. Am. B,* vol. 18(20) pp. 240-243, 2001.

[80] S. Fan, P.R. Villeneuve, J.D. Joannopoulos and E.F. Schubert, " High Extraction Efficiency of Spontaneous Emission from Slabs of Photonic Crystals," *Phys. Rev. Lett,* vol. 78(17), pp. 3294-3297, 1997.

[81] W. D. Zhou, J. Sabarinathan, P. Bhattacharya, B. Kochman, E.W. Berg, P.-C. Yu and S.W. Pang, "Charactristics of a Photonic Bandgap Single Defect Microcavity Electroluminescent Device", *IEEE J. Quantum Electron.,* vol. 37(9), pp. 1153-1160, 2001.

[82] S. Fan, P.R. Villeneuve and J.D. Joannopoulos, "Rate-equation analysis of output efficiency and modulation rate of photonic-crystal light-emitting diodes", *IEEE J. Quantum Electron.,* vol. 36(10), pp. 1123-1130, 2000.

[83] A.A. Erchak, D.J. Ripin, S. Fan, P. Rakich, J.D. Joannopoulos, E.P. Ippen, G.S. Petrich and L.A. Kolodziejsk, "Enhanced coupling to vertical radiation using a two-dimensional photonic crystal in a semiconductor light-emitting diode", *Appl. Phys. Lett.,* vol. 78(5), pp. 563-565, 2001.

[84] M. Rattier, *"Diodes électro-luminescentes à cristaux photoniques: extraction de la lumière guidée"*, Ph. D. these, Ecole Polytechnique, Paris, France, 2001.

[85] M. Boroditsky, T.F. Krauss, R. Coccioli, R. Vrijen, R. Bhat and E. Yablonovitch, "Light extraction from optically pumped light-emitting diode by thin-slab photonic crystal", *Appl. Phys. Lett.,* vol. 75(8), pp. 1036-1038, 1999.

3

Diffractive Nanostructures

DIFFRACTIVE nanostructures are gratings with a one-, two- or three-dimensional periodicity in the order of the wavelength of the light. The periodic corrugation may be in the permittivity or in the conductivity of the respective material. These characteristic features give origin to a 'spectrum' of optical properties such as filtering, coupling, beam-shaping, polarising, etc. Besides the evolution in nanotechnology (see Chapter 1), these unique and versatile properties of diffractive optics are a second driving force for the increasing worldwide interest for nanostructures for optical applications.

A third driving force can be found in the improved methods of modelling diffractive structures, leading to a better understanding of their properties and related design. Numerous methods, ranging from rigorous to approximate theories, have been worked out to analyse diffraction by spatially periodic media.

This chapter will touch upon modelling of diffractive nanostructures. The *Wave vector diagram* is presented as a tool to analyse gratings qualitatively. An overview of diffraction modelling tools is given. Comparison of their optimal working field results in the choice of the *RCWA (Rigorous Coupled Wave Theory)* to be used in this work. This model will be detailed.

3.1 Diffractive nanostructures

The peculiar optical behavior of diffractive structures with a multi-dimensional periodicity in the order of the wavelength of the light and large modulation depth of the refractive index has retrieved attention. When the structure is designed appropriately, a *Photonic Band Gap* (PBG) or a range of optical frequencies that can not propagate in the structure can appear. This "*Photonic Crystal*" (PC) -by analogy with the electron states in crystals- can exhibit a full PBG when the refractive index is strongly modulated in the 3 dimensions. However, 3D PCs are no technological milksops: experimental verifications of the full PBG behavior are rather rare. Although they do not exhibit a complete PBG, 1-D PCs (DBR mirror) and 2-D PCs (gratings) are common and their anomalous and intriguing effects expected around the Bragg-condition are fully exploited.

Besides PBGs, scattering of guided waves, in the form of leaky waves, to the outside medium or the reciprocal case of coupling light of an semi-infinite medium into a guided wave are characteristic features from which many applications gain advantage. These effects can be understood qualitatively using graphical tools such as the *wave vector diagram* (WVD), defining the locus of allowed wave vectors at a fixed optical frequency in k-space, and the *Brillouin diagram* (BD), defining the dispersion relation ($\omega(k)$) of allowed optical modes.

3.1.1 Isotropic media

In an isotropic medium with refractive index n_1, a linearly polarised (TE or TM) electromagnetic plane wave $\mathbf{E}_1$ can be represented by (without loss of generality the xyz co-ordinate system can be chosen such that the wave vector lies in the x-z plane; the structure is y-invariant):

$$\mathbf{E}_1 = \mathbf{E}_{1o}\, e^{-j(k_x x \pm k_z z)+j\omega t} \tag{3.1}$$

with:

$$k_z = \sqrt{k_0^2 n_1^2 - k_x^2} \tag{3.2}$$

the wave vector component normal to the interface, $k_0 = \omega/c$ the vacuum wave vector at optical frequency $\omega/2\pi$. Plotting the allowed wave vectors according to (3.2) results in a circle of radius $k_0 n_1 = 2\pi n_1/\lambda$ in the $k_x - k_z$ plane.

Visualisation in the WVD of reflection and refraction at the interface of 2 media n_1 and n_2 of a plane wave reflects the phase-matching condition or momentum conservation along the interface: $k_{1\,x} = k_{2\,x} = k_x$. Three cases can be considered:

(i) $0 < k_x < k_0 n_2$ light can propagate in both regions, reflection and refraction occurs;

(ii) $k_0 n_2 < k_x < k_0 n_1$ light can only propagate in the high index medium and is evanescent in the low index material, total internal reflection occurs. Evanescent coupling through a thin low index medium is possible;

(iii) $k_0 n_1 < k_x$ light can not propagate in neither medium, the light is evanescent in both media.

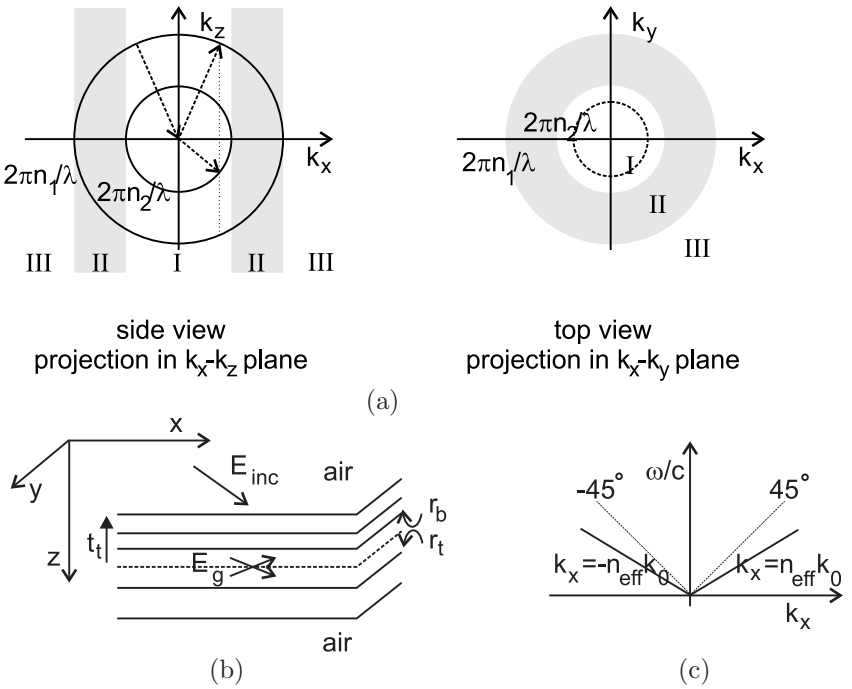

Fig. 3.1: (a) WVD representation of reflection and refraction of a plane wave, marked with the dotted line, with optical frequency ω incident from an isotropic medium n_1 on an isotropic medium n_2 and vice-versa ($n_2 < n_1$).(b) Schematic presentation of an x- and y-invariant multi-layer; (c) sketch of generic dispersion relation in BD of lowest order mode of a multi-layer. The 45°-line presents the lightline.

The dispersion relation of optical modes in a multi-layer, can be found considering the resonant condition (see Chapter 2, Eq.(2.21)) for self-consistency:

$$(1 - r_b(k_x, \omega) r_t(k_x, \omega))\mathbf{E_g} = t_t(k_x, \omega)\mathbf{E}_{inc} \tag{3.3}$$

with $r_b(k_x, \omega)$,$r_t(k_x, \omega)$ the reflection coefficients of the layer stack under and above the (virtual) interface g respectively, $t_t(k_x, \omega)$ the transmission coefficient of the top layer stack (see Fig. 3.1(b)). In the absence of an incident wave from an exterior region, $\mathbf{E}_{inc} = 0$, the first left-side term of the equation has to vanish in order to have a unique solution. Solving the transcendental equation $(1 - r_b(k_x, \omega) r_t(k_x, \omega)) = 0$ graphically or numerically will yield the unknown k_x at an optical frequency ω. For this k_x and ω, k_z is defined by Eq.(3.2), the local dispersion relation. The real part of the solution k_x is called the propagation constant β. A generic dispersion relation of the lowest order in a multi-layer is depicted in Fig. 3.1(c). The dispersion relation associates an effective refractive index n_{eff} with the guided mode. This effective index is, in plain words, the average index felt by the mode. A propagative guided mode in a multi-layer surrounded by air will have an $n_{eff} > 1$ and its dispersion line falls under the 45°

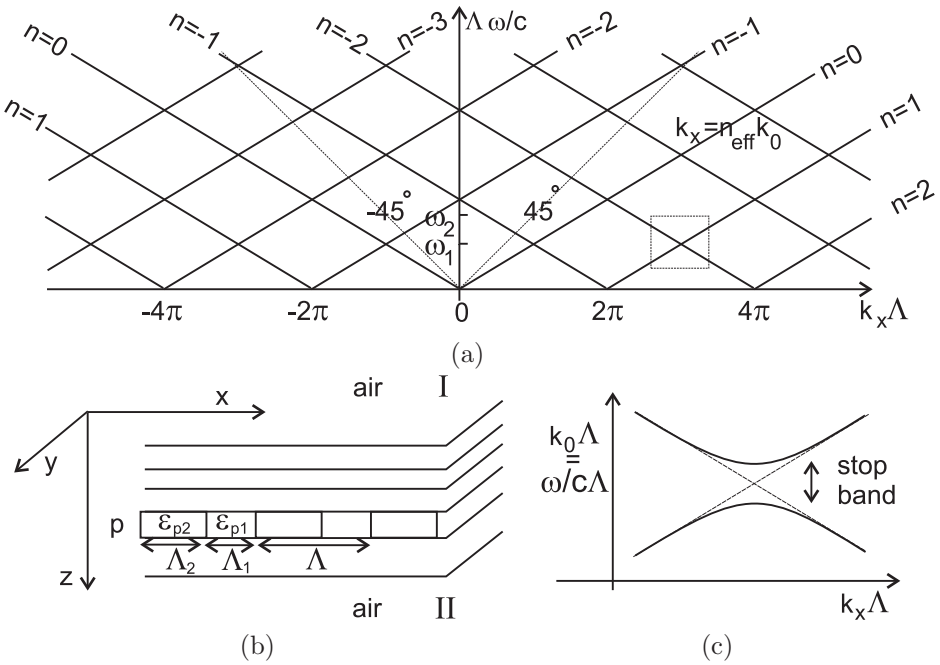

Fig. 3.2: (a) Generic dispersion relation in BD of lowest order mode ($k_y = 0$ and dotted $45°$-line is the lightline) in (b) multi-layered periodic grating with period Λ. (c) Detail of dispersion relation in BD of (a): contra-directional mode coupling results in a band gap.

lightline ($k_x = k_0$). The mode is then evanescent in the surrounding air media. If the dispersion curve is situated above this lightline, or equivalently if $k_x < k_0$, light will leak to the outside medium. The light is propagative in the surrounding air media.

3.1.2 Periodic Corrugated media

Optical behavior of waves in a periodic structure can significantly be described by a representation commonly referred to as the Floquet Theorem [1]. A layered structure with uniaxial periodicity[1] Λ along the x-axis is shown in Fig. 3.2(b). The average permittivity of the grating layer $\varepsilon_p = (\varepsilon_{p1}\Lambda_1 + \varepsilon_{p2}\Lambda_2)/\Lambda$ is the permittivity of the corresponding layer in Fig. 3.1(b). The wave vector of the incident field lies in the x-z plane ($k_y = 0$). The theorem states that the cross-sectional complex field distribution remains unchanged under an axial translation of the observation point over a period Λ, while the mode amplitude multiplies itself by a complex constant $\exp(-jk_{x0}\Lambda)$.

$$\mathbf{E}(x + \Lambda, y, z) = e^{-jk_{x0}\Lambda}\mathbf{E}(x, y, z) \tag{3.4}$$

[1]For sake of simplicity, the theorem is given for uniaxial periodicity, implementation for a multi-dimensional periodicity is straightforward.

Defining $\mathbf{P}(x, y, z)$ as:

$$\mathbf{E}(x, y, z) = e^{-jk_{x0}x}\mathbf{P}(x, y, z) \tag{3.5}$$

from (3.4) it is clear that $\mathbf{P}(x, y, z)$ is a periodic function, which may be expanded in a Fourier series:

$$\mathbf{P}(x + \Lambda, y, z) = \mathbf{P}(x, y, z) = \sum_{n=-\infty}^{+\infty} a_n(y, z)e^{-jn\frac{2\pi}{\Lambda}x} \tag{3.6}$$

or the field can be described in terms of an infinite set of interfering spectral plane waves chosen such that the resulting fringe pattern has a fundamental frequency Λ:

$$\mathbf{E}(x, y, z) = \sum_{n=-\infty}^{+\infty} a_n(y, z)e^{-jk_{xn}x} \tag{3.7a}$$

$$k_{xn} = k_{x0} + n\frac{2\pi}{\Lambda} \tag{3.7b}$$

From (3.7b), it is clear that the dispersion relation of the uniaxially periodic structure repeats in k_x over $2\pi/\Lambda$, giving evidence of the inevitable simultaneous presence of the fundamental and higher order space harmonics. Fig. 3.2(a) represents the BD in the limit of vanishing modulation ($\varepsilon_{p1} \to \varepsilon_{p2}$). Inspection of this graph reveals that the $k_0\Lambda - k_x\Lambda$ diagram is divided into Brillouin zones. the first zone extends from $-\pi < k_x\Lambda < \pi$. Other zones are obtained by translation of the first zone through an integral multiple of 2π. For a given value of $k_0\Lambda = \omega/c\Lambda$ the corresponding points of a dispersion curve in each zone represent the values of $k_{xn}\Lambda$ of the various spatial harmonics. The slope at the dispersion curves at the corresponding points are the same (group velocity, see below), but the phase velocity ω/k_{xn} differs.

Starting from these curves of an infinitesimal periodic corrugation, a qualitative form of the dispersion relation of realistic periodic structures can be obtained when mode coupling is considered (Fig. 3.2(c)). For modes with contra-directional group velocities, mode coupling results in band gaps. For a given ω/c for which a band gap occurs, the propagation constant k_x is complex and the mode is attenuated away from the feed.

The exact shape will depend on the modulation strength and the grating form, and is found by applying the boundary conditions on Maxwell's solutions in each layer, with zero incident fields in the semi-infinite bounding layers. As in the isotropic layered structure (Eq.(3.3)), the resonance condition for self-consistence has to be solved, in the absence of an exterior field. The equation holds the resonant condition that a wave remains unchanged after a round-trip travel across the layers, the trip including one reflection at each of the two boundaries. Due to energy coupling between the fundamental and the higher order space harmonics, a determinantal matrix equation has to be solved:

$$\det\left[\mathbf{I} - \mathbf{R}_t(k_{x0}, \omega)\mathbf{R}_b(k_{x0}, \omega)\right] = 0 \tag{3.8}$$

with $\mathbf{I}$ the diagonal unity matrix, $\mathbf{R}_t(k_{x0},\omega)$,$\mathbf{R}_b(k_{x0},\omega)$ the respective top and bottom reflection matrices (see section 3.2). The roots of the transcendental equation yield the unknown imaginary k_{x0} at optical frequency ω, and according to (3.7b) all $k_{x\mathrm{n}}$, $n \in \mathbb{Z}$. The local dispersion relation (cf. Eq.(3.2)) will then define k_z in every layer n_i ($k_{y\mathrm{n}} = 0$ in our 2-D analysis):

$$k_{z\mathrm{n}} = \sqrt{k_0^2 n_i^2 - k_{x\mathrm{n}}^2 - k_{y\mathrm{n}}^2} \tag{3.9}$$

Besides producing band gaps, the presence of a periodicity may convert guided waves into leaky waves: higher order space harmonics are phase matched to modes in the surrounding media I and/or II of Fig. 3.2(b). In Fig. 3.2(a), this is manifested by the dispersion curve of higher order space harmonics lying above the lightline ($k_0\Lambda/k_x\Lambda = 1$), in case leakage towards vacuum is considered[2]. The coupling efficiency manifests itself in the imaginary part of $k_{x\mathrm{n}}$ (not shown in the figures).

The WVD of Fig. 3.3 confirms the presence of a band gap and of leaky waves at the respective working points ω_1 and ω_2 marked in the BD of Fig. 3.2(a). The allowed propagation constant $\beta = \mathrm{Re}(k_x, k_y)$ is shown in the WVD at the respective optical frequencies. The WVD is symmetric in k_y due to the y-invariant multi-layer, periodic in k_x due to the Floquet-Bloch Theorem, and symmetric in k_x, since for every value of k_x there is a value $-k_x$ corresponding to a Bloch wave progressing in the opposite direction. For an optical frequency ω_1, the projection of the dispersion curve in the $k_x - k_y$-plane opens in the x-direction, giving evidence of a band gap in the x-direction. When $\omega = \omega_2$, the projection of the dispersion curve overlaps the projection of the extraction cone ($k_x^2 + k_y^2 < k_0^2$). The light is phase-matched with optical modes in the surrounding vacuum, power can be coupled from the multi-layer to the surrounding medium and vice versa.

In general, we can predict what waves will be excited in the periodic structure for an arbitrary incident wave, by superimposing the diagrams of the incident medium and the periodic structure. Requiring that the wave vector components tangential to the local boundary are conserved, reveals the set of travelling waves in both media.

The in-plane direction in which the light proceeds, is then given by the normal to the wave vector surfaces pointing in the direction of increasing frequency, via the definition of the group velocity $\mathbf{v}_g$ [2]:

$$\mathbf{v}_g = \nabla_k \omega(\mathbf{k}) \tag{3.10}$$

The slope of the dispersion relation in the BD defines $|\mathbf{v}_g|$. The slope at the band gap edges of the WVD in Fig. 3.3(a) implies that the x-component of $\mathbf{v}_g$ vanishes: photons can not travel within the band gap along the x-direction.

[2]If the surrounding media are not air, the lightline is defined by $k_0\Lambda/k_x\Lambda = 1/n$, with n the refractive index of the surrounding media.

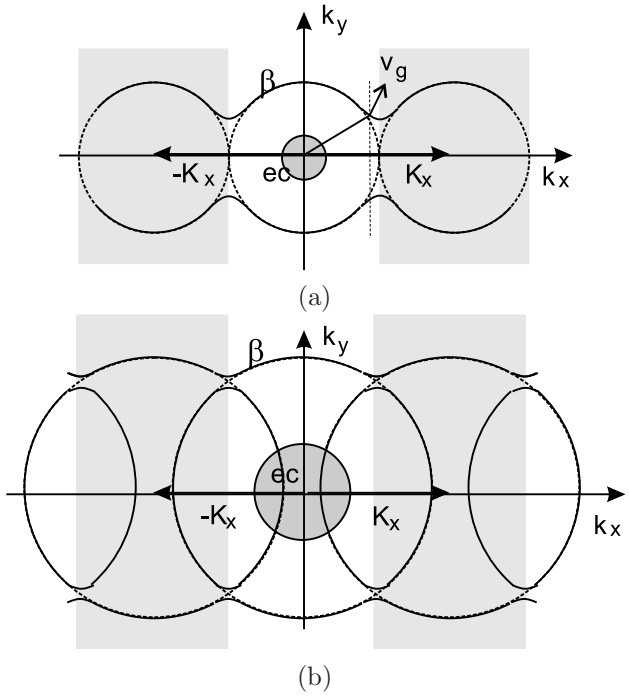

Fig. 3.3: WVD of the multi-layer in Fig. 3.2. The left and right shaded regions are higher order Brillouin zones which are exact replicas of the first zone. (a) optical frequency ω_1: band gap; (b) optical frequency ω_2: leaky wave in extraction cone (ec). The extraction cone corresponds with the lightline in the BD, and is in fact the WVD of the optical modes in surrounding air media.

The WVD generalises very nicely to 2-dimensional (2-D) periodic structures. An example of how it looks for a square lattice is given in Fig. 3.4 [2].

It is clear that a quantitative treatment of periodic nanostructures needs the solution of a transcendental equation, which is, in comparison with the scalar equation of isotropic layered media, more complex because it involves an infinite determinant. Numerical solution is based on the calculation of the respective reflection matrices. Calculation of these matrices is given hereinafter.

The WVD can serve excellently as analysing tool for the qualitative behavior of periodic structures. The GA-RCLED is analysed qualitatively with the WVD in Chapter 4. In this application, the extraction of a guided mode is of primary concern. The extraction of a guided mode by means of a 1-D grating is sketched in Fig. 3.5. The guided mode can be extracted through first (e-h) or higher order (i-j) transmission. In the latter case, other diffracted orders are reflected towards the substrate. The loss of these modes can be countered by placing a mirror under the waveguide. The WVD of the GA-RCLED will be more detailed in Chapter 4.

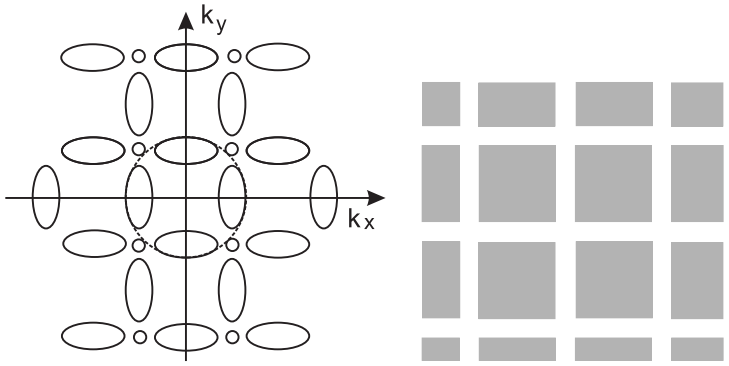

Fig. 3.4: (a) WVD for square lattice depicted in (b) [2].

3.2 Modelling of diffractive structures

3.2.1 General grating diffraction problem

The general grating diffraction problem is depicted in Fig. 3.6. For commodity, the space is separated into three regions: two homogeneous semi-infinite regions I and II characterised by a relative permittivity ε_1 and ε_2, respectively, and an inhomogeneous region which includes the relative permittivity periodic modulation. Magnetic effects are not considered. μ_0 denotes the magnetic permeability of all media. Without any loss of generality, $\mathbf{1}_z$ is chosen to be normal to the boundary and $\mathbf{1}_x$ along one of the two periodic directions. A linearly polarised electromagnetic wave of wavelength λ_0 in vacuum ($k_0 = 2\pi/\lambda_0 = \omega/c$) is obliquely incident at an arbitrary polar angle θ and at an azimuthal angle φ upon a two-dimensional multi-level and/or surface-relief dielectric or lossy grating. The incident normalised electric-field vector is a solution of Maxwell's equations in an infinite homogeneous region with permittivity ε_1 and can thus be represented by a plane wave (temporal dependence $\exp(j\omega t)$ is assumed):

$$\mathbf{E}_{inc} = e^{-j\mathbf{k}_{inc}\cdot\mathbf{r}}\,\mathbf{1}_e \tag{3.11}$$

with

$$\begin{aligned}\mathbf{k}_{inc} &= k_1(\sin\theta\cos\varphi\,\mathbf{1}_x + \sin\theta\sin\varphi\,\mathbf{1}_y + \cos\theta\,\mathbf{1}_z)\\ &= k_{inc,x}\,\mathbf{1}_x + k_{inc,y}\,\mathbf{1}_y + k_{inc,z}\,\mathbf{1}_z\end{aligned} \tag{3.12}$$

$k_1 = k_0\sqrt{\varepsilon_1}$ and $\mathbf{1}_e$ is the unit polarisation vector given by

$$\begin{aligned}\mathbf{1}_e \;=\; &(\cos\xi\cos\theta\cos\varphi - \sin\xi\sin\varphi)\mathbf{1}_x\\ &+(\cos\xi\cos\theta\sin\varphi + \sin\xi\cos\varphi)\mathbf{1}_y\\ &-(\cos\xi\sin\theta)\mathbf{1}_z\end{aligned} \tag{3.13}$$

ξ is the angle between the polarisation vector $\mathbf{1}_e$ and the plane of incidence. For $\xi = 0°$ and $\xi = 90°$, the magnetic field and electric field, respectively, are perpendicular

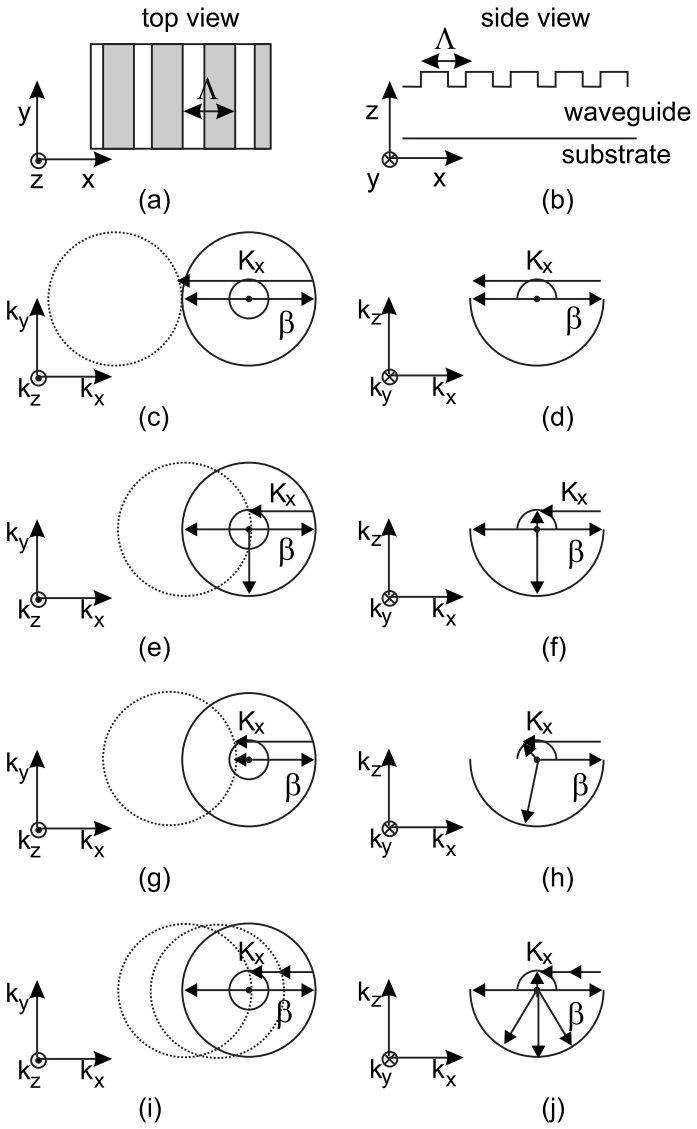

Fig. 3.5: Extraction of guided light by means of a 1-D grating. Left hand side is top view representation, right hand side is side view representation. The dotted circles in the WVD are the higher positive order space harmonics of the guided mode with propagation constant β. The extraction cone is the smaller circle. (a)-(b) Schematic presentation of 1-D grating; (c)-(d) The guided mode is reflected by a first order reflection (cf. standard DBR laser); (e)-(f) the guided mode is reflected by a second order reflection, the first order is reflected towards the substrate and transmitted towards superstrate; (g)-(h) reflection can be suppressed by the lattice of the grating; (i)-(j) the second order can be extracted, the other orders are reflected towards the substrate or the backward propagating mode.

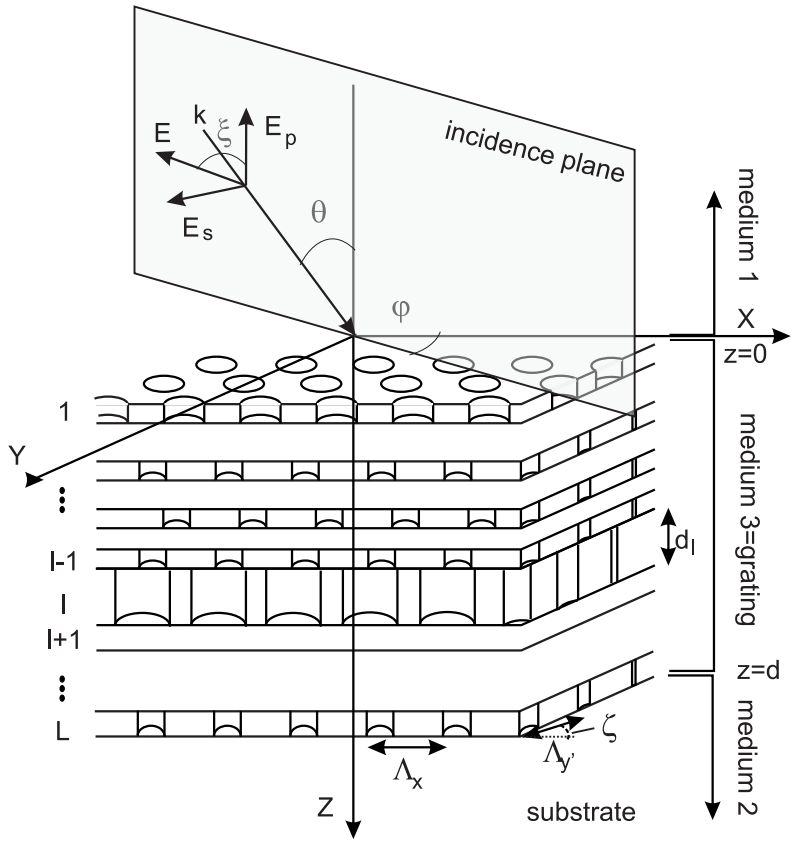

Fig. 3.6: Diffraction problem.

to the plane of incidence corresponding to TM and TE polarisation. The grating is described by a periodic function $\varepsilon(x,y,z) = \varepsilon(x,y',z) = \varepsilon(x+n\Lambda_x, y'+m\Lambda_{y'}, z)$, n,m integers, $\mathbf{1}_x$ and $\mathbf{1}_{y'}$ the unit vectors of the periodicity and $\mathbf{1}_{y'} = \sin\zeta\mathbf{1}_x + \cos\zeta\mathbf{1}_y$. The periodic relative (complex) permittivity can thus be expanded in a Fourier Series:

$$\varepsilon(x,y,z) = \sum_{m,n} \varepsilon_{mn}(z) e^{j\,\mathbf{K}_{mn}\cdot\mathbf{r}} \tag{3.14}$$

where $\varepsilon_{mn}(z)$ is the $(m,n)^{\text{th}}$ Fourier component of the complex relative permittivity in the grating region, a function of z. $\mathbf{K}_{mn}$ is defined as:

$$\begin{aligned} \mathbf{K}_{mn} &= m\,K_x\,\mathbf{1}_x + n\,K_{y'}\,\mathbf{1}_{y'} \\ &= (m\,K_x + n\,K_{y'}\,\sin\zeta)\mathbf{1}_x + n\,K_{y'}\,\cos\zeta\,\mathbf{1}_y \end{aligned} \tag{3.15}$$

where $K_x = 2\pi/\Lambda_x$ and $K_{y'} = 2\pi/\Lambda_{y'}$ are the respective grating vectors.

Invoking the Floquet theorem, the field in the homogeneous media I and II can

be written in terms of a plane-wave expansion, called *Rayleigh expansion*:

$$\mathbf{E}_1 = \mathbf{E}_{inc} + \sum_{m,n} \mathbf{R}_{mn} e^{-j\mathbf{k}_{1mn}\cdot\mathbf{r}} \tag{3.16a}$$

$$\mathbf{E}_2 = \sum_{m,n} \mathbf{T}_{mn} e^{-j\mathbf{k}_{2mn}\cdot(\mathbf{r}-\mathbf{d})} \tag{3.16b}$$

$\mathbf{R}_{mn}$ is the normalised electric field vector of the $(m,n)^{\text{th}}$ backward diffracted (reflected) wave in region 1 with wave vector $\mathbf{k}_{1mn}$ and $\mathbf{T}_{mn}$ is the normalised electric field vector of the $(m,n)^{\text{th}}$ forward diffracted (transmitted) wave in region 2 with wave vector $\mathbf{k}_{2mn}$.

$$\begin{aligned}\mathbf{k}_{1mn} &= k_{inc,x}\,\mathbf{1}_x + k_{inc,y}\,\mathbf{1}_y - \mathbf{K}_{mn} - k_{1,z,mn}\,\mathbf{1}_z \\ &= k_{x,mn}\,\mathbf{1}_x + k_{y,mn}\,\mathbf{1}_y - k_{1,z,mn}\,\mathbf{1}_z\end{aligned} \tag{3.17a}$$

$$\begin{aligned}\mathbf{k}_{2mn} &= k_{inc,x}\,\mathbf{1}_x + k_{inc,y}\,\mathbf{1}_y - \mathbf{K}_{mn} + k_{2,z,mn}\,\mathbf{1}_z \\ &= k_{x,mn}\,\mathbf{1}_x + k_{y,mn}\,\mathbf{1}_y + k_{2,z,mn}\,\mathbf{1}_z\end{aligned} \tag{3.17b}$$

where

$$k_{i,z,mn} = \begin{cases} +\left[(k_0 n_i)^2 - k_{x,mn}^2 - k_{y,mn}^2\right]^{1/2} & k_0 n_i > \left(k_{x,mn}^2 + k_{y,mn}^2\right)^{1/2} \\ -j\left[k_{x,mn}^2 + k_{y,mn}^2 - (k_0 n_i)^2\right]^{1/2} & k_0 n_i < \left(k_{x,mn}^2 + k_{y,mn}^2\right)^{1/2} \end{cases} \tag{3.18}$$

with $i = 1, 2$. Solving the diffraction problem means determining the complex amplitudes of the reflected and transmitted waves $\mathbf{R}_{mn}$ and $\mathbf{T}_{mn}$. This unique solution is achieved by imposing Maxwell's boundary conditions to the field in the grating region and the outer fields at the interfaces $z = 0$ and $z = d$. The choice of the field representation in the modulated region is primordial and characteristic for the chosen method of analysing the diffractive behavior. The magnetic fields are obtained with Maxwell's curl equation $\nabla \times \mathbf{E} = -j\omega\mu_0\mathbf{H}$. We obtain for the incident, reflected magnetic field and transmitted magnetic field:

$$\mathbf{H}_1 = -(\omega\mu_0)^{-1}\mathbf{k}_{inc} \times e^{-j\mathbf{k}_{inc}\cdot\mathbf{r}}\,\mathbf{1}_e - (\omega\mu_0)^{-1}\sum_{m,n}\mathbf{k}_{1mn} \times \mathbf{R}_{mn} e^{-j\mathbf{k}_{1mn}\cdot\mathbf{r}} \tag{3.19a}$$

$$\mathbf{H}_2 = -(\omega\mu_0)^{-1}\sum_{m,n}\mathbf{k}_{2mn} \times \mathbf{T}_{mn} e^{-j\mathbf{k}_{2mn}\cdot(\mathbf{r}-\mathbf{d})} \tag{3.19b}$$

To analyse diffraction from a multi-layered and/or surface-relief grating structure[3], both an appropriate grating model that solves the monolayer and/or binary grating problem and an appropriate algorithm for wave propagation and scattering in layered systems have to be chosen. Independently of the underlying theoretical

[3]Multi-layered gratings are characterised by multiple interfaces. A surface-relief grating only has a single periodically corrugated interface, but some grating models approximate this profile by a stack of sufficiently thin binary grating slabs, which is numerically handled as a multi-layered structure. This approximation will also be used in this work (see section 3.3).

grating method, solving the boundary-condition equations for the multi-layer can cause numerical instabilities due to the presence of exponential functions in the spatial variable in the direction of the layer stack. Operations on these growing exponential functions by a computer of finite precision can result in instabilities due to the loss of significant digits. The most common algorithms are the recursive R-matrix and S-matrix algorithms [3]. Moharam *et al.* [5] use an efficient and stable "enhanced transmission matrix approach", that will be used in this work. It is important to distinguish this multi-layer-algorithm from the grating model when evaluating and comparing diffraction theories.

The most common theoretical methods to analyse binary diffraction gratings treat the problem in the frequency domain, i.e. the time variation of the electromagnetic field is not considered [4]. General rigorous models are the differential coupled wave approach [5, 6, 7, 8, 9] and the differential modal approach [10, 11]. Both of these approaches can produce exact formulations without approximations in the frequency domain. In their full rigorous forms these formulations are completely equivalent [12]. General rigorous theories can be reduced to various approximate theories in the appropriate limits when a series of fundamental assumptions are made. An overview of the principally used models will be given in the following section. This overview does not pretend to be complete and restricts itself to cite main characteristics and validity regions of the respective methods. An overall preferred single method to analyse all binary grating diffraction problems does not exist. Each method has its preferred application field, for which the method shows mathematical simplicity, acceptable convergence rate and computation time, etc. The *Rigorous Coupled Wave Analysis* (*RCWA*), will be enlightened in greater detail in 3.3, as this is the method used in this work. The choice for this model is plural:

(i) Regarding the features of the diffractive gratings that are used in the applications studied in this work, the validity regions of approximate theories do not coincide with the working parameters (see 3.2.2.3). A Rigorous theory has to be used.

(ii) The somewhat more complex rigorous modal theory, both to implement as for physical insight, makes the RCWA preferential for implementation and use. The crenellated cross-section shape of the RIE-etched gratings used in this work results in a derivative of the profile equal to zero everywhere but in a finite number of points where the derivative becomes infinity. This makes the RCWA preferential to the rigorous Chandezon method (see 3.2.2.1).

(iii) Last but not least, at INTEC, a program RODIS [13] based on the RCWA was implemented to simulate diffraction of lossy 1-D gratings. This code has served as starting block for the software implemented in this work.

[4] Time domain approaches, e.g. the finite-difference time-domain (FDTD) method [4], increasingly attract attention of the electromagnetic research community for specific diffraction problems as photonic bandgap calculations, finite extent gratings, etc.

3.2.2 Overview of diffraction modelling tools

3.2.2.1 Integral or differential method?

The rigorous computation of electromagnetic diffraction by a grating resides on the resolution of partial differential equations with suitable boundary conditions. It is possible to transform them to a system of coupled linear integral equations (integral method) [14] or to solve these differential equations directly (differential method). Different methods for direct solution of the differential equations can be considered: finite-difference methods [15], the coupled wave and modal approach using a state variable method for the numerical solution, coordinate transformation methods of which the *Chandezon* (C) method is the most popular [16] and the recursive boundary variation method [17].

Integral methods are better suited to analyse gratings with continuous profiles, whereas differential methods are more appropriate for the analysis of discrete level profiles. Moreover, numerical implementation of integral methods tends to be more involved. The finite-difference methods are very appropriate for aperiodic finite structures (computational space can be restricted by incorporating absorbing boundaries), and can compete with RCWA in the case of highly conducting infinite periodic metallic gratings [18]. The appealing simplicity and non-iterative character of the coupled wave, modal and Chandezon methods make them preferential diffraction analysing tools. Of these three, the Chandezon method is preferred when the derivative of the grating profile is continuous and small [19]. The latter makes a transformation of the coordinates in a way that the surface profile becomes flat. Instead of having a simple wave equation and complicated boundaries, the C-method has simple boundaries but a complicate wave equation.

3.2.2.2 Rigorous coupled wave or modal approach?

The RCWA for binary diffractive gratings and the rigorous *Modal Method by Modal Expansion* (*MMME*) equivalently describe diffraction by periodically corrugated media. Their difference resides within the alternative representation of the electromagnetic field in the binary grating region. Their rigorous nature can be found in the strict solution of the electromagnetic-boundary-value problem: a solution has to be found that strictly satisfies Maxwell's equations in the input, grating and output region and that fulfills the boundary conditions for the tangential electric- and magnetic field components at the respective interfaces. The accuracy of the obtained solution of both methods solely depend on the number of terms retained in their respective field expansions.

The MMME chooses to represent the field inside the grating as a weighted sum of independent "modes", each satisfying Maxwell's equations. These exact eigenfunctions of the grating are similar to modes in a waveguide. They may be either evanescent or propagating, either forward or backward. The boundary conditions can be fulfilled for a weighted summation over the modes; the individual modes, however, do not fulfill these conditions. This is clear considering an incident plane wave: to realise continuity of the tangential components at the respective interfaces, a lot of modes will be exited. Substituting the modal field

expansion in Maxwell's equation for the grating region, will result in the modal equation. Solving this equation leads to the dispersion relation of the individual modes. Although this method has been shown to converge more rapidly than the RCWA, efficient numerical methods to solve the boundary-value problem are known for only a few periodical modulations of the grating. This limits the range of applications of the MMME.

The RCWA on the contrary, expands the field inside the grating in terms of plane waves. The total field is a weighted sum of inhomogeneous coupled plane waves. The individual plane waves are phase matched to the respective diffracted waves of the Rayleigh expansion of the field outside the grating. The individual plane waves do not satisfy Maxwell's equations. The waves are not independent and couple back and forth between each other. Intuitively, this can be seen as follows: the terms of the Rayleigh expansion in the input and output region are phase matched with corresponding plane waves at the respective interfaces. The RCWA will be detailed in section 3.3.

3.2.2.3 Approximate diffraction theories

The computationally demanding rigorous methods can obstruct optimal design of diffraction gratings and their applications. Moreover some nanostructures can not be solved properly with exact numerical methods. Depending on the operating point, assumptions and approximations can be made, leading to a simplification of the model. The model can only be used in a finite parameter space around this operating point. In some limits, the simplification can result in an analytical solvable problem.

- Rayleigh Method: Lord Rayleigh introduced a first approach at the beginning of the 20^{th} century for reflection gratings [20]. It hypothesizes that the Rayleigh expansion, valid in the two homogeneous regions I and II (Eq.(3.16)), is also valid inside the modulated region. During almost 60 years no contradiction to this approach has been found. With the introduction of modern numerical computation tools, failure of the method has been proven, especially for deep grating structures [21]. Coupling between the respective diffraction orders can not be neglected and the field expansion in the modulated region has to be based on the wave equations.

- Two-Wave Theory: This theory starts from a rigorous model but retains only the zero- and first-order waves in the expansion. This results actually in four waves as there are two more waves phase matched to these two. This approximation can be valid near Bragg incidence in reflection gratings (backward diffracted waves dominate) [6].

- Scalar diffraction theory: ignoring the vectorial character of light can be valid when the smallest feature size of the diffractive element is much larger than the wavelength of the incident light. Scalar reflection and transmission coefficients can then be derived using ray optics [22]. A scalar diffraction analysis and the RCWA has been compared for 2-D gratings in [23]. It was quantitatively determined that the error of the scalar analysis increases as the

feature size decreases and as the period-to-wavelength ratio decreases. The scalar analysis is accurate within ±5% for a minimum period-to-wavelength ratio of 10.

- Transmission Theory: the grating behavior can be described by a transmission (reflection) function relating the fields at both sides of the grating. The validity region has been marked out in [13] for a GaAs-air grating: the transmission theory can be used for large grating periods ($\Lambda/\lambda > 2$) and small refractive index contrasts.

- Effective-Medium Theory (EMT): subwavelength gratings with a small period-to-wavelength ratio do not diffract light in the farfield. Only the zeroth reflected and transmitted order are excited, similar to reflection at and propagation through a homogeneous layer. This similarity is exploited: the grating is modelled as an effective homogeneous medium of which the parameters are linked to the parameters of the subwavelength grating [24, 25]. The region of validity is restricted to gratings with small period-to-wavelength ratio in which case the tangential fields may be considered uniform over the alternating media of the grating. Other restrictions (dimensionality of grating, depth, angle of incidence, etc.) can be under discussion depending on the used EMT solution of the effective index.

3.3 Rigorous Coupled Wave Analysis

RCWA was first formulated by Moharam and Gaylord for planar 1-D gratings with principal plane incidence [6, 7] and was subsequently extended to surface relief gratings [8]. A stable and efficient implementation has been proposed for 1-D surface relief gratings, both dealing with principal plane and conical incidence [5, 9]. The slow convergence of the solution when a conducting grating is illuminated with a transverse magnetic (TM) polarised wave has been solved by *Li* [26] and *Lalanne* et al. [27].

Diffraction of principal plane incident and conical incident light on (lossy) surface-relief 1-D gratings has been implemented by B. Dhoedt and the reader is referred to [13] for further detail. This code has been changed with a minor, but important adaptation to enhance convergence in the case of TM polarisation of the incident field.

Diffraction on (lossy) 2-D gratings has been implemented in the framework of this these and will be detailed here.

3.3.1 Slicing of the two-dimensional periodic structure

The first step, common to all modal and wave approaches, is to remove the z dependency of the permittivity function $\varepsilon(x, y, z)$. The complex periodic surface profile can be approximated to an arbitrary degree of accuracy by slicing the surface relief structure into a stack of lamellar layers (Fig. 3.7). The periodic relative permittivity associated with each layer is expandable in a Fourier series.

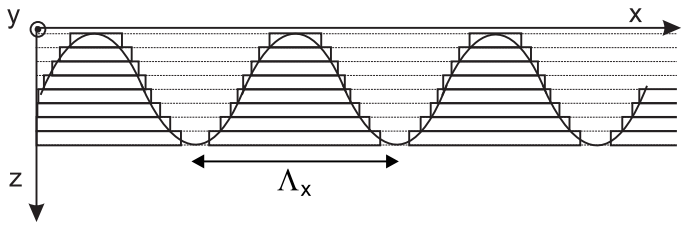

Fig. 3.7: Slicing of a surface relief grating into a stack of lamellar layers.

The Fourier components of the complex relative permittivity are constant inside each thin binary grating layer l with thickness d_l:

$$\begin{aligned} \varepsilon_l(x,y) &= \sum_{m,n} \varepsilon_{l,mn} \exp\left(j\,\mathbf{K}_{mn}\cdot\mathbf{r}\right) \\ \text{with } D_l - d_l < z < D_l &= \sum_{p=1}^{l} d_p \end{aligned} \tag{3.20}$$

where $\varepsilon_{l,mn}$ is the $(m,n)^{\text{th}}$ Fourier component of the relative permittivity of the grating layer l:

$$\varepsilon_{l,mn} = \frac{1}{\Lambda_x \Lambda_{y'}} \int_0^{\Lambda_x} dx \int_0^{\Lambda_{y'}} dy' \varepsilon_l(x,y') e^{j(mK_x x + nK_{y'} y')} \tag{3.21}$$

The diffraction problem of the multi-layer is solved in a sequence of steps. First, the coupled-wave equations are constructed and solved for the electromagnetic fields in each grating layer. Secondly, the electromagnetic boundary conditions (continuity of the tangential electric- and magnetic-field components) are applied between the input region and the first grating layer, then between the first and the second layers, and so forth, and finally between the last grating layer and the output region. Third, the resulting array of boundary-condition equations is solved for the reflected and transmitted diffracted field amplitudes, and the diffraction efficiencies are determined. These steps are discussed in the sections below.

3.3.2 Construction of the coupled-wave equations

In region I, the incident normalised electric field is given by Eq.(3.11) and the normalised solutions in region I and II respectively by Eq.(3.16a) and Eq.(3.16b). In the modulated layer l, the electric and magnetic field vectors, $\mathbf{E}_{l,g}$ and $\mathbf{H}_{l,g}$, may be expressed as a Fourier expansion in terms of the space harmonic fields as:

$$\mathbf{E}_{l,g} = \sum_{m,n} \left[S_{l,x,mn}(z)\mathbf{1}_x + S_{l,y,mn}(z)\mathbf{1}_y + S_{l,z,mn}(z)\mathbf{1}_z \right] e^{-j(k_{x,mn}x + k_{y,mn}y)} \tag{3.22a}$$

$$\mathbf{H}_{l,g} = -j\sqrt{\frac{\varepsilon_0}{\mu_0}}\sum_{m,n}\left[U_{l,x,mn}(z)\mathbf{1}_x + U_{l,y,mn}(z)\mathbf{1}_y + U_{l,z,mn}(z)\mathbf{1}_z\right]e^{-j(k_{x,mn}x+k_{y,mn}y)} \tag{3.22b}$$

$S_{l,i,mn}(z)$ and $U_{l,i,mn}(z)$ $(i = x, y, z)$ are the normalised vector amplitudes of the $(m,n)^{\text{th}}$ space-harmonic fields such that $\mathbf{E}_{l,g}$ and $\mathbf{H}_{l,g}$ satisfy Maxwell's equations in the grating layer l:

$$\begin{aligned}\nabla \times \mathbf{E}_{l,g} &= -j\omega\mu_0\mathbf{H}_{l,g}\\ \nabla \times \mathbf{H}_{l,g} &= j\omega\varepsilon_0\varepsilon_l(x,y)\mathbf{E}_{l,g}\end{aligned} \tag{3.23}$$

Eliminating the z-component of $\mathbf{E}$ and $\mathbf{H}$ yields:

$$\frac{\partial}{\partial z}E_{l,g,x} = -j\omega\mu_0 H_{l,g,y} + \frac{\partial}{\partial x}\left[(j\omega\varepsilon_0\varepsilon_l)^{-1}\left(\frac{\partial}{\partial x}H_{l,g,y} - \frac{\partial}{\partial y}H_{l,g,x}\right)\right] \tag{3.24a}$$

$$\frac{\partial}{\partial z}E_{l,g,y} = j\omega\mu_0 H_{l,g,x} + \frac{\partial}{\partial y}\left[(j\omega\varepsilon_0\varepsilon_l)^{-1}\left(\frac{\partial}{\partial x}H_{l,g,y} - \frac{\partial}{\partial y}H_{l,g,x}\right)\right] \tag{3.24b}$$

$$\frac{\partial}{\partial z}H_{l,g,x} = j\omega\varepsilon_0\varepsilon_l E_{l,g,y} - \frac{\partial}{\partial x}\left[(j\omega\mu_0)^{-1}\left(\frac{\partial}{\partial x}E_{l,g,y} - \frac{\partial}{\partial y}E_{l,g,x}\right)\right] \tag{3.24c}$$

$$\frac{\partial}{\partial z}H_{l,g,y} = -j\omega\varepsilon_0\varepsilon_l E_{l,g,x} - \frac{\partial}{\partial y}\left[(j\omega\mu_0)^{-1}\left(\frac{\partial}{\partial x}E_{l,g,y} - \frac{\partial}{\partial y}E_{l,g,x}\right)\right] \tag{3.24d}$$

Substituting Eqs.(3.22a), (3.22b) and (3.14) into Eqs.(3.23), and assuming Laurent's rule for factorisation of the product of two periodic functions, we obtain the set of coupled wave equations:

$$\frac{\partial S_{l,y,mn}}{\partial z} = k_0 U_{l,x,mn} - k_{y,mn}\sum_{o,p=-\infty}^{+\infty}(k_0\varepsilon_l)^{-1}_{(m-o)(n-p)}\left(-k_{x,op}U_{l,y,op} + k_{y,op}U_{l,x,op}\right) \tag{3.25a}$$

$$\frac{\partial S_{l,x,mn}}{\partial z} = -k_0 U_{l,y,mn} - k_{x,mn}\sum_{o,p=-\infty}^{+\infty}(k_0\varepsilon_l)^{-1}_{(m-o)(n-p)}\left(-k_{x,op}U_{l,y,op} + k_{y,op}U_{l,x,op}\right) \tag{3.25b}$$

$$\frac{\partial U_{l,y,mn}}{\partial z} = \sum_{o,p=-\infty}^{+\infty}k_0\varepsilon_{l,(m-o)(n-p)}S_{l,x,op} - \frac{k_{y,mn}}{k_0}\left(-k_{x,mn}S_{l,y,mn} + k_{y,mn}S_{l,x,mn}\right) \tag{3.25c}$$

$$\frac{\partial U_{l,x,mn}}{\partial z} = -\sum_{o,p=-\infty}^{+\infty}k_0\varepsilon_{l,(m-o)(n-p)}S_{l,y,op} - \frac{k_{x,mn}}{k_0}\left(-k_{x,mn}S_{l,y,mn} + k_{y,mn}S_{l,x,mn}\right) \tag{3.25d}$$

with $\varepsilon_{l(m-o)(n-p)}$ the $(m-o, n-p)^{\text{th}}$ permittivity harmonic component of layer l and $(\varepsilon_l)^{-1}_{(m-o)(n-p)}$ the $(m-o, n-p)^{\text{th}}$ harmonic component of the inverse per-

mittivity of layer l. In matrix form, these equations denote as[5]:

$$\begin{bmatrix} \partial\overline{\mathrm{S}}_{l,y}/\partial(z') \\ \partial\overline{\mathrm{S}}_{l,x}/\partial(z') \\ \partial\overline{\mathrm{U}}_{l,y}/\partial(z') \\ \partial\overline{\mathrm{U}}_{l,x}/\partial(z') \end{bmatrix} = \begin{bmatrix} \overline{\overline{0}} & \overline{\overline{0}} & \overline{\overline{\mathrm{K}}}_y\overline{\overline{\mathrm{A}}}_l\overline{\overline{\mathrm{K}}}_x & \overline{\overline{\mathrm{I}}} - \overline{\overline{\mathrm{K}}}_y\overline{\overline{\mathrm{A}}}_l\overline{\overline{\mathrm{K}}}_y \\ \overline{\overline{0}} & \overline{\overline{0}} & \overline{\overline{\mathrm{K}}}_x\overline{\overline{\mathrm{A}}}_l\overline{\overline{\mathrm{K}}}_x - \overline{\overline{\mathrm{I}}} & -\overline{\overline{\mathrm{K}}}_x\overline{\overline{\mathrm{A}}}_l\overline{\overline{\mathrm{K}}}_y \\ \overline{\overline{\mathrm{K}}}_y\overline{\overline{\mathrm{K}}}_x & \overline{\overline{\mathrm{E}}}_l - \overline{\overline{\mathrm{K}}}_y^2 & \overline{\overline{0}} & \overline{\overline{0}} \\ \overline{\overline{\mathrm{K}}}_x^2 - \overline{\overline{\mathrm{E}}}_l & -\overline{\overline{\mathrm{K}}}_x\overline{\overline{\mathrm{K}}}_y & \overline{\overline{0}} & \overline{\overline{0}} \end{bmatrix} \begin{bmatrix} \overline{\mathrm{S}}_{l,y} \\ \overline{\mathrm{S}}_{l,x} \\ \overline{\mathrm{U}}_{l,y} \\ \overline{\mathrm{U}}_{l,x} \end{bmatrix} \tag{3.26}$$

which may be reduced to

$$\begin{bmatrix} \partial^2\overline{\mathrm{S}}_{l,y}/\partial(z')^2 \\ \partial^2\overline{\mathrm{S}}_{l,x}/\partial(z')^2 \end{bmatrix} = \begin{bmatrix} \overline{\overline{\mathrm{K}}}_x^2 + \overline{\overline{\mathrm{D}}}_l\overline{\overline{\mathrm{E}}}_l & \overline{\overline{\mathrm{K}}}_y\left[\overline{\overline{\mathrm{A}}}_l\overline{\overline{\mathrm{K}}}_x\overline{\overline{\mathrm{E}}}_l - \overline{\overline{\mathrm{K}}}_x\right] \\ \overline{\overline{\mathrm{K}}}_x\left[\overline{\overline{\mathrm{A}}}_l\overline{\overline{\mathrm{K}}}_y\overline{\overline{\mathrm{E}}}_l - \overline{\overline{\mathrm{K}}}_y\right] & \overline{\overline{\mathrm{K}}}_y^2 + \overline{\overline{\mathrm{B}}}_l\overline{\overline{\mathrm{E}}}_l \end{bmatrix} \begin{bmatrix} \overline{\mathrm{S}}_{l,y} \\ \overline{\mathrm{S}}_{l,x} \end{bmatrix} \tag{3.27}$$

where $z' = k_0 z$ and

$$\overline{\overline{\mathrm{D}}}_l = \overline{\overline{\mathrm{K}}}_y\overline{\overline{\mathrm{A}}}_l\overline{\overline{\mathrm{K}}}_y - \overline{\overline{\mathrm{I}}} \tag{3.28a}$$

$$\overline{\overline{\mathrm{B}}}_l = \overline{\overline{\mathrm{K}}}_x\overline{\overline{\mathrm{A}}}_l\overline{\overline{\mathrm{K}}}_x - \overline{\overline{\mathrm{I}}} \tag{3.28b}$$

and where $\overline{\overline{\mathrm{E}}}_l$ is the matrix formed by the permittivity harmonic components, with the (mn, op)-element being equal to $\varepsilon_{l,(m-o)(n-p)}$, also called a Toeplitz matrix formed by the permittivity harmonic coefficients $\varepsilon_{l,mn}$, $\overline{\overline{\mathrm{A}}}_l$ a Toeplitz matrix formed by the inverse-permittivity harmonic coefficients $(\varepsilon_l^{-1})_{mn}$, $\overline{\overline{\mathrm{K}}}_x$ and $\overline{\overline{\mathrm{K}}}_y$ are diagonal matrices, with the (mn, mn)-element being equal to respectively $k_{x,mn}/k_0$ and $k_{y,mn}/k_0$ and $\overline{\overline{\mathrm{I}}}$ is the unity matrix.

3.3.3 Truncation

So far we have not made any approximations yet (except for the slicing of the grating region) and in principle the matrices in Eq.(3.26) and Eq.(3.27) can be viewed as matrices with an infinite dimension. For a numerical implementation of this method, these matrices have to be truncated to a certain order, in order to obtain useful results. In practice $\overline{\overline{\mathrm{B}}}_l$, $\overline{\overline{\mathrm{D}}}_l$ $\overline{\overline{\mathrm{K}}}_x$, $\overline{\overline{\mathrm{K}}}_y$ and $\overline{\overline{\mathrm{E}}}_l$ will be $(n \times n)$ matrices, where n is the number of space harmonics retained in the field expansion. We have chosen to retain diffraction orders that lie in a parallelogram centered around the zeroth diffraction order in the 2-D Fourier space. With M the highest order retained in the $+x$-direction, and N in the $+y'$-direction, this results in $n = (2M+1)(2N+1)$. The $(m,n)^{\text{th}}$ space harmonic of the electric field is found on the $((2N+1)(m+M)+(n+N)+1)^{\text{th}}$ row.

The accuracy of the results is linked with the number of spatial harmonics retained in the calculation. For diffraction by crossed gratings, the size of the matrices involved in computation is squared in comparison with that of a one-dimensional grating problem. Therefore it is of crucial importance to derive the

[5]A vector is denoted with a bold typeface, a 1-D matrix is marked as overlined, a square matrix is twice overlined. e.g. $\overline{\mathrm{S}}_{l,y}$ is a row matrix with scalar elements.

smallest possible eigenvalue problem. This is achieved in the previous section by using a second-order differential operator: the $(2n \times 2n)$ matrix in Eq.(3.26) becomes an $(n \times n)$ matrix in Eq.(3.27) or the overall computational time of the eigenvalue problem is effectively reduced by a factor of 4.

However, Eqs.(3.25) can become ill conditioned as soon as they are truncated. Insofar the summations over the subscripts o and p run over an infinite number of terms. The series are truncated from $-n$ to n for numerical purpose. The truncated equations however, do not longer preserve the continuity of the appropriate field components across the discontinuities of the permittivity function. Li proposed appropriate factorisation rules to preserve that continuity [26]. Indeed, Eqs.(3.25) are derived from Eqs.(3.24), assuming Laurent's rule for factorisation. In 1-D (2-D is similar), this rule states that the Fourier component h_n of $h(x)$, which is the product of two arbitrary functions $f(x)$ and $g(x)$, all with period P, is simply given by:

$$h_n = \sum_{m=-\infty}^{+\infty} f_{n-m} g_m \tag{3.29}$$

Reconstruction of $h(x)$ through its Fourier components will however be erroneous when the summation is truncated, depending on the kind of discontinuities of the functions $f(x)$ and $g(x)$. Li clearly derived three important conclusions (for more detail, the reader is referred to [26]):

1. A product of two piecewise-smooth, bounded, periodic functions that have no concurrent jump discontinuities can be factorised by Laurent's rule:

$$h_n^{(M)} = \sum_{m=-M}^{+M} f_{n-m} g_m = \sum_{m=-M}^{+M} [\![f]\!]_{n,m} g_m \tag{3.30}$$

   and

$$[h^{(M)}(x)]_{M\to\infty} = \left[\sum_{n=-M}^{+M} h_n^{(M)} \exp(jnx) \right]_{M\to\infty} = h(x) \tag{3.31}$$

   where $[\![f]\!]$ denotes the Toeplitz matrix generated by the Fourier components of f such that its $(m,n)^{\text{th}}$ entry is f_{n-m}. The Toeplitz matrix is truncated to the order $M \times M$.

2. A product of two piecewise-smooth, bounded, periodic functions that have only pairwise-complementary jump discontinuities cannot be factorised by Laurent's rule, but in most cases it can be factorised by the inverse rule:

$$h_n^{(M)} = \sum_{m=-M}^{+M} \left[\!\!\left[\frac{1}{f} \right]\!\!\right]_{n,m}^{-1} g_m \tag{3.32}$$

   where -1 denotes the matrix inverse.

3. A product of two piecewise-smooth, bounded, periodic functions that have concurrent but not pairwise-complementary jump discontinuities can be factorised by neither Laurent's rule nor by the inverse rule.

If we focus on square lattice gratings with the grating vectors lying along the $x-y$ axes[6], the boundary conditions at the permittivity discontinuities state that: $E_{l,g,x}$ is continuous in the variable y and z and discontinuous in the variable x. Moreover, the product $\varepsilon_l(x,y)E_{l,g,x}$ is continuous in the variable x. This implies that Laurent's rule has to be applied with respect to the y coordinate and the inverse rule with respect to the x coordinate. Analogous consideration can be made for $\varepsilon_l(x,y)E_{l,g,y}$. In this respect, we introduce the notations $\lceil . \rceil$ and $\lfloor . \rfloor$:

$$\lceil \varepsilon_l \rceil_{mn} = \frac{1}{\Lambda_x} \int_0^{\Lambda_x} \varepsilon_l(x,y) e^{j(m-n)K_x x} dx \tag{3.33a}$$

$$\lfloor \varepsilon_l \rfloor_{mn} = \frac{1}{\Lambda_y} \int_0^{\Lambda_y} \varepsilon_l(x,y) e^{j(m-n)K_y y} dy \tag{3.33b}$$

in analogy with the Toeplitz matrix notation where:

$$[\![\varepsilon_l]\!]_{mn,op} = \varepsilon_{l(m-o)(n-p)} \tag{3.34}$$

$\lceil \varepsilon_l \rceil$ and $\lfloor \varepsilon_l \rfloor$ are still functions of y and x respectively. We introduce two more notations, $\lceil\lfloor . \rfloor\rceil$ and $\lfloor\lceil . \rceil\rfloor$:

$$\left\lfloor\left\lceil \varepsilon_l \right\rceil\right\rfloor_{mn,jl} = \frac{1}{\Lambda_y} \int_0^{\Lambda_y} \left\{ \lceil \varepsilon_l \rceil^{-1} \right\}_{mj} (y) e^{j(n-l)K_y y} dy \tag{3.35a}$$

$$\left\lceil\left\lfloor \varepsilon_l \right\rfloor\right\rceil_{mn,jl} = \frac{1}{\Lambda_x} \int_0^{\Lambda_x} \left\{ \lfloor \varepsilon_l \rfloor^{-1} \right\}_{nl} (x) e^{j(m-j)K_x x} dx \tag{3.35b}$$

If we denote $\overline{\overline{\mathrm{A}}}_{l,x} = \left\lfloor\left\lceil \varepsilon_l \right\rceil\right\rfloor$ and $\overline{\overline{\mathrm{A}}}_{l,y} = \left\lceil\left\lfloor \varepsilon_l \right\rfloor\right\rceil$, a correct Fourier factorisation will replace Eqs.(3.26) and (3.27) by:

$$\begin{bmatrix} \partial\overline{\mathrm{S}}_{l,y}/\partial(z') \\ \partial\overline{\mathrm{S}}_{l,x}/\partial(z') \\ \partial\overline{\mathrm{U}}_{l,y}/\partial(z') \\ \partial\overline{\mathrm{U}}_{l,x}/\partial(z') \end{bmatrix} = \begin{bmatrix} \overline{\overline{0}} & \overline{\overline{0}} & \overline{\overline{\mathrm{K}}}_y \overline{\overline{\mathrm{A}}}_l \overline{\overline{\mathrm{K}}}_x & \overline{\overline{\mathrm{I}}} - \overline{\overline{\mathrm{K}}}_y \overline{\overline{\mathrm{A}}}_l \overline{\overline{\mathrm{K}}}_y \\ \overline{\overline{0}} & \overline{\overline{0}} & \overline{\overline{\mathrm{K}}}_x \overline{\overline{\mathrm{A}}}_l \overline{\overline{\mathrm{K}}}_x - \overline{\overline{\mathrm{I}}} & -\overline{\overline{\mathrm{K}}}_x \overline{\overline{\mathrm{A}}}_l \overline{\overline{\mathrm{K}}}_y \\ \overline{\overline{\mathrm{K}}}_y \overline{\overline{\mathrm{K}}}_x & \overline{\overline{\mathrm{A}}}_{l,y} - \overline{\overline{\mathrm{K}}}_y^2 & \overline{\overline{0}} & \overline{\overline{0}} \\ \overline{\overline{\mathrm{K}}}_x^2 - \overline{\overline{\mathrm{A}}}_{l,x} & -\overline{\overline{\mathrm{K}}}_x \overline{\overline{\mathrm{K}}}_y & \overline{\overline{0}} & \overline{\overline{0}} \end{bmatrix} \begin{bmatrix} \overline{\mathrm{S}}_{l,y} \\ \overline{\mathrm{S}}_{l,x} \\ \overline{\mathrm{U}}_{l,y} \\ \overline{\mathrm{U}}_{l,x} \end{bmatrix} \tag{3.36}$$

which may be reduced to

$$\begin{bmatrix} \partial^2\overline{\mathrm{S}}_{l,y}/\partial(z')^2 \\ \partial^2\overline{\mathrm{S}}_{l,x}/\partial(z')^2 \end{bmatrix} = \begin{bmatrix} \overline{\overline{\mathrm{K}}}_x^2 + \overline{\overline{\mathrm{D}}}_l \overline{\overline{\mathrm{A}}}_{l,y} & \overline{\overline{\mathrm{K}}}_y \left[\overline{\overline{\mathrm{A}}}_l \overline{\overline{\mathrm{K}}}_x \overline{\overline{\mathrm{A}}}_{l,x} - \overline{\overline{\mathrm{K}}}_x \right] \\ \overline{\overline{\mathrm{K}}}_x \left[\overline{\overline{\mathrm{A}}}_l \overline{\overline{\mathrm{K}}}_y \overline{\overline{\mathrm{A}}}_{l,y} - \overline{\overline{\mathrm{K}}}_y \right] & \overline{\overline{\mathrm{K}}}_y^2 + \overline{\overline{\mathrm{B}}}_l \overline{\overline{\mathrm{A}}}_{l,x} \end{bmatrix} \begin{bmatrix} \overline{\mathrm{S}}_{l,y} \\ \overline{\mathrm{S}}_{l,x} \end{bmatrix} \tag{3.37}$$

[6]For other lattices the reader is referred to [29]. However implementing the Fourier factorisation for square lattice gratings onto other structures will show enhanced convergence rate, although not maximal. See similar considerations in [30].

3.3.4 Solution of coupled-wave equations

We solve the set of coupled wave equations in Eq.(3.37) by calculating the eigenvalues and the eigenvectors associated with the matrix $\overline{\overline{\mathrm{Q}}}_l$, if we rewrite Eq.(3.37) as [28]:

$$\left[\partial^2 \overline{\mathrm{S}}_l / \partial (z')^2\right] = \left[\overline{\overline{\mathrm{Q}}}_l\right] \left[\overline{\mathrm{S}}_l\right] \tag{3.38}$$

where $\overline{\mathrm{S}}_l$ is composed of $\overline{\mathrm{S}}_{l,y}$ and $\overline{\mathrm{S}}_{l,x}$. The solutions of the coupled-wave equations may then be expressed as:

$$\begin{aligned} S_{l,i}(z) = \sum_{m=1}^{2n} w_{l,i,m} \left(c_{l,m}^{+} e^{-k_0 q_{l,m}(z - D_l + d_l)} + c_{l,m}^{-} e^{k_0 q_{l,m}(z - D_l)} \right) \\ \text{with } D_l - d_l < z < D_l = \sum_{p=1}^{l} d_p \end{aligned} \tag{3.39}$$

for $i = 1, 2, ..2n$ and $S_{l,i}(z)$ the i^{th} element of $\overline{\mathrm{S}}_l$. $w_{l,i,m}$ are the elements of the eigenvector matrix $\overline{\overline{\mathrm{W}}}_l$ and $q_{l,m}$ the square root with positive real part of the eigenvalues of the matrix $\overline{\overline{\mathrm{Q}}}_l$, respectively. The quantities $c_{l,m}^{+}$ and $c_{l,m}^{-}$ are unknown constants, to be determined from the boundary conditions.

If we decompose $\overline{\overline{\mathrm{W}}}_l$ as $[\overline{\overline{\mathrm{W}}}_{l,1}, \overline{\overline{\mathrm{W}}}_{l,2}]^T$, Eq.(3.39) can be written in matrix notation:

$$\overline{\mathrm{S}}_{l,y} = \overline{\overline{\mathrm{W}}}_{l,1} \overline{\overline{\mathrm{X}}}_l (z - D_l + d_l) \overline{\mathrm{C}}_l^{+} + \overline{\overline{\mathrm{W}}}_{l,1} \overline{\overline{\mathrm{X}}}_l (-z + D_l) \overline{\mathrm{C}}_l^{-} \tag{3.40a}$$

$$\overline{\mathrm{S}}_{l,x} = \overline{\overline{\mathrm{W}}}_{l,2} \overline{\overline{\mathrm{X}}}_l (z - D_l + d_l) \overline{\mathrm{C}}_l^{+} + \overline{\overline{\mathrm{W}}}_{l,2} \overline{\overline{\mathrm{X}}}_l (-z + D_l) \overline{\mathrm{C}}_l^{-} \tag{3.40b}$$

where $\overline{\overline{\mathrm{X}}}_l(z)$ is a diagonal matrix with the diagonal elements $\exp(-k_0 q_{l,m} z)$. $\overline{\mathrm{C}}_l^{+}$ and $\overline{\mathrm{C}}_l^{-}$ are $2n \times 1$ column matrices with respectively the unknown constants $c_{l,m}^{+}$ and $c_{l,m}^{-}$ as elements.

With Eq.(3.36), a solution for $\overline{\mathrm{U}}_{l,x}$ and $\overline{\mathrm{U}}_{l,y}$ can be found:

$$\overline{\mathrm{U}}_{l,y} = \overline{\overline{\mathrm{V}}}_{l,1} \overline{\overline{\mathrm{X}}}_l (z - D_l + d_l) \overline{\mathrm{C}}_l^{+} - \overline{\overline{\mathrm{V}}}_{l,1} \overline{\overline{\mathrm{X}}}_l (-z + D_l) \overline{\mathrm{C}}_l^{-} \tag{3.41a}$$

$$\overline{\mathrm{U}}_{l,x} = \overline{\overline{\mathrm{V}}}_{l,2} \overline{\overline{\mathrm{X}}}_l (z - D_l + d_l) \overline{\mathrm{C}}_l^{+} - \overline{\overline{\mathrm{V}}}_{l,2} \overline{\overline{\mathrm{X}}}_l (-z + D_l) \overline{\mathrm{C}}_l^{-} \tag{3.41b}$$

3.3.5 Electromagnetic boundary conditions

We calculate the amplitudes of the diffracted fields $\mathbf{R}_{mn}$ and $\mathbf{T}_{mn}$, together with $c_{l,m}^{+}$ and $c_{l,m}^{-}$, by matching the tangential field components at the boundaries. For this sake, we decompose the vector $\mathbf{R}_{mn}$ in a s (TE) and p (TM) polarisation $R_{s,mn}$ and $R_{p,mn}$. The latter are respectively the amplitude of the electric and the magnetic (times $-j(\mu_0/\varepsilon_0)^{1/2}$) field vectors normal to the diffraction plane given by an inclination angle:

$$\varphi_{mn} = \tan^{-1}(k_{y,mn}/k_{x,mn}) \tag{3.42}$$

With the sign convention sketched in Fig. 3.8, the boundary conditions at the input boundary ($z = 0$) can be written as:

$$\delta_{mn,0}\sin\xi + R_{s,mn} = \cos\varphi_{mn}S_{1,y,mn}(0) - \sin\varphi_{mn}S_{1,x,mn}(0) \tag{3.43a}$$

$$j[\sin\xi\delta_{mn,0}n_1\cos\theta - \frac{k_{1,z,mn}}{k_0}R_{s,mn}] = -[\cos\varphi_{mn}U_{1,x,mn}(0) + \sin\varphi_{mn}U_{1,y,mn}(0)] \tag{3.43b}$$

$$-\delta_{mn,0}jn_1\cos\xi + R_{p,mn} = -[\cos\varphi_{mn}U_{1,y,mn}(0) - \sin\varphi_{mn}U_{1,x,mn}(0)] \tag{3.43c}$$

$$\delta_{mn,0}\cos\xi\cos\theta - j\frac{k_{1,z,mn}}{k_0n_1^2}R_{p,mn} = \cos\varphi_{mn}S_{1,x,mn}(0) + \sin\varphi_{mn}S_{1,y,mn}(0) \tag{3.43d}$$

where $\delta_{mn,0} = 1$ for $m, n = 0$ and $\delta_{mn,0} = 0$ for $m, n \neq 0$. Eqs.(3.43) can be written in matrix form as:

$$\begin{aligned}
&\begin{bmatrix} \delta_{mn,0}\sin\xi \\ \delta_{mn,0}j\sin\xi n_1\cos\theta \\ -j\delta_{mn,0}n_1\cos\xi \\ \delta_{mn,0}\cos\xi\cos\theta \end{bmatrix} + \begin{bmatrix} \overline{\overline{\mathrm{I}}} & \overline{\overline{0}} \\ -j\overline{\overline{\mathrm{Y}}}_1 & \overline{\overline{0}} \\ \overline{\overline{0}} & \overline{\overline{\mathrm{I}}} \\ \overline{\overline{0}} & -j\overline{\overline{\mathrm{Z}}}_1 \end{bmatrix} \begin{bmatrix} \overline{\mathrm{R}}_s \\ \overline{\mathrm{R}}_p \end{bmatrix} \\
&= \begin{bmatrix} \overline{\overline{\mathrm{F}}}_c\overline{\overline{\mathrm{W}}}_{1,1} - \overline{\overline{\mathrm{F}}}_s\overline{\overline{\mathrm{W}}}_{1,2} & [\overline{\overline{\mathrm{F}}}_c\overline{\overline{\mathrm{W}}}_{1,1} - \overline{\overline{\mathrm{F}}}_s\overline{\overline{\mathrm{W}}}_{1,2}]\overline{\overline{\mathrm{X}}}_1(d_1) \\ -[\overline{\overline{\mathrm{F}}}_c\overline{\overline{\mathrm{V}}}_{1,2} + \overline{\overline{\mathrm{F}}}_s\overline{\overline{\mathrm{V}}}_{1,1}] & [\overline{\overline{\mathrm{F}}}_c\overline{\overline{\mathrm{V}}}_{1,2} - \overline{\overline{\mathrm{F}}}_s\overline{\overline{\mathrm{V}}}_{1,1}]\overline{\overline{\mathrm{X}}}_1(d_1) \\ -\overline{\overline{\mathrm{F}}}_c\overline{\overline{\mathrm{V}}}_{1,1} + \overline{\overline{\mathrm{F}}}_s\overline{\overline{\mathrm{V}}}_{1,2} & -[-\overline{\overline{\mathrm{F}}}_c\overline{\overline{\mathrm{V}}}_{1,1} + \overline{\overline{\mathrm{F}}}_s\overline{\overline{\mathrm{V}}}_{1,2}]\overline{\overline{\mathrm{X}}}_1(d_1) \\ \overline{\overline{\mathrm{F}}}_c\overline{\overline{\mathrm{W}}}_{1,2} + \overline{\overline{\mathrm{F}}}_s\overline{\overline{\mathrm{W}}}_{1,1} & [\overline{\overline{\mathrm{F}}}_c\overline{\overline{\mathrm{W}}}_{1,2} + \overline{\overline{\mathrm{F}}}_s\overline{\overline{\mathrm{W}}}_{1,1}]\overline{\overline{\mathrm{X}}}_1(d_1) \end{bmatrix} \begin{bmatrix} \overline{\mathrm{C}}_1^+ \\ \overline{\mathrm{C}}_1^- \end{bmatrix} \\
&= \begin{bmatrix} \overline{\overline{\mathrm{H}}}_{1,1} & \overline{\overline{\mathrm{H}}}_{1,1}\overline{\overline{\mathrm{X}}}_1(d_1) \\ \overline{\overline{\mathrm{H}}}_{1,2} & -\overline{\overline{\mathrm{H}}}_{1,2}\overline{\overline{\mathrm{X}}}_1(d_1) \\ \overline{\overline{\mathrm{H}}}_{1,3} & -\overline{\overline{\mathrm{H}}}_{1,3}\overline{\overline{\mathrm{X}}}_1(d_1) \\ \overline{\overline{\mathrm{H}}}_{1,4} & \overline{\overline{\mathrm{H}}}_{1,4}\overline{\overline{\mathrm{X}}}_1(d_1) \end{bmatrix} \begin{bmatrix} \overline{\mathrm{C}}_1^+ \\ \overline{\mathrm{C}}_1^- \end{bmatrix}
\end{aligned} \tag{3.44}$$

where $\overline{\overline{\mathrm{Y}}}_1$, $\overline{\overline{\mathrm{Z}}}_1$, $\overline{\overline{\mathrm{F}}}_c$ and $\overline{\overline{\mathrm{F}}}_s$ are $(n \times n)$ diagonal matrices with the diagonal elements $k_{1,z,mn}/k_0$, $k_{1,z,mn}/k_0n_1^2$, $\cos\varphi_{mn}$ and $\sin\varphi_{mn}$, respectively. $\overline{\overline{\mathrm{H}}}_{l,i}$ are $(n \times 2n)$-matrices.

At the boundary between the $l-1$ and l grating layers ($x = D_{l-1}$):

$$\begin{bmatrix} \overline{\overline{\mathrm{H}}}_{l-1,1}\overline{\overline{\mathrm{X}}}_{l-1}(d_{l-1}) & \overline{\overline{\mathrm{H}}}_{l-1,1} \\ \overline{\overline{\mathrm{H}}}_{l-1,2}\overline{\overline{\mathrm{X}}}_{l-1}(d_{l-1}) & -\overline{\overline{\mathrm{H}}}_{l-1,2} \\ \overline{\overline{\mathrm{H}}}_{l-1,3}\overline{\overline{\mathrm{X}}}_{l-1}(d_{l-1}) & -\overline{\overline{\mathrm{H}}}_{l-1,3} \\ \overline{\overline{\mathrm{H}}}_{l-1,4}\overline{\overline{\mathrm{X}}}_{l-1}(d_{l-1}) & \overline{\overline{\mathrm{H}}}_{l-1,4} \end{bmatrix} \begin{bmatrix} \overline{\mathrm{C}}_{l-1}^+ \\ \overline{\mathrm{C}}_{l-1}^- \end{bmatrix} = \begin{bmatrix} \overline{\overline{\mathrm{H}}}_{l,1} & \overline{\overline{\mathrm{H}}}_{l,1}\overline{\overline{\mathrm{X}}}_l(d_l) \\ \overline{\overline{\mathrm{H}}}_{l,2} & -\overline{\overline{\mathrm{H}}}_{l,2}\overline{\overline{\mathrm{X}}}_l(d_l) \\ \overline{\overline{\mathrm{H}}}_{l,3} & -\overline{\overline{\mathrm{H}}}_{l,3}\overline{\overline{\mathrm{X}}}_l(d_l) \\ \overline{\overline{\mathrm{H}}}_{l,4} & \overline{\overline{\mathrm{H}}}_{l,4}\overline{\overline{\mathrm{X}}}_l(d_l) \end{bmatrix} \begin{bmatrix} \overline{\mathrm{C}}_l^+ \\ \overline{\mathrm{C}}_l^- \end{bmatrix} \tag{3.45}$$

and at the boundary with the last grating layer and the output region ($z = D_l$):

$$\begin{bmatrix} \overline{\overline{\mathrm{H}}}_{L,1}\overline{\overline{\mathrm{X}}}_L(d_L) & \overline{\overline{\mathrm{H}}}_{L,1} \\ \overline{\overline{\mathrm{H}}}_{L,2}\overline{\overline{\mathrm{X}}}_L(d_L) & -\overline{\overline{\mathrm{H}}}_{L,2} \\ \overline{\overline{\mathrm{H}}}_{L,3}\overline{\overline{\mathrm{X}}}_L(d_L) & -\overline{\overline{\mathrm{H}}}_{L,3} \\ \overline{\overline{\mathrm{H}}}_{L,4}\overline{\overline{\mathrm{X}}}_L(d_L) & \overline{\overline{\mathrm{H}}}_{L,4} \end{bmatrix} \begin{bmatrix} \overline{\mathrm{C}}_L^+ \\ \overline{\mathrm{C}}_L^- \end{bmatrix} = \begin{bmatrix} \overline{\overline{\mathrm{I}}} & \overline{\overline{0}} \\ j\overline{\overline{\mathrm{Y}}}_2 & \overline{\overline{0}} \\ \overline{\overline{0}} & \overline{\overline{\mathrm{I}}} \\ \overline{\overline{0}} & j\overline{\overline{\mathrm{Z}}}_2 \end{bmatrix} \begin{bmatrix} \overline{\mathrm{T}}_s \\ \overline{\mathrm{T}}_p \end{bmatrix} \tag{3.46}$$

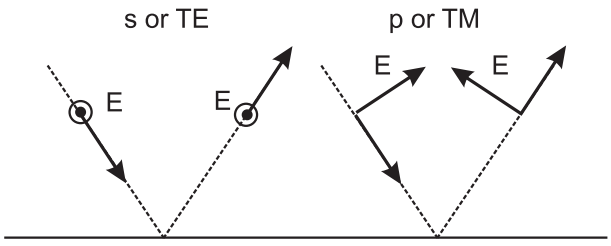

Fig. 3.8: Sign convention for reflection.

where the elements of $\overline{\mathrm{T}}_s$ and $\overline{\mathrm{T}}_p$ are the components of the amplitude of the electric- and magnetic (times $-j(\mu_0/\varepsilon_0)^{1/2}$) field vectors normal to the diffraction plane given by Eq.(3.42). $\overline{\overline{\mathrm{Y}}}_2$ and $\overline{\overline{\mathrm{Z}}}_2$, are diagonal matrices with the diagonal elements $k_{2,z,mn}/k_0$ and $k_{2,z,mn}/k_0 n_2^2$, respectively.

3.3.6 Enhanced transmittance approach for multi-layer gratings

For a grating divided into L grating layers, Eqs.(3.44)-(3.46) would be a $4n(L+1)$ system of equations, where n is the number of field harmonics retained in the formulation. These $4n(L+1)$ equations can be solved simultaneous for the forward- and the backward propagating diffracted amplitudes by standard techniques as LU-decomposition, etc.. When L is large, the entire system of equations is however too large for practical numerical computation. To reduce the size of the system of simultaneous equations, Eqs.(3.44)-(3.46) can be solved by a transmittance matrix approach. This approach denotes $\overline{\mathrm{T}}_s$ and $\overline{\mathrm{T}}_p$ in function of $\overline{\mathrm{R}}_s$ and $\overline{\mathrm{R}}_p$ through a recursive substitution of Eqs.(3.44)-(3.46). The final equation to be solved is:

$$\begin{bmatrix} \delta_{mn,0}\sin\xi \\ \delta_{mn,0} j \sin\xi n_1 \cos\theta \\ -\delta_{mn,0} j n_1 \cos\xi \\ \delta_{mn,0}\cos\xi\cos\theta \end{bmatrix} + \begin{bmatrix} \overline{\overline{\mathrm{I}}} & \overline{\overline{0}} \\ -j\overline{\overline{\mathrm{Y}}}_1 & \overline{\overline{0}} \\ \overline{\overline{0}} & \overline{\overline{\mathrm{I}}} \\ \overline{\overline{0}} & -j\overline{\overline{\mathrm{Z}}}_1 \end{bmatrix} \begin{bmatrix} \overline{\mathrm{R}}_s \\ \overline{\mathrm{R}}_p \end{bmatrix}$$

$$= \left(\prod_{l=1}^{L} \begin{bmatrix} \overline{\overline{\mathrm{H}}}_{l,1} & \overline{\overline{\mathrm{H}}}_{l,1}\overline{\overline{\mathrm{X}}}_l(d_l) \\ \overline{\overline{\mathrm{H}}}_{l,2} & -\overline{\overline{\mathrm{H}}}_{l,2}\overline{\overline{\mathrm{X}}}_l(d_l) \\ \overline{\overline{\mathrm{H}}}_{l,3} & -\overline{\overline{\mathrm{H}}}_{l,3}\overline{\overline{\mathrm{X}}}_l(d_l) \\ \overline{\overline{\mathrm{H}}}_{l,4} & \overline{\overline{\mathrm{H}}}_{l,4}\overline{\overline{\mathrm{X}}}_l(d_l) \end{bmatrix} \begin{bmatrix} \overline{\overline{\mathrm{H}}}_{l,1}\overline{\overline{\mathrm{X}}}_l(d_l) & \overline{\overline{\mathrm{H}}}_{l,1} \\ \overline{\overline{\mathrm{H}}}_{l,2}\overline{\overline{\mathrm{X}}}_l(d_l) & -\overline{\overline{\mathrm{H}}}_{l,2} \\ \overline{\overline{\mathrm{H}}}_{l,3}\overline{\overline{\mathrm{X}}}_l(d_l) & -\overline{\overline{\mathrm{H}}}_{l,3} \\ \overline{\overline{\mathrm{H}}}_{l,4}\overline{\overline{\mathrm{X}}}_l(d_l) & \overline{\overline{\mathrm{H}}}_{l,4} \end{bmatrix}^{-1} \right) \begin{bmatrix} \overline{\overline{\mathrm{I}}} & \overline{\overline{0}} \\ j\overline{\overline{\mathrm{Y}}}_2 & \overline{\overline{0}} \\ \overline{\overline{0}} & \overline{\overline{\mathrm{I}}} \\ \overline{\overline{0}} & j\overline{\overline{\mathrm{Z}}}_2 \end{bmatrix} \begin{bmatrix} \overline{\mathrm{T}}_s \\ \overline{\mathrm{T}}_p \end{bmatrix} \tag{3.47}$$

Note that Eq.(3.47) includes one matrix inversion for each layer. If the quantity $(k_0 q_{l,m} d_l)$ is large and positive real, the associated exponential $\exp(-k_0 q_{l,m} d_l)$ in the diagonal matrix $\overline{\overline{\mathrm{X}}}_l(d_l)$ will be very small and possibly zero. As a result, the elements in one or more columns will be virtually zero. The inversion of an ill-conditioned matrix will produce some very large elements that cannot be rep-

resented with sufficient numerical accuracy because of the finite precision of the numerical representation (truncation error), resulting in numerical instability. Moharam *et al.* [5] presented a numerically stable enhanced transmittance approach to preempt these numerical instabilities associated with the matrix inversion.

We decompose and rewrite the last factor of Eq.(3.47):

$$\begin{aligned}
&\begin{bmatrix} \overline{\overline{\mathrm{H}}}_{L,1} & \overline{\overline{\mathrm{H}}}_{L,1}\overline{\overline{\mathrm{X}}}_L(d_L) \\ \overline{\overline{\mathrm{H}}}_{L,2} & -\overline{\overline{\mathrm{H}}}_{L,2}\overline{\overline{\mathrm{X}}}_L(d_L) \\ \overline{\overline{\mathrm{H}}}_{L,3} & -\overline{\overline{\mathrm{H}}}_{L,3}\overline{\overline{\mathrm{X}}}_L(d_L) \\ \overline{\overline{\mathrm{H}}}_{L,4} & \overline{\overline{\mathrm{H}}}_{L,4}\overline{\overline{\mathrm{X}}}_L(d_L) \end{bmatrix} \begin{bmatrix} \overline{\overline{\mathrm{H}}}_{L,1}\overline{\overline{\mathrm{X}}}_L(d_L) & \overline{\overline{\mathrm{H}}}_{L,1} \\ \overline{\overline{\mathrm{H}}}_{L,2}\overline{\overline{\mathrm{X}}}_L(d_L) & -\overline{\overline{\mathrm{H}}}_{L,2} \\ \overline{\overline{\mathrm{H}}}_{L,3}\overline{\overline{\mathrm{X}}}_L(d_L) & -\overline{\overline{\mathrm{H}}}_{L,3} \\ \overline{\overline{\mathrm{H}}}_{L,4}\overline{\overline{\mathrm{X}}}_L(d_L) & \overline{\overline{\mathrm{H}}}_{L,4} \end{bmatrix}^{-1} \begin{bmatrix} \bar{\bar{\mathrm{I}}} & \bar{\bar{0}} \\ j\overline{\overline{\mathrm{Y}}}_2 & \bar{\bar{0}} \\ \bar{\bar{0}} & \bar{\bar{\mathrm{I}}} \\ \bar{\bar{0}} & j\overline{\overline{\mathrm{Z}}}_2 \end{bmatrix} \begin{bmatrix} \overline{\mathrm{T}}_s \\ \overline{\mathrm{T}}_p \end{bmatrix} \\
&= \begin{bmatrix} \overline{\overline{\mathrm{H}}}_{L,1} & \overline{\overline{\mathrm{H}}}_{L,1}\overline{\overline{\mathrm{X}}}_L(d_L) \\ \overline{\overline{\mathrm{H}}}_{L,2} & -\overline{\overline{\mathrm{H}}}_{L,2}\overline{\overline{\mathrm{X}}}_L(d_L) \\ \overline{\overline{\mathrm{H}}}_{L,3} & -\overline{\overline{\mathrm{H}}}_{L,3}\overline{\overline{\mathrm{X}}}_L(d_L) \\ \overline{\overline{\mathrm{H}}}_{L,4} & \overline{\overline{\mathrm{H}}}_{L,4}\overline{\overline{\mathrm{X}}}_L(d_L) \end{bmatrix} \begin{bmatrix} \overline{\overline{\mathrm{X}}}_L(d_L) & \bar{\bar{0}} \\ \bar{\bar{0}} & \bar{\bar{\mathrm{I}}} \end{bmatrix}^{-1} \begin{bmatrix} \overline{\overline{\mathrm{H}}}_{L,1} & \overline{\overline{\mathrm{H}}}_{L,1} \\ \overline{\overline{\mathrm{H}}}_{L,2} & -\overline{\overline{\mathrm{H}}}_{L,2} \\ \overline{\overline{\mathrm{H}}}_{L,3} & -\overline{\overline{\mathrm{H}}}_{L,3} \\ \overline{\overline{\mathrm{H}}}_{L,4} & \overline{\overline{\mathrm{H}}}_{L,4} \end{bmatrix}^{-1} \begin{bmatrix} \bar{\bar{\mathrm{f}}}_{L+1} \\ \bar{\bar{\mathrm{g}}}_{L+1} \end{bmatrix} \overline{\mathrm{T}}
\end{aligned} \tag{3.48}$$

with $\bar{\bar{\mathrm{f}}}_{L+1}$ and $\bar{\bar{\mathrm{g}}}_{L+1}$ $(2n \times 2n)$-matrices and $\overline{\mathrm{T}}$ the row matrix composed with $\overline{\mathrm{T}}_s$ and $\overline{\mathrm{T}}_p$. The matrix on the right in the product is well conditioned, and its inversion is numerically stable. We write:

$$\begin{bmatrix} \overline{\overline{\mathrm{H}}}_{L,1} & \overline{\overline{\mathrm{H}}}_{L,1}\overline{\overline{\mathrm{X}}}_L(d_L) \\ \overline{\overline{\mathrm{H}}}_{L,2} & -\overline{\overline{\mathrm{H}}}_{L,2}\overline{\overline{\mathrm{X}}}_L(d_L) \\ \overline{\overline{\mathrm{H}}}_{L,3} & -\overline{\overline{\mathrm{H}}}_{L,3}\overline{\overline{\mathrm{X}}}_L(d_L) \\ \overline{\overline{\mathrm{H}}}_{L,4} & \overline{\overline{\mathrm{H}}}_{L,4}\overline{\overline{\mathrm{X}}}_L(d_L) \end{bmatrix} \begin{bmatrix} \overline{\overline{\mathrm{X}}}_L(d_L) & \bar{\bar{0}} \\ \bar{\bar{0}} & \bar{\bar{\mathrm{I}}} \end{bmatrix}^{-1} \begin{bmatrix} \bar{\bar{\mathrm{a}}}_L \\ \bar{\bar{\mathrm{b}}}_L \end{bmatrix} \overline{\mathrm{T}} \tag{3.49}$$

where:

$$\begin{bmatrix} \bar{\bar{\mathrm{a}}}_L \\ \bar{\bar{\mathrm{b}}}_L \end{bmatrix} = \begin{bmatrix} \overline{\overline{\mathrm{H}}}_{L,1} & \overline{\overline{\mathrm{H}}}_{L,1} \\ \overline{\overline{\mathrm{H}}}_{L,2} & -\overline{\overline{\mathrm{H}}}_{L,2} \\ \overline{\overline{\mathrm{H}}}_{L,3} & -\overline{\overline{\mathrm{H}}}_{L,3} \\ \overline{\overline{\mathrm{H}}}_{L,4} & \overline{\overline{\mathrm{H}}}_{L,4} \end{bmatrix}^{-1} \begin{bmatrix} \bar{\bar{\mathrm{f}}}_{L+1} \\ \bar{\bar{\mathrm{g}}}_{L+1} \end{bmatrix} \tag{3.50}$$

The ill-conditioned remaining matrix to be inverted is avoided by introducing the substitution $\overline{\mathrm{T}} = \bar{\bar{\mathrm{a}}}_L^{-1}\overline{\overline{\mathrm{X}}}_L(d_L)\overline{\mathrm{T}}_L$. The last factor $(l = L)$ is than reduced to:

$$\begin{aligned}
&\begin{bmatrix} \overline{\overline{\mathrm{H}}}_{L,1} & \overline{\overline{\mathrm{H}}}_{L,1}\overline{\overline{\mathrm{X}}}_L(d_L) \\ \overline{\overline{\mathrm{H}}}_{L,2} & -\overline{\overline{\mathrm{H}}}_{L,2}\overline{\overline{\mathrm{X}}}_L(d_L) \\ \overline{\overline{\mathrm{H}}}_{L,3} & -\overline{\overline{\mathrm{H}}}_{L,3}\overline{\overline{\mathrm{X}}}_L(d_L) \\ \overline{\overline{\mathrm{H}}}_{L,4} & \overline{\overline{\mathrm{H}}}_{L,4}\overline{\overline{\mathrm{X}}}_L(d_L) \end{bmatrix} \begin{bmatrix} \bar{\bar{\mathrm{I}}} \\ \bar{\bar{\mathrm{b}}}_L\bar{\bar{\mathrm{a}}}_L^{-1}\overline{\overline{\mathrm{X}}}_L(d_L) \end{bmatrix} \overline{\mathrm{T}}_L \\
&= \begin{bmatrix} \overline{\overline{\mathrm{H}}}_{L,1} + \overline{\overline{\mathrm{H}}}_{L,1}\overline{\overline{\mathrm{X}}}_L(d_L)\bar{\bar{\mathrm{b}}}_L\bar{\bar{\mathrm{a}}}_L^{-1}\overline{\overline{\mathrm{X}}}_L(d_L) \\ \overline{\overline{\mathrm{H}}}_{L,2} - \overline{\overline{\mathrm{H}}}_{L,2}\overline{\overline{\mathrm{X}}}_L(d_L)\bar{\bar{\mathrm{b}}}_L\bar{\bar{\mathrm{a}}}_L^{-1}\overline{\overline{\mathrm{X}}}_L(d_L) \\ \overline{\overline{\mathrm{H}}}_{L,3} - \overline{\overline{\mathrm{H}}}_{L,3}\overline{\overline{\mathrm{X}}}_L(d_L)\bar{\bar{\mathrm{b}}}_L\bar{\bar{\mathrm{a}}}_L^{-1}\overline{\overline{\mathrm{X}}}_L(d_L) \\ \overline{\overline{\mathrm{H}}}_{L,4} + \overline{\overline{\mathrm{H}}}_{L,4}\overline{\overline{\mathrm{X}}}_L(d_L)\bar{\bar{\mathrm{b}}}_L\bar{\bar{\mathrm{a}}}_L^{-1}\overline{\overline{\mathrm{X}}}_L(d_L) \end{bmatrix} \overline{\mathrm{T}}_L = \begin{bmatrix} \bar{\bar{\mathrm{f}}}_L \\ \bar{\bar{\mathrm{g}}}_L \end{bmatrix} \overline{\mathrm{T}}_L
\end{aligned} \tag{3.51}$$

Repeating this process for all the layers, we obtain an equation that is easily solved for $R_{s,mn}$,$R_{p,mn}$,$T_{s,mn}$ and $T_{p,mn}$ without numerical instabilities:

$$\begin{bmatrix} \delta_{mn,0}\sin\xi \\ \delta_{mn,0} j \sin\xi n_1 \cos\theta \\ -j\delta_{mn,0} n_1 \cos\xi \\ \delta_{mn,0}\cos\xi\cos\theta \end{bmatrix} + \begin{bmatrix} \bar{\bar{\mathrm{I}}} & \bar{\bar{0}} \\ -j\bar{\bar{\mathrm{Y}}}_1 & \bar{\bar{0}} \\ \bar{\bar{0}} & \bar{\bar{\mathrm{I}}} \\ \bar{\bar{0}} & -j\bar{\bar{\mathrm{Z}}}_1 \end{bmatrix} \begin{bmatrix} \overline{\mathrm{R}}_s \\ \overline{\mathrm{R}}_p \end{bmatrix} = \begin{bmatrix} \bar{\bar{\mathrm{f}}}_1 \\ \bar{\bar{\mathrm{g}}}_1 \end{bmatrix} \overline{\mathrm{T}}_1 \tag{3.52}$$

where:

$$\overline{\mathrm{T}} = \bar{\bar{\mathrm{a}}}_L^{-1}\bar{\bar{\mathrm{X}}}_L(d_L)...\bar{\bar{\mathrm{a}}}_l^{-1}\bar{\bar{\mathrm{X}}}_l(d_l)...\bar{\bar{\mathrm{a}}}_1^{-1}\bar{\bar{\mathrm{X}}}_1(d_1)\overline{\mathrm{T}}_1 \tag{3.53}$$

with $\bar{\bar{\mathrm{f}}}_l$, $\bar{\bar{\mathrm{g}}}_l$, $\bar{\bar{\mathrm{a}}}_l$ and $\overline{\mathrm{T}}_l$ obtained by a process similar to Eqs.(3.47)-(3.50).

3.3.7 Diffraction efficiency

The diffraction efficiency of the $(m,n)^{\text{th}}$ order is defined as the ratio of the $(m,n)^{\text{th}}$-order diffracted energy to the incident energy. It is given by the ratio of the flux of the Poynting vector of the $(m,n)^{\text{th}}$ order integrated over one cell of the periodic structure Λ_{xy} to the corresponding flux of the incident wave. The active power is given by the real part of this Poynting vector:

$$\begin{aligned} \mathrm{Re}(P_z) &= \frac{1}{2}\mathrm{Re}\left(\frac{1}{\Lambda_{xy}}\int\int \mathbf{E}\times\mathbf{H}^* dxdy\right)\cdot\mathbf{z} \\ &= \frac{1}{2}\mathrm{Re}\left(\frac{1}{\Lambda_{xy}}\int\int \left(E_x H_y^* - E_y H_x^*\right) dxdy\right) \end{aligned} \tag{3.54}$$

For the incident field, with $k_{inc,z}$ real, substitution of Eqs.(3.11)-(3.13), (3.16) and (3.19) in (3.54) results in:

$$\mathrm{Re}(P_{inc,z}) = \frac{1}{2}\frac{k_{inc,z}}{\omega\mu_0}\sin^2\xi + \frac{1}{2}\frac{k_{inc,z}}{\omega\mu_0}\cos^2\xi = \frac{1}{2}\frac{k_{inc,z}}{\omega\mu_0} \tag{3.55}$$

For the $(m,n)^{\text{th}}$ reflected diffraction order, the TE power is given by:

$$\mathrm{Re}(P_{z,R_{TE}}^{mn}) = -\frac{1}{2}\frac{\mathrm{Re}(k_{1,z,mn})}{\omega\mu_0}|R_{s,mn}|^2 \tag{3.56}$$

and the TM power by:

$$\mathrm{Re}(P_{z,R_{TM}}^{mn}) = -\frac{1}{2}\frac{\mathrm{Re}(k_{1,z,mn}/n_1^2)}{\omega\mu_0}|R_{p,mn}|^2 \tag{3.57}$$

For the $(m,n)^{\text{th}}$ transmitted diffraction order, the TM power is given by:

$$\mathrm{Re}(P_{z,T_{TE}}^{mn}) = \frac{1}{2}\frac{\mathrm{Re}(k_{2,z,mn})}{\omega\mu_0}|T_{s,mn}|^2 \tag{3.58}$$

and the TM power by:

$$\mathrm{Re}(P_{z,T_{TM}}^{mn}) = \frac{1}{2}\frac{\mathrm{Re}(k_{2,z,mn}/n_2^2)}{\omega\mu_0}|T_{p,mn}|^2 \tag{3.59}$$

The diffraction efficiency is then given by the ratio of Eqs.(3.56)-(3.59) on Eq.(3.55):

$$\mathrm{DE}_{R,mn} = \mathrm{Re}\left(\frac{-k_{1,z,mn}}{k_{inc,z}}\right)|R_{s,mn}|^2 + \mathrm{Re}\left(\frac{-k_{1,z,mn}/n_1^2}{k_{inc,z}}\right)|R_{p,mn}|^2 \tag{3.60a}$$

$$\mathrm{DE}_{T,mn} = \mathrm{Re}\left(\frac{k_{2,z,mn}}{k_{inc,z}}\right)|T_{s,mn}|^2 + \mathrm{Re}\left(\frac{k_{2,z,mn}/n_2^2}{k_{inc,z}}\right)|T_{p,mn}|^2 \tag{3.60b}$$

Conservation of energy for a lossless grating is defined as:

$$\sum_{m,n}(\mathrm{DE}_{R,mn} + \mathrm{DE}_{T,mn}) = 1 \tag{3.61}$$

Regardless of the number of orders retained in the calculation, this condition is achieved. In [31] it is explicitly proven that in the RCWA, the grating as a whole conserves energy even with truncation of the spatial harmonics. As the energy balance is analytically satisfied, this criterion can not be used to check the accuracy of the calculation or convergence. It can only serve as a check for numerical errors.

3.3.8 Convergence

The implementation of the RCWA is stable and will converge to yield the diffracted amplitudes. The accuracy of the solution will depend on the number of orders retained in the expansion of space-harmonic fields in the grating region. The convergence of the diffraction efficiency of a dielectric grating as the number of field harmonics is increased, is shown in Fig. 3.9(a) for a dielectric grating and in Fig. 3.9(b) for a metallic grating. The latter shows the absorption defined as $1 - (\sum_{m,n}(\mathrm{DE}_{R,mn} + \mathrm{DE}_{T,mn}))$ as a function of the truncation order. M is the number of orders retained in the positive k_x direction. N, the number of orders in the positive k_y direction, equals M. The total number of retained orders is then $n = (2M+1)(2N+1)$. The grating parameters correspond with the grating parameters of respectively Fig. 2 and Fig. 4 of [30]. The simulated diffraction efficiency and absorption given in this paper correspond with the numerical results of our simulation tool.

It is clear that in all cases the diffraction efficiency converges to the proper values when a sufficient number of harmonics is included in the formulation. In case of a metallic grating, the convergence rate is smaller. This is due to the larger spatial variation in the fields at the boundaries between the air and the metal. The value does even not converge fully for $M = N = 7$, when we compare the data with the values of [30]. $M = N = 7$ is however the maximum number of orders that our processor can handle.

A cross-section of the gratings representative for those used in the GA-RCLED, are sketched in Fig. 3.10(a) and Fig. 3.10(b), Fig. 3.10(c) plots the convergence rate of the absorption of a 2-D square lattice grating etched in GaAs, covered with Au (Fig. 3.10(a)). The convergence rate of the absorption plus transmission of a

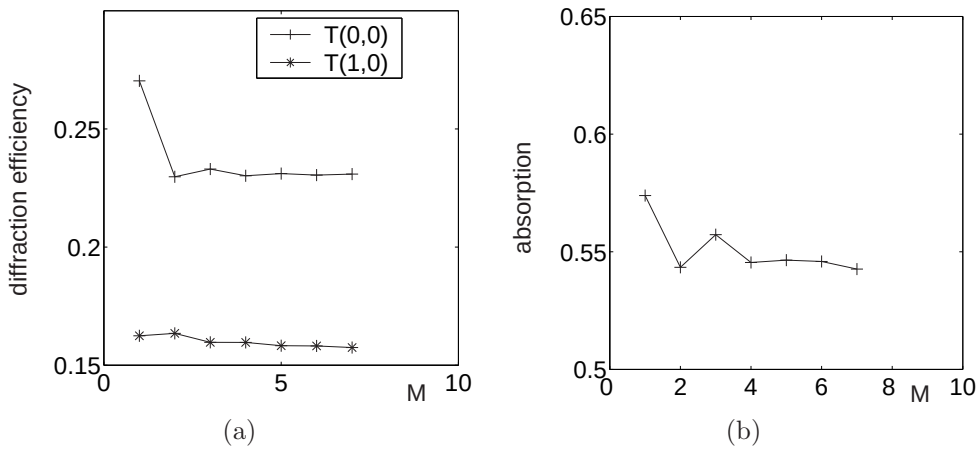

Fig. 3.9: (a)(0,0) and (1,0) transmitted intensities of a lamellar dielectric grating with square lattice etched in a substrate of refractive index $n_2 = 1.5$. The grating parameters are those given in the caption of Fig. 2 of [30]: $n_1 = 1$, one layer grating with $d = \lambda = 1$ μm, $\Lambda_x, \Lambda_y = 1.2\lambda$, filling factor $f_x = f_y = 0.5$, $\theta = \varphi = 0$ and $\xi = 90°$; (b) Absorption of a lamellar grating with square lattice. The grating parameters are those given in the caption of Fig. 4 of [30]: $n_1 = 1$, $n_3 = 1.5$, one layer grating with $n_{g,1} = 2076 - j1.062$, $n_{g,2} = 1$, $d = 0.2\lambda$, $\lambda = 1$ μm, $\Lambda_x, \Lambda_y = 0.5\lambda$, filling factor $f_x = f_y = 0.6$, $\theta = \varphi = 0$ and $\xi = 90°$. $M = N$ is the number of orders retained in respectively the positive k_x direction and the positive k_y direction.

2-D square lattice grating etched in GaAs, top-covered with Au (Fig. 3.10(b)) is depicted in Fig. 3.10(d). Both normal incidence ($\theta = 0°$) and oblique incidence ($\theta = 70°$) are considered. Normal incidence corresponds with the Fabry-Pérot mode in the GA-RCLED, the oblique incidence with the guided mode (see Chapter 4). Note the larger absorption of the massive Au grating in comparison with the absorption plus transmission of the grating top-covered with metal. The absorption coefficient for normal incidence at a plane metallic surface is 0.05, for oblique incidence 0.02. The massive metallic grating greatly surpasses these values.

Fig. 3.11 presents the respective convergence rates for a 2-D triangular lattice grating. As explained in section 3.3.3, the convergence will be slower, especially for metallic gratings, then for square lattice gratings.

The numerical solution of Eq.(3.37) is obtained by the knowledge of the eigenvalues and eigenvectors of matrix $\overline{\overline{Q}}_l$. This is a complex matrix, and the eigenproblem is time consuming. The size of the matrix is $n = 2(2M + 1)(2N + 1)$. For e.g. $M = N = 10$ the size equals 882. Notifying that the time spent to solving an eigenequation of size n is proportional to n^3, it is not hard to imagine that accurate calculations are time consuming when the amount of orders is increased. This emphasizes the importance of the enhanced convergence as denoted in section 3.3.3.

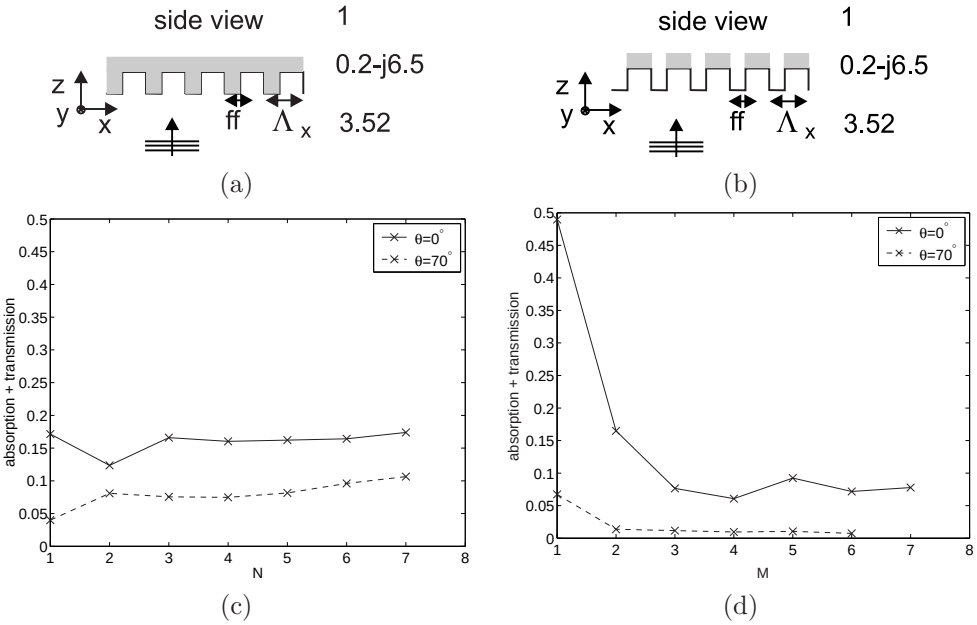

Fig. 3.10: (a)Cross-section of 2-D grating with square lattice etched in GaAs of refractive index $n_1 = 3.52$ *and evaporated metal* $n_2 = 0.2 - j6.5$. $n_{g,1} = 0.2 - j6.5$, $n_{g,2} = 3.52$, $\Lambda_x, \Lambda_y = 0.3$ μm, *filling factor* $f_x = f_y = 0.5$, $\lambda = 0.98$ μm; *(b) Cross-section of 2-D grating with square lattice etched in GaAs of refractive index* $n_1 = 3.52$ *and obliquely evaporated metal* $n_2 = 1$. $n_{g_1,1} = 3.52$, $n_{g_1,2} = 1$, $n_{g_2,1} = 0.2 - j6.5$, $n_{g_2,2} = 1$, $\Lambda_x, \Lambda_y = 0.3$ μm, *filling factor* $f_x = f_y = 0.5$,$\lambda = 0.98$ μm; *(c) absorption of grating (a) with* $\varphi = 0^\circ$, $\xi = 90^\circ$ *and* $\theta = 0^\circ$ *and* 70°; *(d) absorption plus transmission of grating (b) with* $\varphi = 0^\circ$, $\xi = 90^\circ$ *and* $\theta = 0^\circ$ *and* 70°. $M = N$ *is the number of orders retained in respectively the positive* k_x *direction and the positive* k_y *direction.*

3.4 Conclusions

Diffractive nanostructures can qualitatively be understood by using a wave vector diagram, which plots the allowed wave vectors for a fixed optical frequency. Propagating and evanescent waves together with their propagation direction can be read on this WVD. This tool will be used to understand the GA-RCLED in Chapter 4.

Quantitative information is given by the RCWA. The RCWA for 2-D gratings has been presented. It is an exact solution of the Maxwell equations for electromagnetic diffraction by grating structures. The obtained accuracy of the solution solely depends on the number of terms retained in the space-harmonic expansion of the field.

This analysis has been implemented in C++ in a UNIX environment. Simulation results of diffraction on 2-D gratings have been compared and match with data published in literature. Diffraction of light incident on 2-D gratings can thus

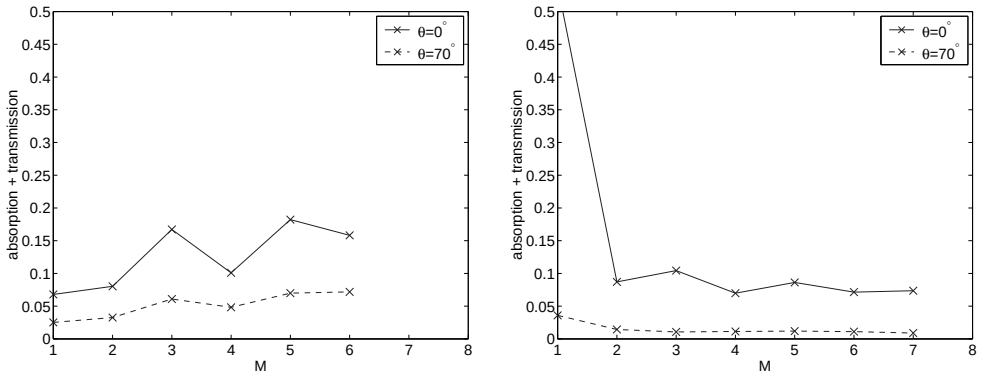

Fig. 3.11: Respective convergence rates for triangular lattice grating (see Fig. 3.10).

be calculated rigorously with the simulation tool developed in this work.

It has been performed as an extension to the available program RODIS to calculate diffraction of light incident on 1-D gratings. For the numerical procedures (equation systems or eigenvalue problems), the same standard FORTRAN routines were used [13]. Accurate calculation of 2-D gratings demands for a large number $n = (2M + 1)(2N + 1)$ of retained terms in the space-harmonic expansion of the field. The CPU time to calculate the eigenvalue problem and the equation system is proportional to n^3. It is therefore not surprising that accurate calculations are time-consuming. Optimisation of the implementation of various numerical procedures to speed up matrix calculations are still more than welcome.

References

[1] R.E. Collin and F.J. Zucker, Eds, *"Antenna Theory",* vol. 2, New York: McGraw-Hill, 1969.

[2] P. St. J Russell, T.A. Birks and F.D. Lloyd-Lucas, *"Confined electrons and photons",* vol. B340, E. Burstein and C. Weisbuch, eds., Plenum Press, New York, 1995.

[3] Lifeng Li, "Formulation and comparison of two recursive matrix algorithms for modeling layered diffraction gratings", *J. Opt. Soc. Am. A,* vol. 13, pp. 1024-1035, 1996.

[4] H. Ichikawa, "Electromagnetic analysis of diffraction gratins by the finite-difference time-domain method", *J. Opt. Soc. Am. A,* vol. 15, pp. 152-157, 1998.

[5] M.G. Moharam, D.A. Pommet, E.B. Grann and T.K. Gaylord, "Stable implementation of the rigorous coupled-wave analysis for surface-relief gratings: enhanced transmittance matrix approach", *J. Opt. Soc. Am. A,* vol. 12, pp. 1077-1086, 1995.

[6] M.G. Moharam and T.K. Gaylord, "Rigorous Coupled-Wave analysis of planar-grating diffraction", *J. Opt. Soc. Am. A,* vol. 71, pp. 811-818, 1981.

[7] M.G. Moharam and T.K. Gaylord, "Three dimensional Coupled-Wave analysis of planar-grating diffraction", *J. Opt. Soc. Am. A,* vol. 73, pp. 1105-112, 1983.

[8] M.G. Moharam and T.K. Gaylord, "Diffraction analysis of dielectric surface-relief gratings", *J. Opt. Soc. Am. A,* vol. 72, pp. 1385-10392, 1982.

[9] M.G. Moharam, E.B. Grann, D.A. Pommet and T.K. Gaylord, "Formulation of stable and efficient implementation of the rigorous coupled-wave analysis of binary gratings", *J. Opt. Soc. Am. A,* vol. 12, pp. 1068-1076, 1995.

[10] Lifeng Li, "A modal analysis of lamellar diffraction gratings in conical mountings", *J. of Modern Optics,* vol. 40, pp. 553-573, 1993.

[11] Lifeng Li, "Multilayer modal method for diffraction gratings of arbitrary profile, depth and permittivity", *J. Opt. Soc. Am. A,* vol. 10, pp. 2581-2591, 1993.

[12] R. Magnusson and T.K. Gaylord, "Equivallence of multiwave coupled-wave theory and modal theroy for periodic-media diffraction", *J. Opt. Soc. Am.,* vol. 68, pp. 1777-1779, 1978.

[13] B. Dhoedt, *"Theoretical and Experimental Study of Free Space Optical Interconnections Based on Diffractive Lens Arrays"* , Ph. D. Thesis, Ghent University, Ghent, 1995.

[14] R. Petit, *Electromagnetic Theory of Gratings* , Berlin: Springer-Verlag, 1980.

[15] S.T. Han, Y.L. Tsao, R.M. Walser and M.F. Becker, "Electromagnetic scattering of two-dimensional surface-relief dielectric gratings", *Appl. Opt.,* vol. 31, pp. 2343-2352, 1992.

[16] J. Chandezon, M.T. Dupuis, G. Cornet and D. Maystre, "Multicoated gratings: a differential formalism applicable in the entire optical region", *J. Opt. Soc. Am. A,* vol. 72, pp. 839-846, 1982.

[17] O.P. Bruno and F. Reitich, "Numerical solution of diffraction problems: a method of variation boundaries", *J. Opt. Soc. Am. A,* vol. 10, pp. 2581-2591, 1993.

[18] P. Lalanne and J.P. Hugonin, "Numerical performance of finite-difference modal methods for the electromagnetic analysis of one-dimensional lamellar gratings", *J. Opt. Soc. Am. A,* vol. 17, pp. 1033-1042, 2000.

[19] Lifeng Li, J. Chandezon, G. Granet and J.P. Plumey, "Rigorous and efficient grating-analysis method made easy for optical engineers," *Appl. Opt.,* vol. 38, pp. 304-313, 1999.

[20] Lord Rayleigh, "On the dynamical theory of gratings", *Proc. Roy. Soc. Ser A* vol. 79, pp. 399-416, 1907.

[21] R.F. Millar, "On the Rayleigh assumptions in scattering by a periodic surface", *Proc. Camb. Phil. Soc.,* vol. 65, pp. 773-791, 1969.

[22] D.A. Pommet, M.G. Moharam and E.B. Grann, "Limits of scalar diffraction theory for diffractive phase elements", *J. Opt. Soc. Am. A,* vol. 11, pp. 1827-1834, 1994.

[23] E.N. Glytsis "Two-dimensioanlly-periodic diffractive optical elements: limitations of scalar analysis", *J. Opt. Soc. Am. A,* vol. 19(4), pp. 702-115, 2002.

[24] P. Lalanne and D. Lemercier-Lalanne, "Depth dependence of the effective properties of subwavelength gratings", *J. Opt. Soc. Am. A,* vol. 14, pp. 450-458, 1997.

[25] E. B. Grann, M.G. Moharam and D.A. Pommet, "Artificial uniaxial and biaxial dielectrics with the use of two-dimensional subwavelength binary gratings", *J. Opt. Soc. Am. A,* vol. 11, pp. 2695-2703, 1994.

[26] Lifeng Li, "Use of Fourier series in the analysis of discontinuous periodic structures", *J. Opt. Soc. Am. A,* vol. 13, pp. 1870-1876, 1996.

[27] P. Lalanne, "Effective properties and band structures of lamellar subwavelength crystals: Plane-wave method revisited", *Phys. Rev. B,* vol. 58, pp. 9801-9807, 1998.

[28] C.L. Liu and J.W.S. Liu, *"Linear system analysis",* New York: McGraw-Hill, 1975.

[29] Lifeng Li, "New formulation of the Fourier modal method for crossed surface-relief gratings", *J. Opt. Soc. Am. A,* vol. 14, pp. 2758-2767, 1997.

[30] P. Lalanne, "Improved formulation of the coupled-wave method for two-dimensional gratings", *J. Opt. Soc. Am. A,* vol. 14, pp. 1592-1598, 1997.

[31] P. St. J Russell, "Power conservtion and field structures in uniform dielectric gratings", *J. Opt. Soc. Am. A,* vol. 1, pp. 293-299, 1984.

4

GA-RCLED: theory and analysis

THE grating-assisted resonant-cavity light-emitting diode, an LED design for high brightness based on a resonant cavity containing one- or two-dimensionally periodically corrugated layers (gratings) is conceptually presented. We give in detail a generally applicable electromagnetic analysis based on the Rigorous Coupled-Wave Theory to calculate the extraction efficiency of spontaneous emission in a periodically corrugated layer structure.

[D. Delbeke, P. Bienstman, R. Bockstaele and R. Baets, "Rigorous Electromagnetic Analysis of Dipole Emission in Periodically Corrugated Layers: the Grating-Assisted Resonant-Cavity Light-Emitting Diode," *J. Opt. Soc. Am. A*, vol. 11(5), pp. 871-880, 2002.]

4.1 Introduction

The increasing use of solid state light sources in commercial applications such as automobile lighting, displays and optical interconnects stimulates the research on high-brightness, highly efficient light emitters. Semiconductor LEDs, mostly showing internal quantum efficiencies close to 100% and having a simple, robust structure and a long lifetime are considered to be suitable candidates for these applications. Ordinary semiconductor LEDs however show an overall efficiency of only a few percent. The external quantum efficiency is limited by total internal reflection at the semiconductor-air interface (e.g. critical angle θ_c for total internal reflection at a GaAs-air interface is only 16°) (see Chapter 2).

Several advanced structures and techniques that enhance the efficiency of the LED have been proposed. They have been presented in Chapter 2 and are shortly listed here. The critical angle θ_c can be increased by embedding the LED in a transparent epoxy dome with high refractive index. If the dome is curved and sufficiently large, all light will hit the epoxy-air interface within the critical angle [1]. Alternatively, the light can be extracted from multiple output planes [1]. Other techniques alter the path of the photon inside the semiconductor until it reaches the semiconductor-air interface within the extraction cone. This can be done in a controlled way, such as the use of LEDs with a radial outcoupling taper [2], [3] or Truncated-Inverted-Pyramid LEDs [4], [5], or in a more randomised way, such as use of the surface-roughened Non-Resonant-Cavity LEDs (NRCLEDs) [6]. The latter achieves overall efficiencies of 46% by redistributing the light at the roughened surface placed on top of the active region and around the mesa [7], [8].

In a Resonant-Cavity LED (RCLED), the spontaneous emission is generated in a Fabry-Pérot resonator, in which interference effects alter the internal angular power distribution (see Chapter 2). The preferential propagation direction of the photons can be forced toward the extraction cone. This increase of directivity and/or efficiency has to be distinguished from the case of enhancement of spontaneous emission rate by the Purcell factor $(3Q/4\pi^2)(\lambda^3/V)$, which occurs in three-dimensional optical cavities of volume V and narrow emission linewidth $\Delta\lambda$ around λ. Because of the rather small reflectivity coefficients of the cavity mirror(s) in most cases, the Purcell factor tends to one, resulting in a negligible enhancement of the spontaneous emission rate. Over the past few years, research on RCLEDs using an electrically pumped p-n diode placed between a metallic mirror/electrical contact and a Distributed Bragg Reflector (DBR) has resulted in devices with overall quantum efficiencies of 28% [9]. However, again, only the resonant power emitted in a limited numerical aperture around the direction perpendicular to the substrate, corresponding to the critical angle θ_c, can be extracted. The optical power coupled to the so-called leaky DBR modes, which are totally internally reflected at the semiconductor-air interface, and the optical power coupled to the laterally propagating modes (the guided modes), which are totally internally reflected at the DBR mirror, is lost (except through partial photon recycling by reabsorption [10]). These losses cause the external extraction efficiency to be substantially lower than 100%.

A solution to this loss of power in the unextractable guided modes can be

found in a two-dimensional (2-D)-periodic wavelength-scaled grating integrated into one or more of the interfaces of the resonant cavity. Several design approaches can be distinguished. Their principle and main assets have been discussed in the last paragraph of Chapter 2. They are shortly listed here. The periodic corrugation can provide a bandgap in the dispersion relation of the guided modes at the frequency of emission. Emission will then initially be prevented in the guided modes [11]. Textured metallic mirrors in thin-film resonant cavities providing a bandgap for the TM_{-1} coupled surface-plasmon polariton mode [12] and the lowest-order TE mode [13] have been demonstrated. Alternatively, the grating can be used for purely optical "photon recycling". The diffractive properties of the periodic grating can redirect the laterally propagating resonant guided mode to an extractable direction in the extraction cone. Because a high fraction of the light is emitted in the guided modes, the use of such gratings should then result in a higher external extraction efficiency. We will hereafter call these devices Grating-Assisted Resonant-Cavity LEDs (GA-RCLEDs) which are the subject of this thesis. This technique has, in parallel with this work, as well been applied to thin film devices [14], [15].

A variation on the latter can be found in a 2-D periodic corrugation at the periphery of the active region. In these devices, the Fabry-Pérot mode is extracted in the central part of the light source where the layers are homogeneous, the guided mode leaves the semiconductor in the surrounding periodically corrugated region [9], [16]- [18].

This chapter presents a model for spontaneous emission in periodically corrugated layer structures. The proposed analysis is equivalent to the one proposed by Rigneault *et al.* [19], but differs in that it includes the dependence of the electric field in the cavity on the in-plane dipole position in relation to the periodic unit cell defined by the Bragg vectors. The electromagnetic analysis presented is applicable for any one-dimensional (1-D)- or 2-D-periodically corrugated layer structure.

First, the device concept is highlighted in greater detail in section 4.2. The section is therefore subdivided in three parts corresponding to the basic issues of a GA-RCLED: *(1)* spontaneous emission in layered structures, a recapitulation of Chapter 2, *(2)* extraction of in-plane propagating waves by means of a grating in passive waveguides and *(3)* the combination of *(1)* and *(2)* or the GA-RCLED. Section 4.3 describes the electromagnetic analysis on which the numerical calculations used to simulate dipole emission inside periodically corrugated layer structures is based. Section 4.4 concludes this chapter.

4.2 Qualitative analysis with Wave-Vector Diagram

4.2.1 Dipole emission in a planar cavity

The angular distribution of spontaneous emission in bulk semiconductors can often be regarded as isotropic. However, when the emitting dipole is placed inside a cav-

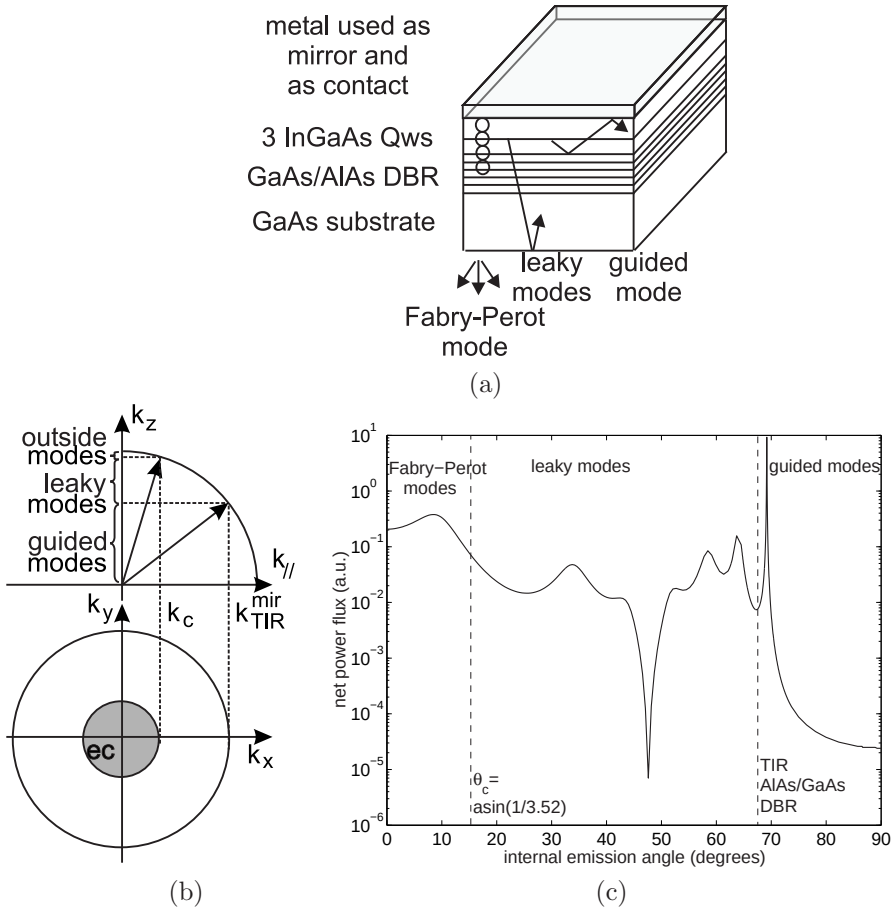

Fig. 4.1: (a)RCLED; (b) k-space presentation of outside, leaky and guided mode with ec the projection of the extraction cone in the $k_x k_y$-plane; (c) typical downwards internal angular emission distribution per unit solid angle in a RCLED, with $\theta = \arcsin(k_{\|}/k)$.

ity, photons can be redistributed by means of interferences (see Chapter 2). Four ways can be distinguished in which the photons are redistributed: *(1)* outside or Fabry-Pérot modes; *(2)* guided modes; *(3)* leaky modes and *(4)* metal absorption in the case in which a metallic mirror is used. The outside modes or Fabry-Pérot modes with $k_{\|} < \omega n_{ext}/c = k_c$ (n_{ext} is the refractive index of the surrounding exterior material and $k_{\|} = k_{xy}$ is the wave vector component lying in the plane of the multi-layer structure) can be extracted (Fig. 4.1(b)). This extraction causes the typically low Q factor of these modes. The guided modes, in contrast, are trapped in the cavity because of total internal reflection (TIR) at the mirror interfaces $\{k_{TIR}^{mir1}, k_{TIR}^{mir2}\}_{max} < k_{\|}$. They show unity round-trip conditions for the complex field amplitude in the absence of damping and consequently a higher Q

factor. When a DBR mirror is used, these guided modes can couple evanescently to the outside medium. In this case they are rather referred to as "quasi"-guided modes. The third channel for redistribution was referred to as leaky modes: photons "leak" through the DBR-mirror when $k_c < k_{\|} < \{k_{TIR}^{mir1}, k_{TIR}^{mir2}\}_{max}$ and are absorbed in the substrate as they total reflect internally at the substrate-vacuum interface. Guided modes, leaky modes and metal absorption cause the external extraction efficiency to be substantially lower than 100%.

The distribution of the photons over the four channels depends strongly on the design of the cavity. An initial distinction has to be made regarding whether a DBR mirror is used in the cavity. Thin-film devices without a DBR mirror do not support leaky modes. The emitted power can be efficiently concentrated in a guided mode when the thin film is adequately designed. Cavities with a DBR mirror, in contrast, do support leaky modes. De Neve optimised a hybrid bottom-emitting cavity with a metallic and a DBR mirror for high extraction efficiency at 980 nm (Fig. 4.1(a)) [20]. Fig. 4.1(c) shows a simulation of the internal angular emission distribution per unit solid angle with an indication of the fraction of the total emitted power in the respective modes ($\theta = \arcsin(k_{\|}/k)$). The outside emission or Fabry-Pérot takes 20-25%. The power lost through the guided mode(s) (power absorbed in absorptive active layer) accounts for 30-35%, through leaky DBR modes 25-35% and through metallic absorption 10-15%. DBR modes cannot be avoided, but they can be minimised by using a higher-contrast DBR mirror, e.g., an AlOx/GaAs DBR [9]. The guided modes can be cut off by using a thinner cavity. However, the power of the latter will be divided over all modes including the leaky DBR-modes, resulting in only marginal extra power in the extractable Fabry-Pérot mode, and most of the power (70%) will be absorbed in the substrate [20]. Since the integration of a more complex doping profile is more accessible in thicker cavities, a thicker cavity supporting the guided mode is to be preferred in electrically pumped devices (see also Chapter 2).

4.2.2 Extraction of in-plane propagating waves by means of a grating

Passive waveguide structures with grating couplers have been widely studied [21]-[23]. A guided mode propagating in a lossless planar waveguide structure equipped with a shallow lossless grating with appropriate period(s) $\mathbf{\Lambda}_i$ ($i = x, y'$) and resulting Bragg vector(s) $\mathbf{K}_i = 2\pi\mathbf{1}_{\Lambda_i}/\Lambda_i$ (see Fig. 4.2 (a) & (d)) can be diffracted entirely toward the extraction cone. This can be easily illustrated by using a wave-vector presentation in the k-space ($(\mathbf{k}_x, \mathbf{k}_y, \mathbf{k}_z) = (\mathbf{k}_{\|}, \mathbf{k}_z)$), with $\mathbf{k}_{\|}$ the projection of $\mathbf{k}$ in the plane of the waveguide (Fig. 4.2). This is called the Wave Vector Diagram (WVD) [19]. Monochromatic light with frequency ν and vacuum wavelength $\lambda_0 = c/\nu$ and wave number $k_0 = 2\pi/\lambda_0$ is considered, with c the velocity of light. In the $\mathbf{k}_{\|}$ plane, the guided mode in the high-refractive-index waveguide (for GaAs $n \approx 3.52$) can be represented by its propagation constant $\beta = |\mathbf{k}_{\|}| = |\mathbf{k}_{0\|}| n_{eff}$ for azimuthal angle φ: $0 \leq \varphi < 2\pi$ and n_{eff} is the effective refractive index of the guided mode. This leads to a circle in the WVD. Waves with in-plane k vector $\mathbf{k}_{\|}$ smaller than $2\pi/\lambda_0$ can escape the waveguide in a non-lateral way. This region of

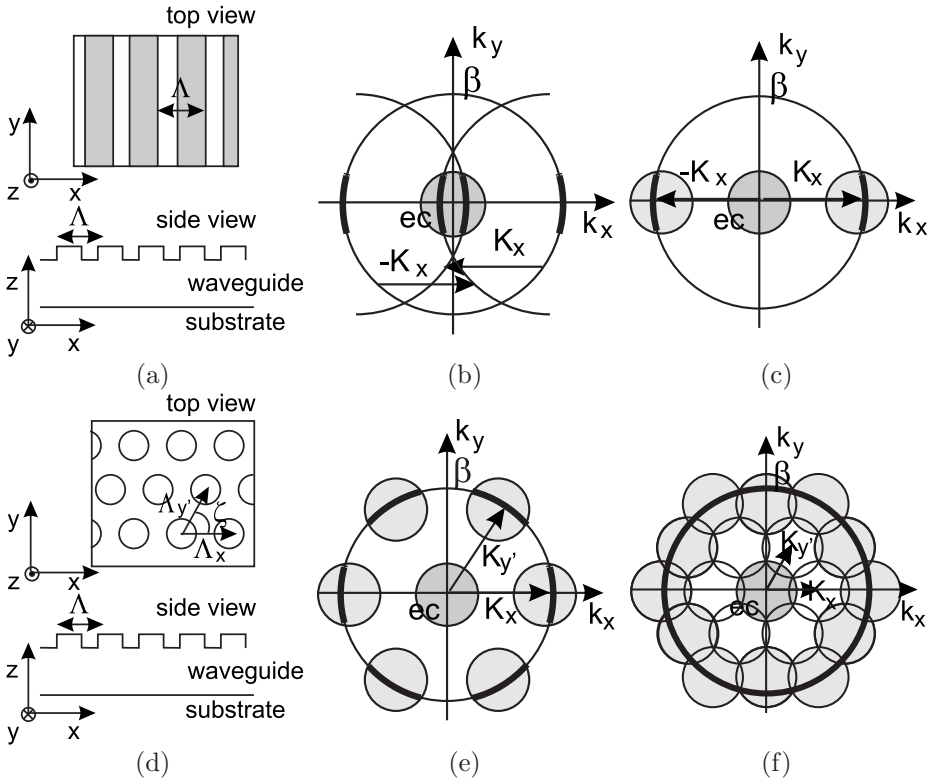

Fig. 4.2: Wave-vector diagram. (a) Top view and side view of waveguide with shallow 1-D grating (b) Extraction of guided mode with propagation constant β using a 1-D first order grating ($\beta \simeq |\mathbf{K}_x|$) presented in the $\mathbf{k}_\parallel$-plane: the guided mode is projected towards the extraction cone (ec), the overlap of the diffracted light and the extraction cone can be extracted. This corresponds with a fraction of 22% of the guided mode. (c) Alternative graphical presentation to calculate upper limit: projection of extraction cone towards guided mode by the Bragg vector. The overlap of the projected cone and the guided mode is limited to 22%. (d) Top view and side view of waveguide with shallow 2-D grating ($\beta \simeq |\mathbf{K}_i|$, i=x,y') (e) analogue graphical presentation for 2-D first order grating (f) 2-D second order grating ($\beta \simeq 2|\mathbf{K}_i|$).

extractable waves is represented in the $\mathbf{k}_\parallel$ plane by the extraction cone disk (ec): $|\mathbf{k}_\parallel| < 2\pi n/\lambda_0$. Since the propagation constant β does not overlap the extraction cone, the guided wave will not be extracted out of the high-refractive-index slab (leaving evanescent coupling aside). However, when the interface of the slab is corrugated with a shallow grating, weakly affecting the propagation constant of the guided wave, waves with $\mathbf{k}_\parallel = \mathbf{k}_{0\parallel} n_{eff} + m\mathbf{K}_x + n\mathbf{K}_{y'}$, m, n integer, will be present according the Floquet-Bloch theorem. The guided mode will continuously couple power to these diffracted waves and vice versa. This can be represented in the WVD by a projection of the "guided" wave, represented in the WVD by the circle

with radius β, toward the extraction cone along the Bragg vector (Fig. 4.2(b)). The overlapping part of the diffracted wave with the extraction cone can escape the waveguide. Thus the guided mode will leak power towards the extraction cone by means of diffracted waves. The appropriate period and lattice structure of the grating to maximise overlap depend on the dielectric-constant differences among the core, cladding and vacuum. With a 1-D grating and a waveguide configuration representative of GaAs RCLEDs, up to 22% of the diffracted guided wave overlaps the extraction cone (marked bold in Fig. 4.2(b)). This 22% represents a maximum of the extractable fraction of the guided wave in this configuration. This can alternatively be represented graphically by a translation of the extraction cone toward the guided wave (Fig. 4.2(c)) instead of the translation of the circle that represents the guided wave toward the extraction cone disk. The overlap of the guided mode and the translated extraction cone (marked bold) again represents an upper limit of the extraction efficiency. With a 2-D grating, the extraction efficiency can be increased. Traditionally the spatial arrangement of 2-D photonic crystals corresponds to one of the five 2-D Bravais lattices. Among these five lattices, the triangular and honeycomb ones possess the highest order of rotational symmetry (six) and the Brillouin zone that is the closest to the circle. A 2-D triangular grating increases the maximal obtainable extraction efficiency of the guided wave to 66% with a first-order grating (the guided mode is coupled toward the extraction cone through first-order diffraction)(Fig. 4.2(e)) and to 100% with a second-order grating (the guided mode is coupled toward the extraction cone through second-order diffraction)(Fig. 4.2(f))[1]. This means that only if extraction would be the sole "loss" mechanism, 100% of the guided mode could be extracted.

Nevertheless, a light propagation direction dependent behavior remains. Photonic quasi-crystals have been studied in the search for structures with even more isotropic optical properties, e.g. the archimedean-like tilings with 12-fold rotational symmetry composed of regular convex polygons arranged identically around each vertex [17], [24]. More sophisticated is a grating which combines refraction or Bragg coupling of the guided wave for propagation directions corresponding to the Bragg vectors and inhibition or a stopband for this wave propagating in all other directions. The guided modes are then supported only in a small angular domain corresponding to the reciprocal lattice points of the diffraction grating. Impeding propagation of the guided waves in most directions has mainly two consequences. The presence of arcs in the spatial distribution of the emitted light is directly linked to the fact that the guided modes are excited in any direction of the XY-plane. Inhibition of the guided waves in all directions but some small angular well defined directions will result in extraction of the light in a very directive manner [25]. Secondly, a first order grating can be used to extract the angularly well-defined propagation guided modes. Competition between diffraction towards the substrate, graphically presented in Fig. 4.2(f) by the inner ring of circles, and

[1]We call a first order grating a grating where the guided mode is diffracted towards the extraction cone via the first order diffraction, a second order grating is a grating that diffracts the guided mode to the extraction cone via the second order. This is a semantic agreement. In other grating applications (e.g. DFB lasers), the grating order is specified by the total amount of propagative diffraction orders. The grating we call a first order grating is in that case a second order grating.

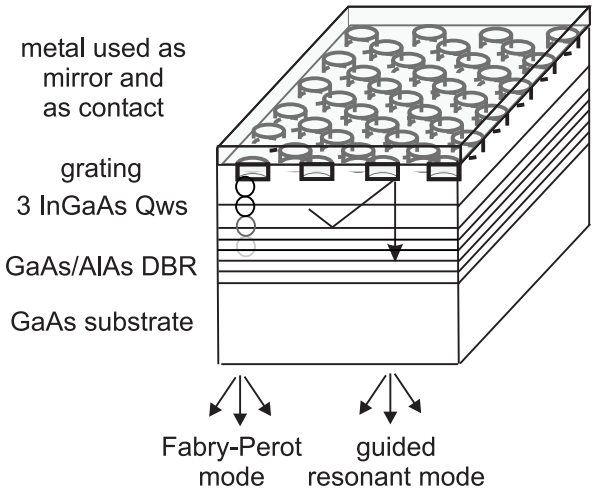

Fig. 4.3: Sketch of Grating-Assisted Resonant-Cavity LED.

extraction, the ec disk, is in this case avoided.

It is worth emphasizing that this graphic analysis indicates qualitatively to what extent a grating structure can extract an in-plane guided mode. It only represents an upper limit of the extractable fraction of the guided wave. Quantitative information, e.g., the fraction of photons in the respective modes or absorption losses has to be found by a rigorous analysis (see Section 4.3).

4.2.3 Grating-Assisted RCLED

In a way similar to the extraction of a guided wave from a corrugated passive waveguide, the guided mode excited by a dipole placed inside a periodically corrugated layer structure can escape the cavity when the period, depth, filling factor, lattice structure of the grating and the cavity thickness are chosen appropriately.

In the case of monomodal thin-film devices, the guided mode can be directly extracted [19].

With the use of a hybrid bottom-emitting cavity with metallic and DBR mirrors sustaining an extractable Fabry-Pérot mode, guided mode(s) and leaky DBR modes, the grating will couple the guided mode to the extractable Fabry-Pérot mode and vice versa. If the extractable resonant surface normal mode has a lower Q-factor than the non-extractable high-Q guided mode, reciprocal coupling of power between the resonant systems will result in a net power flow from the guided mode to the extraction cone, in case of negligible absorptions. This is studied with the rigorous analysis presented in the next paragraph. The conceptual design of a GA-RCLED is depicted in Fig. 4.3.

4.3 Rigorous Analysis

Spontaneous emission in a non-absorbing[2] layer surrounded by two periodically modulated stratified media is theoretically investigated. The source and surrounding layers are infinitely extended in the x and y directions. We derive the radiation pattern of the source plane, i.e., the angular distribution of the light emitted into media 1 and 2 (see Fig. 4.4). The luminescent centers are considered to emit the light in an electric dipole transition. The radiating electric dipole oscillates with fixed frequency ω, fixed dipole moment and arbitrary but fixed orientation θ_d and φ_d. The source plane is then considered as an arrangement of arbitrarily oriented and incoherent dipoles. The theory is classical, i.e. Maxwell's equations are solved together with a constitutive relation between the electric field and displacement field. In section 4.3.2 the radiation pattern of a dipole in bulk media is depicted. In section 4.3.3 the electromagnetic boundary-value problem for a source located between two partially reflecting interfaces is solved. The general expression for the angular distribution of the power is derived, the external quantum efficiency is calculated. First, the radiation dipole transition is related to a classical oscillating dipole.

4.3.1 Electric dipole transition

According to the correspondence principle [28]- [31], the quantum theoretical expression for spontaneous emission radiated by an excited state in an electric dipole transition is obtained from the classical expression for the power radiated by an electric dipole by replacement of the dipole moment by the corresponding transition matrix. This rule, well-known for atomic systems in free space, holds also for systems embedded in a stratified medium in the case of the weak-coupling regime. As is well known, spontaneous emission is not an immutable property of an atom but is a consequence of the coupling between the atom and the electromagnetic field. In the weak-coupling regime, like in low Q-cavities with $\omega/\Delta\omega_c$ small, the spontaneous emission is an irreversible process. The emitted photon is damped rapidly and an atom undergoes radiative decay much as it does in free space. In spite the weakness of the coupling, a modified spontaneous-emission decay rate and altered radiation pattern have been demonstrated e.g. for emission in stratified layered media [31]. [3]

We consider an emitter D at a position $\mathbf{r}(0, 0, z_0)$ in a thin lossless dielectric layer of real refractive index n_s and thickness d_s between two adjoining media 1 and 2 (see Fig. 4.4). Media 1 and 2 are planar stratified in the z-direction

[2] In realistic situations, the dipole emits in an absorbing layer. Due to the lack of Stokes shift at room temperature of most semiconductor materials [27], the light emitted in a layer can be absorbed within this layer. By letting the emission happen in a non-absorbing dielectric thin layer with thickness $d_s = 0$ squeezed in the absorbing layer, the realistic situation will be adequately analysed. A short note on infinitely thin active layers is given in section 4.3.4.1.

[3] In the case of a strong coupling, like in high Q-cavities with $\omega/\Delta\omega_c$ very high, the radiation remains so long in the cavity that there is a high probability it will be reabsorbed by the atom before it dissipates. Spontaneous emission becomes partially reversible, as the atom and the field exchange energy coherently. This strong coupling regime falls outside of the scope of this thesis. The reader is referred to [32] for further information.

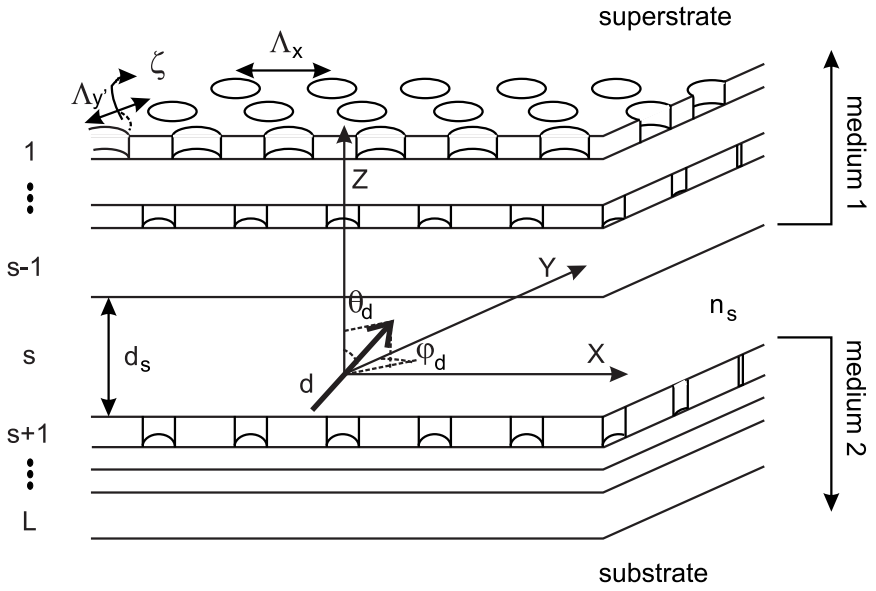

Fig. 4.4: Structure of a light-emitting multi-layer device. The emitting medium has a refractive index n_s. The emitting layer has a thickness d_s. An electric dipole is situated at the origin and has an orientation θ_d and φ_d.

(or growth direction) and periodic in the x- and/or y-direction. All three media are assumed to consist of linear, isotropic and non-magnetic ($\mu = 1$) materials. The spontaneous emission rate $A(z_0)$ for a system D at a location $z = z_0$ times the photon energy $E = \hbar\omega$ is equal to the expectation value $L(z_0)$ of the energy emitted in unit time per excited system:

$$A(z_0) = L(z_0)/\hbar\omega \tag{4.1}$$

According to the correspondence principle, L is given by the expression for the total power radiated by a classical dipole in which the classical dipole moment has been replaced by the transition dipole moment. The classical dipole is located at the position $\mathbf{r}(0, 0, z_0)$ of the emitter D, it oscillates with fixed frequency equal to the transition frequency ω, and with fixed dipole moment and orientation θ_d (angle with positive z-axis) and φ_d(angle with positive y-axis). We are only interested in the normalised spontaneous emission rate $A(z_0)/A_{n_s}$, with A_{n_s} the spontaneous emission rate of the respective emitter D in an infinite homogeneous medium of refractive index n_s. With Eq.(4.1), the normalised spontaneous emission rate of an electric dipole transition is equal to the normalised power radiated by the dipole:

$$A(z_0)/A_{n_s} = L(z_0)/L_{n_s} \tag{4.2}$$

L_{n_s} is the total power radiated by the dipole in the infinite medium of refractive index n_s. Since we assumed linear constitutive relations for media 0,1 and 2, the dipole field is linear in the dipole moment. Consequently, the radiated power is

proportional to the square of the dipole moment and the normalised radiated power $L(z_0)/L_{n_s}$, or with Eq.(4.2) the normalised spontaneous emission rate $A(z_0)/A_{n_s}$ does not depend on the transition dipole moment. The basic assumption leading to Eq.(4.2) is that neither the transition matrix element nor the transition frequency are appreciably changed by the presence of the interfaces.

The radiative lifetime is defined as $\tau(z_0) = 1/A(z_0)$. From Eq.(4.2) follows

$$\tau(z_0)/\tau_{n_s} = [L(z_0)/L_{n_s}]^{-1} \tag{4.3}$$

The total power $L(z_0)$ radiated by the dipole in the stratified medium in units of the power L_{n_s} by the same dipole in an unbounded medium can be calculated through integration of the normalised radiation pattern $P_{s(p)}(\theta_2, \varphi)$ over the solid angle 4π.

$$\int_{2\pi} [P_s(\theta_1, \varphi) + P_p(\theta_1, \varphi)]\, d\Omega_1 + \int_{2\pi} [P_s(\theta_2, \varphi) + P_p(\theta_2, \varphi)]\, d\Omega_2 = \frac{L(z_0)}{L_{n_s}} \tag{4.4}$$

$P_{s(p)}(\theta_i, \varphi) d\Omega$ denotes to the normalised power in medium i emitted as s(p)-polarised light by the dipole in the direction $\mathbf{1}_k$ into the solid angle $d\Omega_i = \sin\theta_i d\theta_i d\phi$, with $i = 1, 2$ (evanescent coupling and absorption are included). The unit vector $\mathbf{1}_k$ in the direction of observation is given by $(\sin\theta_i \cos\varphi, \sin\theta_i \sin\varphi, \cos\theta_i)$, where θ_i denotes the angle θ between the z-axis and $\mathbf{1}_k$ in medium i and φ the azimuthal angle. In an s- and p-polarised wave the electric and magnetic fields, respectively are perpendicular to the plane of emission. We call the plane containing the unit vector $\mathbf{1}_k$ and the z-axis the plane of emission, in analogy to the term plane of incidence. Since s- and p-polarised waves do not interfere, they contribute additively to the total power emitted into $d\Omega$.

The power emitted per unit solid angle in the surface normal direction or z-direction is defined as the projection of the time-averaged energy flow $\langle \mathbf{S} \rangle = \langle \mathbf{E} \times \mathbf{H} \rangle$ on the surface normal direction:

$$L_{n_s} P_{s(p)}(\theta_i, \varphi) \cos(\theta) d\Omega_i = \mathbf{1}_z \cdot \langle \mathbf{S}(\mathbf{r}) \rangle d\Omega_i \tag{4.5}$$

With $\langle \mathbf{S}(\mathbf{r}) \rangle = 1/2 \mathrm{Re}[\mathbf{E}(\mathbf{r}) \times \mathbf{H}^*(\mathbf{r})]$ the radiation pattern can be calculated from the electric and magnetic monochromatic dipole field.

The analysis above states that the radiative lifetime change for electric dipole transitions can be determined by calculating the normalised radiation pattern, which on its turn is defined by the electric and magnetic dipole field. Section 4.3.2 derives the plane wave decomposition of the electric dipole field. The reference total spontaneous emission rate of a dipole suspended in a bulk medium is derived and set to one. In section 4.3.3, an expression for the normalised radiation pattern and power of an in-plane distribution of arbitrary oriented dipoles in a 2-D periodically corrugated stratified medium is formulated. The derivation can be split in several steps. In section 4.3.3.1 a matrix notation is adopted to express Bragg coupling of the plane waves emitted by the dipole. The external field of a single dipole with fixed orientation situated at the origin is derived in section 4.3.3.2.

The dependence of the reflection and transmission coefficients at the interface of the periodically modulated media on the position of the source stipulated in section 4.3.3.3 is used in section 4.3.3.4 to calculate the external field of an arbitrary positioned dipole. The intensity of an in-plane distribution of mutually incoherent dipoles with identical orientation is given in section 4.3.3.5. This expression is averaged over the source's orientation in section 4.3.3.6. This final expression is used in section 4.3.3.7 to calculate the extraction efficiency of an in-plane distribution of monochromatic dipoles in a GA-RCLED. Some numerical implementation aspects are discussed in section 4.3.4 and section 4.3.5 formulates the external efficiency.

4.3.2 Unperturbed electric dipole radiation pattern

The calculation of the radiation pattern of a dipole will make use of the transfer matrix formalism. In this formalism, the radiation pattern of a source in a layered medium is calculated by letting the plane wave components of the source, both propagative and evanescent, propagate through the layered medium. The dipole field has to be decomposed into plane waves of the form:

$$\mathbf{E}_{dip}(\mathbf{k},\mathbf{r}) = \mathbf{A}(\mathbf{k})e^{-j\mathbf{k}.\mathbf{r}} \tag{4.6}$$

where $|\mathbf{k}| = n_s k_0$ to satisfy Maxwell's sourceless equations, with $k_0 = \omega/c = 2\pi/\lambda_0$ the vacuum wave vector, λ_0 the vacuum wavelength. The $\mathbf{k}$-vector of propagative wave components is normal to the phasefront and its direction is that of the energy flow. Plane waves form a set of orthogonal eigenfunctions of a uniform medium [35], [36].

We consider a dipole with dipole moment $\mathbf{d}$ embedded in a loss-free medium with refractive index n_s. Its orientation is described by the angle θ_d and the azimuthal angle φ_d (Fig. 4.4). Medium 1 and 2 are planar stratified. SI units are used and the time dependence $\exp(j\omega t)$ of monochromatic fields is suppressed. An electric dipole can be decomposed in a horizontal electric dipole (with dipole moment $\mathbf{d}_h$ in the (x-y) plane) and a vertical electric dipole (with dipole moment $\mathbf{d}_v$ along the z-axis). In bulk semiconductor material the dipole can have any orientation or equivalently one third of the power generated by the dipoles is generated by vertical dipoles and two thirds by horizontal dipoles.

$$\langle \mathbf{d} \rangle = \frac{2}{3}\langle \mathbf{d}_h \rangle + \frac{1}{3}\langle \mathbf{d}_v \rangle \tag{4.7}$$

In unstrained quantum wells there is a substantial preference for emission through horizontal dipoles [33]. Furthermore, if a compressive strain is added to the QW, a strong enhancement of radiation through horizontal dipoles is realised, while tensile strain enhances vertical dipoles [34].

In the uniform layer with refractive index n_s, Maxwell's equations can be written in phasor notation as:

$$\begin{aligned} \nabla^2 \mathbf{E}_{dip} + k_0^2 n_s^2 \mathbf{E}_{dip} &= \mathbf{source} \\ \mathbf{H}_{dip} &= \frac{j}{\omega\mu_0}\nabla \times \mathbf{E}_{dip} \end{aligned} \tag{4.8}$$

with **source** $= \delta(x,y,z).\mathbf{p}$ representing the spontaneous emission and $\mathbf{E}_{dip} = \mathbf{E}_{dip}(x,y,z)$, $\mathbf{H}_{dip} = \mathbf{H}_{dip}(x,y,z)$ the phasor representations of the time dependent electric and magnetic field, respectively. The distinction between the field of the horizontal component $\mathbf{p}_h$ and the vertical component $\mathbf{p}_v$ is omitted for clarity. The time dependent field can be obtained taking the real part of the phasor times $\exp(j\omega t)$.

In order to derive the plane wave expansion, the two-dimensional Fourier transform of the field solution of Eq.(4.8) is taken with respect to x and y (in the stratified medium with interfaces normal to the z-axis, the source layer is homogenous in both the x and y direction):

$$\mathbf{E}_{dip}(k_x,k_y,z) = \int_{-\infty}^{+\infty}\int_{-\infty}^{+\infty} \mathbf{E}_{dip}(x,y,z)e^{j(k_x x+k_y y)}dxdy \tag{4.9}$$

$\mathbf{E}_{dip}(k_x,k_y,z)$ denotes the Fourier transform of $\mathbf{E}_{dip}(x,y,z)$. The spatial frequencies are real and have a range from $-\infty$ to $+\infty$. The inverse Fourier transform is given by:

$$\mathbf{E}_{dip}(x,y,z) = \frac{1}{(2\pi)^2}\int_{-\infty}^{+\infty}\int_{-\infty}^{+\infty} \mathbf{E}_{dip}(k_x,k_y,z)e^{-j(k_x x+k_y y)}dk_x dk_y \tag{4.10}$$

or equivalently:

$$\mathbf{E}_{dip}(x,y,z) = \frac{1}{(2\pi)^2}\int_{-\infty}^{+\infty}\int_{-\infty}^{+\infty} \mathbf{E}_{dip}(k_x,k_y,z)e^{jk_z z}e^{-j(k_x x+k_y y+k_z z)}dk_x dk_y \tag{4.11}$$

with

$$k_z = \pm\sqrt{n_s^2k_0^2 - k_x^2 - k_y^2} = \pm\sqrt{n_s^2k_0^2 - k_\parallel^2} \tag{4.12}$$

The term $\exp(-j(k_x x + k_y y + k_z z))$ is a plane wave with **k**-vector (k_x,k_y,k_z)[4]. The expression (4.11) has the meaning of a plane wave expansion. The $\mathbf{k}_\parallel = \mathbf{k}_x + \mathbf{k}_y$ Fourier spectrum contains arbitrarily large wave vectors $\mathbf{k}_x$ and $\mathbf{k}_y$, spanning propagative ($|\mathbf{k}_\parallel| \le n_s k_0$) and evanescent contributions ($|\mathbf{k}_\parallel| > n_s k_0$). The sign of the expression in Eq.(4.12) can be known from the a priori knowledge of a dipole field: waves propagate upwards for $z > 0$ and downwards for $z < 0$.

An analytical expression for $\mathbf{E}_{dip}(k_x,k_y,z)$ can be found either by calculating the Fourier transform of $\mathbf{E}_{dip}(x,y,z)$ directly or -more conveniently- by taking the 2-D Fourier transform of the wave equation Eq.(4.8):

$$\frac{d^2}{dz^2}\mathbf{E}_{dip}(k_x,k_y,z) + \left(n_s^2k_0^2 - k_x^2 - k_y^2\right)\mathbf{E}_{dip}(k_x,k_y,z) = \delta(z)\mathbf{p}(k_x,k_y) \tag{4.13}$$

[4]The conventional definition of Fourier transform uses a minus-sign in front of the argument $j(k_x x+k_y y)$ for the forward transform and a plus-sign for the inverse transform. Here we use the opposite convention so that a spatial frequency component with positive k_x and k_y corresponds to a plane wave travelling in the positive x- and y-direction. This choice is related to the (arbitrary) sign choice of the argument $+j\omega t$ in the field-phasor notation.

of which the solution is:

$$\mathbf{E}_{dip}(k_x,k_y,z)=\frac{j}{2\sqrt{n^2k_0^2-k_x^2-k_y^2}}e^{-j\sqrt{n^2k_0^2-k_x^2-k_y^2}|z|}\mathbf{p}(k_x,k_y) \tag{4.14}$$

for the square root the solution with zero or negative imaginary part has to be chosen. Inserting this solution in Eq.(4.10) leads to:

$$\begin{aligned}&\mathbf{E}_{dip}(x,y,z)\\&=\frac{1}{(2\pi)^2}\int_{-\infty}^{+\infty}\int_{-\infty}^{+\infty}\frac{j}{2\sqrt{n^2k_0^2-k_x^2-k_y^2}}e^{-j\left(k_xx+k_yy+\sqrt{n^2k_0^2-k_x^2-k_y^2}|z|\right)}\mathbf{p}(k_x,k_y)dk_xdk_y\end{aligned} \tag{4.15}$$

Arranging the integrand of the Fourier transformation properly, the plane wave under consideration -in Eq.(4.15) a density per unit spatial frequency dk_xdk_y- can be expressed as a density per unit solid angle $d\Omega=\sin\theta d\theta d\varphi=dk_xdk_y/n_sk_0k_z$:

$$\begin{aligned}&\mathbf{E}_{dip}(x,y,z)\\&=\int_{-\infty}^{+\infty}\int_{-\infty}^{+\infty}\left[\frac{jn_sk_0}{2(2\pi)^2}\mathbf{p}(k_x,k_y)\right]e^{-j\left(k_xx+k_yy+\sqrt{n^2k_0^2-k_x^2-k_y^2}|z|\right)}\left[\frac{dk_xdk_y}{n_sk_0k_z}\right]\\&=\left(\int_0^{\pi/2}+\int_{\pi/2+j0}^{\pi/2+j\infty}\right)\int_0^{2\pi}\left[\frac{jn_sk_0}{2(2\pi)^2}\mathbf{p}(\theta,\varphi)\right]e^{-j\left(k_xx+k_yy+\sqrt{n^2k_0^2-k_x^2-k_y^2}|z|\right)}\left[\sin\theta d\theta d\varphi\right]\end{aligned} \tag{4.16}$$

In both expressions, the second factor is a plane wave, upwards propagating for $z>0$, downwards propagating for $z<0$. The third factor is the solid angle and the first factor represents the plane wave field (per unit solid angle), we call $\mathbf{A}$:

$$\mathbf{A}=\left[\frac{jn_sk_0}{2(2\pi)^2}\mathbf{p}\right] \tag{4.17}$$

The field resulting from an electric dipole (with orientation angles θ_d and φ_d and situated at $(x,y,z)=(0,0,0)$) has its electric field in the plane of the dipole moment and the direction of observation $\mathbf{1}_k$, vanishing sinusoidally for emission in the direction of the dipole moment [37] (Fig. 4.5). Decomposing the dipole moment in a vertical and horizontal dipole, disintegrating the linear polarisation into s and p and normalising the over the dipole orientation φ_d and θ_d averaged L_{n_s} (the total power radiated by the dipole in the infinite medium n_s) yields for $\mathbf{A}=[A_s,A_p]$ the values summarised in Table 4.1 (the term of proportion $1/2\sqrt{\varepsilon/\mu_0}$ in the power expression is omitted for simplicity). The sign of upwards ($\uparrow$) and downwards ($\downarrow$) propagating fields is related with the arbitrary choice of the sign conventions for s and p as illustrated in Fig. 4.6.

The unperturbed dipole field is represented as a superposition of s- and p-polarised plane and evanescent waves ($|\mathbf{k}_\parallel|=k_\parallel>n_sk_0$). This representation is rigorously valid both in the dipole's far field and near field.

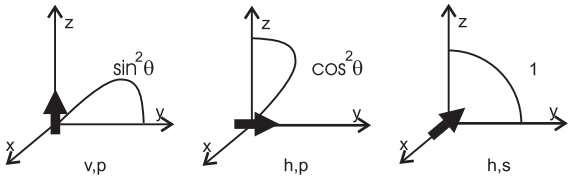

Fig. 4.5: Emission pattern of dipoles in bulk media (a) vertical dipole emitting p-polarised light; (b) horizontal dipole emitting p-polarised light; (c) horizontal dipole emitting s-polarised light.

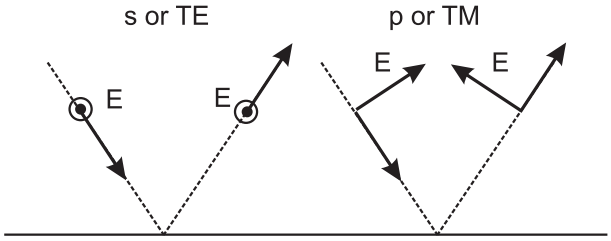

Fig. 4.6: Sign convention for s and p.

4.3.3 Dipoles in periodically modulated stratified medium

4.3.3.1 Bragg-coupled set of plane waves

To calculate the radiation pattern of the dipole, we use the transfer matrix formalism. In this formalism, the radiation pattern of the source in a layered medium is calculated by letting the plane wave components, both propagative and evanescent, of the source propagate through the layered medium. This formalism has been elaborated by Benisty *et al.* [38] and De Neve [20] for dipole emission in homogeneous layered media and was shortly recapitulated in Chapter 2. The formalism applied in periodically modulated stratified medium is detailed here.

The layered medium under consideration shows a 2-D periodic modulation with Λ_x the period along $\mathbf{1}_x$ and $\Lambda_{y'}$ the period along $\mathbf{1}_{y'} = \cos\zeta\mathbf{1}_x + \sin\zeta\mathbf{1}_y$. In Chapter 3, we showed that according to the Bragg condition, an incident plane wave with an in-plane wave vector component $\mathbf{k}_{\|}^{in} = \mathbf{k}_{\|}^{00}$ gives rise to a set of plane waves with in-plane wave vector component $\mathbf{k}_{\|}^{mn}$ and vice versa.

$$\mathbf{k}_{\|}^{mn} = \mathbf{k}_{\|}^{in} + (m - M)\mathbf{K}_x + (n - N)\mathbf{K}_{y'} \tag{4.18}$$

$\mathbf{K}_x = 2\pi/\Lambda_x\mathbf{1}_x$ and $\mathbf{K}_{y'} = 2\pi/\Lambda'_y\mathbf{1}'_y$ are the respective Bragg vectors of the periodic corrugation. m, n are integers. In the numerical calculations, we restrict the number of diffracted orders for the respective periodic directions to M and N. To express this Bragg coupling between a set of plane waves, we define the field matrix $\overline{\mathbf{E}}$[5], a $MN \times 1$ column matrix, the field reflection matrix $\overline{\overline{\mathbf{R}}}$, the field

[5]A vector is denoted with a bold typeface, a 1-D matrix is marked as overlined, a square matrix is twice overlined. e.g. $\overline{\overline{\mathbf{B}}}$ is a square matrix with vectorial elements.

TABLE. 4.1: Source Terms for Horizontal and Vertical dipoles.

	s	p
Hor.	$A^h_{s\uparrow\downarrow} = \sqrt{\frac{3}{8\pi}}\sin(\varphi_d - \varphi)\sin\theta_d$	$A^h_{p\uparrow\downarrow} = \pm\sqrt{\frac{3}{8\pi}}\cos\theta\cos(\varphi_d - \varphi)\sin\theta_d$ $= \pm\sqrt{\frac{3}{8\pi}}\frac{k_z}{n_s k_0}\cos(\varphi_d - \varphi)\sin\theta_d$
Vert.	$A^v_{s\uparrow\downarrow} = 0$	$A^v_{p\uparrow\downarrow} = \sqrt{\frac{3}{8\pi}}\sin\theta\cos\theta_d$ $= \sqrt{\frac{3}{8\pi}}\frac{k_\parallel}{n_s k_0}\cos\theta_d$

transmission matrix $\overline{\overline{\mathbf{T}}}$ and the field propagation matrix $\overline{\overline{\mathbf{P}}}$, $MN \times MN$ matrices. The elements of the respective matrices are defined in Eq.(4.19)-Eq.(4.22):

$$\overline{\mathbf{E}}[Nm+n] = \mathbf{E}^{mn} \tag{4.19}$$

with $\mathbf{E}^{mn}$ the electric field with in-plane wave vector $\mathbf{k}_\parallel^{mn}$,

$$\overline{\overline{\mathbf{R}}}[Nm+n, Nm'+n'] = \mathbf{r}^{mn,m'n'} \tag{4.20}$$

with $\mathbf{r}^{mn,m'n'}$ the field reflection coefficient when excited from a direction with in-plane wave vector $\mathbf{k}_\parallel^{m'n'}$ to a direction with in-plane wave vector $\mathbf{k}_\parallel^{mn}$,

$$\overline{\overline{\mathbf{T}}}[Nm+n, Nm'+n'] = \mathbf{t}^{mn,m'n'} \tag{4.21}$$

with $\mathbf{t}^{mn,m'n'}$ the field transmission coefficient when excited from a direction with in-plane wave vector $\mathbf{k}_\parallel^{m'n'}$ to a direction with in-plane wave vector $\mathbf{k}_\parallel^{mn}$,

$$\overline{\overline{\mathbf{P}}}(z) = \mathrm{diag}[\exp(-jk_z^{mn}z)] \tag{4.22}$$

with $\exp(-jk_z^{mn}z)$ the field propagation coefficient for waves with in-plane wave vector $\mathbf{k}_\parallel^{mn}$.

The elements of the respective matrices are vectors. To go over to scalar matrix expressions, the vectors are decomposed in s and p polarisation. This results in a $2MN \times 1$ field matrix $\overline{\mathrm{E}}$, and a $2MN \times 2MN$ field reflection matrix $\overline{\overline{\mathrm{R}}}$, field transmission matrix $\overline{\overline{\mathrm{T}}}$ and diagonal field propagation matrix $\overline{\overline{\mathrm{P}}}$. The field matrix and field reflection matrix are given in Eq.(4.23) and Eq.(4.24). The transmission matrix and field propagation matrix can analogously be derived from Eq.(4.21)

and Eq.(4.22).

$$\overline{\mathrm{E}} = \begin{bmatrix} E_s^{00} \\ E_s^{01} \\ \vdots \\ E_s^{0N} \\ E_s^{10} \\ E_s^{11} \\ \vdots \\ E_s^{MN} \\ -j\sqrt{\mu_0/\varepsilon_0}H_p^{00} \\ -j\sqrt{\mu_0/\varepsilon_0}H_p^{01} \\ \vdots \\ -j\sqrt{\mu_0/\varepsilon_0}H_p^{0N} \\ -j\sqrt{\mu_0/\varepsilon_0}H_p^{10} \\ -j\sqrt{\mu_0/\varepsilon_0}H_p^{11} \\ \vdots \\ -j\sqrt{\mu_0/\varepsilon_0}H_p^{MN} \end{bmatrix} \tag{4.23}$$

where E_s^{mn} and H_p^{mn} are the complex amplitudes of the electric- and magnetic-field vectors normal to the diffraction plane with an in-plane wave vector $\mathbf{k}_\parallel^{mn}$. They are considered to be respectively the s and p polarisation factor of the corresponding diffraction order. The term $-j\sqrt{\mu_0/\varepsilon_0}$ is in accordance with the reflection and transmission coefficients calculated by the RCWA (see Chapter 3).

$$\overline{\overline{\mathrm{R}}} = \begin{bmatrix} r_{ss}^{00,00} & r_{ss}^{00,01} & \cdots & r_{ss}^{00,MN} & r_{sp}^{00,00} & r_{sp}^{00,01} & \cdots & r_{sp}^{00,MN} \\ r_{ss}^{01,00} & r_{ss}^{01,01} & \cdots & r_{ss}^{01,MN} & r_{sp}^{01,00} & r_{sp}^{01,01} & \cdots & r_{sp}^{01,MN} \\ \vdots & \vdots & \ddots & \vdots & \vdots & \vdots & \ddots & \vdots \\ r_{ss}^{0N,00} & r_{ss}^{0N,01} & \cdots & r_{ss}^{0N,MN} & r_{sp}^{0N,00} & r_{sp}^{0N,01} & \cdots & r_{sp}^{0N,MN} \\ r_{ss}^{10,00} & r_{ss}^{10,01} & \cdots & r_{ss}^{10,MN} & r_{sp}^{10,00} & r_{sp}^{10,01} & \cdots & r_{sp}^{10,MN} \\ r_{ss}^{11,00} & r_{ss}^{11,01} & \cdots & r_{ss}^{11,MN} & r_{sp}^{11,00} & r_{sp}^{11,01} & \cdots & r_{sp}^{11,MN} \\ \vdots & \vdots & \ddots & \vdots & \vdots & \vdots & \ddots & \vdots \\ r_{ss}^{MN,00} & r_{ss}^{MN,01} & \cdots & r_{ss}^{MN,MN} & r_{pp}^{MN,00} & r_{pp}^{MN,01} & \cdots & r_{pp}^{MN,MN} \\ r_{ps}^{00,00} & r_{ps}^{00,01} & \cdots & r_{ps}^{00,MN} & r_{pp}^{00,00} & r_{pp}^{00,01} & \cdots & r_{pp}^{00,MN} \\ r_{ps}^{01,00} & r_{ps}^{01,01} & \cdots & r_{ps}^{01,MN} & r_{pp}^{01,00} & r_{pp}^{01,01} & \cdots & r_{pp}^{01,MN} \\ \vdots & \vdots & \ddots & \vdots & \vdots & \vdots & \ddots & \vdots \\ r_{ps}^{0N,00} & r_{ps}^{0N,01} & \cdots & r_{ps}^{0N,MN} & r_{pp}^{0N,00} & r_{pp}^{0N,01} & \cdots & r_{pp}^{0N,MN} \\ r_{ps}^{10,00} & r_{ps}^{10,01} & \cdots & r_{ps}^{10,MN} & r_{pp}^{10,00} & r_{pp}^{10,01} & \cdots & r_{pp}^{10,MN} \\ r_{ps}^{11,00} & r_{ps}^{11,01} & \cdots & r_{ps}^{11,MN} & r_{pp}^{11,00} & r_{pp}^{11,01} & \cdots & r_{pp}^{11,MN} \\ \vdots & \vdots & \ddots & \vdots & \vdots & \vdots & \ddots & \vdots \\ r_{ps}^{MN,00} & r_{ps}^{MN,01} & \cdots & r_{ps}^{MN,MN} & r_{ps}^{MN,00} & r_{ps}^{MN,01} & \cdots & r_{ps}^{MN,MN} \end{bmatrix} \tag{4.24}$$

with $r_{sp}^{mn,m'n'}$ the amplitude field reflection coefficient when excited from a

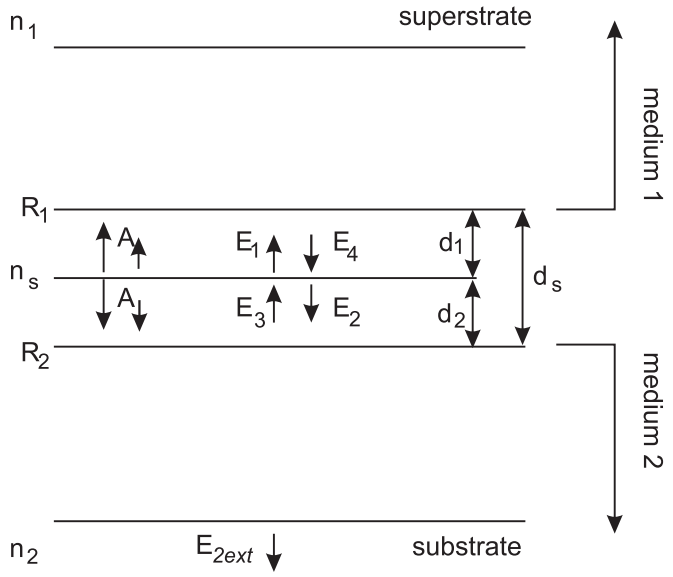

Fig. 4.7: Plane-wave formalism in multi-layer periodically corrugated structure.

direction with in-plane wave vector $\mathbf{k}_{\|}^{m'n'}$ and polarisation p to a direction with in-plane wave vector $\mathbf{k}_{\|}^{mn}$ and polarisation s. Analogous interpretations account for respectively $r_{ps}^{mn,m'n'}$, $r_{ss}^{mn,m'n'}$, $r_{pp}^{mn,m'n'}$. The field reflection matrix $\overline{\overline{\mathrm{R}}}$ clearly reflects coupling between s and p polarisation.

4.3.3.2 External field and intensity of a single dipole at (x_d, y_d, z_d)=(0, 0, 0)

The transfer matrix formalism is now applied to a set of coupled plane waves $\overline{\mathrm{E}}^0$ excited by a dipole situated at $(x_d, y_d, z_d) = (0, 0, 0)$. Self consistency requires that the field reproduces itself after a cavity round-trip or with Fig. 4.7:

$$\begin{aligned}
\overline{\mathrm{E}}_2^0 &= \overline{\mathrm{E}}_4^0 + \overline{\mathrm{A}}_{\downarrow}(\theta_d, \phi_d) \\
\overline{\mathrm{E}}_4^0 &= \overline{\overline{P}}_1 \overline{\overline{R}}_1 \overline{\overline{P}}_1 \overline{\mathrm{E}}_1^0 \\
\overline{\mathrm{E}}_1^0 &= \overline{\mathrm{E}}_3^0 + \overline{\mathrm{A}}_{\uparrow}(\theta_d, \phi_d) \\
\overline{\mathrm{E}}_3^0 &= \overline{\overline{P}}_2 \overline{\overline{R}}_2 \overline{\overline{P}}_2 \overline{\mathrm{E}}_2^0
\end{aligned} \tag{4.25}$$

the superscript 0 denotes the localisation of the dipole at the origin, $\overline{\overline{P}}_i = \overline{\overline{P}}(d_i)$ with $i = 1, 2$ and $\overline{\mathrm{A}}_{\uparrow}(\theta_d, \phi_d)$ and $\overline{\mathrm{A}}_{\downarrow}(\theta_d, \phi_d)$ the $2MN \times 1$ source field matrices with:

$$\overline{\mathrm{A}}_{\uparrow\downarrow}(\theta_d, \phi_d) = \begin{bmatrix} \overline{\mathrm{A}}_{s\uparrow\downarrow}(\theta_d, \phi_d) \\ \overline{\mathrm{A}}_{p\uparrow\downarrow}(\theta_d, \phi_d) \end{bmatrix} \tag{4.26}$$

The source terms in Eq.(4.26) correspond with the expressions given in Table 4.1.

Solving the set of equations in Eq.(4.25) yields for $\overline{\mathrm{E}}_2$:

$$\overline{\mathrm{E}}_2^0 = \begin{bmatrix} \overline{\mathrm{E}}_{2s}^0 \\ \overline{\mathrm{E}}_{2p}^0 \end{bmatrix} = \left[\overline{\overline{I}} - \overline{\overline{P}}_1\overline{\overline{R}}_1\overline{\overline{P}}_1\overline{\overline{P}}_2\overline{\overline{R}}_2\overline{\overline{P}}_2\right]^{-1}\left[\overline{\overline{P}}_1\overline{\overline{R}}_1\overline{\overline{P}}_1\overline{A}_{\uparrow} + \overline{A}_{\downarrow}\right] \tag{4.27}$$

and for the downwards external field $\overline{\mathrm{E}}_{2ext}^0$

$$\overline{\mathrm{E}}_{2ext}^0(\theta_d, \varphi_d, x_d = 0, y_d = 0, z_d = 0) = \overline{\overline{T}}_2\overline{\overline{P}}_2\overline{\mathrm{E}}_2^0 \tag{4.28}$$

The time-averaged normalised power per solid angle $P(\theta_d, \varphi_d, x_d, y_d, z_d, k_x^{mn}, k_y^{mn})$ or intensity radiated in a direction (k_x^{mn}, k_y^{mn}) is, according to Eq.(4.5), proportional to the square of the electric field in this direction. For the dipole located at the origin we have:

$$P_s(\theta_d, \varphi_d, 0, 0, 0, k_x^{mn}, k_y^{mn}) = \frac{1}{2}\sqrt{\frac{\varepsilon_0\varepsilon_2}{\mu_0}}\left|\overline{\mathrm{E}}_{2ext\,s}^0[Nm+n]\right|^2 \tag{4.29a}$$

$$P_p(\theta_d, \varphi_d, 0, 0, 0, k_x^{mn}, k_y^{mn}) = \frac{1}{2n_2^2}\sqrt{\frac{\varepsilon_0\varepsilon_2}{\mu_0}}\left|\overline{\mathrm{E}}_{2ext\,p}^0[Nm+n]\right|^2 \tag{4.29b}$$

Calculation of the intensity according to Eq.(4.29), takes into account the coherent interaction of the dipole components. For a single dipole, it is obvious that the respective contributions of the dipole field in direction $(k_x^{m'n'}, k_y^{m'n'})$, $\forall m', n'$, to a specific direction of observation (k_x^{mn}, k_y^{mn}) will interact in a coherent way. Moreover, contributions of the horizontal and vertical dipole components with corresponding polarisation are added coherently.

4.3.3.3 Dependence of reflection and transmission matrices on position of source

The reflection and transmission matrices in Eq.(4.20),(4.21) and (4.24) are defined for a source location $(x_d = 0, y_d = 0, z_d = 0)$. The element $r_{s(p)s(p)}^{mn,m'n'}$ expresses the amplitude field reflection coefficient at the interface of a plane wave with an in-plane wave vector $\mathbf{k}_{\parallel}^{m'n'}$ to a plane wave in-plane wave vector $\mathbf{k}_{\parallel}^{mn}$ for $x = 0$ and $y = 0$. The same goes for the transmission coefficient $t_{s(p)s(p)}^{mn,m'n'}$.

When the source is located at an arbitrary in-plane displacement $\mathbf{r}_d = (x_d, y_d, 0)$, the coefficients experience a phase shift inversely proportional to the period(s). Indeed, the source-position dependent reflection coefficient $r_{s(p)s(p)}^{mn,m'n'}(\mathbf{r}_d)$ can be written as a function of $r_{s(p)s(p)}^{mn,m'n'}(\mathbf{0})$ (see Fig. 4.8):

$$r_{s(p)s(p)}^{mn,m'n'}(\mathbf{r}_d) = e^{-j\mathbf{k}_{\parallel}^{m'n'}.\mathbf{r}_d}\; r_{s(p)s(p)}^{mn,m'n'}(\mathbf{0})\; e^{j\mathbf{k}_{\parallel}^{mn}.\mathbf{r}_d} \tag{4.30}$$

Together with the Bragg condition in Eq.(4.18) we find:

$$r_{s(p)s(p)}^{mn,m'n'}(\mathbf{r}_d) = e^{j(m'-m)\mathbf{K}_x.\mathbf{r}_d}\; e^{j(n'-n)\mathbf{K}_{y'}.\mathbf{r}_d}\; r_{s(p)s(p)}^{mn,m'n'}(\mathbf{0}) \tag{4.31}$$

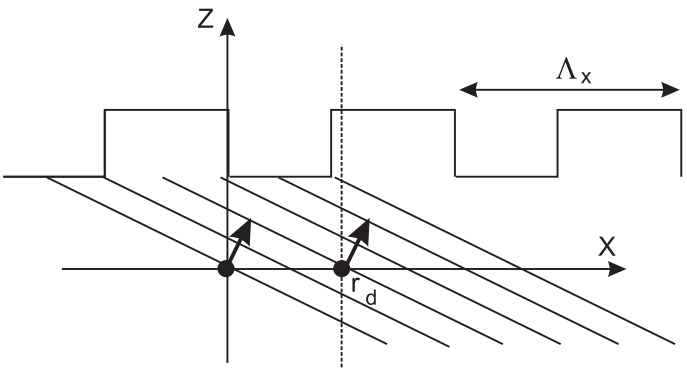

Fig. 4.8: Dependence of reflection and transmission matrices on position of source.

The same goes for the transmission coefficient $t^{mn,m'n'}_{s(p)s(p)}(\mathbf{r}_d)$.

Taking this phase shift into account, we can write the reflection and transmission matrix for a displacement $\mathbf{r}_d = (x_d, y_d, 0)$ of the source as:

$$\overline{\overline{\mathrm{R}}}(\mathbf{r}_d) = \overline{\overline{\mathrm{C}}}(\mathbf{r}_d)\overline{\overline{\mathrm{R}}}(\mathbf{0})\overline{\overline{\mathrm{C}}}^*(\mathbf{r}_d) \tag{4.32a}$$

$$\overline{\overline{\mathrm{T}}}(\mathbf{r}_d) = \overline{\overline{\mathrm{C}}}(\mathbf{r}_d)\overline{\overline{\mathrm{T}}}(\mathbf{0})\overline{\overline{\mathrm{C}}}^*(\mathbf{r}_d) \tag{4.32b}$$

With * the complex conjugate and with

$$\overline{\overline{\mathrm{C}}} = \begin{bmatrix} \overline{\overline{\mathrm{C1}}} & 0 \\ 0 & \overline{\overline{\mathrm{C1}}} \end{bmatrix} = \begin{bmatrix} \mathrm{diag}\left[e^{j(m\mathbf{K}_x + n\mathbf{K}_{y'}).\mathbf{r}_d}\right] & 0 \\ 0 & \mathrm{diag}\left[e^{j(m\mathbf{K}_x + n\mathbf{K}_{y'}).\mathbf{r}_d}\right] \end{bmatrix} \tag{4.33}$$

4.3.3.4 External field and intensity of a dipole at an arbitrary in-plane location $(x_d, y_d, 0)$

Eq.(4.27) expresses the electric field of a Bragg-coupled set excited by a dipole located at $(x_d = 0, y_d = 0, z_d = 0)$. For an arbitrary in-plane location $\mathbf{r}_d = (x_d, y_d, 0)$ of the dipole, the dependence of the reflection coefficients on x_d and y_d has to be taken into account. The other matrices are independent of the source location. Consequently, the electric field of a Bragg-coupled set of plane waves excited by a dipole located at $\mathbf{r}_d$ can be written as:

$$\begin{aligned} \overline{\mathrm{E}}_2(\mathbf{r}_d) &= \begin{bmatrix} \overline{\mathrm{E}}_{2s}(\mathbf{r}_d) \\ \overline{\mathrm{E}}_{2p}(\mathbf{r}_d) \end{bmatrix} \\ &= \left[\overline{\overline{I}} - \overline{\overline{P}}_1\overline{\overline{C}}\,\overline{\overline{R}}_1\overline{\overline{C}}^*\overline{\overline{P}}_1\overline{\overline{P}}_2\overline{\overline{C}}\,\overline{\overline{R}}_2\overline{\overline{C}}^*\overline{\overline{P}}_2\right]^{-1}\left[\overline{\overline{P}}_1\overline{\overline{C}}\,\overline{\overline{R}}_1\overline{\overline{C}}^*\overline{\overline{P}}_1\overline{A}_\uparrow + \overline{A}_\downarrow\right] \\ &= \overline{\overline{N}}_1\overline{A}_\uparrow + \overline{\overline{N}}_2\overline{A}_\downarrow \end{aligned} \tag{4.34}$$

and for the downwards external field $\overline{\mathrm{E}}_{2ext}$

$$\overline{\mathrm{E}}_{2ext}(\mathbf{r}_d) = \overline{\overline{C}}\,\overline{\overline{T}}_2\overline{\overline{C}}^*\overline{\overline{P}}_2\overline{\mathrm{E}}_2(\mathbf{r}_d) = \overline{\overline{M}}_1\overline{A}_\uparrow + \overline{\overline{M}}_2\overline{A}_\downarrow \tag{4.35}$$

The intensity $P(\theta_d, \varphi_d, k_x^{mn}, k_y^{mn})$ radiated in a direction (k_x^{mn}, k_y^{mn}) is:

$$P_s(\theta_d, \varphi_d, x_d, y_d, 0, k_x^{mn}, k_y^{mn}) = \frac{1}{2}\sqrt{\frac{\varepsilon_0\varepsilon_2}{\mu_0}}\left|\overline{\mathrm{E}}_{2ext\,s}[Nm+n]\right|^2 \tag{4.36}$$

$$P_p(\theta_d, \varphi_d, x_d, y_d, 0, k_x^{mn}, k_y^{mn}) = \frac{1}{2n_2^2}\sqrt{\frac{\varepsilon_0\varepsilon_2}{\mu_0}}\left|\overline{\mathrm{E}}_{2ext\,p}[Nm+n]\right|^2 \tag{4.37}$$

4.3.3.5 Intensity of an in-plane distribution of mutually incoherent dipoles with identical orientation

In the calculation of the field of an in-plane arbitrary located dipole (Eq.(4.34)) - again - the coherent radiation of the dipole components is taken into account. The respective contributions of the dipole field in directions $(k_x^{m'n'}, k_y^{m'n'})$, $\forall m', n'$, to a direction of observation (k_x^{mn}, k_y^{mn}) interact in a *coherent* way.

We will show that when the emitted intensity of an in-plane arbitrary located dipole in a cavity is averaged over the dipole location in the periodic unit cell, the respective contributions of the dipole field to a specific direction of observation (k_x^{mn}, k_y^{mn}) will interact *incoherently*. For that, we write Eq.(4.35) as a series:

$$\begin{aligned}\overline{\mathrm{E}}_{2ext}(\mathbf{r}_d) &= \sum_{l=0}^{\infty} \overline{\overline{C}}\,\overline{\overline{T}}_2\overline{\overline{C}}^*\overline{\overline{P}}_2\left[\overline{\overline{P}}_1\overline{\overline{C}}\,\overline{\overline{R}}_1\overline{\overline{C}}^*\overline{\overline{P}}_1\overline{\overline{P}}_2\overline{\overline{C}}\,\overline{\overline{R}}_2\overline{\overline{C}}^*\overline{\overline{P}}_2\right]^l\left[\overline{\overline{P}}_1\overline{\overline{C}}\,\overline{\overline{R}}_1\overline{\overline{C}}^*\overline{\overline{P}}_1\overline{A}_{\uparrow} + \overline{A}_{\downarrow}\right] \\ &= \sum_{l=0}^{\infty}\overline{\mathrm{E}}_{2ext,l}(\mathbf{r}_d)\end{aligned} \tag{4.38}$$

For clarity, we will omit the subscript *ext* in the derivation of the proof.

The intensity of a set of mutually incoherent dipoles is the sum of the respective intensities. Equivalently, the normalised aggregate intensity can be found by averaging the intensity of an individual dipole over its position in a periodic unit cell Λ_{Bragg}.

$$\begin{aligned}P_s(\theta_d, \varphi_d, k_x^{mn}, k_y^{mn}) &= \left\langle P_s(\theta_d, \varphi_d, x_d, y_d, 0, k_x^{mn}, k_y^{mn})\right\rangle \\ &= \frac{1}{2}\sqrt{\frac{\varepsilon_0\varepsilon_2}{\mu_0}}\frac{1}{\Lambda_{Bragg}}\int\limits_{\Lambda_{Bragg}}\int\left|\overline{\mathrm{E}}_{2s}[Nm+n]\right|^2 dx_d dy_d\end{aligned} \tag{4.39}$$

An analogous expression is found for p-polarised light.

For simplicity we restrict the proof to a one dimensional grating. The proof for a two dimensional grating is similar. The polarisation subscript will be omitted for clarity:

$$\begin{aligned}P(\theta_d, \varphi_d, k_x^{m}, k_y^{m}) &= \frac{1}{2}\sqrt{\frac{\varepsilon_0\varepsilon_2}{\mu_0}}\frac{1}{\Lambda_x}\int\limits_{\Lambda_x}\left|\overline{\mathrm{E}}_2[m]\right|^2 dx_d \\ &= \frac{1}{2}\sqrt{\frac{\varepsilon_0\varepsilon_2}{\mu_0}}\frac{1}{\Lambda_x}\int\limits_{\Lambda_x}\sum_{l}\overline{\mathrm{E}}_{2,l}[m]\sum_{l'}\overline{\mathrm{E}}_{2,l'}[m]^* dx_d\end{aligned} \tag{4.40}$$

The integral can be calculated by considering the individual terms of the sum.

The first term of the integral of Eq.(4.40), when $l = 0$ and $l' = 0$, can be written as:

$$
\begin{aligned}
&\frac{1}{\Lambda_x}\int_{\Lambda_x} \overline{\mathrm{E}}_{2,0}[m]\overline{\mathrm{E}}_{2,0}[m]^* dx_d = \\
&\frac{1}{\Lambda_x}\int_{\Lambda_x} \sum_{k_0,k_1,k_2,k_3} \Big(\overline{\overline{C}}[m,m]\overline{\overline{T}}_2[m,k_0]\overline{\overline{C}}[k_0,k_0]^*\overline{\overline{P}}_2[k_0,k_0]\overline{\overline{P}}_1[k_0,k_0]\overline{\overline{C}}[k_0,k_0] \\
&\overline{\overline{R}}_1[k_0,k_1]\overline{\overline{C}}[k_1,k_1]^*\overline{\overline{P}}_1[k_1,k_1]\overline{\overline{C}}[m,m]^*\overline{\overline{T}}_2[m,k_2]^*\overline{\overline{C}}[k_2,k_2]\overline{\overline{P}}_2[k_2,k_2]^*\overline{\overline{P}}_1[k_2,k_2]^* \\
&\overline{\overline{C}}[k_2,k_2]^*\overline{\overline{R}}_1[k_2,k_3]^*\overline{\overline{C}}[k_3,k_3]\overline{\overline{P}}_1[k_3,k_3]^*\Big)\overline{A}_\uparrow[k_1]\overline{A}_\uparrow[k_3]^* \\
+&\sum_{k_0,k_1,k_2} \Big(\overline{\overline{C}}[m,m]\overline{\overline{T}}_2[m,k_0]\overline{\overline{C}}[k_0,k_0]^*\overline{\overline{P}}_2[k_0,k_0]\overline{\overline{P}}_1[k_0,k_0]\overline{\overline{C}}[k_0,k_0]\overline{\overline{R}}_1[k_0,k_1] \\
&\overline{\overline{C}}[k_1,k_1]^*\overline{\overline{P}}_1[k_1,k_1]\overline{\overline{C}}[m,m]^*\overline{\overline{T}}_2[m,k_2]^*\overline{\overline{C}}[k_2,k_2]\overline{\overline{P}}_2[k_2,k_2]^*\Big)\overline{A}_\uparrow[k_1]\overline{A}_\downarrow[k_2]^* \\
+&\sum_{k_0,k_1,k_2} \Big(\overline{\overline{C}}[m,m]^*\overline{\overline{T}}_2[m,k_0]^*\overline{\overline{C}}[k_0,k_0]\overline{\overline{P}}_2[k_0,k_0]^*\overline{\overline{P}}_1[k_0,k_0]^*\overline{\overline{C}}[k_0,k_0]^*\overline{\overline{R}}_1[k_0,k_1]^* \\
&\overline{\overline{C}}[k_1,k_1]\overline{\overline{P}}_1[k_1,k_1]^*\overline{\overline{C}}[m,m]\overline{\overline{T}}_2[m,k_2]\overline{\overline{C}}[k_2,k_2]^*\overline{\overline{P}}_2[k_2,k_2]\Big)\overline{A}_\uparrow[k_1]^*\overline{A}_\downarrow[k_2] \\
+&\sum_{k_0,k_1} \Big(\overline{\overline{C}}[m,m]\overline{\overline{T}}_2[m,k_0]\overline{\overline{C}}[k_0,k_0]^*\overline{\overline{P}}_2[k_0,k_0]\overline{\overline{C}}[m,m]^* \\
&\overline{\overline{T}}_2[m,k_1]^*\overline{\overline{C}}[k_1,k_1]\overline{\overline{P}}_2[k_1,k_1]^*\Big)\overline{A}_\downarrow[k_0]^*\overline{A}_\downarrow[k_1]dx_d
\end{aligned}
\tag{4.41}
$$

With the definition of the dipole position dependence of $\overline{\overline{C}}$ in Eq.(4.33) the integral can be evaluated:

$$
\begin{aligned}
&\text{term 1:} \int_{\Lambda_x} e^{j(m-k_0-k_1-m+k_2-k_2+k_3)\frac{2\pi x}{\Lambda_x}} dx_d \\
&\qquad\qquad \neq 0 \text{ if } k_1 = k_3 \\
&\text{term 2:} \quad \int_{\Lambda_x} e^{j(m-k_0+k_0-k_1-m+k_2)\frac{2\pi x}{\Lambda_x}} dx_d \\
&\qquad\qquad \neq 0 \text{ if } k_1 = k_2 \\
&\text{term 3:} \quad \int_{\Lambda_x} e^{j(-m+k_0-k_0+k_1+m-k_2)\frac{2\pi x}{\Lambda_x}} dx_d \\
&\qquad\qquad \neq 0 \text{ if } k_1 = k_2 \\
&\text{term 4:} \quad \int_{\Lambda_x} e^{j(m-k_0-m+k_1)\frac{2\pi x}{\Lambda_x}} dx_d \\
&\qquad\qquad \neq 0 \text{ if } k_0 = k_1
\end{aligned}
\tag{4.42}
$$

These non-zero conditions eliminate cross terms $\overline{A}[i]\overline{A}[j]^*$ and the first term of the series Eq.(4.40) denotes as:

$$\begin{aligned}\frac{1}{\Lambda_x}\int_{\Lambda_x}\overline{\mathrm{E}}_{2,0}[m]\overline{\mathrm{E}}_{2,0}[m]^* dx_d = \\ \sum_{k_0} a_{k_0}\left|\overline{A}_{\uparrow}[k_0]\right|^2 \\ +\sum_{k_0} 2\mathrm{Re}\left(b_{k_0}\overline{A}_{\uparrow}[k_0]\overline{A}_{\downarrow}[k_0]\right)+\sum_{k_0} c_{k_0}\left|\overline{A}_{\downarrow}[k_0]\right|^2\end{aligned} \tag{4.43}$$

In the case $l = 0$ and $l' = 1$, the cross terms in $\overline{A}[i]\overline{A}[j]^*$ again disappear when averaging over the dipole position:

$$\begin{aligned}\text{term 1:}\quad & \overline{A}_{\uparrow}[k_1]\overline{A}_{\uparrow}[k_5]^*\int_{\Lambda_x} e^{j(m-k_0+k_0-k_1-m+k_2-k_2+k_3-k_3+k_4-k_4+k_5)\frac{2\pi x}{\Lambda_x}}dx_d \\ & \neq 0 \text{ if } k_1 = k_5 \\ \text{term 2:}\quad & \overline{A}_{\uparrow}[k_1]\overline{A}_{\downarrow}[k_4]^*\int_{\Lambda_x} e^{j(m-k_0+k_0-k_1-m+k_2-k_2+k_3-k_3+k_4)\frac{2\pi x}{\Lambda_x}}dx_d \\ & \neq 0 \text{ if } k_1 = k_4 \\ \text{term 3:}\quad & \overline{A}_{\downarrow}[k_0]\overline{A}_{\uparrow}[k_4]^*\int_{\Lambda_x} e^{j(-m+k_0+m-k_1+k_1-k_2+k_2-k_3+k_3-k_4)\frac{2\pi x}{\Lambda_x}}dx_d \\ & \neq 0 \text{ if } k_0 = k_4 \\ \text{term 4:}\quad & \overline{A}_{\downarrow}[k_0]\overline{A}_{\downarrow}[k_3]^*\int_{\Lambda_x} e^{j(m-k_0-m+k_1-k_1+k_2-k_2+k_3)\frac{2\pi x}{\Lambda_x}}dx_d \\ & \neq 0 \text{ if } k_0 = k_3\end{aligned} \tag{4.44}$$

The case $l = 1$ and $l' = 0$ yields similar terms 1-4. This reasoning can be extended for arbitrary l and l'. The cross terms are averaged out due to the period proportionality of the phase-shift variation of the reflection coefficients as a function of the position of the emitter. The averaged intensity for a direction of observation (k_x^m, k_y^m) is determined by the sum of the intensities generated by the respective plane waves emitted by the dipole in the Bragg-coupled directions $(k_x^{m'n'}, k_y^{m'n'})$, $\forall m', n'$. For a 2-D grating, the averaged intensity for a direction of

observation (k_x^{mn}, k_y^{mn}) is thus given by (p polarisation is analogous):

$$P_s(\theta_d, \varphi_d, k_x^{mn}, k_y^{mn}) = \frac{1}{2}\sqrt{\frac{\varepsilon_0\varepsilon_2}{\mu_0}} \sum_k^{2MN} \Big| \overbrace{\overline{\overline{M}}_1[Nm+n,k]\overline{A}_\uparrow[k] + \overline{\overline{M}}_2[Nm+n,k]\overline{A}_\downarrow[k]}^{s \to s} + \underbrace{\overline{\overline{M}}_1[Nm+n,k+MN]\overline{A}_\uparrow[k+MN] + \overline{\overline{M}}_2[Nm+n,k+MN]\overline{A}_\downarrow[k+MN]}_{p \to s} \Big|^2 \tag{4.45}$$

In conclusion we can state that in case of a set of $\mathbf{k}_\parallel$-vectors coupled by the Bragg condition, the contributions of the source terms of the respective emission directions to a specific spatial frequency $\mathbf{k}_\parallel^{mn}$ of this set are considered to interact incoherently. Although the respective contributions of a single dipole at a specific location to a certain diffraction order do interact coherently, the dependency of the intensity on the dipole position is averaged out when all dipole positions are considered in a Bragg unit cell. This incoherent interaction of the respective contributions of a single dipole, is justified by the fact that the phase of the reflection coefficients $r_{m'n'\to mn}$ depends on the in-plane position of the dipole. This phase shift variation in function of the position of the emitter is proportional to $\mathbf{k}_\parallel^{mn} - \mathbf{k}_\parallel^{m'n'} = (m-m')\frac{2\pi}{\Lambda_x}\mathbf{1}_x + (n-n')\frac{2\pi}{\Lambda_{y'}}\mathbf{1}_{y'}$, and thus shows a proportional periodicity. Considering dipole emission intensity over a periodic unit cell will average out this phase shift variation, resulting in an incoherent interaction of the distinct Bragg coupled contributions with a single spatial frequency.

4.3.3.6 Intensity of mutually incoherent dipoles with isotropic orientation (θ_d,φ_d)

We have assumed that the axis of the dipole, or, to express it differently, that the transition dipole moment has a fixed azimuthal angle φ_d and angle θ_d with the z-axis. We consider an ensemble of incoherently radiating dipoles with different orientation (θ_d,φ_d), radiating with equal dipole moments. The radiation pattern of an ensemble of electric dipoles with three-dimensional isotropical random orientation of their dipole moments is given by:

$$\begin{aligned} P_{s(p)}(k_x^{mn}, k_y^{mn}) &= \langle P_{s(p)}(\theta_d, \varphi_d, k_x^{mn}, k_y^{mn}) \rangle \\ &= \frac{1}{4\pi} \int_0^{2\pi} \int_{-\pi}^{+\pi} P_{s(p)}(\theta_d, \varphi_d, k_x^{mn}, k_y^{mn}) \sin\theta_d d\theta_d d\varphi_d \end{aligned} \tag{4.46}$$

With $P_{s(p)}(\theta_d, \varphi_d, k_x^{mn}, k_y^{mn})$ defined in Eq.(4.45). Transposing the integral and summation after Eq.(4.45) is inserted in Eq.(4.46), the sum of integrals can easily

be calculated. Using Table 4.1, the k^{th} element of the summation can be written as:

$$\begin{aligned}
&\frac{1}{2}\sqrt{\frac{\varepsilon_0\varepsilon_2}{\mu_0}}\frac{2}{4\pi}\int_0^{2\pi}\int_0^{+\pi}\Big|\overline{\overline{M}}_1[Nm{+}n,k]\overline{A}_\uparrow[k]+\overline{\overline{M}}_2[Nm{+}n,k]\overline{A}_\downarrow[k]\\
&+\overline{\overline{M}}_1[Nm{+}n,k{+}MN]\overline{A}_\uparrow[k{+}MN]+\overline{\overline{M}}_2[Nm{+}n,k{+}MN]\overline{A}_\downarrow[k{+}MN]\Big|^2\sin\theta_d d\theta_d d\varphi_d\\
&=\frac{1}{2}\sqrt{\frac{\varepsilon_0\varepsilon_2}{\mu_0}}\frac{2}{4\pi}\int_0^{2\pi}\int_0^{+\pi}\Bigg|m_{1+2}^{Nm+n,k}\sqrt{\frac{3}{8\pi}}\sin(\varphi_d-\varphi^k)\sin\theta_d\\
&+m_1^{Nm+n,k+MN}\left(\sqrt{\frac{3}{8\pi}}\cos\theta^k\cos(\varphi_d-\varphi^k)\sin\theta_d+\sqrt{\frac{3}{8\pi}}\sin\theta^k\cos\theta_d\right)\\
&+m_2^{Nm+n,k+MN}\left(\sqrt{\frac{3}{8\pi}}\cos\theta^k\cos(\varphi_d-\varphi^k)\sin\theta_d-\sqrt{\frac{3}{8\pi}}\sin\theta^k\cos\theta_d\right)\Bigg|^2\sin\theta_d d\theta_d d\varphi_d\\
&=\frac{2}{3}\frac{3}{16\pi}\left|m_{1+2}^{Nm+n,k}\right|^2+\frac{2}{3}\frac{3}{16\pi}\cos^2\theta^k\left|m_{1+2}^{Nm+n,k+MN}\right|^2+\frac{1}{3}\frac{3}{8\pi}\sin^2\theta^k\left|m_{1+2}^{Nm+n,k+MN}\right|^2
\end{aligned}\tag{4.47}$$

with $m_{1+2}^{m,n}=\overline{\overline{M}}_1[m,n]+\overline{\overline{M}}_2[m,n]$. From this it is clear that the radiation pattern of a set of isotropicly oriented dipoles is identical to that produced by three incoherently radiating dipoles with the axes oriented along the x,y and z direction. With Eq.(4.45), (4.46) and (4.47), the intensity can be evaluated as (analogous for p-polarisation) :

$$\begin{aligned}
P_s(k_x^{mn},k_y^{mn}) =&\frac{1}{2}\sqrt{\frac{\varepsilon_0\varepsilon_2}{\mu_0}}\sum_k^{MN}\left|\overline{\overline{M}}_1[Nm{+}n,k]\langle\overline{A}_{s\uparrow}^h\rangle[k]+\overline{\overline{M}}_2[Nm{+}n,k]\langle\overline{A}_{s\downarrow}^h\rangle[k]\right|^2\\
&+\left|\overline{\overline{M}}_1[Nm{+}n,k{+}MN]\langle\overline{A}_{p\uparrow}^h\rangle[k]+\overline{\overline{M}}_2[Nm{+}n,k{+}MN]\langle\overline{A}_{p\downarrow}^h\rangle[k]\right|^2\\
&+\left|\overline{\overline{M}}_1[Nm{+}n,k{+}MN]\langle\overline{A}_{p\uparrow}^v\rangle[k]+\overline{\overline{M}}_2[Nm{+}n,k{+}MN]\langle\overline{A}_{p\downarrow}^v\rangle[k]\right|^2\\
=&\frac{1}{2}\sqrt{\frac{\varepsilon_0\varepsilon_2}{\mu_0}}\sum_k^{MN}\left|m_h^s(Nm{+}n,k)\langle A_{s\uparrow}^h(\theta^k)\rangle\right|^2\\
&+\left|m_h^p(Nm{+}n,k)\langle A_{p\uparrow}^h\rangle(\theta^k)\right|^2+\left|m_v^p(Nm{+}n,k)\langle A_{p\uparrow}^v\rangle(\theta^k)\right|^2
\end{aligned}\tag{4.48}$$

with $m_h^s(Nm{+}n,k)=m_{1+2}^{Nm+n,k}$, $m_h^p(Nm{+}n,k)=m_v^p(Nm{+}n,k)=m_{1+2}^{Nm+n,k+MN}$ and $\langle\overline{A}_{s(p)\uparrow\downarrow}^{h(v)}\rangle[k]=\langle A_{s(p)\uparrow\downarrow}^{h(v)}\rangle(\theta^k)$ defined in Table 4.2. These values correspond with the values in Table 4.1 for dipoles with the axes respectively oriented along the x,y and z direction.

TABLE. 4.2: Averaged source terms for horizontal and vertical dipoles.

	s	p
Horizontal	$\langle A^h_{s\uparrow\downarrow}\rangle = \sqrt{\frac{3}{16\pi}}$	$\langle A^h_{p\uparrow\downarrow}\rangle = \pm\sqrt{\frac{3}{16\pi}}\cos\theta$ $= \pm\sqrt{\frac{3}{16\pi}}\frac{k_z}{n_s k_0}$
Vertical	$\langle A^v_{s\uparrow\downarrow}\rangle = 0$	$\langle A^v_{p\uparrow\downarrow}\rangle = \sqrt{\frac{3}{8\pi}}\sin\theta$ $= \sqrt{\frac{3}{8\pi}}\frac{k_\parallel}{n_s k_0}$

4.3.3.7 Extraction Efficiency

In the sections above, we proved that the intensity $P_{s(p)}(k_x^{mn}, k_y^{mn})$ in a direction (k_x^{mn}, k_y^{mn}) is achieved by combining the respective contributions of the Bragg-coupled set in an incoherent way, or:

$$\begin{aligned} P_{s(p)}(\theta_2,\varphi_2) &= P_{s(p)}(k_x^{mn}, k_y^{mn}) \\ &= \sum_{v,h,s,p}\sum_{pq}^{MN}\frac{1}{2}\mathrm{Re}\left[\mathbf{E}_{pq\to mn}\times\mathbf{H}^*_{pq\to mn}\right]_{s(p)}\cdot\frac{k}{k_z}\mathbf{1}_z \end{aligned} \tag{4.49}$$

with $\mathbf{E}_{pq\to mn}$ and $\mathbf{H}^*_{pq\to mn}$ the electric and magnetic field in the direction (k_x^{mn}, k_y^{mn}) due to a source field in a direction (k_x^{pq}, k_y^{pq}). The source field is given in Table 4.2. According to Eq.(4.4), we can calculate the total normalised power L_2 in medium 2 through integration of the normalised radiation pattern $\langle P_{(s,p)}(\theta_2,\varphi_2)\rangle$ over the solid angle 4π.

$$\mathrm{L}_2 = \int_{4\pi}\left[P_s(\theta_2,\varphi) + P_p(\theta_2,\varphi)\right]d\Omega_2 \tag{4.50}$$

The total s-polarised power due to a horizontal dipole emitting s polarised light can be denoted as:

$$\begin{aligned} \mathrm{L}_{2s}(\mathbf{d}_s^h) &= \int_{4\pi}\sum_{pq}^{MN}\frac{1}{2}\mathrm{Re}\left[\mathbf{E}^s_{pq\to mn}\times\mathbf{H}^{s*}_{pq\to mn}\right]\cdot\frac{k}{k_z}\mathbf{1}_z\sin\theta_2 d\theta_2 d\varphi_2 \\ &= \int_{4\pi}\frac{1}{2}\sqrt{\frac{\varepsilon_0}{\mu_0}}\sum_{pq}^{MN}\left|E^s_{pq\to mn}(\theta_2)\right|^2 n_2\sin\theta_2 d\theta_2 d\varphi_2 \end{aligned} \tag{4.51}$$

Analogously, we find for the total p-polarised power due to a horizontal dipole emitting s polarised light:

$$\begin{aligned} \mathrm{L}_{2p}(\mathbf{d}_s^h) &= \int_{4\pi} \sum_{pq}^{MN} \frac{1}{2} \mathrm{Re}\left[\mathbf{E}^p_{pq\to mn} \times \mathbf{H}^{p*}_{pq\to mn}\right] \cdot \frac{k}{k_z} \mathbf{1}_z \sin\theta_2 d\theta_2 d\varphi_2 \\ &= \int_{4\pi} \frac{1}{2}\sqrt{\frac{\varepsilon_0}{\mu_0}} \sum_{pq}^{MN} \left|E^p_{pq\to mn}(\theta_2)\right|^2 \frac{1}{n_2} \sin\theta_2 d\theta_2 d\varphi_2 \end{aligned} \tag{4.52}$$

Same expressions account for the power due to vertical dipoles. We consider the source plane waves $\langle A^h_{s\uparrow\downarrow}\rangle$ which are emitted by the dipole in the direction of the interface with an angle of incidence θ_s and which are partially transmitted into medium 2. According to Eq.(4.17), A^h_s denotes a field density per unit solid angle $d\Omega_s$. From Eq.(4.48) where the source terms are still expressed as a function of θ_2, we derivate:

$$\begin{aligned} \left|E^s_{pq\to mn}(\theta_2)\right|^2 &= \left|E^s_{pq\to mn}(\theta^{pq}_s)\right|^2 = \left|m^s_h(mn,pq) A^h_{s\uparrow}(\theta^{pq}_s)\right|^2 \\ \left|E^p_{pq\to mn}(\theta_2)\right|^2 &= \left|E^p_{pq\to mn}(\theta^{pq}_s)\right|^2 = \left|m^s_h(mn+MN,pq) A^h_{s\uparrow}(\theta^{pq}_s)\right|^2 \end{aligned} \tag{4.53}$$

With Snellius'law $n_s \sin\theta_s = n_2 \sin\theta_2$ and:

$$d\theta_\mathrm{i} = d \arcsin\left[\frac{\sqrt{(k_{\mathrm{i}x})^2 + (k_{\mathrm{i}y})^2}}{k_\mathrm{i}}\right] = \frac{d\sqrt{(k_{\mathrm{i}x})^2 + (k_{\mathrm{i}y})^2}}{k_{\mathrm{i}z}} \tag{4.54}$$

for which the numerator is independent of the considered medium and $i = s, 2$, the integral in Eqs.(4.51) and (4.52) can be calculated by evaluating the integrand over the solid angle in medium n_s:

$$\begin{aligned} \mathrm{L}_{2s}(\mathbf{d}_s^h) &= \int_{4\pi} \frac{1}{2}\sqrt{\frac{\varepsilon_0}{\mu_0}} \sum_{pq}^{MN} \left|m^s_h(mn,pq) A^h_{s\uparrow}(\theta^{pq}_s)\right|^2 n_s \sin\theta_s \frac{d\theta_2}{d\theta_s} d\theta_s d\varphi_s \\ &= \int_{4\pi} \frac{1}{2}\sqrt{\frac{\varepsilon_0}{\mu_0}} \sum_{pq}^{MN} \left|m^s_h(mn,pq) A^h_{s\uparrow}(\theta^{pq}_s)\right|^2 n_s \sin\theta_s \frac{n_2\cos\theta_2}{n_s\cos\theta_s} d\theta_s d\varphi_s \\ \mathrm{L}_{2p}(\mathbf{d}_s^h) &= \int_{4\pi} \frac{1}{2}\sqrt{\frac{\varepsilon_0}{\mu_0}} \sum_{pq}^{MN} \left|m^s_h(mn+MN,pq) A^h_{s\uparrow}(\theta^{pq}_s)\right|^2 \frac{1}{n_2^2} n_s \sin\theta_s \frac{d\theta_2}{d\theta_s} d\theta_s d\varphi_s \\ &= \int_{4\pi} \frac{1}{2}\sqrt{\frac{\varepsilon_0}{\mu_0}} \sum_{pq}^{MN} \left|m^s_h(mn+MN,pq) A^h_{s\uparrow}(\theta^{pq}_s)\right|^2 n_s \sin\theta_s \frac{\cos\theta_2}{n_s n_2 \cos\theta_s} d\theta_s d\varphi_s \end{aligned} \tag{4.55}$$

Calculations for a horizontal dipole emitting p-polarised light and a vertical dipole emitting p-polarised light are similar. We restrict ourselves to the results.

Omitting the term of proportion $1/2\sqrt{\varepsilon_0\varepsilon_s/\mu_0}$ in analogy with the normalisation of the power of a unperturbed dipole that led to Table 4.1, relapsing into

matrix notation and using $d\Omega_s = \sin\theta_s d\theta_s d\varphi_s = dk_x dk_y / n_s k_0 k_z$, brings us to the final expression of the normalised power L_2 emitted by a in-plane distribution of incoherent electric dipoles with arbitrary orientation in a 2-D periodically modulated stratified medium:

$$\begin{aligned} \mathrm{L}_{2s} &= 2/3\mathrm{L}_{2s}(\mathbf{d}_s^h) + 2/3\mathrm{L}_{2s}(\mathbf{d}_p^h) + 1/3\mathrm{L}_{2s}(\mathbf{d}_p^v) \\ \mathrm{L}_{2p} &= 2/3\mathrm{L}_{2p}(\mathbf{d}_s^h) + 2/3\mathrm{L}_{2p}(\mathbf{d}_p^h) + 1/3\mathrm{L}_{2p}(\mathbf{d}_p^v) \end{aligned} \tag{4.56}$$

$\mathrm{L}_{2s(p)}(\mathbf{d}_{s(p)}^{h(v)})$ are defined in defined in Eq.(4.57). It is important to notice that, when a matrix notation is used, the integral to be calculated is limited to the k-space restricted by the Bragg vectors $\mathbf{K}_x$ and $\mathbf{K}_{y'}$. The parallelogram is denoted as K_{Bragg}.

$$\begin{aligned} \mathrm{L}_{2s}(\mathbf{d}_s^h) &= \int\!\!\int_{K_{Bragg}} \overline{I}\ \overline{\Pi}_{ss}^h dk_x dk_y \\ \text{with}\quad \Pi_{ss}^h[Nm+n] &= P(\theta_s^{mn}, \varphi_s^{mn}) = P(k_x^{mn}, k_y^{mn}) \\ &= \sum_{pq}^{MN} \left| m_h^s(mn, pq) A_{s\uparrow}^h(\theta_s^{pq}) \right|^2 \frac{n_2 \cos\theta_2}{n_s \cos\theta_s} \frac{1}{n_s^2 k_0^2 \cos\theta_s} \end{aligned} \tag{4.57a}$$

$$\begin{aligned} \mathrm{L}_{2p}(\mathbf{d}_s^h) &= \int\!\!\int_{K_{Bragg}} \overline{I}\ \overline{\Pi}_{sp}^h dk_x dk_y \\ \text{with}\quad \Pi_{sp}^h[Nm+n] &= P(\theta_s^{mn}, \varphi_s^{mn}) = P(k_x^{mn}, k_y^{mn}) \\ &= \sum_{pq}^{MN} \left| m_h^s(mn+MN, pq) A_{s\uparrow}^h(\theta_s^{pq}) \right|^2 \frac{\cos\theta_2}{n_s n_2 \cos\theta_s} \frac{1}{n_s^2 k_0^2 \cos\theta_s} \end{aligned} \tag{4.57b}$$

$$\begin{aligned} \mathrm{L}_{2s}(\mathbf{d}_p^h) &= \int\!\!\int_{K_{Bragg}} \overline{I}\ \overline{\Pi}_{ps}^h dk_x dk_y \\ \text{with}\quad \Pi_{ps}^h[Nm+n] &= P(\theta_s^{mn}, \varphi_s^{mn}) = P(k_x^{mn}, k_y^{mn}) \\ &= \sum_{pq}^{MN} \left| m_h^p(mn, pq) A_{p\uparrow}^h(\theta_s^{pq}) \right|^2 \frac{n_s n_2 \cos\theta_2}{\cos\theta_s} \frac{1}{n_s^2 k_0^2 \cos\theta_s} \end{aligned} \tag{4.57c}$$

$$\begin{aligned} \mathrm{L}_{2p}(\mathbf{d}_p^h) &= \int\!\!\int_{K_{Bragg}} \overline{I}\ \overline{\Pi}_{pp}^h dk_x dk_y \\ \text{with}\quad \Pi_{pp}^h[Nm+n] &= P(\theta_s^{mn}, \varphi_s^{mn}) = P(k_x^{mn}, k_y^{mn}) \\ &= \sum_{pq}^{MN} \left| m_h^p(mn+MN, pq) A_{p\uparrow}^h(\theta_s^{pq}) \right|^2 \frac{n_s \cos\theta_2}{n_2 \cos\theta_s} \frac{1}{n_s^2 k_0^2 \cos\theta_s} \end{aligned} \tag{4.57d}$$

$$\mathrm{L}_{2s}(\mathbf{d}_p^v) = \int\limits_{K_{Bragg}}\int \overline{I}\ \overline{\Pi}_{ps}^v dk_x dk_y$$

$$\text{with} \quad \Pi_{ps}^v[Nm+n] = P(\theta_s^{mn}, \varphi_s^{mn}) = P(k_x^{mn}, k_y^{mn}) \tag{4.57e}$$

$$= \sum_{pq}^{MN} \left| m_v^p(mn,pq) A_{p\uparrow}^v(\theta_s^{pq}) \right|^2 \frac{n_s n_2 \cos\theta_2}{\cos\theta_s} \frac{1}{n_s^2 k_0^2 \cos\theta_s}$$

$$\mathrm{L}_{2p}(\mathbf{d}_p^v) = \int\limits_{K_{Bragg}}\int \overline{I}\ \overline{\Pi}_{pp}^v dk_x dk_y$$

$$\text{with} \quad \Pi_{pp}^v[Nm+n] = P(\theta_s^{mn}, \varphi_s^{mn}) = P(k_x^{mn}, k_y^{mn}) \tag{4.57f}$$

$$= \sum_{pq}^{MN} \left| m_v^p(mn+MN,pq) A_{p\uparrow}^v(\theta_s^{pq}) \right|^2 \frac{n_s \cos\theta_2}{n_2 \cos\theta_s} \frac{1}{n_s^2 k_0^2 \cos\theta_s}$$

Eqs.(4.57) denote the respective radiation patterns Π in medium 2 and powerflux through interface $L+1$ (see Fig. 4.4). This calculation can be repeated for every layer and the powerflux can be calculated in an analogous way through every interface. Both backward and forward propagating waves have to be taken into account. The ratio of the power L_2 in medium 2 on the total powerflux L_{dip} through interface s and interface $s+1$ will express the extraction efficiency of the structure towards medium 2.

$$\eta_{extr}^{n_2} = \frac{L_2}{L_{dip}} \tag{4.58}$$

This analysis has been implemented in C++, in a UNIX environment.

4.3.4 Implementation aspects

4.3.4.1 Infinitely thin active layer: absorbing active layers and evanescent coupling

The power calculated in Eqs.(4.57) of a dipole in an active layer with refractive index n_s squeezed between periodically modulated stratified media is normalised to the power emitted by the dipole placed in a bulk medium with refractive index n_s. Due to this normalisation, the calculated power in medium 2 will not depend on the choice of n_s when the thickness of the active layer $d_s = 0$ and when the integration extends the entire in-plane k-space ($-\infty < k_{x(y)} < \infty$). This has been investigated and demonstrated by H. De Neve for a dipole emitting in a planar stratified medium [20], and holds as well for periodically modulated stratified media. The reason of placing the dipole in an infinitely thin layer with arbitrary refractive index n_s is twofold and is summarised in this section, for further detail, the reader is referred to [20].

Firstly, due to the infinite integration of the Fourier transform of the dipole field, evanescent coupling of this dipole field to metals or high refractive index media can be found in the calculation. The numerical implementation however, restricts the integration: $|\theta| < \pi/2$ or $|k_{\|}| < 2\pi n_s/\lambda$. Due to the zero thickness of the source layer, an arbitrary n_s physically does not influence the structure. The

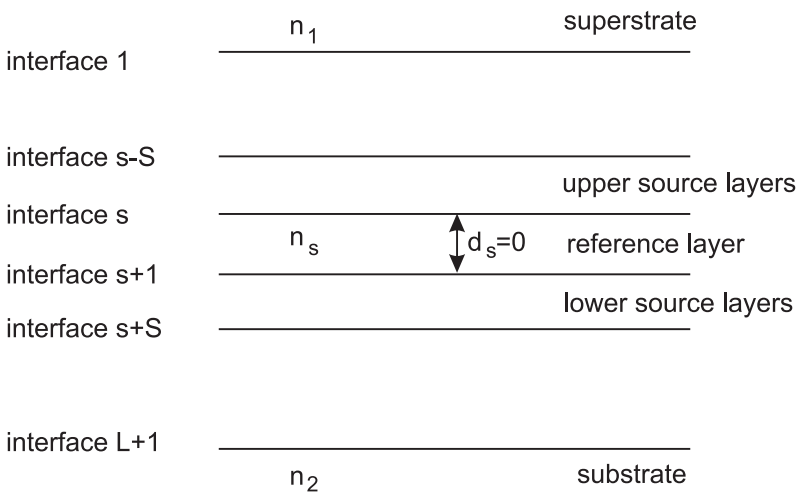

Fig. 4.9: Infinitely thin reference layer.

k-space over which the integration is taken, however, increases with the refractive index n_s of the active layer. Therefore, to include evanescent coupling, n_s has to be chosen as high as possible. This loads of course the numerical implementation, as the discretisation has to be refined to attain the same accuracy.

Secondly, as mentioned in the footnote of the introduction of section 4.3, the analysis is correct for a dipole emitting in a nonabsorbing layer. The dipole field is expanded in plane waves and this decomposition only holds in media with real refractive index. This layer may be sandwiched in between absorbing media. The realistic situation, in that a dipole is embedded in an absorbing layer (in the weak coupling regime a layer with complex refractive index $n_a = \mathrm{Re}(n_a) - j\mathrm{Im}(n_a)$) can be represented adequately by a dipole in an infinitely thin layer ($d_s = 0$) with real refractive index n_s squeezed between the absorbing layer with refractive index n_a (see Fig. 4.9). Due to the infinitely thin thickness of the layer, however, the power absorbed in the active layer before escaping this layer, does not converge for increasing n_s. To calculate the extraction efficiency, this practical convergence problem is circumvented by calculating L_{dip} as the power flux through interface $s - S$ and $s + S$, the interfaces of the source layer.

4.3.4.2 Finite spectral width

Until now, we considered monochromatic dipoles. In reality, the spontaneous emission spectrum is finite and determined by two mechanisms: homogeneous and inhomogeneous broadening. The homogeneous broadening caused by the lifetime τ is typically a few tens picometer and much smaller than the inhomogeneous broadening. Inhomogeneous broadening is caused by the difference of the emission energies of the individual transitions in the system. This distribution of electrons and holes in the conduction and valence band depends on the carrier density and

is called band filling. A Gaussian profile with carrier density dependent FWHM comes close to the intrinsic spontaneous emission spectrum for low carrier densities. After discretisation of the spectrum $S(\lambda)$, the total power emitted by the dipole can be found by a weighted sum of the monochromatically calculated contributions. The Gaussian spectrum with central wavelength λ_0 and free spectral width σ denotes as:

$$S(\lambda) = \frac{e^{\frac{-(\lambda-\lambda_0)^2}{2\sigma^2}}}{\sqrt{2\pi}\sigma} \tag{4.59}$$

4.3.5 External Efficiency

According to Eq.(2.1), the external efficiency η_{ext} of an LED is given by the product of the injection efficiency η_{inj}, the internal efficiency η_{int} with the extraction efficiency η_{extr}. If the quality of the active material is high, a photon-recycling factor η_{rec} can be added (Eq.(2.46)).

$$\eta_{ext} = \eta_{inj}\eta_{int}\eta_{extr}\eta_{rec} \tag{4.60}$$

η_{inj} treats the electrical efficiency of the LED and is beyond the scope of this chapter.

In Chapter 2 we have shown that the spontaneous emission rate of a dipole can be enhanced or suppressed when the dipole is placed in a cavity, increasing or decreasing the internal efficiency. The η_{int} of the LED can be related to the internal efficiency of the dipole in bulk η_{int}^{bulk}, a value which can be determined experimentally.

$$\eta_{int}^{bulk} = \frac{1/\tau_\infty^{rad}}{1/\tau_\infty^{rad} + 1/\tau_\infty^{nrad}} \tag{4.61a}$$

$$\eta_{int} = \frac{1/\tau^{rad}}{1/\tau^{rad} + 1/\tau_\infty^{nrad}} = \frac{L_{dip}}{L_{dip} + (1-\eta_{int}^{bulk})/\eta_{int}^{bulk}} \tag{4.61b}$$

The η_{int} can be calculated if the experimentally defined η_{int}^{bulk} is given. L_{dip} is the power flux through intefaces $s - S$ and $s + S$.

The single side extraction efficiency $\eta_{extr}^{n_2}$ to vacuum is given by Eq.(4.58) only if the substrate n_2 is transparent and no reflections occur at the substrate-vacuum interface. The substrate is in most cases thicker than the coherence length of the spontaneous emission. The numerical analysis that supposes infinite coherency of the light emitted by a single dipole would deviate from the realistic situation and the substrate is therefore not incorporated in the stratified structure. The absorption in the substrate and the reflection at the interface can easily be calculated and can be resumed in a factor r_{sub}:

$$\eta_{extr} = \eta_{extr}^{n_2} r_{sub} \tag{4.62}$$

The same holds for the superstrate if any.

Photon-recycling is the process in which photons emitted by the dipole are absorbed in the source layer and create a new electron-hole pair that on its turn

spontaneously recombines. Absorption in the source layer, surrounding the non absorbing active layer n_s with zero thickness, is not completely lost, it is partly recycled [20]. The photon-recycling factor is given by:

$$\eta_{rec} = \frac{1}{1 - \eta_{int} abs} \tag{4.63}$$

with *abs* the fraction of the emitted light that is absorbed in the source layer after it has escaped this layer once.

4.4 Conclusions

A new design for highly efficient light-emitting diodes is presented: the GA-RCLED. Simplistically spoken, the idea of the GA-RCLED is to let spontaneous emission happen in a planar microcavity. Doing so, the optical power is concentrated in several discrete modes. Modes that have a propagation constant that is larger than the vacuum wave vector can not escape the cavity by the extraction interface (top or/and bottom) and are lost unless their photon momentum is changed. This can be accomplished by a periodic shallow grating with appropriate Bragg vectors integrated in one of the interfaces of the cavity: the propagation of the guided modes will be broken and they are diffracted towards the outside media. The device is essentially planar, the extraction is single (eventually double) sided and the area of extraction of the light and of electrical injection (the active layer) coincidence or the available surface is efficiently used. Due to the shallow grating, surface recombination at the etched interfaces of the grating is avoided.

The WVD has been presented as an ideal tool to analyse the GA-RCLED on a qualitative level. The WVD graphically predicts to what extent a grating can suppress in-plane propagating guided light.

To analyse dipole radiation into a grating structure quantitatively, a rigorous analysing tool has been developed. With this tool we can calculate the extraction (and external) efficiency and radiation pattern of a plane of randomly oriented dipoles in an arbitrary grating structure. The main conclusion to distil out of the derivation of the emission of an in-plane distribution of dipoles is that in case of a set of $\mathbf{k}_{\|}$-vectors coupled by the Bragg condition, the contributions of the source terms of the respective emission directions to a specific spatial frequency $\mathbf{k}_{\|}^{mn}$ of this set can be considered to interact incoherently.

The analysis is implemented in C++ in a UNIX environment. Numerical calculations have been performed to design GA-RCLEDs and are presented in Chapter 6 and Chapter 7.

References

[1] K. Gillessen and W. Schairer, *Light Emitting Diodes: an Introduction,* (Prentice-Hall International, UK, 1987).

[2] W. Schmid, F. Eberhard, R. Jäger, R. King, M. Miller, J. Joos and K.J. Ebeling, "45% Quantum Efficiency Light-Emitting Diodes with Radial Outcoupling Taper", in *Light-Emitting Diodes : Research, Manufacturing, and Applications IV, Proc. SPIE,* vol. 3938, pp. 90-97, 2000.

[3] W. Schmid, M. Scherer, C. Karnutsch, A. Ploessl, W. Wegleiter, S. Schad, B. Neubert and K. Streubel, "High efficiency, red and infrared light-emitting diodes using radial outcoupling taper", *IEEE J. Sel. Top. Quantum Electron.,* vol. 8(2), pp. 256-263, 2002.

[4] M.O. Holcomb, M.R. Krames, G.E. Hofler, C. Carter-Coman, E. Chen, P. Grillot, K. Park, N.F. Gardner, J.-W. Huang, J. Posselt, D. Collins, S.A. Stockman, G. M. Craford, F.A. Kish, I.-H. Tan, T.S. Tan, C.P. Kocot and M. Hueschen, "High power Truncated-Inverted-Pyramid $(Al_xGa_{1-x})_{0.5}In_{0.5}P$ Light-Emitting Diodes", in *Light-Emitting Diodes : Research, Manufacturing, and Applications IV, Proc. SPIE,* vol. 3938, pp. 77-81, 2000.

[5] M.O. Holcomb, M.R. Krames, G.E. Hofler, C. Carter-Coman, E. Chen, P. Grillot, K. Park, N.F. Gardner, J.-W. Huang, J. Posselt, D. Collins, S.A. Stockman, G. M. Craford, F.A. Kish, I.-H. Tan, T.S. Tan, C.P. Kocot and M. Hueschen, "High-power truncated-inverted-pyramid $(Al_xGa_{1-x})_{0.5}In_{0.5}P$ light-emitting diodes exhibiting $> 50\%$ external quantum efficiency", *Appl. Phys. Lett.,* vol. 75(16), pp. 2365-2367, 1999.

[6] I. Schnitzer, E. Yablonovitch, C. Carneau, T.J. Gmitter and A. Scherer, "30% external quantum efficiency from surface textured, thin-film light-emitting diodes", *Appl. Phys. Lett.,* vol. 63(16), pp. 2174-2176, 1993.

[7] R. Windisch, C. Rooman, S Meinlschmidt, P. Kiesel, D. Zipperer, G. H. Doehler, B. Dutta, M. Kuijk, G. Borghs, and P. Heremans, "Impact of texture-enhanced transmission on high-efficiency surface-textured light-emitting diodes", *Appl. Phys. Lett.,* vol. 79(15), pp. 2315-2317, 2001.

[8] R. Windisch, C. Rooman,B. Dutta, A. Knobloch, G. Borghs, G. H. Dölher and P. Heremans, "Light-extraction mechanisms in high-efficiency surface-textured light-emitting diodes," *IEEE J. Sel. Top. Quantum Electron.,* vol. 8(2), pp. 248-255, 2002.

[9] M. Rattier, H. Benisty, R.P. Stanley, J.F. Carlin, R. Houdré, U. Oesterle, C.J.M. Smith, C. Weisbuch and T.F. Krauss, "Toward ultrahigh-efficiency aluminum oxide microcavity light-emitting diodes: guided mode extraction by photonic crystals", *IEEE J. Sel. Top. Quantum Electron.,* vol. 8(2), pp. 238-247, 2002.

[10] I. Schnitzer, E. Yablonovitch, C. Caneau and T.J. Gmitter, "Ultrahigh spontaneous emission quantum efficiency, 99.7% internally and 72% externally, from AlGaAs/GaAs/AlGaAs double heterostructures", *Appl. Phys. Lett.,* vol. 62(2), pp. 131-133, 1993.

[11] M.G. Salt, P. Andrew and W.L. Barnes, "Microcavities, texture symmetry, and photonic bandgaps", *J. Opt. Soc. Am. B,* vol. 18(20), pp. 240-243, 2001.

[12] S.C. Kitson, W.L. Barnes and J.R. Sambles, "Photonic Bandgaps in metallic microcavities", *J. of Appl. Phys.,* vol. 84(5), pp. 2399-2403, 1998.

[13] M.G. Salt and W.L. Barnes, "Flat photonic bands in guided modes of textured metallic microcavities", *Phys. Rev. B,* vol. 61(16), pp. 11125-11135, 2000.

[14] H. Rigneault, F. Lemarchand, A. Sentenac and H. Giovannini, "Extraction of light from source located inside waveguide grating structures", *Opt. Lett.,* vol. 24(3), pp. 148-150, 1999.

[15] J.M. Lupton, B.J. Matterson, I.D.W. Samuel, M.J. Jory and W.L. Barnes, "Bragg scattering from periodically microstructured light emitting diodes", *Appl. Phys. Lett.,* vol. 77(21), pp. 3340-3342, 2000.

[16] M. Rattier, H. Benisty and C. Weisbuch, "Photonic crystal extractor", in *Electromagnetic Crystal Structures: Proceedings of Workshop on Photonic and Electromagnetic Crystal Structures III (PECS3), 9-14 June 2001, St. Andrews, United Kingdom,* T.F. Krauss (Ed.), 2001.

[17] M. Rattier, *Diodes électro-luminescentes à cristaux photoniques: extraction de la lumière guidée,* (Ph. D. dissertation, Ecole Polytechnique, Paris, France) 2001.

[18] M. Boroditsky, T.F. Krauss, R. Coccioli, R. Vrijen, R. Bhat and E. Yablonovitch, "Light extraction from optically pumped light-emitting diode by thin-slab photonic crystal", *Appl. Phys. Lett.,* vol. 75(8), pp. 1036-1038, 1999.

[19] H. Rigneault, F. Lemarchand and A. Sentenac, "Dipole radiation into grating structures", *J. Opt. Soc. Am. A,* vol. 17(6), pp. 1048-1058, 2000.

[20] H. De Neve, *Design and Fabrication of Light Emitting Diodes based on the MicroCavity Effect,* Ph. D. dissertation, Ghent University, Ghent, Belgium, 1997.

[21] E.G. Loewen and E. Popov, "Diffraction Gratings and Application", *Marcel Dekker, New York,* 1997.

[22] S. Zhang and T. Tamir, "Rigorous theory of grating assisted couplers," *J. Opt. Soc. Am. A,* vol. 13(12), pp. 2403-2413, 1996.

[23] N.H. Sun, J.K. Butler, G.A. Evans, L. Pang and P. Congdon, "Analysis of grating-assisted directional couplers using the Floquet-Bloch theory", *Appl. Phys. Lett.,* vol. 13(12), pp. 2301-2315, 1997.

[24] S. David, A. Chelnokov and J.M. Lourtioz, "Isotropic photonic structures: Archimedean-like tilings and quasi-crystals", *IEEE J. of Quantum Electron.,* vol. 37(11), pp. 1427-1434, 2001.

[25] A.-L. Fehrembach, S. Enoch and A. Sentenac, "Highly directive light sources using two-dimensional photonic crystal slabs", *Appl. Phys. Lett.*, vol. 79(26), pp. 4280-4283, 2001.

[26] D. Kajfez and P. Guillon, eds., *"Dielectric resonators"*, Noble Publishing Corporation, Georgia, USA,, 1998.

[27] D.S. Chemla, D.A.B. Miller, P.W. Smith, A.C. Gossard and W. Wiegmann, "Room temperature excitonic nonlinear absorption and refraction in GaAs/AlGaAs multiple quantum well structures", *IEEE J. of Quantum Electron.*, 20(3), pp.265-269, 1984.

[28] W. Lukosz and R. E. Kunz, "Light Emission by Magnetic and Electric Dipoles Close to a Plane Interface. I Total radiated power", *J. Opt. Soc. Am.*, vol. 67(12), pp. 1607-1615, 1977.

[29] W. Lukosz and R. E. Kunz, "Light Emission by Magnetic and Electric Dipoles Close to a Plane Interface. II Radiation Patterns of Perpendicular Oriented Dipoles", *J. Opt. Soc. Am.*, vol. 67(12), pp. 1615-1619, 1977.

[30] W. Lukosz and R. E. Kunz, "Light Emission by Magnetic and Electric Dipoles Close to a Plane Interface. III Radiation Patterns of Dipoles with Arbitrary Orientation", *J. Opt. Soc. Am.*, vol. 69(11), pp. 1495-1503, 1979.

[31] W. Lukosz, "Theory of optical-environment-dependent spontaneous-emission rates for emitters in thin layers", *Phys. Rev. B*, vol. 22(6), pp. 3030-3037, 1980.

[32] Y. Yamamoto, F. Tassone and H. Cao, *Semiconductor Cavity Quantum Electrodynamics*, Springer Tracts in Modern Physics 169, Springer-Verlag Heidelberg Berlin, Germany, 2000.

[33] M. Yamanishi, I. Suemune, "Comment on polarization dependent momentum matrix elements in quantum well lasers", *Jap.J. Appl. Phys.*, 23, pp. L35-L36, 1984.

[34] G. Jones, A. Ghiti, M. Silver, E.P. O'Reilly and A.R. Adams, "Radiative perfomance of strained-layer lasers", *IEE Proceedings-J*, 140(1), pp. 85-89, 1993.

[35] R. Baets, *"Micro-cavity light emitting diodes"*, in Semiconductor Quantum Optoelectronics, A. Miller, M. Ebrahimzadeh and D.M. Finlayson, eds., St.-Andrews, UK, 1998.

[36] R. Baets, P. Bienstman and R. Bockstaele, *"Basics of Dipole Emission from a Planar Cavity"*, in Confined Photon Systems, Fundamentals and applications, H. Benisty, J.-M. Gérard, R. Houdré., J.Rarity and C. Weisbuch, eds., Springer-Verlag, 1999.

[37] J. Van Bladel, *"Electromagnetic fields"*, McGraw-Hill, 1964.

[38] H. Benisty, R. Stanley and M. Mayer, "Method of source terms for dipole emission modification in modes of arbitrary planar structures", *J. Opt. Soc. Am. A*, 15(5), pp. 1192-1201, 1998.

5

Fabrication of GA-RCLED

THE principle of the GA-RCLED has been pointed out in Chapter 4. Realisation of this concept is discussed in this chapter. The processing scheme of the GA-RCLED is given. The holographical procedure to define 2-D triangular and square lattice gratings is discussed in detail.

5.1 Introduction

The principle of the GA-RCLED has been discussed in Chapter 4. Spontaneous emission in a cavity is enhanced towards discrete modes. In a RCLED, the laterally propagating guided modes are not extractable and their carried power is lost. The diffractive grating incorporated in one or both mirrors of a GA-RCLED, redirects the laterally propagating mode to a direction within the extraction cone, enhancing the extraction efficiency.

The basic block of the GA-RCLED is the RCLED. In this work, we have chosen to work with the RCLED that has been optimised by H. De Neve in [1] for high overall extraction efficiency. The RCLED, emitting at 980 nm uses the GaAs/Al(Ga)As material system, with InGaAs high quality strained QWs as active material. The bottom-emitting devices are grown by *Metal-Organic Chemical Vapour Deposition* (MOCVD). With an Au/(GaAs/AlAs)-DBR asymmetric λ-cavity, the metal layer both serving as electrical contact and as mirror, and three InGaAs strained QWs, the overall external efficiency of 80 μm devices is up to 17%. When the diameter is larger, photon-recycling is more significant. An overall external efficiency up to 23% is obtained for large diameter ($\pm$1 mm) RCLEDs, or a 1.4 enhancement. The epilayer of this RCLED can more or less be adopted in the GA-RCLED and is given in Table 5.1. The thickness of the bottom and top spacer layer and the number of DBR pairs have to be optimised using the numerical tool presented in Chapter 4. This optimisation process is related with the choice of the grating (depth, lattice, dimensions, filling factor, etc.) and is discussed in Chapter 6-7. The implications of choosing this RCLED as basis for the GA-RCLED will also be discussed in these chapters.

The layer structure has been grown in a horizontal MOCVD reactor. More information can be found in [2]. It is important that the layer thicknesses are grown as accurate as possible. In practice, a small deviation caused by minuscule gas flow non-uniformities over the wafer and inefficient gas mixing in the growth chamber is inevitable. This deviation is typically a few percent or smaller. Deviations in layer thicknesses result in a cavity detuning: the cavity resonance wavelength differs from the desired value. The deviation can be estimated by comparing the measured and the calculated reflection spectrum [3]. To calculate the reflection spectrum, it is assumed that there is a uniform deviation of the thickness of the layers in the structure. The deviation in all layers will then be compensated by a regrowth (typically in the order of 10 nm). The structure will not be ideal – as only the top spacer is changed in thickness – but the cavity resonance wavelength will be tuned to the desired value, which is of utmost importance for the extraction efficiency (see Chapter 2).

Besides the accuracy of the layer thicknesses, the grown material has to be of high quality to reduce the optical absorption losses and to increase the internal quantum efficiency of the active layers.

The processing of the GA-RCLED begins with the definition of the grating in the top surface of the epilayer. Subsequently, the LEDs are processed (mesa, contacts, etc.). These processing steps are discussed in more detail in next sections.

A cross-section of a processed GA-RCLED is shown in Fig. 5.1. The grating,

thickness	material	doping level	remarks
40 nm	GaAs	p++-doped (1e19)	contact layer
XX nm	GaAs	p-doped (5e18)	top spacer
30 nm	$Al_{40}Ga_{60}As$	p-doped ramp down	GRIN spacer
20 nm	$Al_{20}Ga_{80}As$	intrinsic	GRIN spacer
2 nm	GaAs	intrinsic	barrier
6 nm	InGaAs	intrinsic	QW
2 nm	GaAs	intrinsic	barrier
6 nm	$Al_{20}Ga_{80}As$	intrinsic	barrier
2 nm	GaAs	intrinsic	barrier
6 nm	InGaAs	intrinsic	QW
2 nm	GaAs	intrinsic	barrier
6 nm	$Al_{20}Ga_{80}As$	intrinsic	barrier
2 nm	GaAs	intrinsic	barrier
6 nm	InGaAs	intrinsic	QW
2 nm	GaAs	intrinsic	barrier
20 nm	$Al_{20}Ga_{80}As$	intrinsic	GRIN spacer
30 nm	$Al_{40}Ga_{60}As$	n-doped ramp up	GRIN spacer
XX nm	GaAs	n-doped (1.85e18)	bottom spacer
84.5 nm	AlAs	n-doped (1.85e18)	first DBR pair
70 nm	GaAs	n-doped (1.85e18)	
X x (84.5 nm	AlAs	n-doped (1.85e18)	X DBR pairs
+70 nm)	GaAs	n-doped (1.85e18)	
	GaAs	n-doped (1.85e18)	buffer layer

TABLE. 5.1: Layer structure of GA-RCLED. Top spacer, bottom spacer and amount of DBR pairs will be determined in next chapters.

DBR, cavity, mesa, isolation and p-contact are clearly visible.

5.2 Grating fabrication

5.2.1 Introduction

The extensive technology base that has been developed by the microelectronics industry for the miniaturisation of integrated circuits has made it possible to fabricate nanoscaled diffractive optical structures, such as photonic crystals. Key tools such as e-beam pattern generators, reactive-ion etchers and mask-aligners permit the fabrication of surface-relief binary gratings with very small minimum feature sizes, tight alignment errors and high etch-depth accuracies. The most economical, and therefore dominant technology for pattern delineation in microelectronics still is optical lithography. Well known advantages obtainable by decreasing the exposure wavelength, such as higher resolution, greater depth of focus, and steeper wall profiles, have promoted wide interest in photolithography at wavelengths be-

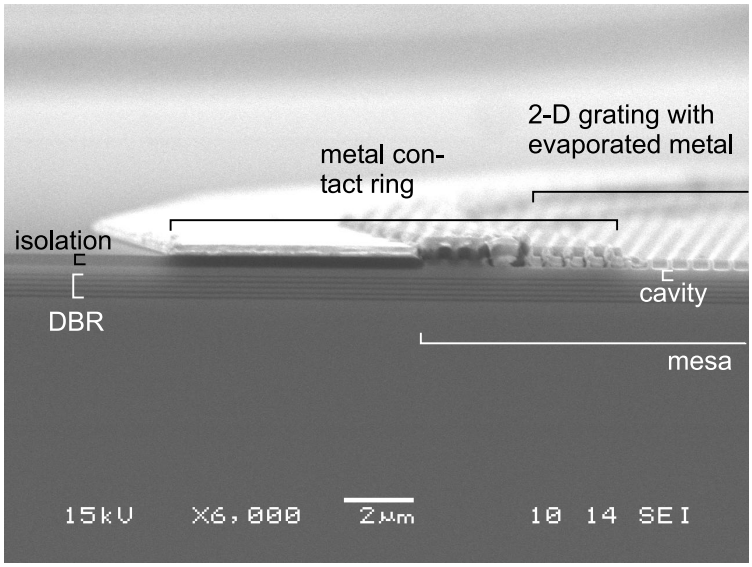

Fig. 5.1: SEM picture of cross-section of processed GA-RCLED. Only half of the circular mesa is shown.

low the conventional 365 nm (mercury arc lamp), and more and more 248 nm (krypton fluoride laser). The latter enables imaging of features down to 250 nm. Optical diffractive gratings, however, demand features in the order of 100-300 nm (period 250-600 nm), in combination with large aspect ratio (depth/pitch), shutting the door on standard photolithography. The required features can be realised with deep UV photolithography. With an argon fluoride laser operating at 193 nm in combination with additional resolution enhancement techniques based on the use of the phase of the light, such as the use of phase-shifting masks, it is believed that a resolution of 120 nm can be realised. The use of deep UV photolithography for fabrication of photonic crystals in SOI is under development [4], [5]. With the use of a 157 nm wavelength it is expected that features smaller than 100 nm can be printed [6]. However, the inherent physical limitations become more and more evident. For wavelengths below 120 nm, no optical materials are transparent and the development of diffraction limited lenses is improbable.

This explains the enhanced interest for alternative techniques witnessed in recent years. Electron-beam lithography is one of them. State-of-the-art photonic crystal (PC) structures are defined using e-beam. E-beam lithography writes in the resist, spinned on the semiconductor epilayer, a mask with nanometer-scale periodic features. The writing is done by strongly accelerating electrons (50 keV) which break the polymer chains of the resist (PMMA). The attacked resist is soluble in aceton. The unmasked regions of the substrate are removed by reactive ion etching, which results in a 2-D PC with air voids in a high-dielectric background. While this method permits rapid integration of user-defined mask patterns, high-volume production on large area substrates will be limited by the throughput of

this sequential writing technique. Therefore, the production application of e-beam writing is nowadays restricted to mask making (for optical and x-ray production tools) and small-scale 'direct-write' specialities, in spite of its obtainable resolution which is much better than with optical production tools today. E-beam is considered to be primarily a research tool. The electron wavelength at 50 keV is about 0.005 nm, which is far below atomic sizes and, hence, diffraction is not the limiting resolution [6]. Electron beams can be focussed to a spot size of a few nanometers. The resolution-limiting factors in electron-beam lithography strongly depend on the resist properties. The high accuracy, high resolution and build up experience of e-beam patterning of photonic nanostructures has been exploited in this work. GA-RCLEDs have been fabricated in cooperation with the University of Glasgow (Prof. Thomas F. Krauss and Prof. Richard De La Rue). The epitaxial layers, grown in INTEC, are patterned in Glasgow with an e-beam pattern generator (Leica EPBG-HR5) exhibiting resolution specifications of 5 nm. RIE translates the resist pattern into the semiconductor (see section 5.2.2.3). Further processing to LEDs is performed in INTEC (see section 5.3). Some SEM pictures of e-beam defined gratings will be given in Chapter 7.

It is clear that this sequential writing tool, although having the required accuracy, is far too time-consuming to be employed in mass-fabrication of photonic nanostructures. Besides deep UV, studied in another research program [4], holography can be used for this purpose. Holography is a standard optical interferometric technique. A photoresist coated epilayer is exposed to an interference pattern generated by the use of two or more coherent laser beams. Exposure to light induces a reaction in the photoresist modifying its solubility in a developer solution. Thus, the intensity profile in the interference pattern is converted into a periodically modulated solubility. Subsequent development converts this into a modulated topography. We have used this patterning technique to define 1-dimensional and 2-dimensional gratings. Its principle, accuracy and possibilities are detailed in the next section.

5.2.2 Holographic definition

The holographical procedure used in this work has been optimised by S. Goeman for the definition of 1-D gratings with a period > 700 nm [7]. We applied and optimised this process for patterning 1-D gratings with period < 700 nm and 2-D gratings. The procedure, common for 1-D and 2-D gratings is shortly presented, for details the reader is referred to [7]. 2-D patterning will be further discussed.

5 subsequent steps can be distinguished in the holographical procedure.

1. **sample preparation**
   The sample is prepared for illumination. This implies cleaning and drying of the samples, spinning and baking of an anti-reflection coating (eliminating surface normal standing wave patterns in the photoresist layer) and spinning and baking of the photoresist layer. We will not go any deeper into these basically conventional and well known processing steps.

2. **holographic illumination** (section 5.2.2.1)

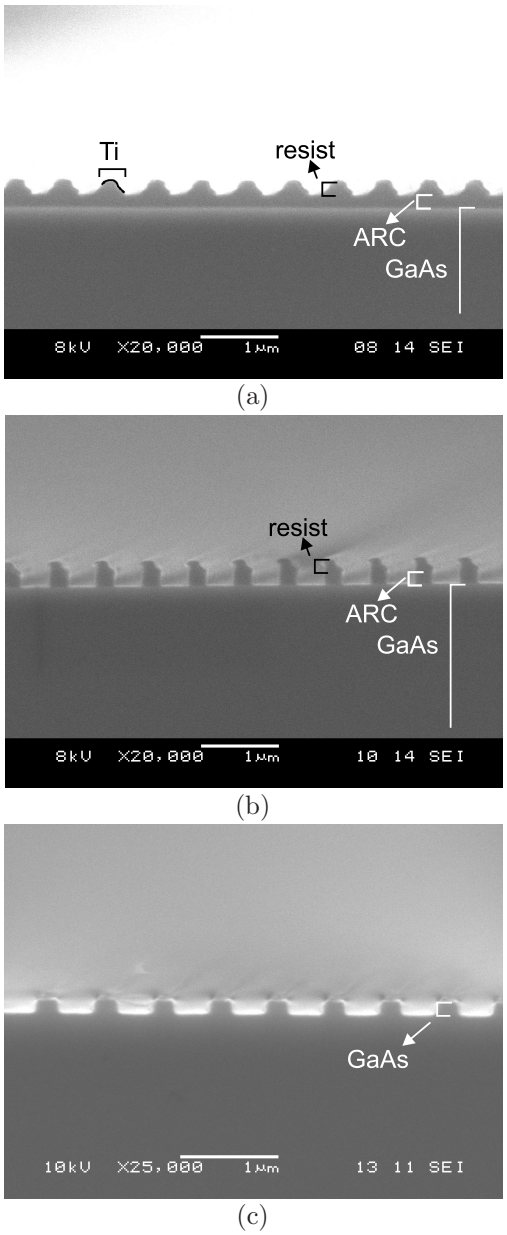

Fig. 5.2: SEM pictures of the subsequent stages of holographical procedure of a 1-D grating (period 600 nm, filling factor 0.33): (a) sinusoidal resist partially covered with Ti; (b) after RIE etch of resist and anti-reflection coating; (c) final state after etching the semiconductor and cleaning the sample.

During the holographic illumination, the photoresist layer is exposed with interfering laser beams. Development of the exposed resist results in a photoresist grating.

3. **Ti evaporation** (section 5.2.2.2)
   To protect the resist during the etching step and to control the filling factor of the grating, Ti is obliquely evaporated on the photoresist grating.

4. **RIE etching** (section 5.2.2.3)
   The anisotropic etch process: Reactive Ion Etching (RIE) is used to translate the photoresist grating into the semiconductor.

5. **sample cleaning**
   The process winds up by cleaning the samples. The Ti is removed with a HF dip. A subsequent O_2 plasma etch removes the residual photoresist and anti-reflection coating.

In Fig. 5.2, SEM pictures of the subsequent stages are presented for a 1-D grating after illumination and development. Fig. 5.2(a) clearly shows the sinusoidal resist partially covered with Ti. In Fig. 5.2(b), a RIE etch removed the resist and anti-reflection coating not covered by Ti. Fig. 5.2(c) shows the final state after etching the semiconductor and cleaning the sample.

5.2.2.1 Holographic illumination

The interference set-up that we use in this work is based on an interferometer known as Lloyd's mirror [8]. A lens focuses light from a UV laser onto a pinhole acting as spatial filter. A quasi-Gaussian diverging beam leaves the pinhole. At a distance r that is large[1] in comparison with the dimensions of the area that has to be exposed, this diverging spherical beam can be well approximated by a plane wave (see Fig. 5.3). The sample is mounted on a sample holder. The latter is fixed closely to a mirror (see Fig. 5.3). One part of the beam exposes the sample directly while the other part reaches the sample after reflecting on the mirror. These two contributions -direct and indirect- will interfere and create a 1-D periodic intensity pattern of which the period is defined by:

$$\Lambda = \frac{\lambda_{UV}}{2 \sin\alpha \sin\beta} \tag{5.1}$$

with λ_{UV} the wavelength of the UV laser, and α and β angles as defined in Fig. 5.3. β is chosen such that the mirror is perpendicular to the sample. α is adjusted to control the period of the interference pattern. The smallest realizable period is thus $\lambda_{UV}/2$. The laser in the set-up is an argon-ion laser (Spectra Physics 2024) operating at the MID UV wavelength $\lambda_{UV} = 363.8$ nm and output power over 100 mW ($\pm$1.5 mW/cm^2 on the sample). The polarisation of the laser is chosen

[1] Ideally, the distance r is as large as possible to get a uniform exposure over the finite area of sample and mirror. However, this distance r is limited in practice to about 100 cm to attain reasonable energy densities at the sample.

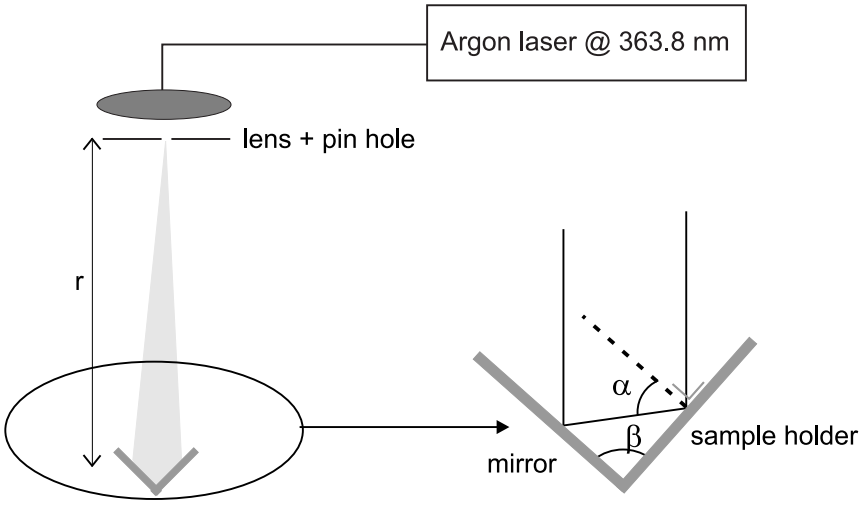

Fig. 5.3: Holography setup.

such that the samples are always exposed using TE polarised light with respect to the mirror and the sample, since this is known to give the best results [9]. The set-up is placed on an optical table and in a closed room to minimise mechanical vibrations, air turbulences and temperature variations as much as possible.

The accuracy of the set-up depends on the error $\Delta\alpha$ of the exposure angle. The error of the generated period $\Delta\Lambda$ is denoted as:

$$\Delta\Lambda = \frac{\Lambda}{\tan\alpha}\Delta\alpha \tag{5.2}$$

For setting the exposure angle α, a rotation stage is used. The error in the exposure angle is estimated to be about 0.1°. With increasing Λ, the exposure angle becomes smaller, leading to a significant increase in the error $\Delta\Lambda$. For a grating period $\Lambda = 600$ nm the error is estimated to be 3.29 nm. This error is acceptable and will have little effect on the grating performance for the grating applications in this work (see Chapter 6-7). Other factors are more important for determining the actual grating performance.

This is a classical set-up for defining 1-D gratings. To define 2-D gratings, different techniques can be used.

A first technique, to define triangular gratings, is the use of the interference of three coherent plane waves of equal power, separated by 120° (see Fig. 5.4(a)). Indeed, the in-plane field distribution of the interference pattern of three coherent waves with wavevectors $\mathbf{k}_i = \mathbf{k}_\perp + \mathbf{k}_{\parallel,i}$ and $|\mathbf{k}_{\parallel,i}| = k\sin\theta$, i =1,2,3 is given by (normalised to the intensity of a single wave):

$$E(x,y) = e^{-jk_\parallel x}\left(1 + e^{j\frac{3}{2}k_\parallel x} 2\cos\left(\frac{\sqrt{3}}{2}k_\parallel y\right)\right) \tag{5.3}$$

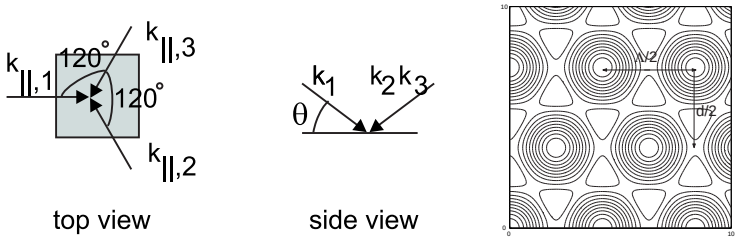

Fig. 5.4: (a) k-vector presentation of three interfering plane waves producing a (b) calculated triangular intensity distribution. 20 lines of equal intensity are shown with linear distribution. Adjacent circles are thus representing respectively a minimum and a maximum.

This results in a triangular intensity distribution as depicted in Fig. 5.4(b), with $d = 2\pi/\sqrt{3}k_{\|}$ and period $\Lambda = 4\pi/3k_{\|}$. d and Λ are defined in Fig. 5.4(b).

To obtain the three coherent plane waves, two beam splitters can be used. The use of beam-splitters however complicates the experimental set-up and suffers from low stability [10]. The consequence is a high sensitivity to vibrations and a resulting fuzzy pattern. An alternative technique is the use of a single monolithic diffracting object which splits one incident plane wave into three coherent parts. A schematic diagram of the diffraction gratings on the diffracting object is given in Fig. 5.5(a). This technique is described in [10] and [11]. The fabricated periodicities mentioned are at least a few microns and are equal to 2/3 of the period of the diffraction grating of the mask. Using more interfering beams and playing with their relative phase difference, intensity and polarisation, more complex structures can be realised (e.g. graphite structure, 3-D face-centered cubic structures [12]). One paper presents some experimental results of a square lattice grating with period 700 nm using 4 interfering beams [13]. A SEM picture of the resist profile reveals a rather low uniformity. All the cited examples do not transfer the resist pattern into a semiconductor grating.

An alternative method to obtain three coherent waves, is the 2-D equivalent of the Lloyd's mirror. A sketch is depicted in Fig. 5.5(b). Beam 1, lying in the bisectrices of the mirrors, illuminates the sample directly. The reflections of beam 1 on mirror 1 and 2 do as well illuminate the sample. This set-up is not found in literature and was one of the options to extend our 1-D holographical setup.

Instead of triple beam interference, a 2-D grating can be fabricated by multiple exposure in a two-beam interferometer. This technique is far more straightforward and simpler than previous methods. Considering the satisfactory experimental results obtained with this technique, previous methods have not been implemented and all holographically defined gratings are defined using this multiple-exposure interferometry. A triangular grating can be obtained by exposing the sample twice to the same interference pattern, with the sample rotated by 60° between the exposures. The exposure energy of each illumination is half the exposure energy used to define a 1-D grating. For a square lattice, the sample needs to be rotated

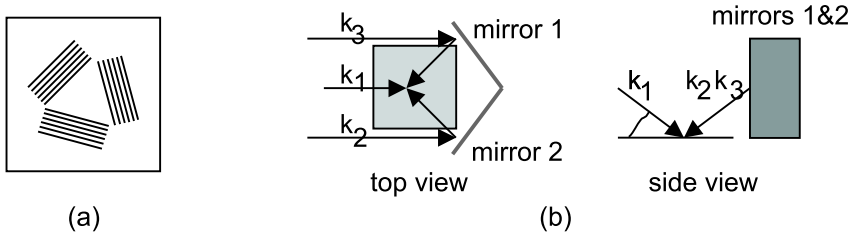

Fig. 5.5: (a) diffraction grating mask [10]; (b) 2-D Lloyd's mirror set-up.

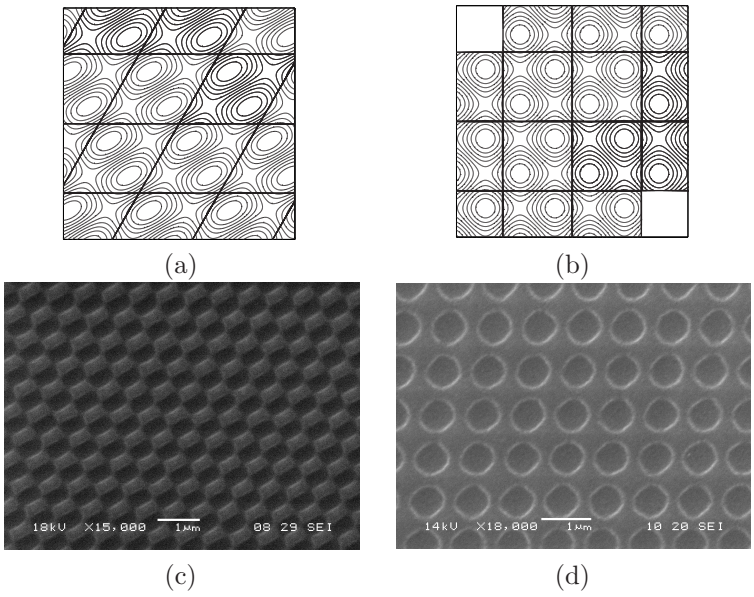

Fig. 5.6: (a)Calculated triangular intensity distribution using multiple exposure. 10 lines of equal intensity are shown with linear distribution, adjacent cells are thus representing respectively a minimum and a maximum; (b) idem but for square intensity distribution; (c) SEM picture of triangular lattice resist profile defined by multiple exposure; (d) SEM picture of square lattice resist profile defined by multiple exposure.

by 90° between the exposures. A calculated intensity distribution of a triangular lattice is sketched in Fig. 5.6(a). The intensity profile of each exposure is sinusoidal. The sum of both exposures does not have a triangular symmetry: the valleys in the profile are elongated in one direction. This asymmetry will partially be compensated by the subsequent step: evaporation of Ti. A square lattice intensity distribution is sketched in Fig. 5.6(b). A SEM picture of the corresponding resist profiles after development is shown in Fig. 5.6(c) and Fig. 5.6(d).

After holographic illumination, the sample is immersed in a diluted KOH solution to develop the exposed photoresist. The develop time is typically 2 to 3

seconds and happens manually. Due to this short development time and the manual character, this process in not fully controlled and results in a reproducibility decrease of the developed profile. The sinusoidal developed profile (see Fig. 5.2 and Fig. 5.6) does influence the filling factor of the grating under process, as will be clear in the next paragraph.

5.2.2.2 Ti evaporation

The transfer of the grating relief pattern to the substrate by RIE is discussed in section 5.2.2.3. Due to the nature of this process, both resist and substrate are etched. Although the etching rate of GaAs is several times faster than photoresist, this holds a considerably low limit on groove aspect ratio (groove depth/grating period) and vertical grating edges attainable in GaAs. To increase the attainable aspect ratio, the resist profile can be protected. Moreover it is desired to have control over the filling factor f of the grating. Although the wavelength of the application will be of the same order as the unit cell dimension and thus below the *Rayleigh resolution limit*[2], the fine detail in the cell geometry matter. Because of the Rayleigh expansion (see Chapter 3), the higher order wave vectors $\mathbf{k}_{mn}$ in this expansion are many times larger than the average $\mathbf{k}_{00}$-vector in the medium. Since their effective wavelength, given by $2\pi/|\mathbf{k}_{mn}|$, is therefore much shorter, and since the amplitudes of the higher order plane waves become large at high modulation depths, a kind of super-resolution occurs. Therefore it is important to control the filling factor and in-plane shape of the grating.

Both requirements, attainable aspect ratio and filling factor, are met by oblique evaporation of Ti on the resist. The Ti evaporation process is sketched in Fig. 5.7(a). The sample is fixed on a wedge with a well specified angle θ, mounted on a mounting block. This block is then placed in the evaporation unit. The result is sketched in Fig. 5.7(b) for a 1-D grating. Ti is deposited under an angle θ. Due to the shadowing effect of the resist pattern, only part of the grating will be covered with Ti. This Ti forms the actual etch mask for the subsequent RIE. The uncovered parts will be etched. The high resistance of Ti against the RIE does allow a large aspect-ratio. For a 1-D grating the evaporation plane (plane defined by the surface normal and the evaporation direction) contains the Bragg vector of the grating. The grating filling factor f will be determined by the photoresist grating depth, the period Λ and the Ti evaporation angle θ (see [7]). For a 2-D grating, the angle φ between the evaporation plane and the Bragg vector $\mathbf{K}_{y'}$ will influence the shape of the uncovered regions directly. This is shown in Fig. 5.8 where the numerically calculated profile of the Ti mask is compared with a SEM picture of the realised GaAs grating. The simulated profiles are calculated with a (in this work developed) tool that numerically solves the set of equations formed by the 2-D sinusoidal resist pattern and the tangent plane corresponding with the Ti evaporation.

Both simulation and experiment do use a single evaporation and concern a triangular lattice grating. The evaporation plane of Fig. 5.8(a)-(f) contains the Bragg vector $\mathbf{K}_x$ ($\varphi = 60°$), the evaporation angle θ, the angle of the evaporation

[2]The Rayleigh resolution limit states that the smallest feature that light can resolve is half the wavelength.

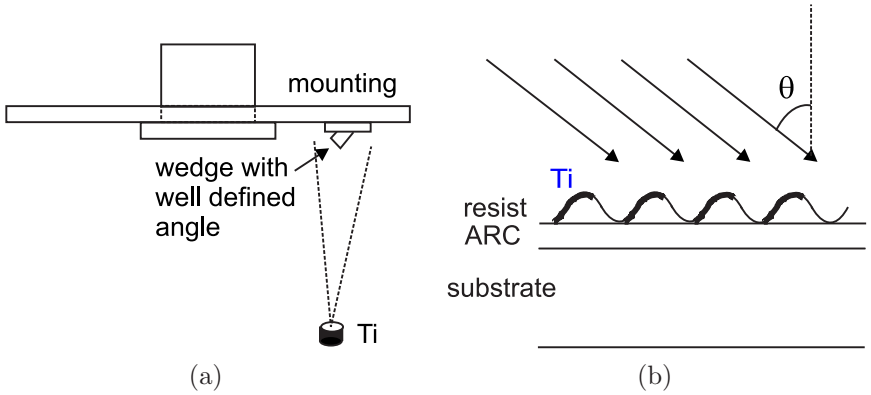

Fig. 5.7: (a)Schematic representation of the Ti evaporation process; (b) 1-D resist profile with obliquely evaporated Ti.

and the surface normal, is respectively 80°, 72° and 62°. The evaporation plane of Fig. 5.8(g)-(j) coincidences with the bisectors of the Bragg vectors ($\varphi = 90°$), the evaporation angle θ with the surface normal is respectively 80°, 72°. Although the filling factor f is well predicted with the numerical tool, the shape of the etched parts does slightly deviate. The difference can be attributed to the linear behavior of the resist which is assumed in the model. In reality however, the resist shows a threshold like behavior. Due to this non-linear behavior, the etched parts will be more elongated. Moreover, the uncertainty on resist profile due to the manual development will influence the grating shape. The grating does not show a true triangular symmetry: the holes are not circular in cross section but are elongated in one direction (Fig. 5.8(a)-(f)). Moreover, Fig. 5.8(g)-(j) do have a special cross section. It is clear from Chapter 4 that the grating for our applications optimally needs to show an as large as possible in-plane symmetry. Optimising φ can avoid asymmetrical cross-sections like holes elongated in one direction or with a special cross section. Evaporating twice with different φ can minimize elongation and enhance the symmetry as shown in Fig. 5.9 for a square lattice grating of period 600 nm. Although the evaporation angle θ is 80° for both samples, the filling factor is slightly different due to the the variation in resist pattern thickness, which is due to the uncontrolled nature of the development process. The influence of these fluctuations on the filling factor f of a 1-D grating are discussed S. Goeman in [7]. The influence on the filling factor f of a 2-D grating are similar. The fluctuation in filling factor f increases as the grating period decreases and is bigger for large filling factors.

5.2.2.3 Reactive Ion Etching

Reactive ion etching (RIE) is a technique for removing material from the wafer surface with both a reactive chemical process and a physical process using ion bombardment. The sample is mounted in a low pressure reaction chamber where the etching takes place. An RF power is applied between two electrodes. The

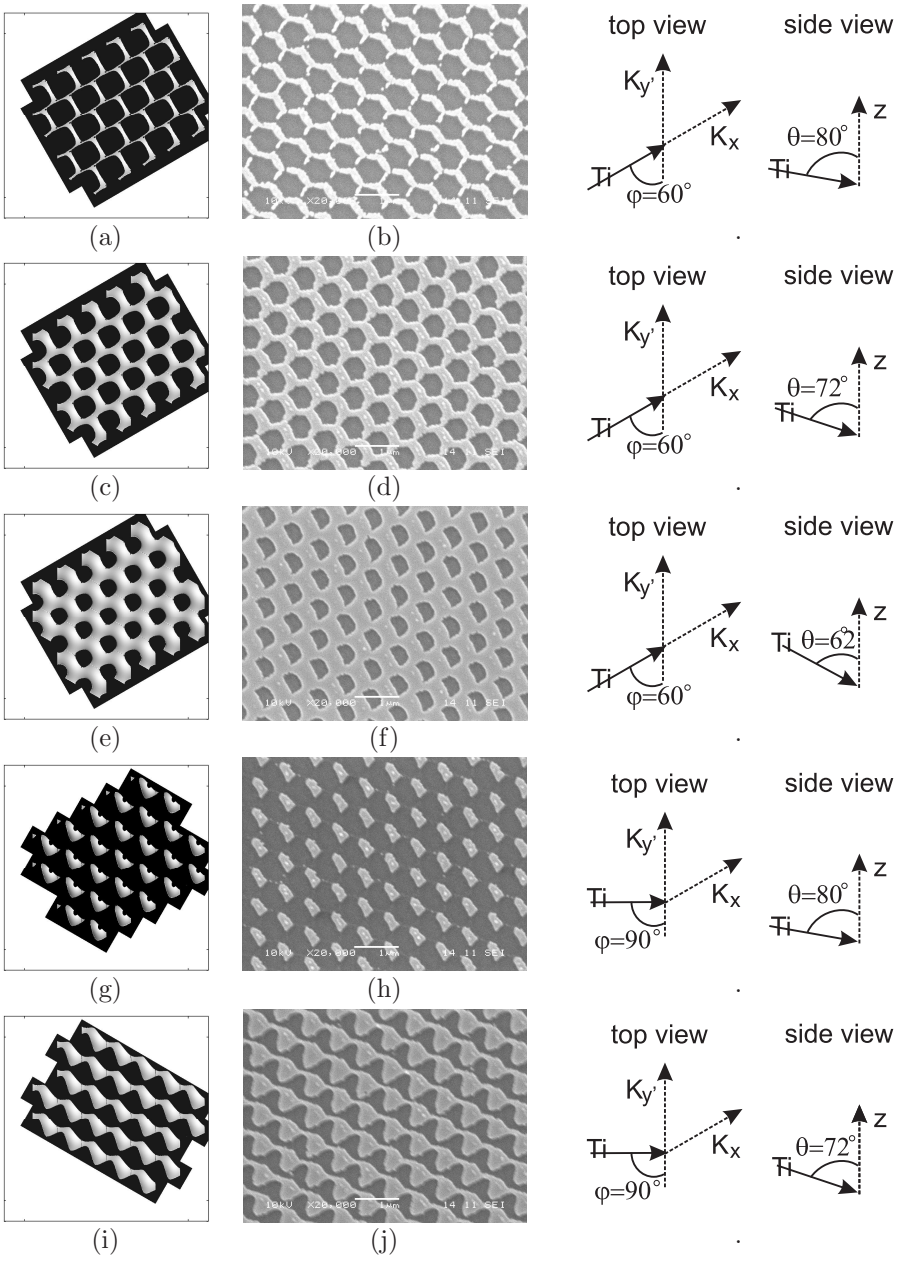

Fig. 5.8: (left) Numerical calculation of evaporation profile or Ti mask. The Ti-mask is white. (middle) Corresponding SEM picture of a triangular GaAs grating with period 600 nm and a single evaporation. The etched holes are dark. (right) The evaporation angles are schematically presented on the right hand side. (a)-(b) $\theta = 80°$, $\varphi = 60°$; (c)-(d) $\theta = 72°$, $\varphi = 60°$; (e)-(f) $\theta = 62°$, $\varphi = 60°$; (g)-(h) $\theta = 80°$, $\varphi = 90°$; (i)-(j) $\theta = 72°$, $\varphi = 90°$.

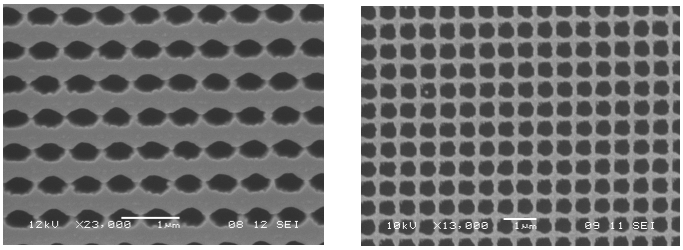

(a) (b)

Fig. 5.9: SEM picture of square grating with period 600 nm and (a) single Ti evaporation with $\theta = 80^\circ$; (b) double Ti evaporation with $\theta = 80^\circ$, $\varphi_1 = 0^\circ$, $\varphi_2 = 90^\circ$.

sample is mounted on one of these electrodes (the cathode). The RF field creates a plasma of the inserted gas ($SiCl_4$ for GaAs, O_2 for ARC). A DC self-bias develops on the cathode and the wafer acquires a large voltage difference with respect to the plasma. This condition creates directionality for the ionised species moving towards the wafer. The extremely reactive ions etch the wafer anisotropically. This results in vertical sidewalls.

Two successive RIE process steps have to be carried out. The evaporated Ti layer serves as mask for both etch steps. The uncovered resist and ARC is etched using an O_2 plasma, see Fig. 5.2(b). Subsequently $SiCl_4$ gas is ionised to etch the GaAs sample (Fig. 5.2(c)). The anisotropic characteristic of RIE results in a crenellated cross-section shape of the grating.

5.2.2.4 Possibilities and limitations

We have demonstrated that by using a double exposure in a two-beam interferometer it is possible to fabricate square lattice and triangular lattice gratings with submicron pitches. Although it is possible to fabricate such structures via e-beam lithography and deep UV lithography, the holographical technique has the potential of being a cheap and versatile alternative that avoids the need of a mask [14]. However, some limitations goes with this one-step process.

Traditionally the spatial arrangement of 2-D photonic crystals corresponds with one of the five 2-D Bravais lattices. Among these five lattices, the triangular and honeycomb ones possess the highest order of rotational symmetry (six) and a Brillouin zone that is the closest to a circle. Nevertheless, the band diagram of these lattices remains strongly dependent on the light propagation direction. The in-plane symmetry, an important characteristic for the GA-RCLED, can be augmented by using more sophisticated gratings, showing an enhanced in-plane rotational symmetry (e.g. Archimedean-like tilings and quasi-crystals [15]). The possibilities of the double exposure holographical technique however is restricted to square lattice and triangular lattice gratings. Moreover, in case of a triangular lattice, the superposition of two sinusoidal patterns does not result in a fully triangular symmetry. This asymmetry is partially resolved with the oblique evaporation of Ti.

Due to the short development times and the manual character, the development process is not fully controlled. The developed profile, together with the oblique evaporation of Ti, is important to determine the filling factor and shape of the grating. Uncontrolled variations on the latter make it difficult to obtain a grating with the optimum grating parameters. Deviation of these parameters from the optimal values will have a direct influence on the resonance conditions of the GA-RCLED. Unlike the RCLED, for which a simple regrowth compensates for deviations from the optimal resonant condition, there are no correction possibilities for the GA-RCLED when grating parameters deviate from the optimal value. This emphasizes the importance of a well controlled technological process to define the gratings. Reproducibility of the holographical process could be enhanced by optimising this development step.

SEM pictures reveal a certain degree of roughness at the edges of the grating holes. This roughness causes surface scattering and can be harmful for the efficiency of the application. The roughness can be linked to the Ti mask and further optimising this step can eventually reduce surface scattering.

5.3 Processing of LED

Once a grating is defined in the surface of the epilayer, the standard RCLED processing will finish the processing scheme. This processing was developed in [1] and [2] to whom the reader is referred for further detail. The processing scheme is only adjusted for the p-contact of the GA-RCLED and is summarised in this section.

First, lithography defines the p-contacts. After spinning the photoresist AZ5214 at 4000 rpm during 40 s, it is baked at 90°C. The resist is illuminated through the mask and subsequently developed in a diluted KOH solution. After development of the resist, the p-contact is deposited. Two kinds of gratings have been studied in this work: filled metal gratings and partially metal-covered air-semiconductor gratings (Fig. 5.10). For filled metal gratings we follow the same processing scheme as the RCLED: Au is deposited on the surface of the mesa by Joule-evaporation. The thickness is such that the grating is well covered with metal (> 200 nm). To obtain partially metal-covered air-semiconductor gratings, Au is obliquely evaporated on the mesa. Only the teeth of the grating will thus be covered with Au ($\pm$ 80 nm). After deposition, the Au surplus is removed using lift-off.

The second step is lithography of the mesa. A wet chemical etch using H_2SO_4/ H_2O_2/DI (1:1:18) of circular moats defines the mesa. This mesa should be deep enough to ensure lateral current confinement. This prevents a current threshold behavior associated with current spreading. However, to avoid excessive surface recombination in an exposed active layer, the mesa may not be etched through the QWs. This depth can be determined accurately by timing. The etch rate is 250 nm/min.

An isolation layer, 120 nm Al_2O_3, is evaporated. Other dielectrics as nitride, polyimide could also be used, but Al_2O_3 has been chosen, as it was the only available dielectric which could be deposited at a low temperature. The maximum tem-

Fig. 5.10: (a) Filled metal grating; (b)top-covered air-semiconductor grating.

perature before the reflection of the Au-mirror starts to degrade is about 200°C. The temperature increases to only 40-50 degrees when Al_2O_3 is evaporated. If the grating is defined all over the surface – which is the case for holographically defined gratings – , a corrugation will maintain in spite of the mesa etch. Precaution has to be taken to fully cover this corrugation surrounding the mesa with dielectric. On this dielectric, the contact ring and pad are deposited (40 nm Ti/400 nm Au). A layer of 40 nm Ti precedes the deposition of Au to ameliorate adhesion.

The sample is thinned to 100 μm to reduce substrate absorption of the bottom-emitting device. Polishing of the substrate reduces the surface roughness. The n-metallisation (AuGe/Ni) is deposited at the backside of the sample. Only the edges of the sample are metallised. The AuGe is deposited by Joule-evaporation, the Ni is sputtered. And finally, an anti-reflection coating is applied to eliminate Fresnel reflections.

5.4 Conclusion

We presented the fabrication process of the GA-RCLED. Except for a prior definition of a grating and the metallisation of this grating, as mirror and electrical contact, the processing scheme is identical to the one of a standard RCLED: straightforward and at low cost.

For the grating definition, several techniques can be used. In this work, we used both e-beam lithography and optical holography to define the nanostructures. E-beam is a relatively mature technique, but due to its sequential writing nature, it is far too time-consuming to be employed in mass-fabrication of gratings. An optical holography technique has been developed in this work. Characterisation by visualisation points out that the two-beam double exposure can be used to define 2-D triangular and square lattice gratings. In contrast with sequential e-beam writing tool, this single step process is adequate to be used in mass-fabrication of GA-RCLEDs. No advanced processing techniques are needed that can boost up costs.

Research on the use of deep UV lithography to define photonic crystals is very promising [4]. With illumination wavelengths of 248nm or less, this technique offers both the resolution and the speed required for the mass manufacturing of applications with submicron features. Even though the use of deep UV lithography for the fabrication of electronic ICs is already widespread, the techniques optimised for CMOS cannot be ported to other fields in a straightforward way. Contrary to holography, deep UV lithography demands a mask and sophisticated optics.

The holographic process can still be further improved: the manual development of the resist limits the reproducibility. Due to this, deviation of the grating

parameters from the optimal values is inevitable. In the GA-RCLED however, post corrections can not be executed anymore. Deviations of the grating parameters directly influence the resonance condition and thus the intrinsic behavior of the device. Secondly, due to the Ti evaporation, the edges show a small degree of roughness which can have baleful scattering effects.

References

[1] H. De Neve, *"Ontwerp en realisatie van Licht Emitterende Diodes op basis van het Microcaviteitseffect"*, Ph. D. Thesis, Ghent University, Ghent, Belgium, 1997.

[2] J. Blondelle, *"Realisatie van hoogefficiente substraatemitterende InGaAs/(Al)GaAs microcaviteitsLEDs met behulp van MOCVD"*, Ph. D. Thesis, Ghent University, Ghent, Belgium, 1997.

[3] R. Bockstaele, *"Resonant Cavity Light Emitting Diode Based Parallel Interconnections"*, Ph. D. these, Ghent University, Ghent, Belgium, 2001.

[4] European IST project: *"Photonic Integrated Circuits using photonic Crystal Optics"*, 1/3/2000-28/2/2003.

[5] W. Bogaerts, D. Taillaert, R. Baets, V, Wiaux, S. Beckx, M. Maenhoudt and G. Vandenberghe, "SOI Photonic Crystal Fabrication Using Deep UV Lithography", *proceedings PECS III, St. Andrews, UK, 06/2001* 2001.

[6] A. Ten Wolde, *Nanotechnology*, Netherlands Study Centre for Technology Trends, The Netherlands, 1998.

[7] S. Goeman, *"Integration of surface relief structures with vertical cavity surface emitting lasers for polarisation and mode control"*, Ph. D. Thesis, Ghent University, Ghent, Belgium, 2001.

[8] E. Hecht, *"Optics",* Addison-wesley Publishing Company, reading, Massachusetts, 1987.

[9] L. Johnson, "Generation of periodic surface corrugations", *Appl. Opt.,* vol. 17(8), pp. 1165-1181, 1978.

[10] V. Berger, O. GauthierLafaye and E. Costard, "Fabrication of a 2D photonic bandgap by a holographic method", *Electron. Lett.,* vol. 33(5), pp. 425-426, 1997.

[11] V. Berger, O. GauthierLafaye and E. Costard, "Photonic band gaps and holography", *J. Appl. Phys.,* vol. 82(1), pp. 60-64, 1997.

[12] D.N. Sharp, M. Campbell, E.R. Dedman, M.T. Harrison, R.G. Denning and A.J. Turberfield "Photonic crystals for the visible spectrum by holographic lithography", *Opt. and Quantum Electron.,* vol. 34(1-3), pp. 1-3, 2002.

[13] T. Kondo, S. Matsuo, S. Juodkazis and H. Misawa "Femtosecond laser interference technique with diffractive beam splitter for fabrication of three-dimensional photonic crystals", *Appl. Phys. Lett.,* vol. 79(6), pp. 725-727, 2001.

[14] S.C. Kitson, W.L. Barnes and J.R. Sambles, "The fabrication of submicron hexagonal arrays using multiple-exposure optical interferometry", *IEEE Phot. Tech. Lett.,* vol. 8(12), pp. 1662-1664, 1996.

[15] S. David, A. Chelnokov and J.M. Lourtioz, "Isotropic photonic structures: Archimedean-like tilings and quasi-crystals", *IEEE J. of Quantum Electron.,* vol. 37(11), pp. 1427-1434, 2001.

6

GA-RCLED with 1-D grating

IN this chapter, the GA-RCLED with a 1-D grating is presented. This includes the choice of the structure: do we use a bottom-emitting or a top-emitting device, dielectric or metallic mirrors, etc.? The design of a GA-RCLED, based on the numerical tool developed in Chapter 4, is discussed. The implementation of this design is characterised in terms of spectral behavior, farfield and efficiency.

6.1 Introduction

The operation principle of the GA-RCLED is detailed in Chapter 4. The microcavity effect is used to concentrate the optical power in discrete modes. A grating is then integrated in one of the mirrors to extract those modes that can not escape the cavity directly. These laterally propagating modes do have an in-plane symmetrical behavior: they propagate in all directions with uniform intensity. This in-plane symmetry of the guided modes demands the same rotational symmetry of the grating. Referring to Photonic Crystals, the traditionally used spatial arrangement corresponds with one of the five 2-D Bravais lattices. The triangular grating possesses the highest rotational symmetry and a Brillouin zone that is the closest to a circle. The use of 2-D gratings to enhance the extraction efficiency of a RCLED is discussed in Chapter 7.

In this chapter, we settle physical insight and focus on the conceptually more simple and straightforward 1-D gratings. Due to their low rotational symmetry, 1-D gratings used in a RCLED do not help to boost the extraction efficiency. Using the WVD-diagram (Chapter 4), we showed that, in the upper limit, only 22% of the guided mode can be extracted (GaAs RCLED with emission wavelength 980 nm). On the other hand, incorporation of a 1-D grating gives rise to an asymmetric, polarisation selective emission related to the orientation of the electric field **E** with respect to the Bragg vector of the grating.

Initially, a main structure has to be chosen. This is discussed in the next section and accounts both for GA-RCLEDs with 1-D and with 2-D gratings.

6.2 Structure of the GA-RCLED

A GA-RCLED is essentially a vertical emitter or more precisely the GA-RCLED emits in the growth direction of the multi-layer. The directly extractable Fabry-Pérot mode is enhanced in the vertical direction and the guided mode is diffracted to the corresponding direction. The propagation direction however can freely be chosen: light can be extracted at the top of the LED or at the backside (through the substrate) or at both sides. However, in practical applications, the latter is less appreciated than single facet extraction. The choice between top and bottom emitting has important consequences for the design of the mirrors.

6.2.1 Top- or bottom-emitting?

The consequences of the choice of the propagation direction on the design of the mirrors has been discussed for the RCLED in Chapter 2. Analogous consequences hold for the GA-RCLED. The different mirror types available are shortly recapitulated here.

(i) Metal has a high reflection coefficient over all wavelengths and all incidence angles. In practice, gold or silver is used. Gold is preferred, in spite of the slightly smaller power reflection coefficient (0.94 at 980 nm) compared to

silver (0.97 at 980 nm), but silver oxidises fast and needs therefore extra precautionary protection. Other metals show a higher absorption.

Metal can only be used as top mirror: it is not possible to grow semiconductor structures on the metal using the standard LED processing scheme as discussed in Chapter 5 [1]. In this case, the device is a bottom-emitting device: metal is not transparent and extraction through the metal would cause exuberant losses. Occasionally, a thin metal film can be used as outcouping mirror in a top-emitting RCLED. The thickness of the metal has to be chosen to minimise absorption in combination with the desired reflection coefficient.

The metal can serve as electrical contact and shows a low penetration depth.

(ii) A semiconductor DBR in contrary is easily integrated in the epilayer of the LED. It is electrically conductive, although in most cases special attention must be paid to the design of the DBR to minimise voltage drop across successive layers, especially for p-type DBRs. The big advantage is its optical transparency (although a small absorption can not be avoided[2]). Its disadvantage is the limited wavelength and angle range over which the DBR is highly reflective, due to the limited refractive index contrast. Selective oxidation [2] of the Al-containing DBR layers results in a higher index contrast, but removes its electrical conductivity.

(iii) An alternative is the dielectric DBR. The dielectrics (for example $ZnSe/CaF_2$ [3]) are chosen to maximise the index contrast, improving the reflection properties of the mirror. However, these types of DBR are in general not electrically conducting and are not integrable as bottom mirror. Furthermore, the thermal properties of the dielectrics need to be matched with the underlying semiconductor, to reduce thermal stresses.

Using the standard processing scheme, a top-emitting configuration demands the use of a highly reflective bottom semiconductor DBR and a moderately reflective top semiconductor or dielectric DBR (Fig. 6.1(a)). In Chapter 2, we showed that the large penetration depth of the high reflective bottom DBR, especially if the refractive index contrast is moderate, can be detrimental to the extraction efficiency. In this way, the performance of a top-emitting device will thus be smaller compared to its bottom-emitting counterpart. The penetration depth can be restricted using the selective oxidation process, in case of Al containing layers. Besides the reduced effective cavity length and the smaller amount of necessary DBR-layers, the fraction of leaky modes is suppressed [4] .

A transparent contact or ring contact should be used to perform the electrical current injection. There are several conducting and transparent materials available (such as Indium Tin Oxide, ITO). In case of a ring contact, special care must

[1] In thin-film technologies, metal can also serve as back mirror: by epitaxial lift-off, an upper thin-film of the epitaxial layer structure is taken off. The thin-film is flip-chipped and metal can be evaporated on its backside (see for example [1]).

[2] An important example is the p-type GaAs/AlGaAs DBR, due to the band tailing effect. This effect is caused by excessive p-type doping, and results in a smaller bandgap, implying that light with photon energy larger than the bandgap will be absorbed. Therefore, an n-type DBR is preferably uses as outcoupling mirror.

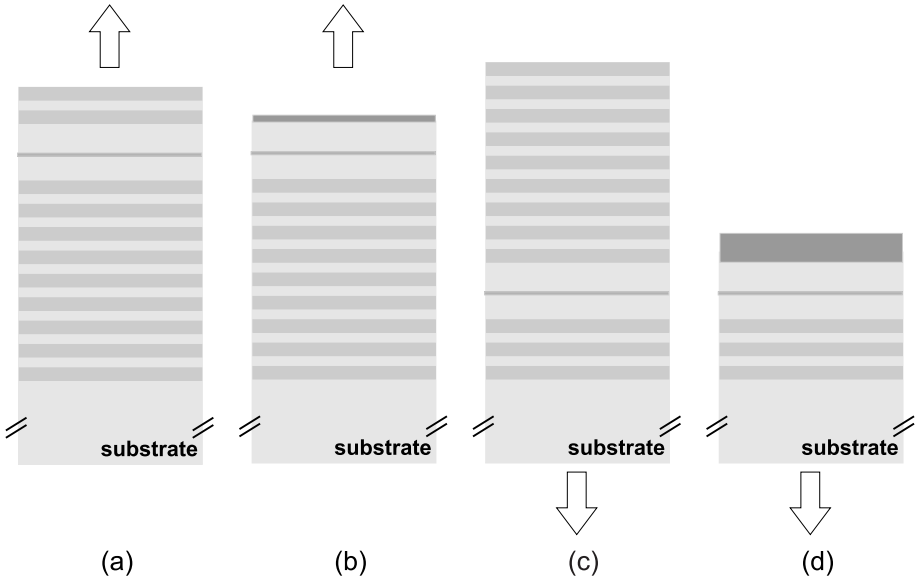

Fig. 6.1: Schematic presentation of different RCLED structures (a) top-emitting using a DBR/DBR cavity; (b) top-emitting using a metal/DBR cavity; (c) bottom-emitting using a DBR/DBR cavity; (d) bottom-emitting using a metal/DBR cavity.

be taken to confine the current, so that the light emission occurs mainly in the cavity and not under the metal contacts. A current confining structure based on selectively oxidised AlAs, can be used. An alternative is a grid contact. In that case, a part of the emitted light is shadowed by the contact, decreasing the efficiency. The bottom electrical contact is in general easier to realise. In most cases, an electrical conducting substrate is used, and a metal contact at the backside of the substrate is sufficient. In case of non-conducting mirrors (dielectric or oxidised DBR), electrical current injection is accomplished by intra-cavity contacts, like tunnel contact junctions [5]. The use of these contacts complicates the design and processing scheme of the LED.

The occasionally used thin metal film as outcouping mirror in a top-emitting RCLED is sketched in Fig. 6.1(b). Absorption in the top mirror is inevitable.

In a bottom-emitting RCLED, the emitted light travels through the substrate. The top mirror can be a highly reflective DBR (Fig. 6.1(c)) or a low absorptive thick metallic mirror (Fig. 6.1(d)) . The latter is preferred as it can serve both as mirror and electrical contact and as it shows a lower penetration depth. The bottom mirror is in general a moderately reflective DBR mirror. To reduce the penetration depth of this outcoupling mirror and to suppress leaky modes, an oxidised DBR can be used. This, however, has important complications on the design of the layer structure, especially because of the its electrically isolating character. Moreover, due to the higher electrical field amplitude at the top mirror, absorption will be higher in case of a metallic top mirror.

Special attention must be paid to reduce the absorption of light in the substrate and to avoid reflection losses at the substrate-air interface. For substrate-emitting RCLEDs on GaAs with emission wavelength 980 nm, well above the bandgap wavelength of GaAs, the absorption coefficient is about 5 cm^{-1} [6], corresponding to a 22% absorption after propagation through a 500 μm thick substrate. The substrate can be thinned or removed by mechanical grinding and chemical etching (see Chapter 5). An anti-reflection (AR) coating on the semiconductor-air interface can reduce the reflection losses.

At the time of the start of this work, bottom-emitting RCLEDs with metallic top mirror and semiconductor bottom DBR (Fig. 6.1(d)), were successfully optimised in our laboratory and showed world record overall efficiencies up to 22.4% [7]. The use of oxidised mirrors in RCLEDs, bottom- and top-emitting, was investigated in research program parallel with this work [8]. The availability of the mature technology of GaAs bottom-emitting devices emitting at 980 nm, its simple electrical design and technological straightforward processing scheme, inspired us to use this design to demonstrate efficiency improvement by inclusion of a grating in the top surface of the LED. However, the principle is applicable to all design structures.

6.2.2 Grating location

The ability to epitaxially deposit material on patterned surfaces is a key fabrication step for the realisation of many optical devices, such as distributed feedback (DFB) lasers [9], Bragg resonant filters [10], resonant grating waveguides [11], etc.. The devices need epitaxy of waveguide layers over the corrugated grating surfaces. Mastery of the overgrowth process, specifically the minimisation of overgrowth-generated defects, increases the design flexibility by allowing the placement of the corrugation anywhere within the device (Fig. 6.2(a)). The rectangular profiles of the grating are fabricated by RIE which introduces crystallographic damage at the etched surface. Unlike epitaxy on a planar (100) substrate, overgrowth of the corrugated substrate surface can lead to an uncontrollable variation in local composition during epitaxy, and thereby results in strong localised misfit stresses. These localised misfit stresses further affect the subsequent growth of high quality layers which constitute the active device structures.

Because of the absence of experience in this field in our laboratory, we decided to focus on devices with a grating etched in the top surface of the epilayer. The impact of this choice on the design of the GA-RCLED is clear (Fig. 6.2(b)). The fabrication process is given in Chapter 5: the complete epilayer is grown first, as second step a grating is etched in the surface of this epilayer. Deposition of metal on the grating makes this interface a suitable top mirror.

6.2.3 Material system

In paragraph 2.3.3, we mentioned the state-of-the-art of RCLEDs classified by wavelength. Unlike the 650 and 850-880-nm RCLEDs, there is no important application for 980-nm infrared devices. Moreover, there is a strong competition of

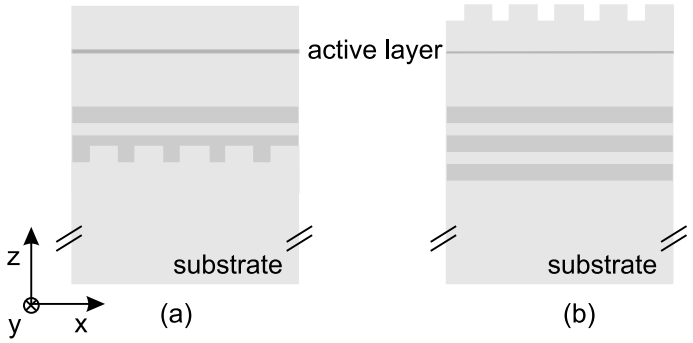

Fig. 6.2: Schematic presentation of GA-RCLED epilayer with (a) overgrown grating; (b) without overgrown grating.

980-nm VCSELs. Nevertheless, thorough investigation on these devices has been carried out and is still going on. The GaAs/Al(Ga)As material system is used with InGaAs high quality strained QWs for the active material. Contrary to 650/850-880 nm, GaAs is transparent for 980-nm light. This makes devices emitting at 980 nm preferable for proof of principle experiments.

Moreover, the device to which we referred in the previous paragraph emits at 980 nm, using the GaAs/Al(Ga)As material system. This mature system will be used for the fabrication of GA-RCLEDs. Nevertheless, the principle is again applicable for all material systems.

The epilayer of the LED is tabulated in Table 5.1.

6.3 Design of GA-RCLED with 1-D grating

With the use of a hybrid bottom-emitting cavity with metallic and DBR mirrors sustaining an extractable Fabry-Pérot mode, guided mode(s) and leaky DBR modes, the grating will couple the guided mode to the extractable Fabry-Pérot mode and vice versa. In Chapter 4 we mentioned that if the extractable resonant surface normal mode has a lower Q-factor than the non-extractable high-Q guided mode, reciprocal coupling of power between the resonant systems will result in a net power flow from the guided mode to the extraction cone, in case of negligible absorptions. In Chapter 7 we will see that the absorption of the guided mode in a RCLED is < 100 dB/mm. The Q-factor can be calculated to be in the order of 1000 [12]. The Q-factor of the Fabry-Pérot mode in the corresponding RCLED can analogously be calculated to be in the order of 60. The Q-factor of the guided mode is thus orders of magnitudes larger than the Q-factor of the Fabry-Pérot mode, and although one can not longer speak of two modes in the GA-RCLED due to coupling but rather of a "super mode", this coupling is so weak, that the "resonances" are minimally affected. This will be clear in the simulations shown further in this paragraph: the angular width of the diffracted guided mode remains small. Although, this criterion is not enough to guarantee an optimal operation of

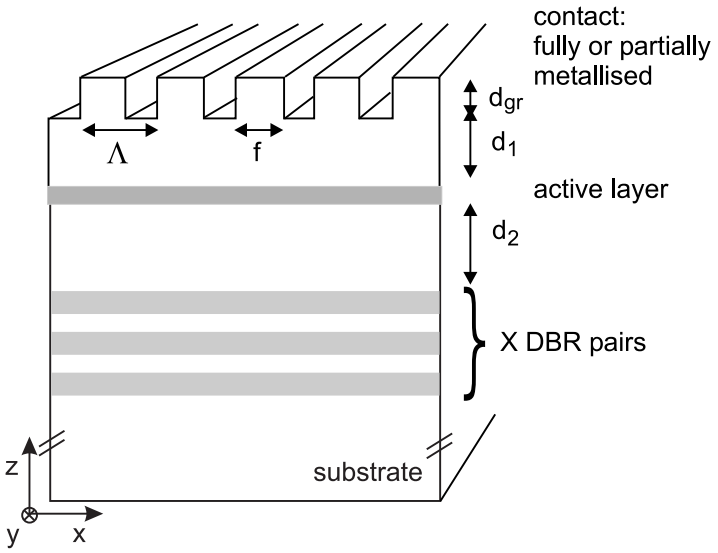

Fig. 6.3: Schematic presentation of GA-RCLED with indication of various parameters to be defined.

the GA-RCLED. Losses in the mirror, coupling strength of dipole emission, etc. do play as well an important role. To quantify these effects, rigorous simulations are needed. In this paragraph, the design of a GA-RCLED will be discussed while attention will be focussed on the influence of these effects on the behavior of the device.

Design of a GA-RCLED includes optimisation of the extraction efficiency by choosing the correct parameter values for the various parameters sketched in Fig. 6.3. It is immediately clear that the parameter space is large: period Λ, filling factor f, depth of grating d_{gr}, thickness of top spacer d_1 (including the contact layer), thickness of bottom spacer d_2, amount X of DBR pairs and type of contact (see Fig. 5.10: filled (f) metallic grating or top-covered (t) grating). The active layer is tabulated in Table 2.1. The optimisation is carried out with the numerical tool developed in Chapter 4. The behavior can be studied in the plane spanned by the Bragg vector and the surface normal (2-D behavior) or in three dimensions (3-D behavior). As the numerical tool is quite time-consuming, 2-D simulations will be used to get physical insight and to optimise roughly the device. To fine-tune the optimisation, a 3-D calculation is indispensable.

6.3.1 2-D behavior

The information given by the internal power flux distribution provides us physical insight in the behavior of a GA-RCLED. The downwards s-polarised internal angular net power flux distribution per unit spatial frequency in the RCLED of [7]

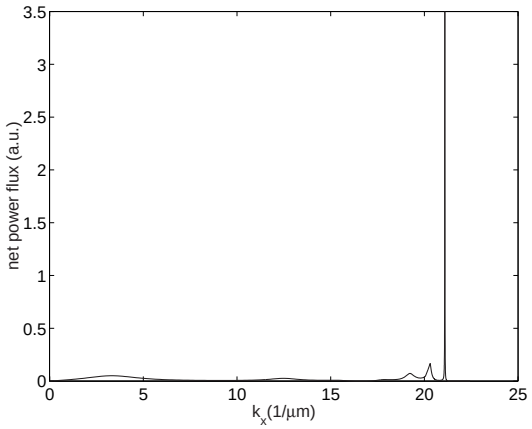

param.	value
Λ	\
d_{gr}	\
d_1	118 nm
d_2	70 nm
f	\
X	6
cont.	\
λ	976 nm

Fig. 6.4: Downwards s-polarised internal net power flux per unit spatial frequency in the RCLED of [7].

is shown in Fig. 6.4 (inside GaAs with $n_s = 3.52$). It is the net power flux per unit spatial frequency through an x-y plane under the active layer, with the distance between the plane and the active layer going to zero. The optical power can only be extracted if $|\mathbf{k}_x| < 2\pi/\lambda = 6.44$ [$1/\mu$m]. The Fabry-Pérot mode, which is extracted, the leaky modes, which are absorbed in the substrate, and the guided mode, which is absorbed in the QWs, can clearly be distinguished. The power distribution in the respective modes is approximately 27%, 30% and 37%. ±6% is absorbed in the metallic top mirror (both Fabry-Pérot, leaky and guided modes) .

Some of the parameters to be optimised in a GA-RCLED are discussed in this paragraph.

6.3.1.1 The period of the grating

If a grating is integrated in the top mirror of the RCLED, the guided mode will be diffracted according to the Bragg condition:

$$\mathbf{k}_{\|}^{m} = \mathbf{k}_{\|}^{gm} - m\mathbf{K}_x \tag{6.1}$$

$\mathbf{K}_x = 2\pi/\Lambda\mathbf{1}_x$ is the Bragg vector of the periodic corrugation, $\mathbf{k}_{\|}^{gm}$ is the parallel wave vector component of the guided mode ($|\mathbf{k}_{\|}^{gm}|$ is the fundamental space harmonic's propagation constant β) and m is an integer.

The minimum requirement for enhancement is that at least one diffraction order falls in the extraction cone, through which the optical power of the guided mode can leak to the surrounding air. The period of the grating determines the angle of the diffracted order and is thus the first parameter to be determined if we want to enhance extraction.

If the guided mode is coupled out by first order diffraction, the grating is called a first order grating (see Fig. 3.5(e)-(f)). The second order is reflected backwards,

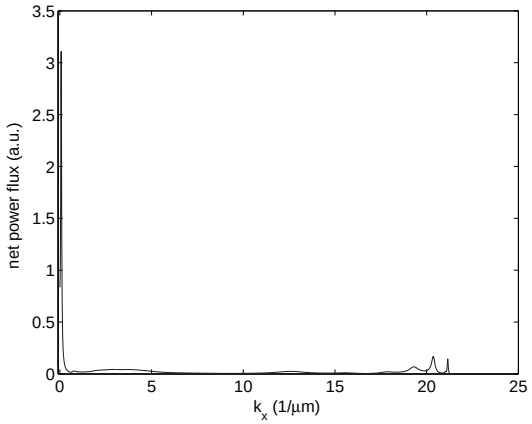

param.	value
Λ	298 nm
d_{gr}	25 nm
d_1	104 nm
d_2	70 nm
f	0.5
X	5
cont.	f
λ	976 nm

Fig. 6.5: Downwards s-polarised internal net power flux per unit spatial frequency in a GA-RCLED with first order grating.

the higher orders are evanescent. The internal power flux per unit spatial frequency of a GA-RCLED with a first order grating is denoted in Fig. 6.5. The diffracted guided mode, a peak located at the angle $\theta_{diff} \approx 0$, is as it were superposed on the Fabry-Pérot mode, with:

$$\theta_{diff} = \arcsin\left(\sin\theta_{gm} - \frac{\lambda/n_s}{\Lambda}\right) \tag{6.2}$$

The emitted intensity in the direction corresponding to the original guided mode θ_{gm} is strongly diminished. The in-plane extraction efficiency, the efficiency calculated with this 2-D numerical approach, is as high as 46.8%. The in-plane extraction efficiency is however quantitatively not representative, although indicative, for the exact extraction efficiency of the 3-D device as the rotational symmetry of the 1-D grating is very low. A full 3-D calculation, as will be presented in the next paragraph, is needed for this purpose.

A variation of the period Λ is reflected in a shift of the diffracted peak according to Eq.(6.1) and Eq.(6.2). For a larger period Λ, or equivalently a smaller Bragg vector $\mathbf{K}_x$, the peak will shift to larger k_x, and vice versa. The internal power flux per unit spatial frequency is plotted for several Λ around 298 nm in Fig. 6.6. If the Bragg vector $\mathbf{K}_x$ is larger than $\mathbf{k}_{\|}^{gm}$, the plotted diffracted mode corresponds with the minus first diffraction order of the guided mode propagating in the negative x-direction (Fig. 6.7(a)). If the Bragg vector $\mathbf{K}_x$ is smaller than $\mathbf{k}_{\|}^{gm}$, the plotted diffracted mode corresponds with the first diffraction order of the guided mode propagating in the positive x-direction (Fig. 6.7(b)). The power in the (minus) second diffraction order, the reverse propagating wave, is small due to the zero optical mode density around $\mathbf{k}_{\|}^{m}$ with $m = (-)2$. The minus second order diffraction of the guided mode propagating in the negative x direction is visible on the plot for $\Lambda = 318$ nm and 328 nm around k_x =18.5 and 17.4 respectively.

The guided mode can also be coupled out by second order diffraction. The

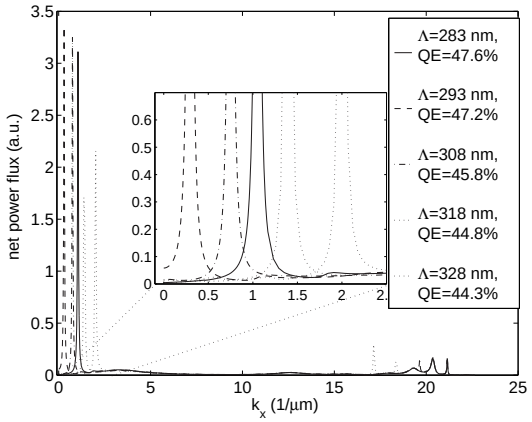

param.	value
Λ	*variable*
d_{gr}	25 nm
d_1	104 nm
d_2	70 nm
f	0.5
X	5
cont.	f
λ	976 nm

Fig. 6.6: Downwards s-polarised internal net power flux per unit spatial frequency in a GA-RCLED with first order grating with varying period.

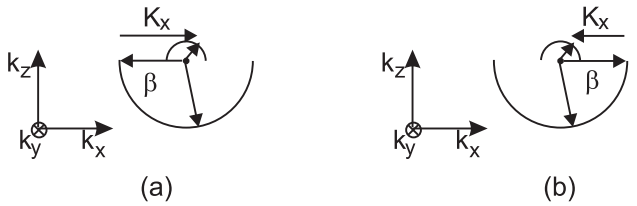

Fig. 6.7: WVD of first order 1-D diffraction grating with (a)$|\boldsymbol{K}_x| > |\boldsymbol{k}_{\|}^{gm}| = \beta$; (b) $|\boldsymbol{K}_x| < |\boldsymbol{k}_{\|}^{gm}| = \beta$.

grating is then called a second order grating (see Fig. 3.5(i)-(j)). The internal power flux per unit spatial frequency is plotted for Λ =578 nm, 598 nm and 618 nm in Fig. 6.8. Due to the presence of a continuum of optical modes, the leaky modes, the first diffraction order does carry a fraction of optical power, although smaller than the second diffraction order which couples with the Fabry-Pérot mode. The loss caused by the first diffraction order, which will be absorbed in the substrate, leads to an intrinsically lower in-plane extraction efficiency in comparison to a GA-RCLED using a first order grating. By means of an extra DBR, showing a high reflection for angles corresponding to the first diffraction order, this loss can partially be omitted (see Chapter 7, as second order gratings are more important when a 2-D grating is used).

6.3.1.2 The cavity thickness

Changing the cavity thickness is mainly translated in a shift of the resonance wavelength of the Fabry-Pérot mode. A larger cavity corresponds with a larger resonance wavelength. For a monochromatic dipole emission, a larger cavity thickness means a stronger pronounced lobed farfield or "rabbit ears" (see Chapter 2).

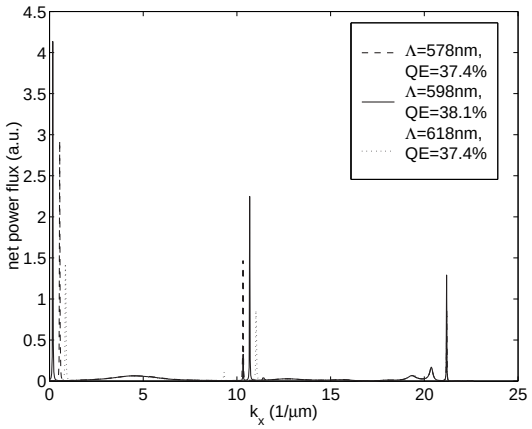

param.	value
Λ	*variable*
d_{gr}	25 nm
d_1	104 nm
d_2	70 nm
f	0.25
X	5
cont.	f
λ	976 nm

Fig. 6.8: Downwards s-polarised internal net power flux per unit spatial frequency in a GA-RCLED with second order grating with varying period around $\Lambda = 598$ nm.

If the thickness variation is small, $|\mathbf{k}_{\|}^{gm}|$ stays more or less unaffected.

The angular resonance shift of the Fabry-Pérot mode will influence the coupling strength of the guided mode and this Fabry-Pérot mode. This is shown in Fig. 6.9 for two different periods $\Lambda = 298$ nm and $\Lambda =$248 nm. Diffraction is enhanced and the extraction efficiency ameliorated if the diffracted guided wave corresponds with the resonance peak of the Fabry-Pérot mode. The respective extraction efficiencies are denoted in the legend of the plots: the optimal value for d_1 is 104 nm when $\Lambda =$298 nm, and 109 nm when $\Lambda = 248$ nm.

6.3.1.3 The depth of the grating

The depth of the grating determines the reflection and transmission coefficient and the absorption of a wave incident on the grating interface.

The phase of the zeroth order reflection coefficient of the (quasi) normal incident planes defines the resonant condition of the Fabry-Pérot mode (Eq.(2.22)). This is schematically presented in Fig. 6.10. An equivalent-phase plane can be associated with the grating. The location of this plane depends on the depth of the grating but also on the refractive index contrast, the filling factor and period. Changing the depth of the grating will shift the equivalent-phase plane and thus the effective cavity thickness and the effect on the extraction efficiency will be similar as discussed in the previous paragraph.

The depth will also affect the diffraction efficiency through the amplitude of the reflection coefficients. The impact on the extraction efficiency of both effects can be separated by changing the depth of the grating while the effective cavity thickness remains unchanged. This is presented in Fig. 6.11. The in-plane extraction efficiency will decrease for $d_{gr} > 25$ nm due to the increasing absorption in the metallic grating with increasing grating depth.

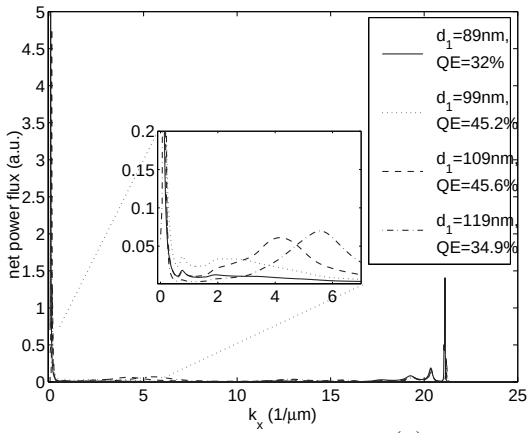

(a)

param.	value
Λ	298 nm
d_{gr}	25 nm
d_1	*variable*
d_2	70 nm
f	0.5
X	5
cont.	f
λ	976 nm

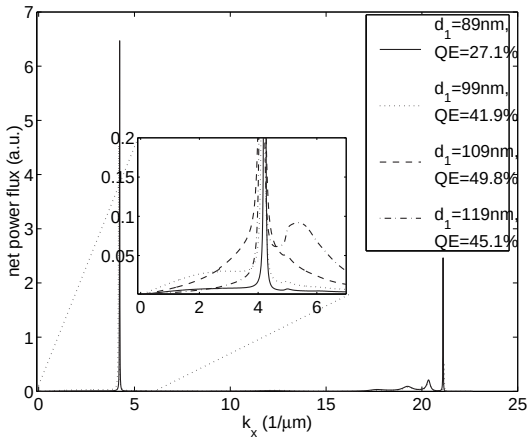

(b)

param.	value
Λ	248 nm
d_{gr}	25 nm
d_1	*variable*
d_2	70 nm
f	0.5
X	5
cont.	f
λ	976 nm

Fig. 6.9: Downwards s-polarised internal net power flux per unit spatial frequency in a GA-RCLED with first order grating and with varying cavity thickness d_1 (a) $\Lambda = 298\ nm$; (b) $\Lambda = 248\ nm$.

6.3.1.4 Wavelength of monochromatic dipole

Fig. 6.4-Fig. 6.11 assume a monochromatic dipole emission. In reality, the spectrum of spontaneous emission has a finite spectral width. The intrinsic spectral width depends on the injected current density level, as pointed out in Chapter 2. The working-point of the devices under consideration will result typically in an intrinsic spectral width with a more or less Gaussian shape with a FWHM of ± 20 nm. The internal power flux per unit spatial frequency is plotted for several wavelengths in this range around the central wavelength 976 nm in Fig. 6.12. The extraction efficiency falls away for wavelengths out of this spectral range.

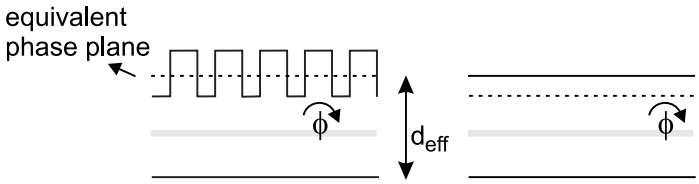

Fig. 6.10: Equivalent-phase plane of grating interface.

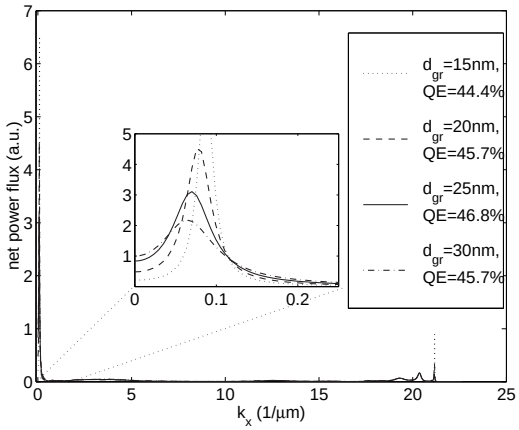

param.	value
Λ	298 nm
d_{gr}	*variable*
d_1	*variable*
d_2	70 nm
f	0.5
X	5
cont.	f
λ	976 nm

Fig. 6.11: Downwards s-polarised internal net power flux per unit spatial frequency in a GA-RCLED with first order grating with varying grating depth and constant effective cavity thickness.

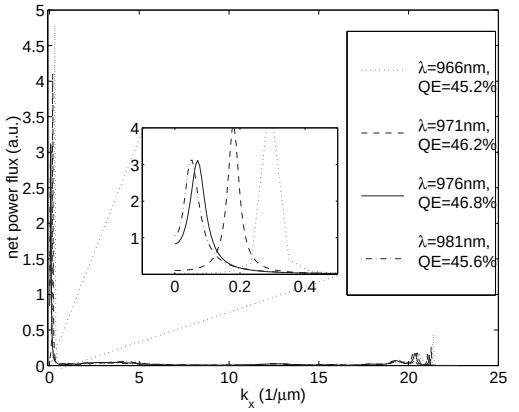

param.	value
Λ	298 nm
d_{gr}	25 nm
d_1	104 nm
d_2	70 nm
f	0.5
X	6
cont.	f
λ	*variable*

Fig. 6.12: Downwards s-polarised internal net power flux per unit spatial frequency in a GA-RCLED with first order grating for different wavelengths.

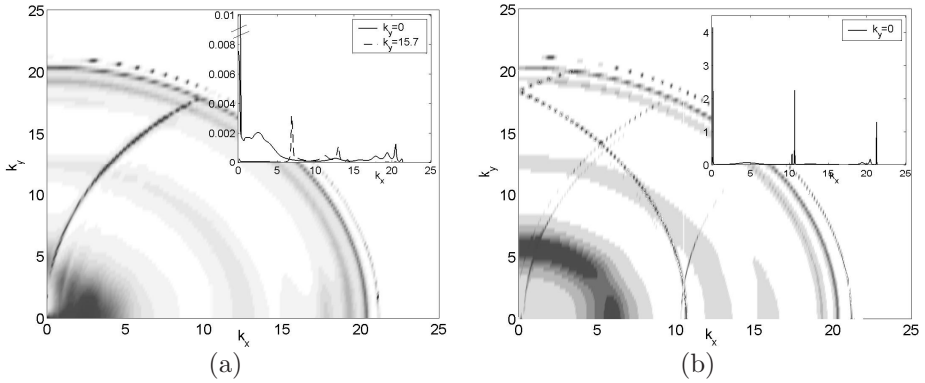

Fig. 6.13: 2-D plot of downwards s-polarised internal net power flux per unit spatial frequency in a GA-RCLED with first order grating (cfr. Fig. 6.4); (b) in a GA-RCLED with second order grating (cfr. Fig. 6.8).

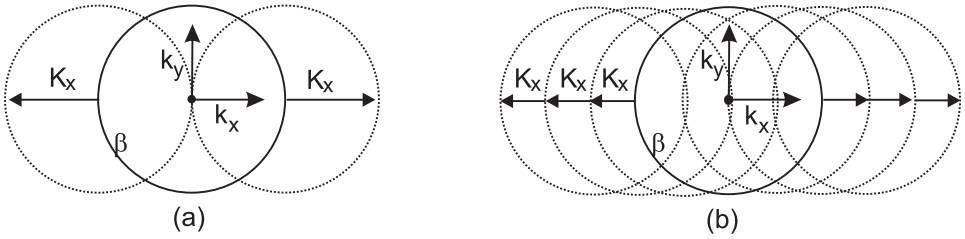

Fig. 6.14: WVD of first order 1-D diffraction grating (cfr. Fig. 6.13(a)); (b) second order 1-D diffraction grating (cfr. Fig. 6.13(b)). With β the propagation constant of the first order and the dotted lines the higher order spatial harmonics.

6.3.2 3-D behavior

As mentioned above, a quantitative correct analysis of a GA-RCLED with a 1-D grating is only possible if a 3-D calculation is performed. As the simulation time of a 3-D calculation spans several hours (due to the numerical complexity of the diffraction problem which is proportional with $L * n^3$, with L the amount of layers, and $n = 2N + 1$ the amount of orders in the calculation, see Chapter 4), optimisation of the design is first carried out by 2-D simulations. A 3-D simulation will fine-tune this optimisation. Fig. 6.13(a) and (b) present a 2-D plot of the internal power flux per unit spatial frequency of the GA-RCLED with a first order grating of Fig. 6.4 and of the GA-RCLED with a second order grating of Fig. 6.8 respectively. The WVD of these devices, sketched in Fig. 6.14, can easily be recognised in the calculated intensity distribution. The extraction efficiency of the respective devices is 23% and 14.7%. The higher absorption losses ($> 25\%$) of the corrugated interface in comparison with a flat mirror and the low rotational symmetry of the 1-D grating cause the extraction efficiency to be lower than a standard high efficiency RCLED.

6.3.3 Design rules

The 2-D and 3-D simulations show the influence of the different parameters on the behavior of a GA-RCLED. The parameter space is large and, moreover, the parameters can reinforce or counteract each other (e.g. d_{gr} and d_1). This makes the design procedure of a GA-RCLED more difficult. Yet, some basic rules of thumb can be concluded from the simulations in Fig. 6.5-Fig. 6.14 to design a bottom-emitting semiconductor GA-RCLED. Starting from these rules, the design has to be completed by 3-D simulations.

First, the period has to be chosen such that at least one of the diffracted orders of the guided mode has a propagation constant that is smaller than the vacuum wave vector. Only then, the guided mode can be diffracted towards the outside medium. The optimal lattice can be chosen by using the WVD.

Secondly, the presence of the Fabry-Pérot mode reinforces diffraction of the guided mode. The power emitted in the diffracted guided mode is indeed related with the presence of an optical mode with an in-plane wave vector $\mathbf{k}_{\|} = \mathbf{k}_{\|}^{gm} - m\mathbf{K}_x$. If the optical mode density at $\mathbf{k}_{\|}^{gm} - m\mathbf{K}_x$ equals zero, diffracted power is marginal. This is shown in Fig. 6.9 and confirmed in Fig. 6.15, where the downwards s-polarised internal net power flux per unit spatial frequency is shown for both a cavity with and without Fabry-Pérot mode. The extraction efficiency is reduced to 3.6% when the cavity is not resonant in the surface normal direction. The second rule when designing a bottom-emitting GA-RCLED is thus to ensure the presence of the Fabry-Pérot mode at the diffracted angle of the guided mode by realising an optimal effective cavity thickness. This is done by choosing a correct combination of values for d_{gr}, d_1, d_2, f. The sensitivity of the behavior of the GA-RCLED to deviations of the effective cavity thickness is in the same time the drawback of the device. Technological control on the growth of the epistructure and the etch depth of the grating are primordial.

Finally, the grating parameters have to be chosen such that the diffraction efficiency of the guided mode is higher than the absorption losses, both in the QW and in the metallic mirror. Especially filled metal gratings can show increasing losses in function of their depth.

Although presented chronologically, these three rules of thumb have to be executed simultaneously as the parameters to be optimised do influence the presented rules at the same time, but not necessary in the same direction. It also should be emphasized that due to the numerical complexity of 3-D simulations and the multi-parameter character of the device, this optimisation process will lead to a local optimum. The ultimate quantitative potential of the GA-RCLED could not be proven in the time-frame of this research work with the available tools.

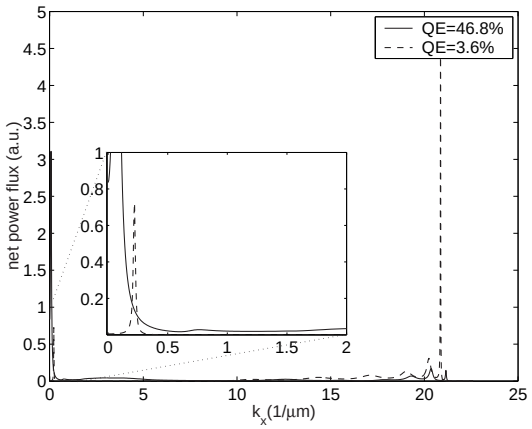

param.	value
Λ	298 nm
d_{gr}	25 nm
d_1	*variable*
d_2	70 nm
f	0.5
X	5
cont.	f
λ	976 nm

Fig. 6.15: Downwards s-polarised internal net power flux per unit spatial frequency in a GA-RCLED with first order grating. Full line represents cavity with Fabry-Pérot mode ($d_1 = 104$ nm). Dotted line represents a cavity without Fabry-Pérot mode ($d_1 = 34$ nm).

6.4 Characterisation of GA-RCLED with 1-D grating

6.4.1 Realisation of GA-RCLEDs with 1-D grating

GA-RCLEDs with a 1-D grating were fabricated by the processing scheme presented in Chapter 5. The 1-D gratings were fabricated by holography. The cross section of a GA-RCLED with a filled metallic grating, d_{gr} =190 nm, $f = 0.46$ is shown in the SEM picture of Fig. 6.16. Fig. 6.18 and Fig. 6.17 depict SEM pictures of 1-D gratings with varying f and with respective periods 300 nm and 600 nm. The legend specifies the intended and the realised filling factor. For the 600 nm period gratings, good agreement is attained. For the 300 nm period grating the agreement is less. This is in accordance with the finding in [13], which states that the filling factor is less reproducible for smaller periods.

6.4.2 Spectral behavior

The spectral behavior of the GA-RCLED of Fig. 6.16 is presented in Fig. 6.19, Fig. 6.21 and Fig. 6.22, in all of which the left hand side denotes measured data and the right hand side calculated data. The measurement of the spectrum of the device is carried out with a low numerical aperture fiber (NA=0.12). Apart from the striking similarity between the experiment and the simulation, the data show some noteworthy phenomena.

Fig. 6.19 plots the polarisation selective behavior in the surface normal direction. The polarisation as denoted in the plot, defines the orientation of the electric field $\mathbf{E}$ with respect to the Bragg vector $\mathbf{K}_x$ of the 1-D grating. TE refers to an in-plane $\mathbf{E}$ component normal to $\mathbf{K}_x$ (or in other words, parallel with the

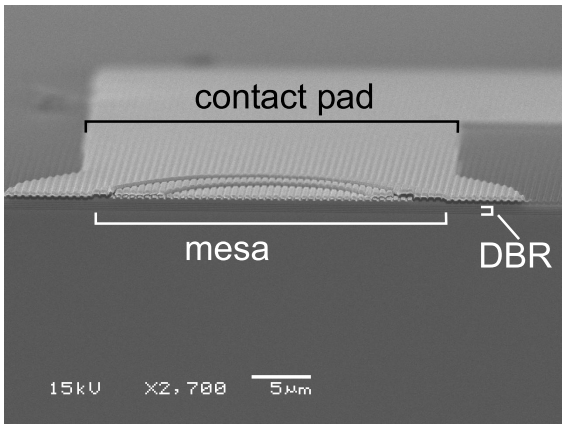

(a)

param.	value
Λ	600 nm
d_{gr}	190 nm
d_1	80 nm
d_2	70 nm
f	0.46
X	5
cont.	f

(b)

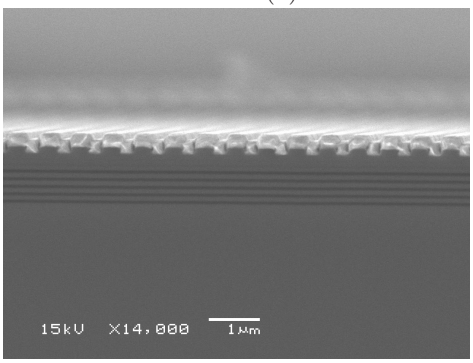

(c)

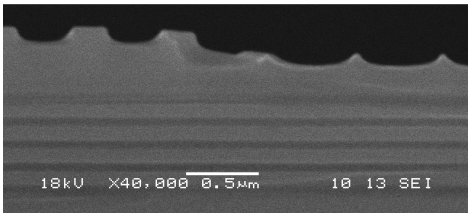

(d)

Fig. 6.16: SEM picture of (a) cross section of GA-RCLED; (b) parameter values; (c) detail of grating; (d) detail at mesa edge.

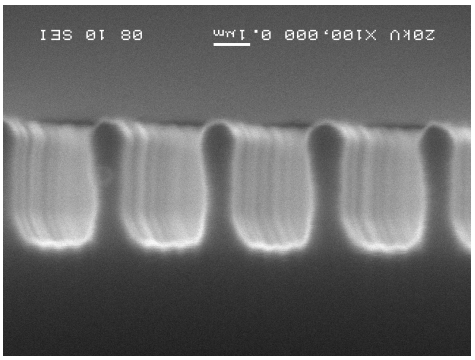

(a)

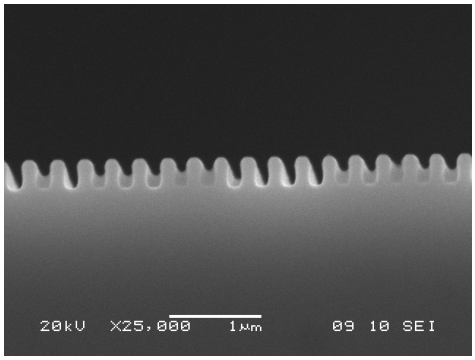

(b)

Fig. 6.17: SEM picture of 1-D grating, $\Lambda = 300$ nm (a) $f = \pm 0.22$, intended $f = 0.35$; (b) $f = \pm 0.55$, intended $f = 0.45$.

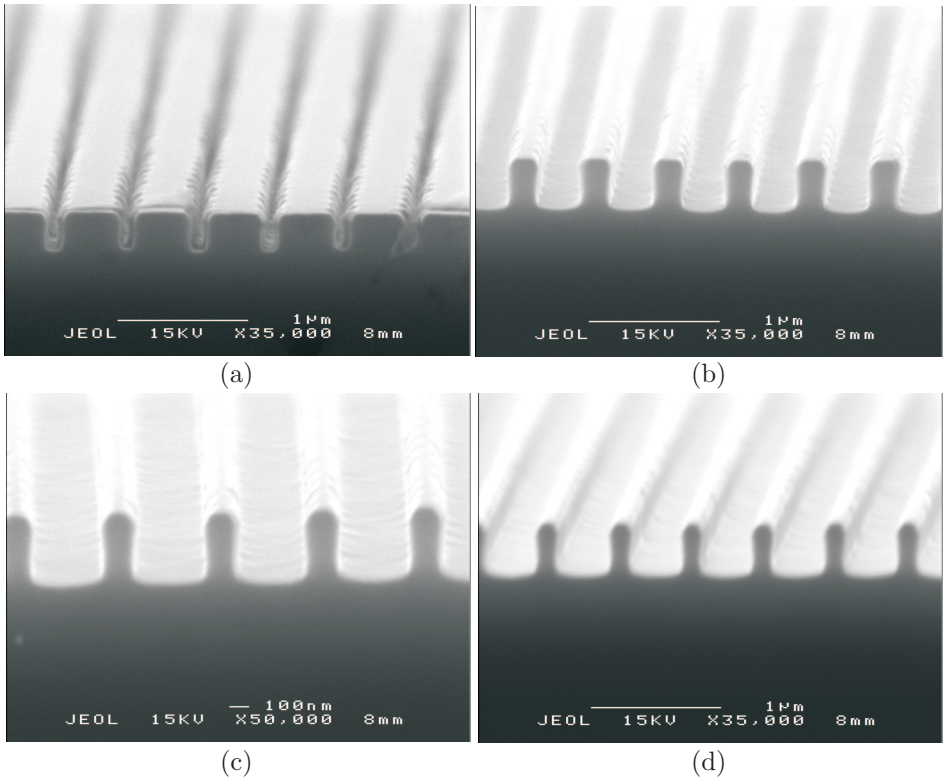

Fig. 6.18: SEM picture of 1-D grating, $\Lambda = 600$ nm (a) $f = \pm 0.18$, intended $f = 0.23$; (b) $f = \pm 0.3$, intended $f = 0.3$; (c) $f = \pm 0.34$, intended $f = 0.37$;(d) $f = \pm 0.66$, intended $f = 0.6$.

grating ridges). Only TE-polarised light is diffracted, which can be seen in the internal power flux per unit spatial frequency in Fig. 6.20. A diffraction peak is only present when the in-plane **E** component is normal to $\mathbf{K}_x$.

Fig. 6.21 shows the measured and the simulated angle resolved spectrum in the plane spanned by the Bragg vector and the surface normal (see Fig. 6.23(a)). The peak extracted in the surface normal direction splits when observed from more oblique angles θ. According to the WVD diagram expressing the Bragg condition, a guided wave is extracted with an angle θ_{diff} corresponding to $\mathbf{k}_{\parallel}^{diff}$ with:

$$\mathbf{k}_{\parallel}^{gm} = \mathbf{k}_{\parallel}^{diff} \pm m\mathbf{K}_x \tag{6.3}$$

with, in this case, m=2 for the second order grating. This condition is fulfilled by two counter propagating modes. For $\theta = 0°$, Bragg coupling is symmetric, and the two counter propagating modes do have the same wavelength. For oblique angles $\theta \neq 0°$, the symmetry is lost and the counter propagating modes which fulfill Eq.(6.3) do have a different wavelength, resulting in a splitting of the angle resolved spectrum.

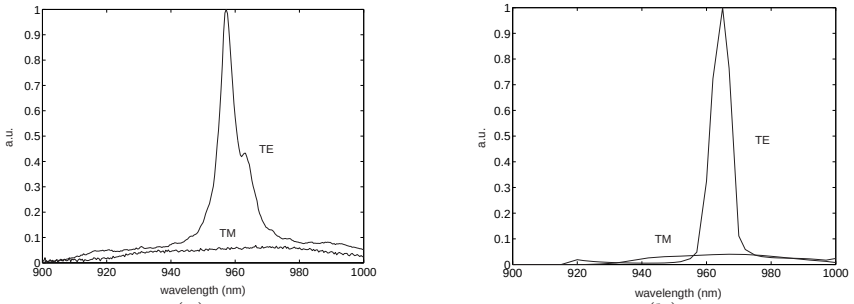

Fig. 6.19: Polarisation selective emission of GA-RCLED with 1-D second order grating (see Fig. 6.16) (a) experimental data; (b) calculated data.

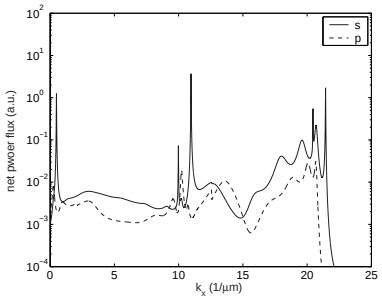

Fig. 6.20: s-polarised and p-polarised downwards internal net power flux per unit spatial frequency in a GA-RCLED for λ =960 nm ($k_y = 0$).

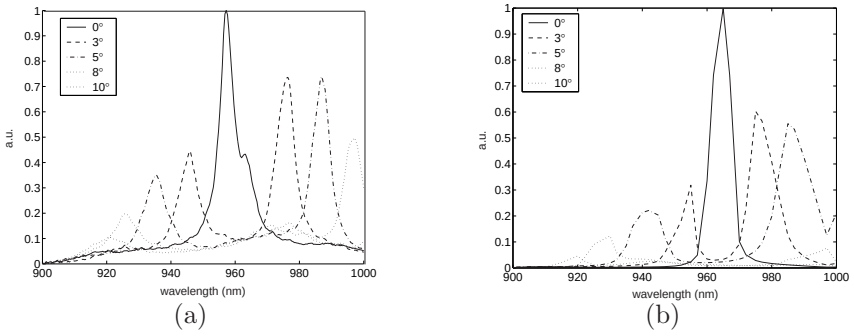

Fig. 6.21: Angle resolved spectrum in the plane spanned by the Bragg vector and the surface normal of GA-RCLED with 1-D second order grating (see Fig. 6.16) (a) experimental data; (b) calculated data.

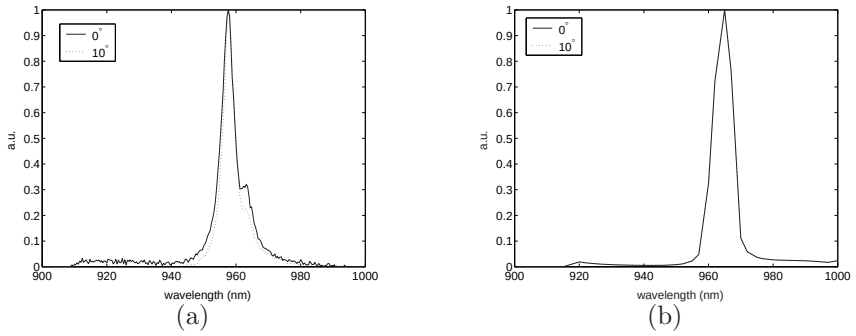

Fig. 6.22: Angle resolved spectrum in the plane spanned by the grating ridge and the surface normal of GA-RCLED with 1-D second order grating (see Fig. 6.16) (a) experimental data; (b) calculated data.

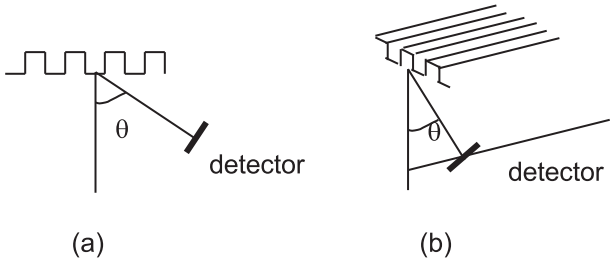

Fig. 6.23: (a) measurement in the plane spanned by the Bragg vector and the surface normal; (b) measurement in the plane spanned by the grating ridge and the surface normal.

Due to the 1-D character of the grating, this phenomena is not observed in the plane spanned by the grating ridge and the surface normal (Fig. 6.22 and Fig. 6.23(b)).

6.4.3 Farfield

Fig. 6.24 shows the farfield measured in the respective planes sketched in Fig. 6.23. The power is integrated over the spectral width of the LED. The asymmetry caused by the 1-D character of the grating is clear. It also shows that the guided modes are coupled to a restricted angular range around the surface normal when $k_y = 0$.

6.4.4 Efficiency

The numerical tool to design GA-RCLEDs was not yet available during the fabrication of the device discussed in this paragraph. The device was optimised intuitively and serves only as proof of principle: the guided modes can be extracted by means of a grating. Spectral and farfield measurements confirm the extraction of the guided modes, moreover post-process calculations are consistent with the

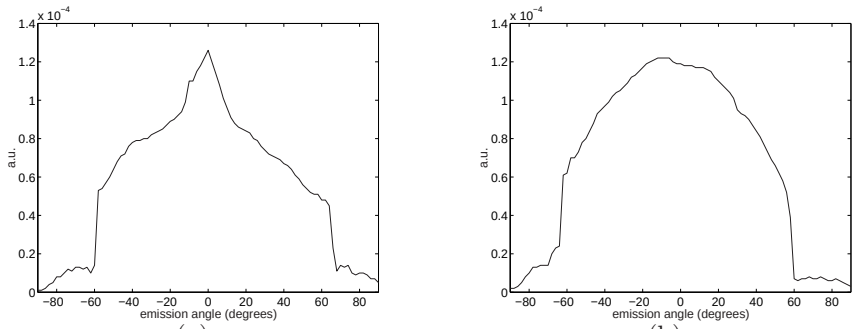

Fig. 6.24: Farfield of GA-RCLED with 1-D second order grating (see Fig. 6.16)(a) measured in the plane spanned by the Bragg vector and the surface normal; (b) measured in the plane spanned by the grating ridge and the surface normal.

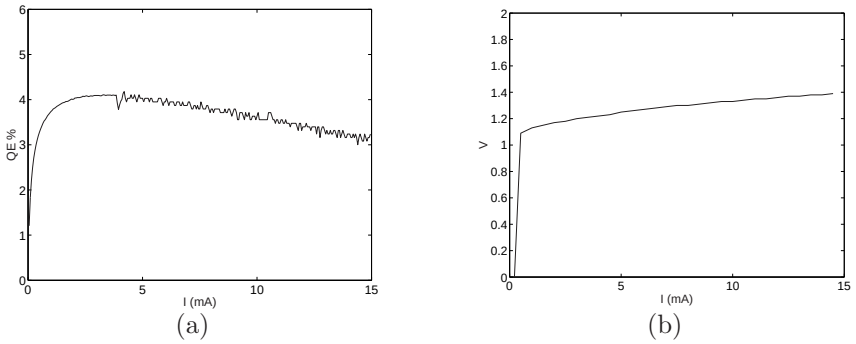

Fig. 6.25: (a) External efficiency and (b) IV characteristic of of GA-RCLED with 1-D second order grating (see Fig. 6.16 and diameter 72 μm).

experimental data. The external efficiency, however, is low: $\eta_{ext} = 4.1\%$[3]. The reason is triple: the Fabry-Pérot resonance condition is not fulfilled (clearly not visible in Fig. 6.19 and Fig. 6.20), the total metallic absorption losses of a metallic grating ($\pm 25\%$) are higher than in the case of a flat metallic mirror ($\pm 6\%$) and as already mentioned a 1-D grating exhibits a low in-plane rotational symmetry. The external efficiency is plotted in Fig. 6.25 together with the IV curve. The IV curve points out that the electrical conditions are maintained when a metallic grating is used as electrical contact.

[3]The η_{ext} is defined by the ratio of the measured optical power divided by the photon energy on the injected current divided by the electron charge. The total emitted optical power is measured with a large area Si detector (1 cm^2) positioned under the sample holder. The sample holder is a perforated copper plate with thickness=1 mm^2. Shadowing of the sample holder and the finite size of the detector result in a detector capture efficiency lower than one. For simplicity, although at our disadvantage, we assume the detector capture efficiency to be equal to one.

6.4.5 Roughening

Even unsuccessful experiments can lead to nice results. In one case, the holographical definition of the grating went wrong. The cross section of a device of this run is shown in Fig. 6.26. Rather than a binary grating, the surface was roughened. Due to this roughening, the photons are scattered and the escape probability is enhanced. This principle is successfully used by Windisch *et al.* [1].

Evidence of the non-resonant character of the LED is given by the farfield measurements. Fig. 6.27(a) shows the farfield of the roughened LED, while Fig. 6.27(b) plots the farfield of the respective LED where no roughening has been applied. The Lambertian emission profile of the non-resonant cavity LED (NRCLED) is in strong contrast with the "rabbit-ear" emission profile of the RCLED.

The differential external quantum efficiency is as high as 22%, the external quantum efficiency is somewhat lower due to the shallow mesa etch. The 3dB spectral bandwidth increases fast with increasing current, again pointing out the non-resonant character of the device. The diameter of the device 72 μm, the substrate has been thinned to 100 μm and an AR coating minimises Fresnel losses.

6.5 Conclusion

Although 1-D gratings are not expected to boost the efficiency of the RCLED, they serve very well to settle physical insight and can be used as proof of principle.

The numerical tool was used to study the influence of the different grating and cavity parameters on the behavior of the GA-RCLED. It was found that a simultaneous presence of the Fabry-Pérot resonance and the diffracted guided mode enhances the extraction efficieny.

Holographical fabrication of 1-D gratings is very successful. The technology is mature to be used to fabricate gratings with periods down to at least 300 nm.

Experiments and simulations are consistent. The phenomena observed in the measured and calculated data can be explained. Remarkable are the asymmetric emission and the polarisation selective behavior. This polarisation selective behavior could be exploited in numerous applications, like liquid crystal displays, etc..

Evidence of guided mode extraction is definitely given.

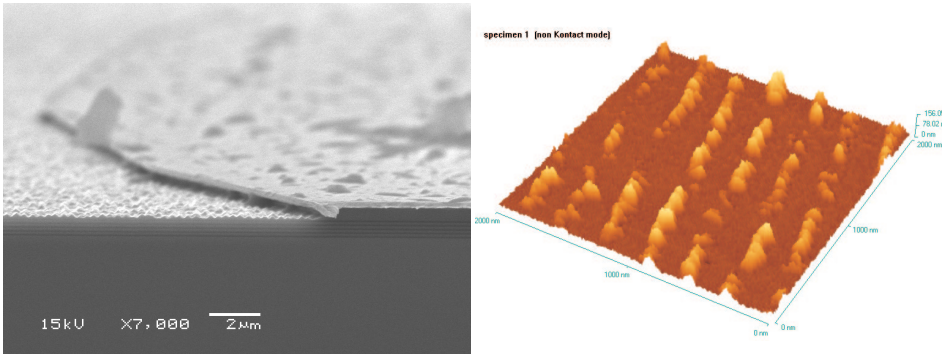

(a) (b)

Fig. 6.26: (a) SEM picture of surface roughened LED; (b) AFM image of the rough surface.

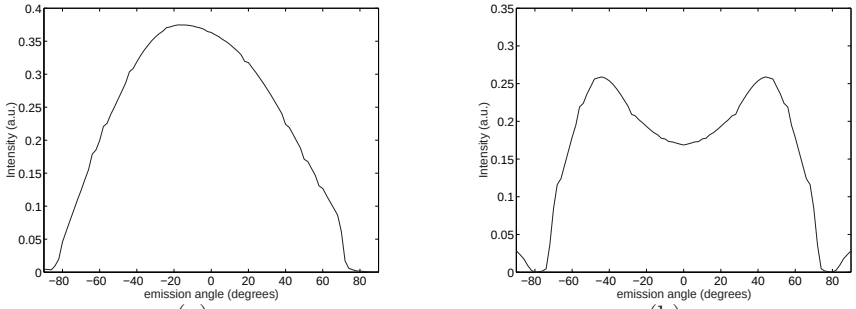

(a) (b)

Fig. 6.27: (a) Measurement of farfield of roughened NRCLED; (b) Measurement of farfield of corresponding RCLED.

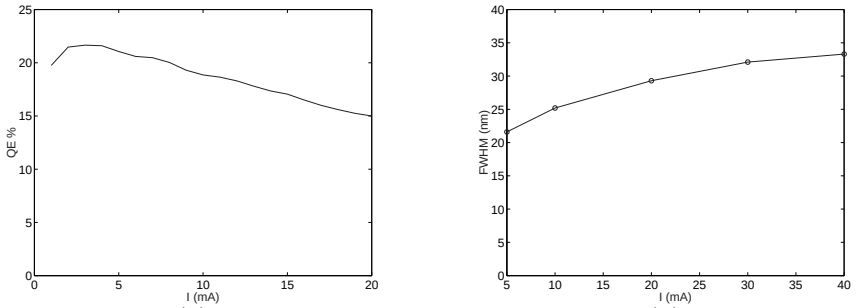

(a) (b)

Fig. 6.28: (a) Measured differential η_{ext} and (b) measured 3dB spectral bandwidth of roughened NRCLED, diameter 72 µm, the substrate has been thinned to 100 µm and an AR coating minimises Fresnel losses.

References

[1] R. Windisch, M. Kuijk, B. Dutta, A. Knobloch, P. Kiesel, G.H. Dölher, G. Borghs and P. Heremans, "Non-Resonant Cavity Light-Emiotting Diodes," in *Light-Emitting Diodes: Research, Manufacturing, and Applications IV, Proc. SPIE,* vol. 3938, pp. 71-76, 2000.

[2] J.M. Dallesasse, N. Holonyak, A.R. Sugg, T.A. Richard and N. Elzein, "Hydrolization oxidation of AlxGa(1-x)As-AlAs-GaAs Quantum-well heterostructures and superlattices," *Appl. Phys. Lett.,* 57(26), pp. 2844-2846, 1990.

[3] C. Lei, T. Rogers, D. Deppe and B. Streetman, "ZnSe/CaF2 quarter-wave Bragg reflector for the vertical cavity surface emitting laser," *J. Appl. Phys.,* 69(11), pp. 7430-7434, 1991.

[4] J.J. Wierer, D.A. Kellogg and N. Holonyak, "Tunnel contact junction native-oxide aperture and mirror vertical-cavity surface-emitting lasers and resonant-cavity light-emitting diodes," *Appl. Phys. Lett.,* vol. 74(7), pp. 926-928, 1999.

[5] J.J. Wierer, P.W. Evans, N. Holonyak and D.A. Kellogg, "Lateral electron current operation of vertical cavity surface emitting lasers with buried tunnel contact hole sources," *Appl. Phys. Lett.,* vol. 71(24), pp. 3468-3470, 1997.

[6] H.C. Casey, D.D. Sell and K.W. Wecht, "Concentration-dependence of absorption-coefficient for n-type and p-type GaAs between 1.3 and 1.6 eV," *J. Appl. Phys.,* vol. 46(1), pp. 250-257, 1975.

[7] H. De Neve, *"Ontwerp en realisatie van Licht Emitterende Diodes op basis van het Micro-caviteitseffect,"* Ph. D. Thesis, Ghent University, Ghent, Belgium, 1997.

[8] R. Bockstaele, *"Resonant Cavity Light Emitting Diode Based Parallel Interconnections"*, Ph. D. Thesis, Ghent University, Ghent, Belgium, 2001.

[9] S. N. G. Chu, T. Tanbun-Ek, Ralph A. Logan, J. Vandenberg, P. F. Sciortino, Jr., P. Wisk, and T. L. Pernell, "Grating Overgrowth and Defect Structures in Distributed-Feedback-Buried Heterostructure Laser Diodes," *IEEE J. Sel. Top. Quantum Electron.,* 14(5), pp. 812-821, 1996.

[10] J. N. Damask, "Practical design of side-coupled quarter-wave shifted distributed-Bragg resonant filters", *J. Lightwave Tech.* vol. 14(5), pp. 812-821, 1996.

[11] D. Rosenblatt, A. Sharon and A. A. Friesem, "Resonant grating waveguide structures", *IEEE J. Quantum Electron.*, vol. 33(11), pp. 2038-2059, 1997.

[12] A. Yariv, *"Quantum Electronics, 3rd ed.,"* John Wiley and sons, New York, 1988.

[13] S. Goeman, *"Integration of surface relief structures with vertical cavity surface emitting lasers for polarisation and mode control"*, Ph. D. Thesis, Ghent University, Ghent, Belgium, 2001.

7

GA-RCLED with 2-D grating

THIS chapter describes the GA-RCLED with a 2-D grating. Two fabrication technologies have been applied to define the grating. Holography was used to generate mainly square lattice gratings. E-beam was employed to define triangular lattice gratings. The design, realisation and characterisation of bottom-emitting GA-RCLEDs with a 2-D grating are detailed. Design and realisation of thin-flim GA-RCLEDs are shortly introduced.

7.1 Introduction

To enhance the extraction efficiency η_{etxr} of an RCLED by the use of a grating, this grating has to show a rotational in-plane symmetry, in accordance with the in-plane rotational symmetry of the guided modes. Of the 2-D Bravais lattices, the triangular grating shows the highest rotational symmetry and a Brillouin zone that is the closest to a circle. We mentioned in section 5.2.2.4 that the rotational symmetry of a triangular grating can even further be enhanced using more sophisticated gratings [1]. The pattern of these gratings can be rather complex: they can not be defined holographically, e-beam definition is slowed down. Deep-UV lithography (see Chapter 1) can bring a solution to these limitations. The use of Deep-UV for photonic applications is still under investigation [2]. In this work we will therefore focus in the first place on the use of square and triangular lattice gratings, manufacturable with holography and e-beam.

The basic structure and design objectives are analogous to those of a GA-RCLED with a 1-D grating. The reader is referred to Chapter 6 for more details on these issues.

7.2 GA-RCLED with holographically defined square lattice grating

7.2.1 Design of GA-RCLED with square lattice grating

Square lattice gratings do not show as high a rotational symmetry as triangular gratings do, but using the WVD presented in Chapter 4, it can be shown graphically that a second order square lattice grating can fully extract the guided mode. The WVD of a first order square lattice grating in the GaAs system ($n_s = 3.52$) and for $\lambda = 980$ nm is shown in Fig. 7.1(a). Useful diffraction of the guided mode is limited to a fraction of 44%. The WVD of a second order grating (Fig. 7.1(b)) shows full extraction possibility of the guided mode (remember: this graphical analysis indicates qualitatively to what extent a grating-structure can extract the guided wave, it only represents an upper limit for the extractable fraction of the guided wave). It also shows the inevitable first diffraction orders, which can leak power to the absorptive substrate.

7.2.1.1 First order square lattice grating

To design a GA-RCLED with a 2-D grating, we follow the same procedure as pointed out in Chapter 6. The numerical tool is first applied in a plane spanned by a Bragg-vector and the surface normal to analyse the 2-D behavior of the device. This optimisation is then fine-tuned by a full 3-D calculation. Due to the numerical complexity which is proportional to the number of diffraction orders cubed, a 3-D calculation of a 2-D grating, in which the amount of orders is at least the amount of the respective 1-D grating squared, can span several days and is thus not practical as optimisation tool. Fig. 7.2-7.5 plot some simulation results. The main difference with the gratings discussed in the previous chapter is, except for their periodic

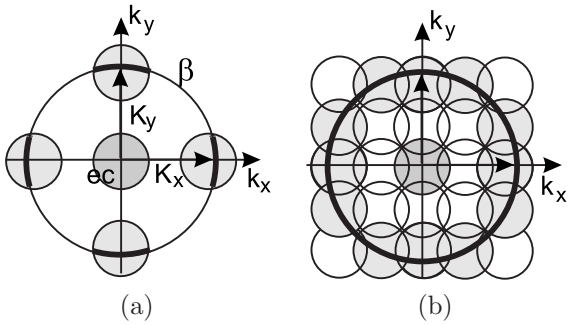

Fig. 7.1: WVD of (a) first order square lattice grating; (b) second order square lattice grating. The thick lines correspond with the extractable fractions of the guided mode. ec is the extraction cone.

dimensionality, their metallisation. In Chapter 6, filled metallic gratings were considered (see Fig. 5.10(a), filled contact or cont. f). A thick metallic layer is deposited on the grating, filling the air space between the semiconductor teeth of the grating. It was found however by simulation that the total metallic absorption of a 1-D periodically corrugated metallic interface is about 4 times higher than in the case of a flat metallic mirror. Ideally, metal should be omitted. In that case however, electrical current injection needs to be redesigned and an extra top DBR should be inserted to augment the normal incidence semiconductor-grating reflection. An alternative that maintains homogeneous current injection and a high normal incidence reflection is the grating sketched in Fig. 5.10(b) and tabulated as top-covered contact or cont. t. The metal is obliquely evaporated on the grating, covering only the teeth of the grating without filling the air gaps in-between (see SEM pictures in the next paragraph). For the grating with parameters tabulated in Fig. 7.2(d), the total optical power absorption and transmission is ±10% for a horizontal dipole[1]. For an optimised device with filled metallic grating, this would amount to ±25% (3-D simulation results).

Fig. 7.2 plots the internal net power flux per unit spatial frequency along $\mathbf{k}_x$ in a GA-RCLED with a 2-D square lattice first order grating for varying grating depth d_{gr}, varying top spacer thickness d_1 and different wavelengths. The main influence of these three parameters, is translated in a shift of the Fabry-Pérot resonance. The same behavior was notified for the GA-RCLED with a 1-D first order grating, as discussed in Chapter 6. For more details on the influence of d_{gr},d_1 and λ, the reader is referred to this chapter.

A 2-D plot of the internal net power flux per unit spatial frequency is given in Fig. 7.3 for a period $\Lambda_x = \Lambda_y = 300$ nm and $\Lambda_x = \Lambda_y = 380$ nm. The different diffraction orders of the guided mode are clearly visible and can be recognised in the WVD sketches of the respective gratings. The 3-D calculations were used to fine-tune the optimisation process. Fig. 7.4 shows the internal net power flux, both s-and p-polarised, for an optimised GA-RCLED with filled metallic first order

[1]The InGaAs QWs are compressively strained in the GaAs material, resulting in a strong enhancement of radiation through horizontal dipoles (see Chapter 2).

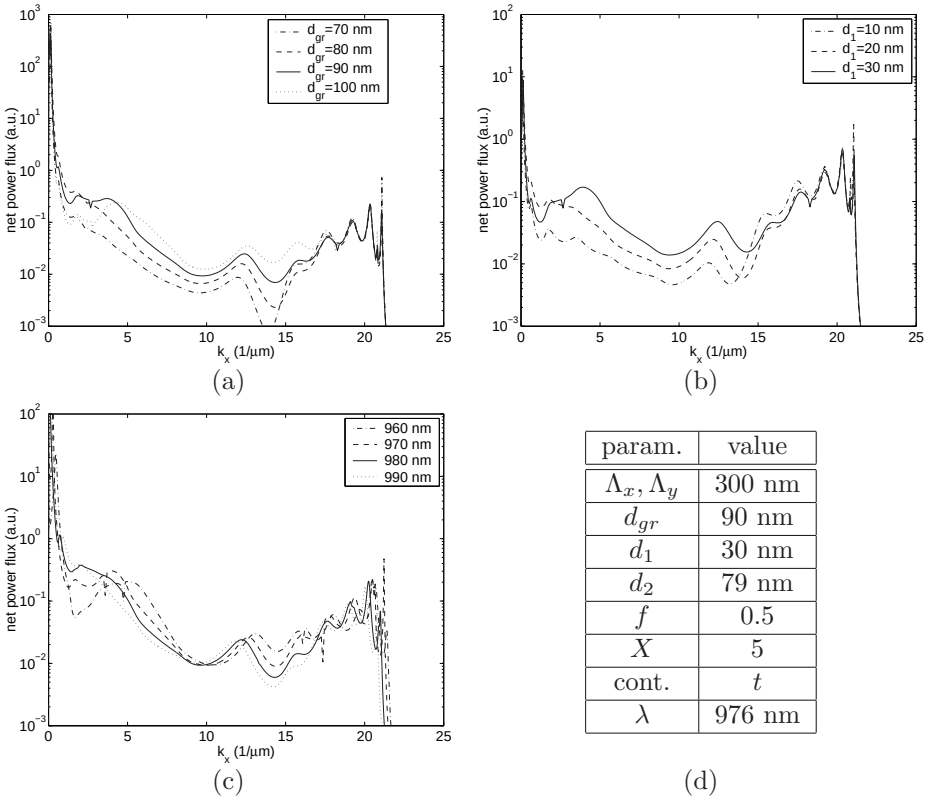

param.	value
Λ_x, Λ_y	300 nm
d_{gr}	90 nm
d_1	30 nm
d_2	79 nm
f	0.5
X	5
cont.	t
λ	976 nm

(d)

Fig. 7.2: Downwards s-polarised internal net power flux per unit spatial frequency along $\boldsymbol{k}_x$ in a GA-RCLED with 2-D square lattice first order grating for (a) varying grating depth d_{gr}; (b) varying top spacer thickness d_1; (c) varying wavelength; (d) parameter values. The behavior along $\boldsymbol{k}_y$ is analogous.

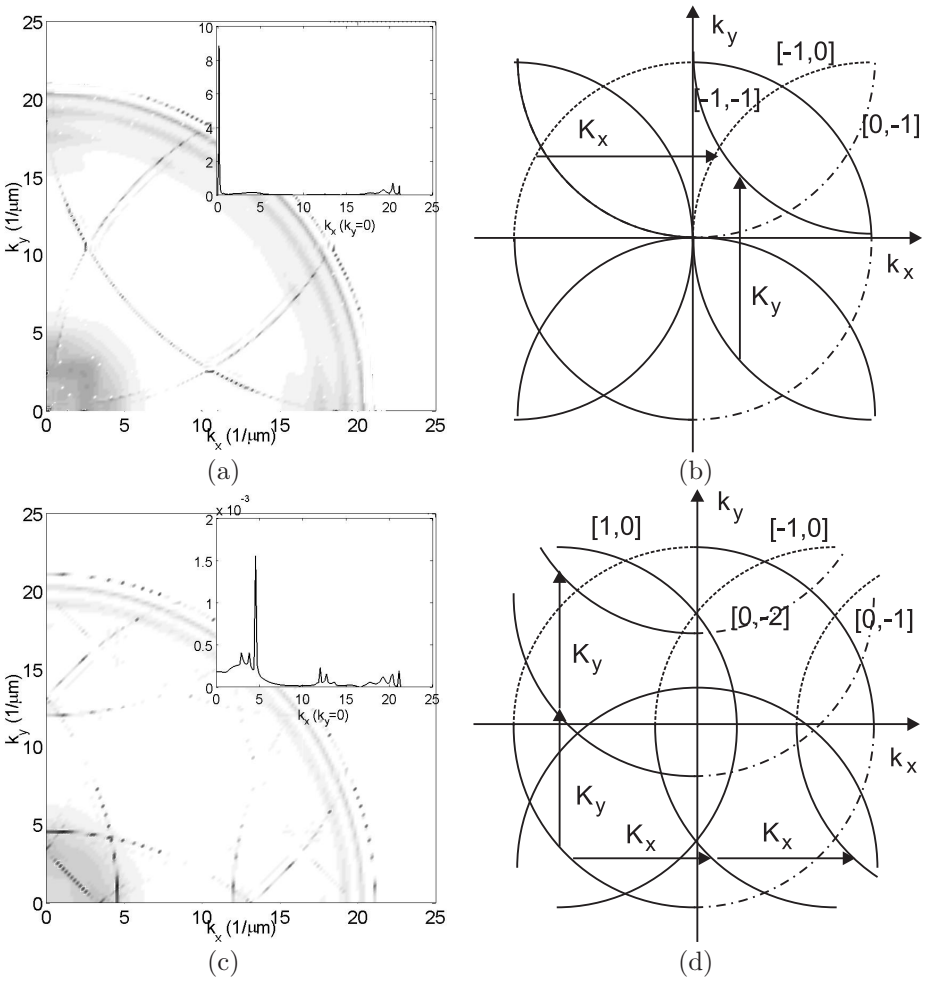

Fig. 7.3: 2-D plot of downwards s-polarised internal net power flux per unit spatial frequency in a GA-RCLED with 2-D square lattice first order grating and schematic presentation of corresponding WVD with (a)-(b) $\Lambda = 298$ nm; (c)-(d) $\Lambda = 380$ nm. The insets of (a) and (c) plot the corresponding power flux distribution along $\boldsymbol{k}_x$ when $k_y = 0$.

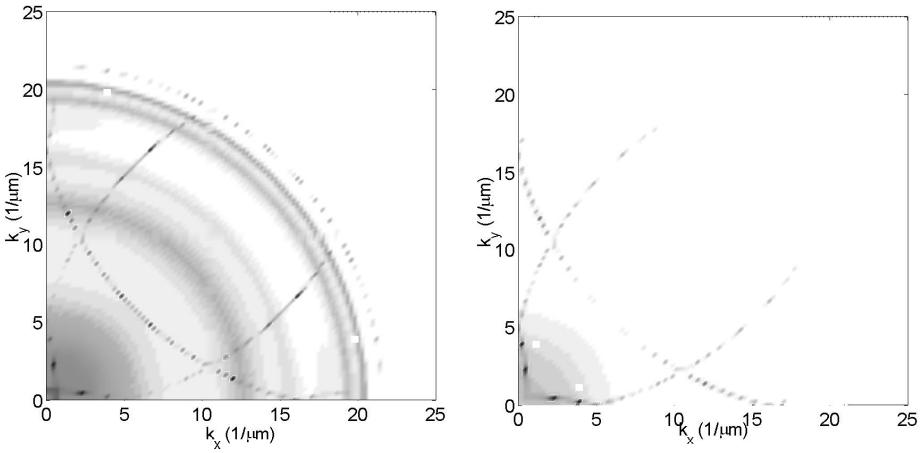

(a)

(b)

param.	value
Λ_x, Λ_y	300 nm
d_{gr}	25 nm
d_1	104 nm
d_2	79 nm
f	0.5
X	5
cont.	f
λ	976 nm

(c)

param.	value
Λ_x, Λ_y	300 nm
d_{gr}	90 nm
d_1	30 nm
d_2	79 nm
f	0.5
X	5
cont.	t
λ	976 nm

(d)

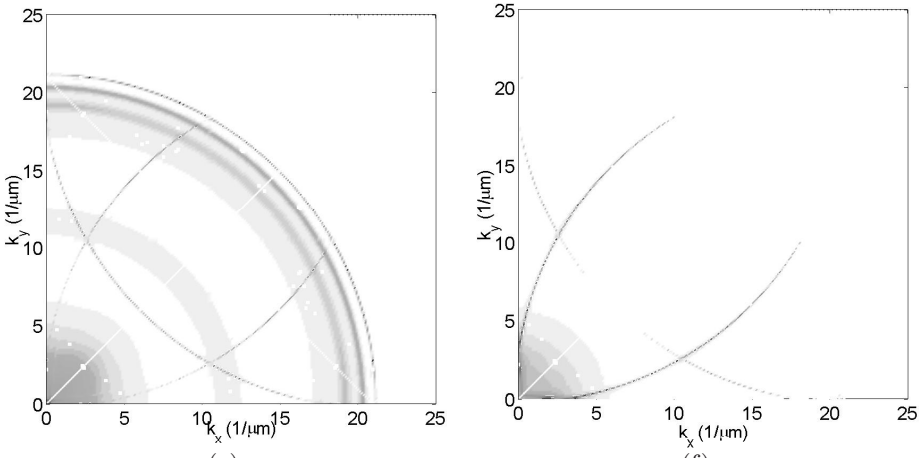

(e)

(f)

Fig. 7.4: 2-D plot of downwards internal net power flux per unit spatial frequency with 2-D square lattice first order grating (a) s-polarised in GA-RCLED with filled metallic grating; (b) p-polarised in GA-RCLED with filled metallic grating; (c) parameter values filled metallic grating. (d) Parameter values of top-covered grating; (e) s-polarised in GA-RCLED with top-covered grating; (f) p-polarised in GA-RCLED with top-covered grating.

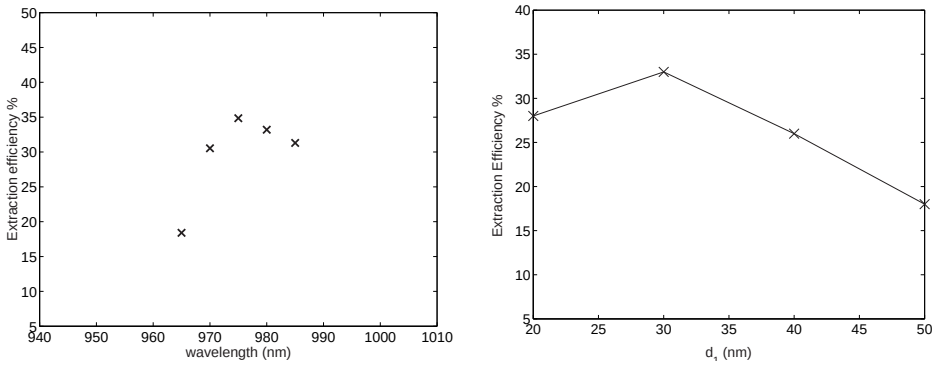

(a) (b)

Fig. 7.5: Extraction efficiency of GA-RCLED with 2-D square lattice first order grating (a) variable wavelength; (b) variable top spacer thickness d_1.

square lattice grating and for an optimised GA-RCLED with a first order square lattice grating top-covered with metal. The Fabry-Pérot mode is for both devices clearly visible (dark zone for $(k_x^2 + k_y^2)^{1/2} < 6$). The p-polarised diffraction orders are caused by polarisation coupling induced by the 2-D grating. The p-polarised (diffracted) guided light is too weak to be visible on the plot. Optimisation of the latter led to a device design showing simulated efficiencies up to 34% to extract the light of a monochromatic horizontal dipole (Fig. 7.5). The extraction efficiency remains high for a wavelength range representative for the intrinsic spontaneous emission spectrum of the device (970-990 nm). The influence of the thickness of the top spacer layer is depicted in Fig. 7.5(b). The sensitivity of the device's behavior to the cavity tuning is clear.

7.2.1.2 Second order square lattice grating

We consider second order square lattice gratings for their ability to diffract guided modes propagating in all in-plane directions to the extraction cone. As mentioned above, first order diffractions are inevitable with a second order grating (see Fig. 7.1(b)). These diffraction orders do not fall in the high reflective zone of the DBR (periodic $\lambda/4$-stack of GaAs/AlAs) and will leak through this mirror to be absorbed in the substrate.

To minimise these losses, an extra DBR is inserted underneath the present DBR. This DBR is designed to reflect optical waves with an incident angle $\pm 27°$, corresponding to the angle of the first diffraction order. If this diffracted light is reflected back towards the cavity, the light gets another chance to be diffracted towards the extraction cone. Due to the high reflectivity of the DBR for incident angles around $\pm 27°$, the mode density is set to zero around $\mathbf{k}_x = 101/\mu m$, so that no light will be diffracted in this angular range. The extraction probability is enhanced. The angular power reflection characteristic of the standard DBR (top-down 5 pairs of 70 nm GaAs and 84.5 nm AlAs) and the extended DBR (top-down

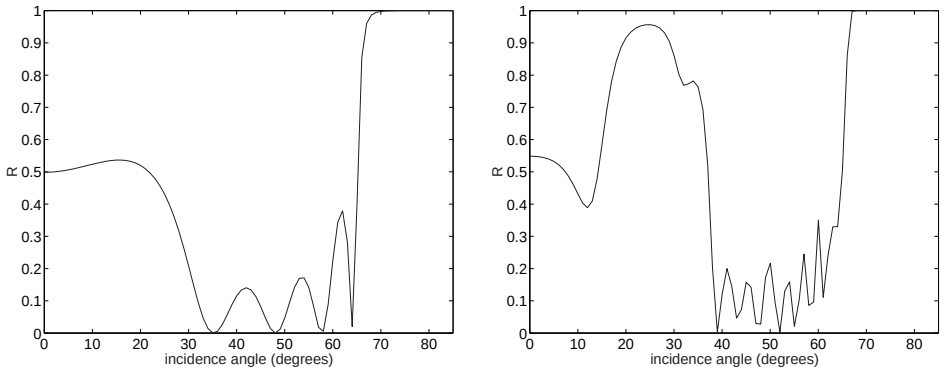

Fig. 7.6: Power reflection coefficient for s-polarised incident light of (a) standard DBR (top-down 5 pairs of 70 nm GaAs and 84.5 nm AlAs); (b) extended DBR (top-down 5 pairs of 70 nm GaAs and 84.5 nm AlAs and 8 pairs of 81 nm GaAs and 96,6 nm AlAs).

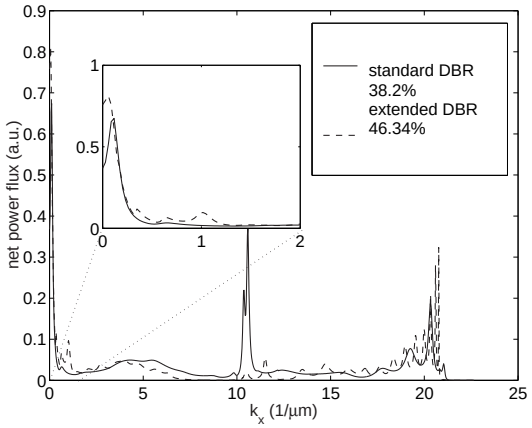

param.	value
Λ_x, Λ_y	600 nm
d_{gr}	100 nm
d_1	20 nm
d_2	79 nm
f	0.45
X	5(+8)
cont.	t
λ	976 nm

Fig. 7.7: Downwards s-polarised internal net power flux per unit spatial frequency along $\boldsymbol{k}_x$ in a GA-RCLED with 2-D square lattice second order grating with and without second DBR.

5 pairs of 70 nm GaAs and 84.5 nm AlAs and 8 pairs of 81 nm GaAs and 96.6 nm AlAs) are plotted in Fig. 7.6.

The internal net power flux per unit spatial frequency along $\mathbf{k}_x$ in a GA-RCLED with a 2-D square lattice second order grating and with and without extended DBR are plotted in Fig. 7.7. The optical power fraction absorbed in the substrate via the first order diffraction is clearly decreased when the extended DBR is used.

An accurate diffraction analysis demands to take at least the propagative spatial harmonics and some evanescent contributions in the Floquet-Bloch series development of the electromagnetic field (see Chapter 3). For a second order grating,

this implements a total amount of orders of at least 7×7 (7 in each periodic direction). The available processors are not able to solve the numerical analysis in a reasonable time. The design of a GA-RCLED with a second order square lattice grating falls back on a 2-D optimisation process.

7.2.1.3 Absorption versus diffraction

Two competing processes determine the propagation length of the guided mode: the diffraction efficiency of the grating and the absorption of the guided mode in the active layer. The simulations in previous paragraphs point out that diffraction of the grating is stronger than the absorption of the guided mode in the active layer. The order of magnitude of both processes is given in this paragraph.

Absorption of the guided mode has shortly been discussed in view of photon-recycling in Chapter 2. The absorption length depends on the overlap between the profile of the guided mode and the active region and on the absorption coefficient of the active region. This absorption coefficient depends on the carrier density: if the active region is pumped above transparency, no reabsorption occurs at all. A typical value[2] for the absorption of the s-polarised guided mode (in planar RLCED with λ-cavity and 3QWs under moderate injection) is $\pm$100 dB/mm.

The diffraction efficiency in function of the propagation distance can not directly be calculated with the tools developed in this work. We have used the framework CAMFR for this purpose [4]. This tool has been developed in INTEC and is a full vectorial Maxwell solver based on eigenmode expansion. At the time of this work, only 2-D calculations can be performed. The results are thus indicative: the attenuation coefficient for the s-polarised guided mode in the optimised structure with a first order grating is 718 dB/mm, with a second order grating 407 dB/mm.

These results indicate that indeed the propagation distance of the guided mode will be determined by diffraction losses to the outside medium, more than by its absorption in the active layer.

7.2.2 Realisation of GA-RCLED with holographically defined square lattice grating

The optimised designs were implemented according to the processing scheme presented in Chapter 5. The cross section of a device is shown in Fig. 7.8(a). The grating region, top-covered with metal, the contact ring to connect the evaporated metal with the contact pad, the mesa, DBR and black isolation layer can be distinguished. Fig. 7.8(b)-(c) are details of the grating. It shows nicely that even for small filling factors f, oblique evaporation of the contact and mirror covers only the teeth of the grating. Fig. 7.8(d) shows a detail of grating with larger filling factor that is top-covered with metal.

[2] This has been calculated with the commercial simulation tool Fimmwave, a 2-D mode solver based on a transverse resonance method. An imaginary index between 0.1 and 0.01 of the active layer was presumed.

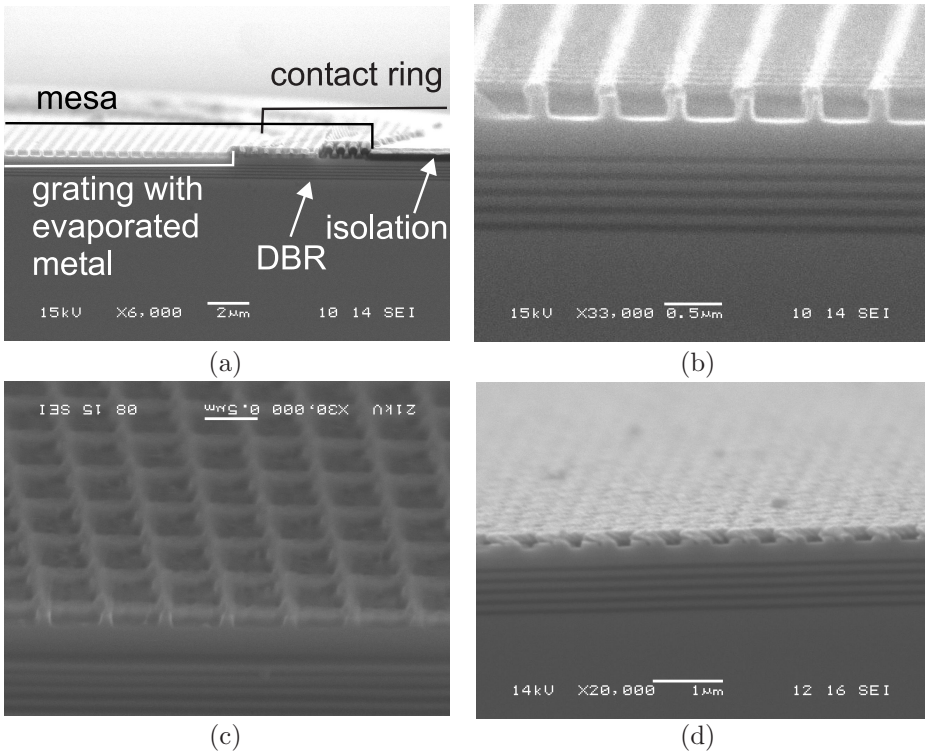

Fig. 7.8: SEM picture of (a) cross section of GA-RCLED with holographically defined square lattice second order grating ($\Lambda = 600$ nm) ; (b) detail of grating with obliquely evaporated metal and small filling factor; (c) detail of grating with obliquely evaporated metal and small filling factor; (d) detail of grating with obliquely evaporated metal and large filling factor.

7.2.3 Characterisation of GA-RCLED with holographically defined square lattice grating

During this research, we had the opportunity to realise 3 runs to experiment GA-RCLEDs with holographically defined gratings. Each run uses a different epilayer and consists of 8 samples. The grating parameters of each sample can be varied (grating depth d_{gr}, filling factor f, lattice, type of grating f, t). Each sample contains several arrays of LED devices.

In spite of the low number of runs, interpretation of the experimental data led to important conclusions. Due to the variation of grating parameters in each run (8 samples = 8 variations), we could distil several reasons for the rather moderate measured external efficiencies.

At the time of the first run, the numerical tool to design a GA-RCLED was not available yet. The parameters were chosen relatively intuitively and the aim of the run was to verify the possibilities of both types of contacts: filled metallic gratings

(f) or top-covered semiconductor gratings (t) shown in Fig. 7.8. Fig. 7.9 plots the angle resolved spectrum, the total emitted optical power and IV curve of a GA-RCLED with second order square lattice grating for a filled metallic grating (left hand side or (a)) and a semiconductor/air grating, top-covered with metal (right hand side or (b)) respectively. The angle resolved spectrum is measured in the plane spanned by $\mathbf{K}_x$ and the surface normal. The same behavior is achieved when measuring in the plane spanned by $\mathbf{K}_y$ and the surface normal. The spectrum in Fig. 7.9(b) reveals guided mode extraction. The guided mode at a wavelength 948 nm is diffracted towards the surface normal direction, manifested by the peak located at 948 nm when the observation angle $\theta = 0°$. This observation direction corresponds with the surface normal direction. At oblique observation angles, two modes with a different wavelength fulfill the Bragg condition, and the diffraction peak will split (see Chapter 6). This behavior is measured for the $[2,0]^{th}$ diffraction order, or the second order in the x-direction, the zeroth order in the y-direction. The peak observed at the observation angle $\theta = 0°$ does not disappear for small oblique observation angles as is the case in a 1-D grating. This is due to the 2-D character of the grating: at small oblique angles in the plane spanned by $\mathbf{K}_x$ and the surface normal, the $[0,(-)2]^{th}$ diffraction order of the guided mode is still observed (see Fig. 7.1).

This spectral behavior is less pronounced, although present, in Fig. 7.9(a). Due to the filled metallic grating, metal absorption is high and the guided mode will be strongly damped. The broad overall spectral bandwidth of both devices is attributed to the mistuned cavity: the central wavelength of the Fabry-Pérot mode (λ_{FP}) is located at lower wavelengths than the central wavelength of the intrinsic spectrum (λ_c) (e.g. for Fig. 7.9(a) $\lambda_{FP} = \pm 924$ nm and $\lambda_c = \pm 976$ nm).

The quantum efficiency of both devices is low due to the non-optimised design ($\eta_{ext} < 1\%$). More important is the nice IV curve for the filled metallic grating, but especially for the top-covered grating. The nice diode characteristic shows that the series resistance is low in both cases.

The second run (Fig. 7.8(d)) shows the importance of a correctly tuned cavity. The design is optimised by the numerical tool, but due to a deviation of -3.5% in the grown epilayer, the cavity was not correctly tuned, and a moderate quantum efficiency is the result. The cavity mistuning due to the small growth error is shown in Fig. 7.10. Calculation of the angle resolved spectrum of a RCLED based on the optimised epilayer is plotted in Fig. 7.10(a). A Gaussian intrinsic spectrum with FWHM=20 nm and $\lambda_c = 976$ nm is assumed. The RCLED behaves as a too thick cavity, which is normal for a GA-RCLED design: a grating with a certain depth will be integrated for the GA-RCLED. Insertion of a grating will decrease the effective thickness of the cavity (see Fig. 6.10). Fig. 7.10(b) shows the measured angle resolved spectrum of a RCLED made out of the grown epilayer. The cavity's central wavelength is located at a smaller wavelength ($\lambda_{FP} = 962$ nm). Simulation of the optimised epilayer with a deviation of -3.5% yields a similar angle resolved spectrum. It is not hard to imagine that insertion of a grating, which even further decreases the effective thickness of the cavity, results in a strongly mistuned cavity.

A plot of the simulated monochromatic (976 nm) s-polarised and p-polarised

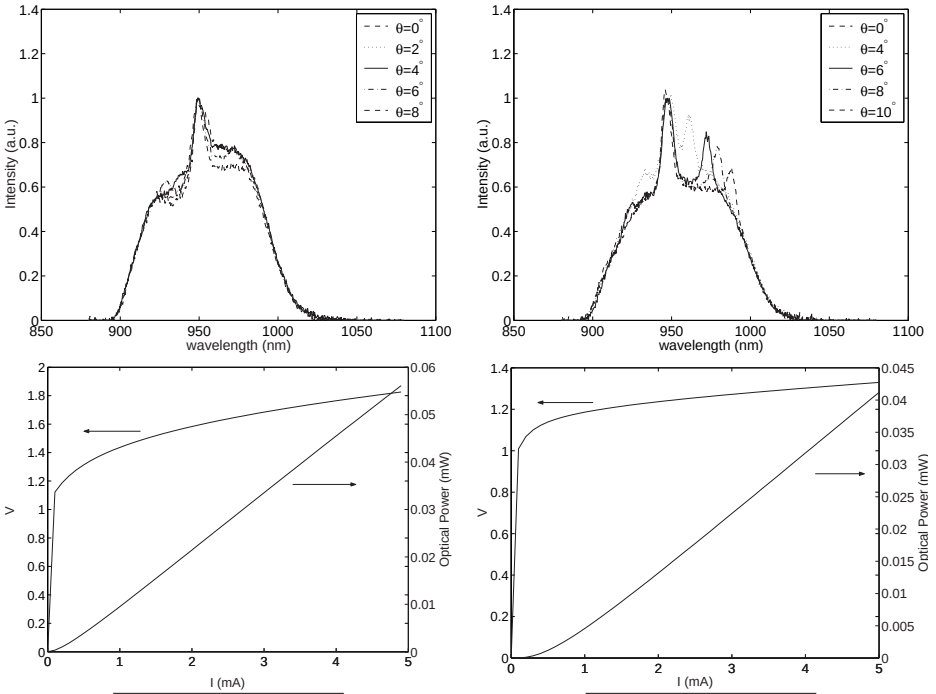

param.	value
Λ_x, Λ_y	600 nm
d_{gr}	210 nm
d_1	60 nm
d_2	79 nm
f	0.28
X	5
cont.	f

(a)

param.	value
Λ_x, Λ_y	600 nm
d_{gr}	210 nm
d_1	60 nm
d_2	79 nm
f	0.28
X	5
cont.	t

(b)

Fig. 7.9: Angle resolved spectrum (at 10mA) in the plane spanned by $\boldsymbol{K}_x$ and the surface normal, optical power and IV of GA-RCLED, diameter 72 μm, with square lattice second order grating for (a) filled metallic grating; (b) top-covered semiconductor/air grating.(run 1)

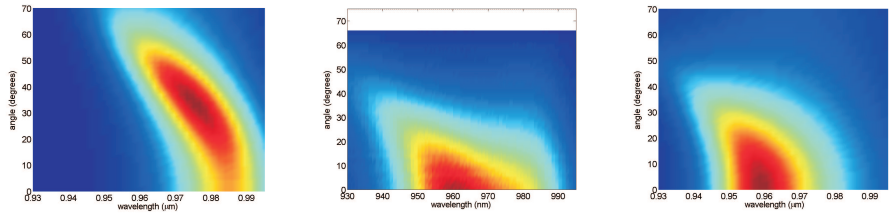

(a) (b) (c)

Fig. 7.10: (a) Simulation of angle resolved spectrum of RCLED based on optimised epilayer; (b) measured angle resolved spectrum of RCLED with epilayer of run 2 at 10 mA and diameter 215 μm; (c) simulation of angle resolved spectrum of RCLED based on optimised epilayer with deviation of −3.5%. (run 2)

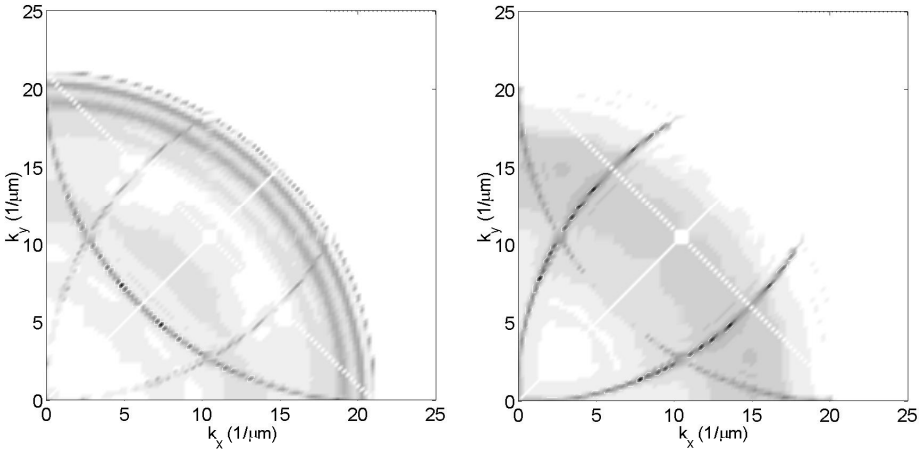

(a) (b)

Fig. 7.11: 2-D monochromatic plot of (a) s-polarised and (b) p-polarised downwards internal net power flux per unit spatial frequency along $\boldsymbol{k}_x$ in a GA-RCLED with 2-D square lattice first order grating using the epilayer of run 2 with a deviation of −3.5%. (run 2)

internal net power flux per unit spatial frequency of a horizontal dipole in a GA-RCLED with 2-D square lattice first order grating using the erroneous epilayer is shown in Fig. 7.11. The difference with the optimised design in Fig. 7.4(e) and (f) is obvious: the Fabry-Pérot mode is missing when the erroneous epilayer is used. The diffraction is weak for $(k_x^2 + k_y^2)^{1/2} < 6$, due to the missing Fabry-Pérot mode.

The measured angle resolved spectrum gives evidence of guided mode extraction (Fig. 7.12). The intrinsic spectrum is revealed when the spectrum is observed at an oblique angle where no guided mode is diffracted to ($\theta = 15°$, $\phi = 15°$). The η_{ext} is as high as 7%, which lies in the order of the simulated $\eta_{ext} = 5\%$ of the GA-RCLED with erroneous epilayer (Fig. 7.11). This run did not have the extended DBR yet.

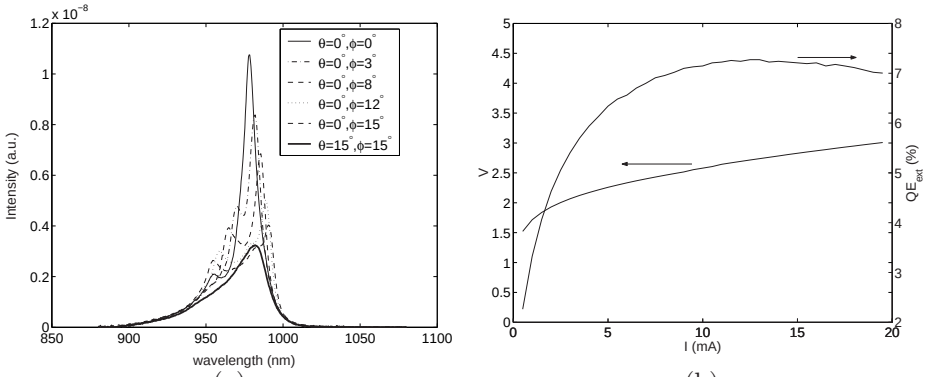

(a) (b)

param.	value
Λ_x, Λ_y	600 nm
d_{gr}	100 nm
d_1	< 20 nm
d_2	< 79 nm
f	0.68
X	5
cont.	t

(c)

Fig. 7.12: (a) Measured angle resolved spectrum (at 15mA), θ is defined in the plane spanned by $\boldsymbol{K}_x$ and the surface normal, ϕ is the azimuthal angle between the measurement plane and $\boldsymbol{K}_x$; (b) external quantum efficiency and IV. The GA-RCLED with 2-D square lattice grating has a diameter of 215 μm and the parameters are tabulated in (c). (run 2)

Some SEM pictures of the grating (before metallisation) of the third run are presented in Fig. 7.13. The period of the grating in Fig. 7.13(a) and (b) is 600 nm, $d_{gr} = 45$ nm, in Fig. 7.13(c) $\Lambda_x = \Lambda_y = 300$ nm, $d_{gr} = 50$ nm. A metallic layer of ± 150 nm is evaporated obliquely on the surface, to serve as mirror and as contact. Resist and ARC residues are clearly visible on the SEM pictures. Even after a long O_2-plasma etch, the residue could not be removed. These remainders affect the quality of the evaporated metallic mirror and cause scattering losses of the guided mode. This is shown in the plot of the angle resolved spectrum of a device of run 3 in Fig. 7.14: the diffracted guided mode does cause only a small perturbation in the angle resolved spectrum. The cavity is slightly detuned towards smaller wavelengths: the Fabry-Pérot's central wavelength λ_{FP} is situated at about 970 nm. The guided mode is diffracted to the surface normal direction at a wavelength of 980 nm. The Bragg condition to diffract the guided mode to the extraction cone falls more or less outside the intrinsic spectral range for observation angles $> 10°$. This is revealed in the angle resolved spectrum, where the diffracted guided mode for $\theta = 10°$ is already situated at wavelengths as small

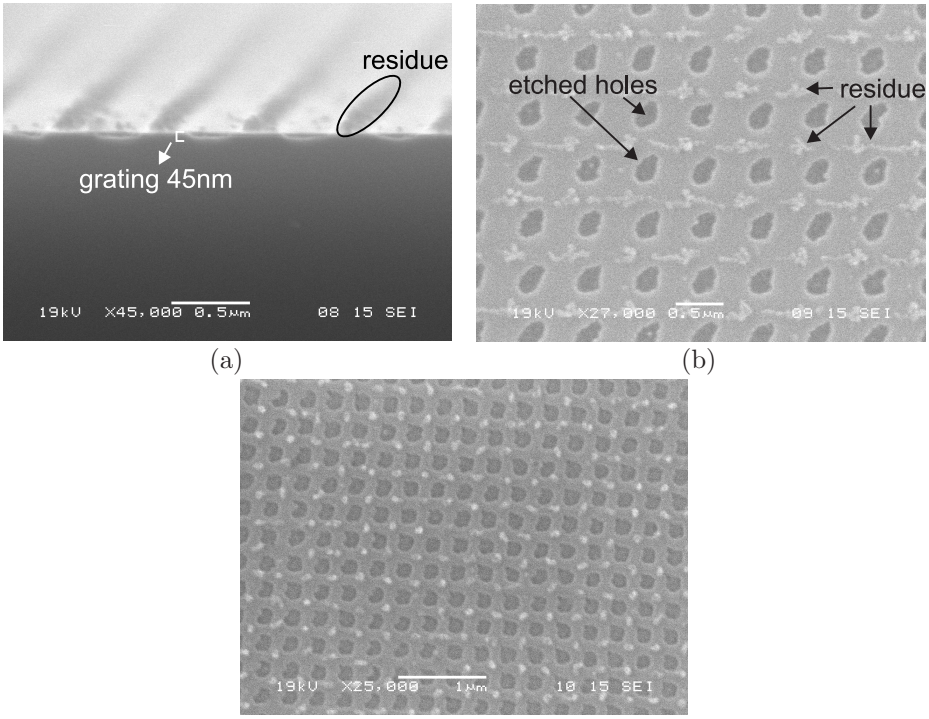

Fig. 7.13: SEM pictures of holographically defined gratings with a clearly visible residue of ARC and resist (a)-(b) $\Lambda = 600$ nm $d_{gr} = 45$ nm; (c) $\Lambda = 300$ nm, $d_{gr} = 50$ nm. (run 3)

as 942 nm, but also in the farfield where the diffracted guided mode creates an enhanced radiance for angles $< 10°$. This enhanced radiance of a GA-RCLED can be important in any application where light needs to be focused to a small spot or where light needs to be coupled into a fiber with finite core size and numerical aperture. The η_{ext} is 12.5%. The substrate is 500 μm thick and no ARC was deposited.

7.3 GA-RCLED with e-beam defined triangular lattice grating

7.3.1 Design of GA-RCLED with triangular lattice grating

The design of a GA-RCLED with a triangular lattice grating is analogous to the design of a GA-RCLED with a square lattice grating. The optimisation process is not repeated and we restrict ourselves to the main results plotted in Fig. 7.15. The monochromatic extraction efficiency of a first order triangular lattice GA-RCLED is as high as 43%. The efficiency is well over 40% in the wavelength range which

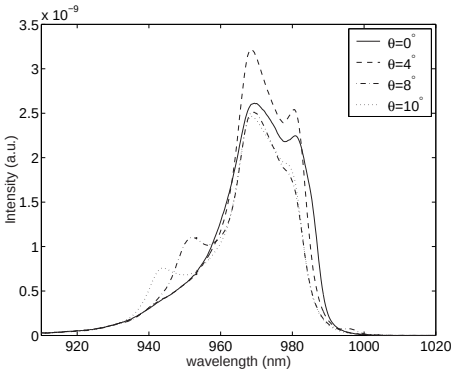

(a)

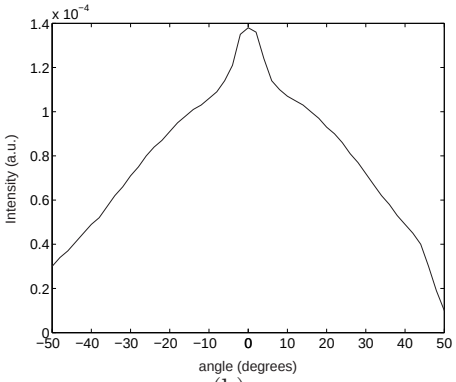

(b)

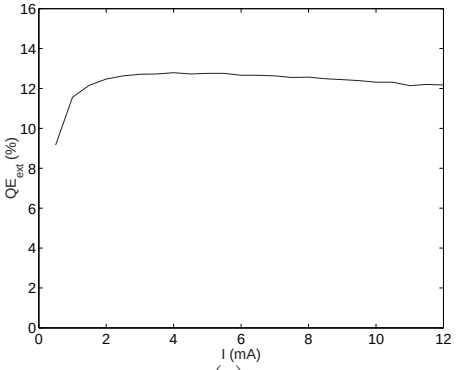

(c)

param.	value
Λ_x, Λ_y	598 nm
d_{gr}	50 nm
d_1	70 nm
d_2	79 nm
f	0.66
X	5 (0°) + 8 (30°)
cont.	t

(d)

Fig. 7.14: (a) Measured angle resolved spectrum (at 20 mA, diameter 215 μm), with θ in the plane spanned by $\boldsymbol{K}_x$ and the surface normal; (b) farfield measurement; (c) external quantum efficiency; (d) parameter values of the GA-RCLED with 2-D square lattice. (run 3)

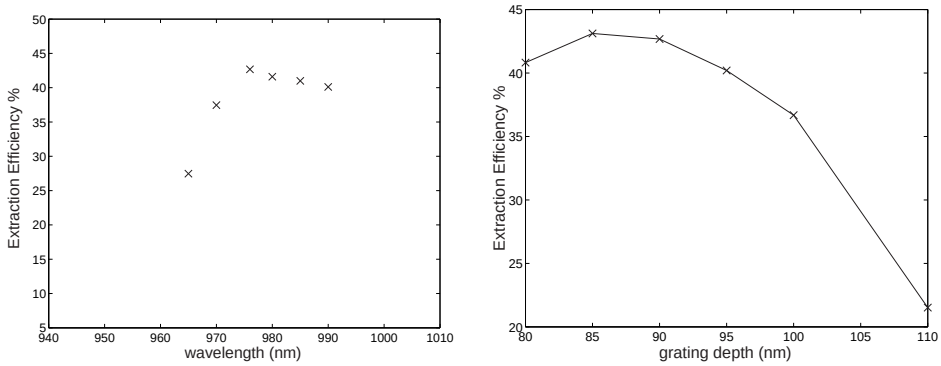

(a) (b)

Fig. 7.15: Extraction efficiency of the light of a horizontal dipole in a GA-RCLED with 2-D triangular lattice first order grating (a) for variable wavelength; (b) for variable grating depth.

is representative for the spectral bandwidth of the device under normal working conditions. The influence of a varying grating depth d_{gr} is stronger. The efficiency drops to 22% for a grating depth increase of 20 nm. Deviations of 10 to 20 nm of the intended grating depth are not abnormal in the fabrication process of the GA-RCLED.

7.3.2 Realisation of GA-RCLED with e-beam defined triangular lattice grating

The grating pattern is written in resist using e-beam. RIE translates the pattern into the semiconductor. These two steps have been carried out at the University of Glasgow. The patterned samples were subsequently processed to an array of LEDs in the cleanrooms of INTEC. A SEM picture of a GA-RCLED with an e-beam defined grating is shown in Fig. 7.16(a). Fig. 7.16(b) and Fig. 7.16(c) show details of the 2-D triangular lattice gratings before metallisation.

7.3.3 Characterisation of GA-RCLED with e-beam defined triangular lattice grating

Four e-beam runs have been carried out in the framework of this research work. During each run, two samples were patterned, with on each sample 3 LED arrays. Contrary to holographically defined gratings, the parameters of the grating can be varied within the sample.

Only two runs seemed to be useful: the second run encountered electrical problems. The mesa mask was an inscribed circle in the squared patterned region. The patterning remains when the mesa is etched, both inside and outside the mesa. The etched holes pierced the active layer and caused a short circuit, in spite of the isolation layer which did not cover adequately due to the patterning. In the

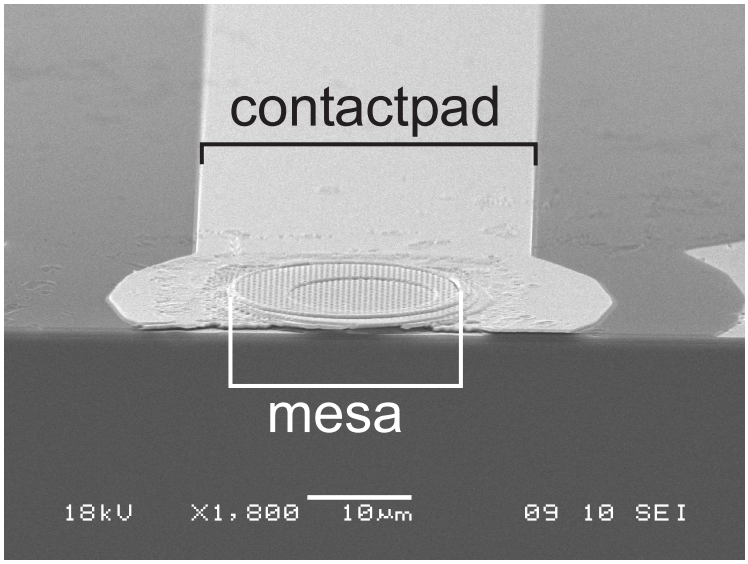

(a)

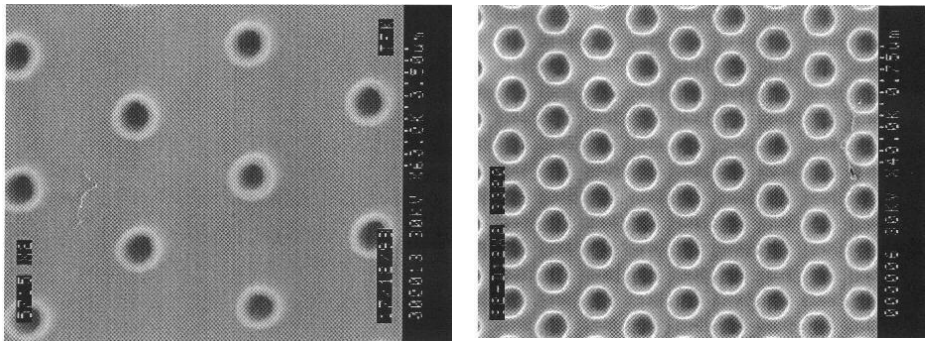

(c) (d)

Fig. 7.16: SEM picture of (a) cross section of GA-RCLED with e-beam defined triangular lattice grating; (b) detail of e-beam defined grating before metallisation $\Lambda_x = \Lambda_{y'} = \pm 570$ *nm, diameter hole*$= \pm 154$ *nm,* $d_{gr} = 150$ *nm; (c) detail of e-beam defined grating before metallisation* $\Lambda_x = \Lambda_{y'} = \pm 360$ *nm, diameter hole*$= \pm 180$ *nm,* $d_{gr} = 190$ *nm.*

subsequent runs, the patterning was written in the inscribed square of the mesa. A circular patterned region was more complex to program the e-beam.

SEM pictures of the fourth run revealed the rather low quality of the etched holes. Instead of a crenellated profile, the etched surface was rather pockmarked by crater-looking holes. Scattering losses dominated the behavior of the LEDs.

The first (see Fig. 7.16) and third run are discussed in this paragraph and demonstrate the importance of the extended DBR.

The measured spectrum and farfield of GA-RCLEDs of the first run are given in Fig. 7.17. Fig. 7.17(a) concerns a GA-RCLED with $\Lambda_x = \Lambda_{y'} = 570$ nm, Fig. 7.17(b) a GA-RCLED with $\Lambda_x = \Lambda_{y'} = 600$ nm and Fig. 7.17(c) a GA-RCLED with $\Lambda_x = \Lambda_{y'} = 630$ nm. The dotted lines in the spectra mark the Fabry-Pérot mode and the extracted diffracted guided light. The central wavelength of the Fabry-Pérot mode is in the three cases about 995 nm. The phase of the reflection coefficient is more or less equal for the three gratings, having a different period but the same filling factor. When $\Lambda_x = \Lambda_{y'} = 570$ nm, diffraction to the surface normal direction happens for a guided mode with $\lambda_{gm} = 940$ nm. For $\Lambda_x = \Lambda_{y'} = 600$ nm, the guided mode which is diffracted to an observation angle $\theta = 0°$ has $\lambda_{gm} = 979$ nm and for $\Lambda_x = \Lambda_{y'} = 630$ nm we have $\lambda_{gm} = \pm 1020$ nm. This is in accordance with the Bragg condition (Eq.(6.1)) for extraction to the surface normal direction, which can roughly be simplified to:

$$2\frac{2\pi}{\Lambda} = \frac{2\pi n_s}{\lambda} sin\theta_{gm} \tag{7.1}$$

with $\Lambda = \Lambda_x = \Lambda_{y'}$ and θ_{gm} the internal emission angle which corresponds with the guided mode. It is found that $\theta_{gm} = \pm 68°$, varying only little as a function of the wavelength (see Fig. 7.2(c)). A different period will thus correspond to a different wavelength diffracted to the surface normal direction.

We can also notice that the diffracted power is rather weak and the resonances are broad, both due to the absorption in the filled metallic grating and that the diffraction is enhanced when coupled to or close to the resonant Fabry-Pérot mode (compare spectrum of Fig. 7.17(b) with (a) and (c)), which again emphasizes the importance of a well tuned cavity.

The latter is also reflected in the farfield pattern measured in the plane spanned by $\mathbf{K}_x$ and the surface normal. We see the farfield of a RCLED tuned to larger wavelengths (lobed or "rabbit-ear" farfield), modified due to diffraction of the guided mode. If $\Lambda_x = \Lambda_{y'} = 570$ nm, the wavelength of the guided mode which is diffracted towards an observation angle of $\pm 15°$ is $\lambda_{gm} \pm 980$ nm. This diffraction will be more enhanced due to the presence of the Fabry-Pérot resonance, which explains the two lumps located at $-15°$ and $15°$ in the farfield. The WVD of the grating at a wavelength 980 nm also explains the two lumps in the farfield measured along $\mathbf{K}_x$.

For $\Lambda_x = \Lambda_{y'} = 600$ nm, this condition (diffracted guided mode and Fabry-Pérot resonance correspond) is fulfilled in the surface normal direction (see spectrum). If $\Lambda_x = \Lambda_{y'} = 630$ nm, the condition is fulfilled for a respective observation angle $\theta = \pm 20°$. If we measure in the plane spanned by the y-direction and the

surface normal (see dotted line in the WVD), the diffracted contributions will be less enhanced or smoothed. The WVD, showing the diffraction orders, does elucidate this behavior along the dotted line. The asymmetrical farfield reflects the limited in-plane rotational symmetry of the triangular lattice grating.

The external efficiency of the first run is low: $\eta_{ext} = 6\%$. Replacing the filled metallic grating by the top-covered semiconductor/air grating and extending the standard DBR (see Fig. 7.6) resulted during the third run in devices with a $\eta_{ext} = 14.8\%$ for a first order triangular grating and $\eta_{ext} = 15.1\%$ for a second order grating. The diameter of the device is 115 μm, the substrate is not thinned and no ARC is provided. The measured η_{ext} and VI is plotted in Fig. 7.18(a) and (b).

If we take into account an absorption of 22% after propagation through the 500 μm thick GaAs substrate (absorption coefficient ≈ 5 cm^{-1} [5]) and the Fresnel reflections (± 0.3 at normal incidence), the η_{ext} is as high as 27%[3]. Compared with the RCLEDs optimised in a previous research work [3] with an overall $\eta_{ext} = \pm 20\%$, the grating in the GA-RCLED results in an efficiency increase of 35%.

The extraction efficiency η_{extr} can be deduced from the relation between the optical power and the LED's current [6]. The optical power is directly proportional to the radiative recombination rate Bn^2:

$$P_{out} = \hbar\omega \eta_{extr} B n^2 Vol \tag{7.2}$$

with $\hbar\omega$ the photon energy, B the bimolecular recombination coefficient, n the carrier concentration and Vol the volume of the active region (see also Chapter 2).

With Eq.(2.12) expressing the total recombination rate, we can write the balance equation (the η_{inj} is supposed to be 1):

$$\frac{I}{qVol} = \frac{n}{\tau_{nrad}} + Bn^2 \tag{7.3}$$

This equation can be solved for the carrier density n:

$$n = \frac{1}{2B\tau_{nrad}} \left(\sqrt{1 + \frac{4BI\tau_{nrad}^2}{qVol}} - 1 \right) \tag{7.4}$$

Combining Eq.(7.2) and Eq.(7.4), we find a linear relation between the optical power and the current:

$$\begin{aligned} &\sqrt{P_{out}} = \alpha\beta \frac{I}{\sqrt{P_{out}}} \pm 2\sqrt{\alpha} \\ &\text{with } \alpha = \hbar\omega\eta_{extr} \frac{Vol}{4B\tau_{nrad}^2} \quad \beta = \frac{4B\tau_{nrad}^2}{qVol} \end{aligned} \tag{7.5}$$

[3]Substrate removal and deposition of an ARC can, however, not be carried out anymore. Due to a wrong mounting of the sample in a packaging, in the view of low temperature measurements, and a trial to release it from the mounting, the isolation layer dissolved.

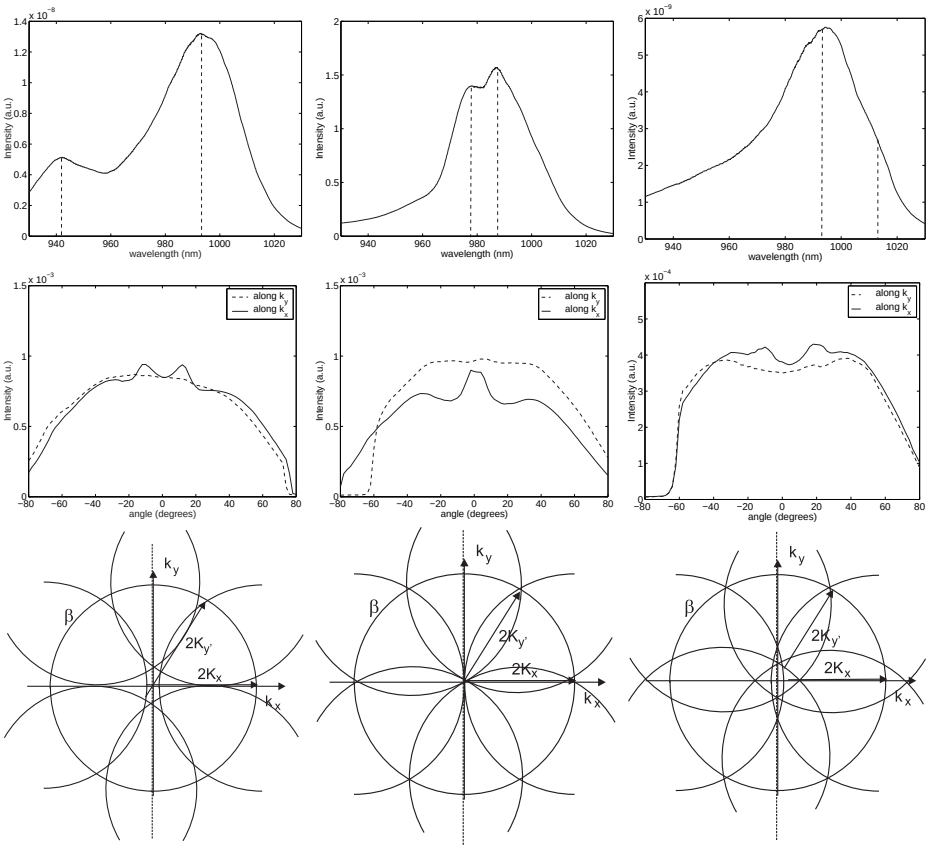

param.	value
$\Lambda_x, \Lambda_{y'}$	570 nm
d_{gr}	150 nm
d_1	153 nm
d_2	70 nm
hole diam.	154 nm
X	5
cont.	f

(a)

param.	value
$\Lambda_x, \Lambda_{y'}$	600 nm
d_{gr}	150 nm
d_1	153 nm
d_2	70 nm
hole diam.	162 nm
X	5
cont.	f

(b)

param.	value
$\Lambda_x, \Lambda_{y'}$	630 nm
d_{gr}	150 nm
d_1	153 nm
d_2	70 nm
hole diam.	170 nm
X	5
cont.	f

(c)

Fig. 7.17: Measured (at 30 mA, diameter 70 µm) spectrum observed in the surface normal direction ($\theta = 0^\circ$); farfield measured along x- and y-direction; schematic presentation of WVD and GA-RCLED parameters for (a) $\Lambda = 570$ nm; (b) $\Lambda = 600$ nm; (c) $\Lambda = 630$ nm, respectively. The dotted lines in the spectra mark the Fabry-Pérot mode and the extracted diffracted mode.

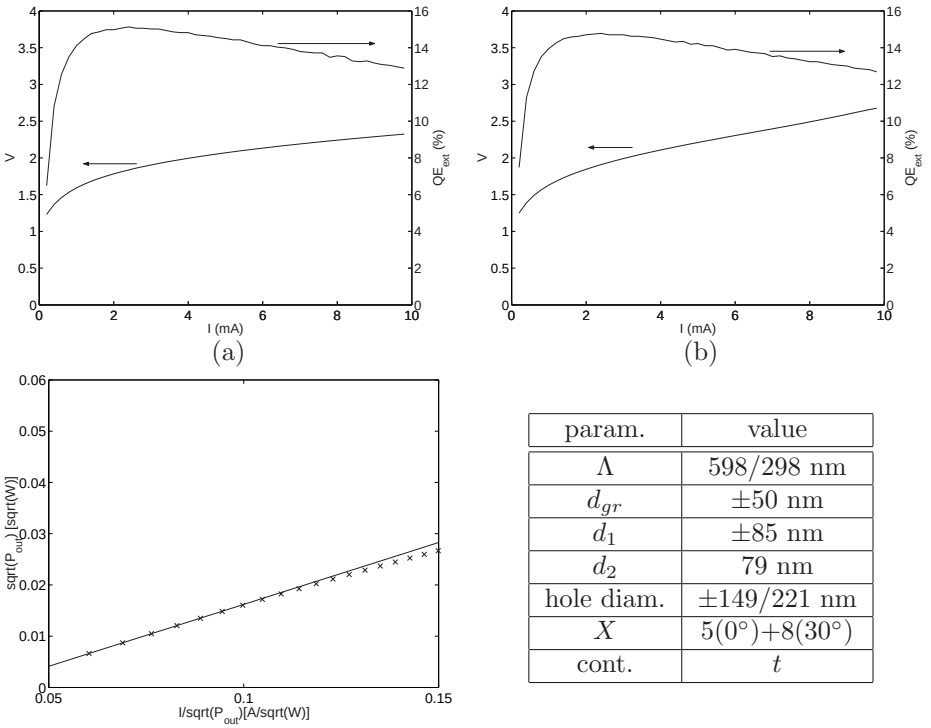

param.	value
Λ	598/298 nm
d_{gr}	$\pm$50 nm
d_1	$\pm$85 nm
d_2	79 nm
hole diam.	$\pm$149/221 nm
X	5(0°)+8(30°)
cont.	t

(d)

Fig. 7.18: Measured IV and QE for GA-RCLED with (a) second order triangular lattice grating; (b) first order triangular lattice grating; (c) measured and fitted curve of output power according to Eq.(7.5) *for device (a); (d) GA-RCLED parameter values. The diameter of the device is 115 μm, the substrate is not thinned and no ARC is provided.*

Fig. 7.18(c) plots this relation for the measured data (crosses). Parameter extraction of the linear curve fitted with the experimental data, reveals an $\eta_{extr} = 19\%$. Taking into account the above mentioned fresnel and absorption losses, the extraction efficiency is as high as 35%.

Due to a detuned cavity, the experimental results do not reach the numerically calculated or predicted efficiency of over 40%. The marginal difference in efficiency of the first order grating and the second order grating is attributed to the extended DBR which minimises the excess losses of the first order diffraction in case of the second order grating. Due to the erroneous tuning of the cavity, the efficiency of the second order grating is not higher however than the first order grating, which could be expected by the higher rotational symmetry of extraction of the second order grating.

7.4 Thin film GA-RCLED

Until now, we focussed attention on a bottom-emitting GA-RCLED with a periodically modulated top mirror and a DBR bottom mirror. A second configuration, on which research started only recently [7], is the thin film GaAs GA-RCLED (Fig. 7.19(a)). This substrate-less LED still uses the GaAs substrate for crystal growth, but afterwards it functions without the base material, which effectively becomes ballast. The upper side of the LED is coated with a metal layer after the epitaxy process. The epistructure is waferbonded upside down with benzocyclobutene (BCB) to an arbitrary substrate. BCB is a polymer with promising properties for heterogeneous integration. The BCB is spun on the transfer substrate, the sample is mounted on the BCB. The ensemble is baked in an oven under a nitrogen atmosphere, by which the sample is fixed on the substrate. Consequently, the LED substrate is thinned to ± 50 μm by means of a mechanical grinding process. Further thinning is carried out with a wet chemical etch. Due to an etch stop layer and the selectivity of the etchant, the thin film thickness is fully controlled. Moreover, the wet etch assures a smooth surface. The thickness of the device in the end is around 400 nm. Using holography, a grating is defined in the surface of the thin film. Some SEM pictures of the first realised thin film GA-RCLED are shown in Fig. 7.19. The carrier, BCB, thin film and grating can clearly be distinguished.

On the SEM picture of Fig. 7.19(a), the BCB layer can be measured to be ± 3.86 μm. However, because of the low thermal conductivity of BCB (0.4 W/mK), the BCB-layer is at best kept as thin as possible, to avoid excessive heating. The BCB thickness can be reduced using low-viscosity BCB and patterning the transfer substrate with bulges. The devices are then aligned on the bulges. The BCB layer can be as thin as 900 nm under the devices and excellent planarisation is achieved. This is shown in Fig. 7.20, before thinning of the sample.

Due to the absence of leaky DBRs and substrate, leaky modes are avoided. Moreover, a semiconductor/air grating can be used omitting enhanced metallic absorptions. First 2-D simulations of the angular power distribution and calculation of the in-plane extraction efficiency of a thin film GA-RCLLED with 2-D first order grating are shown in Fig. 7.21. Comparison with the results presented for the bottom-emitting GA-RCLED, reveals the promising behavior of these devices in view of efficiency. The internal angular net power flux looks different than the internal angular net power flux of the bottom-emitting devices. The guided mode is coupled out by the grating through the first order in reflection, but most of all through the first order in transmission. The upwards internal angular power distribution will thus not show a positive peak of the diffracted guided mode at $k_x = k_{\|}^{gm} - K_x$ (Fig. 7.21(a)). It does show a small negative peak, revealing that the reflected first order of the guided light is partially absorbed in the metallic mirror. The power flux in the surrounding medium (air) however, does confirm the transmitted first order diffraction of the guided mode (Fig. 7.21(b)). The peak at $k_{\|}^{gm}$ in the internal net power flux represents the power emitted in the diffracted guided light.

Thin film technology is not that exotic as one might think. Osram Opto Semiconductors has made a breakthrough in the luminous efficacy of AIGaInP LED

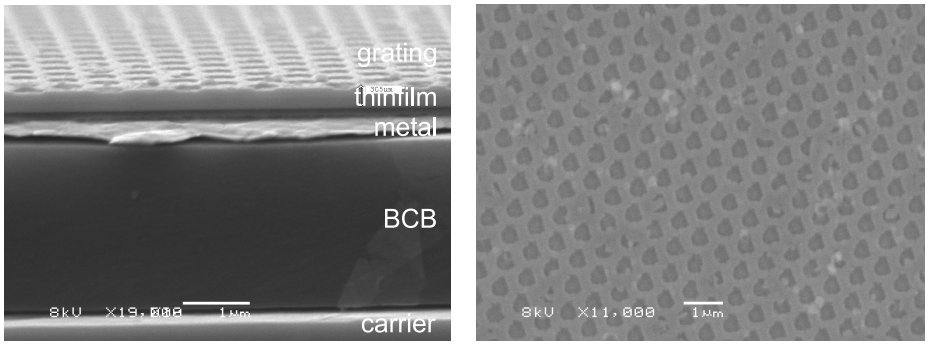

(a) (b)

Fig. 7.19: SEM picture of first realised thin film GA-RCLEDs (a) cross section of device with indication of carrier, BCB and thin film; (b) top view of thin film showing nice holographically defined triangular grating.

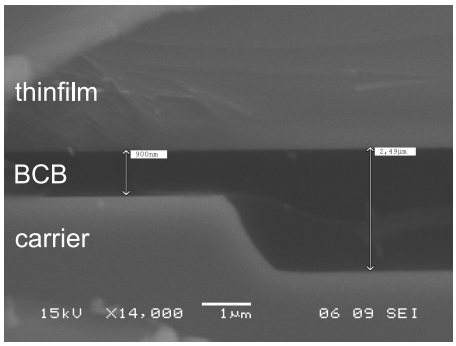

Fig. 7.20: SEM picture of sample mounted on carrier bulge. The thickness of the BCB is reduced from 2.49 μm to ± 900 nm.

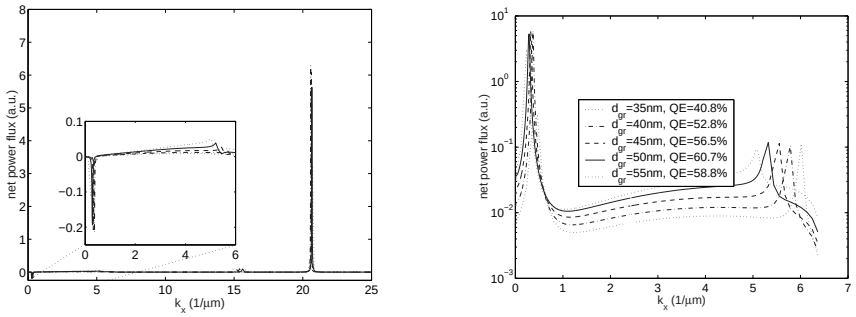

(a) (b)

Fig. 7.21: (a) Upwards s-polarised internal net power flux per unit spatial frequency along $\boldsymbol{k}_x$ in a thin film GA-RCLED with a 2-D first order grating (through interface underneath grating); (b) upwards s-polarised net power flux per unit spatial frequency in the surrounding air along k_x (through interface above grating).

with the aid of thin-film technology [8]. Moreover thin film devices are more compatible for wafer scale integration with electronic circuits.

7.5 Conclusion

Bottom-emitting GA-RCLEDs, with a periodically modulated top mirror and DBR bottom mirror, have been designed for a high extraction quantum efficiency η_{extr}. Both square lattice and triangular lattice gratings have been considered. The simulated η_{extr} of an optimised square lattice first order grating is over 30% and of an optimised triangular lattice first order grating over 40%. These results are obtained by a 3-D calculation of the device. Due to the numerical complexity of the numerical tool as a function of the number of spatial harmonics retained in the calculation, 3-D simulations of second order gratings were not feasible. Due to their higher rotational symmetry of extraction in comparison with first order gratings, even higher η_{extr} (up to 46%) are expected, when an extended DBR is used to minimise losses caused by the first diffraction order.

Square lattice gratings have been defined using a holographical technique that has been described in Chapter 5. Triangular lattice gratings have been realised by e-beam in cooperation with the University of Glasgow.

GA-RCLEDs with a triangular lattice grating showed an η_{ext} of 15%. The substrate of the devices was not yet thinned and they were not provided with an ARC. Taking into account these losses, which are not intrinsic to the final device, and knowing that the $\eta_{int} = \pm 79\%$, an $\eta_{extr} = 35\%$ has been proven experimentally.

Evidence of guided mode extraction is demonstrated in several runs, however in combination with a moderate η_{ext}. The reason is triple: metallic absorptions in a filled metallic grating. These losses are outsmarted by using a top-covered semiconductor/air grating. This technique preserves homogeneous current injection. The losses are reduced, although still higher than a flat metallic interface. The quality of the mirror has to be high. Aberrations of the binary cross section of the grating result in a scattering of the guided mode and is the second reason for a possible low η_{extr}. Thirdly, the cavity tuning has to be perfect. This drawback of the device forms the main reason of the moderate η_{extr}. Errors of the order of 3.5% on the thickness of grown epilayers are inevitable, depth deviations of 20 nm of the intended grating depth are not unimaginable. Unless control on these technological parameters is increased, the search for a high efficiency GA-RCLED will be a process of trial-and-error.

First research on thin film GA-RCLED is very promising. The absence of leaky DBR modes and the use of a semiconductor grating promise higher η_{extr} (50-60%) than the bottom-emitting devices.

References

[1] S. David, A. Chelnokov and J.M. Lourtioz, "Isotropic photonic structures: Archimedean-like tilings and quasi-crystals", *IEEE J. of Quantum Electron.,* vol. 37(11), pp. 1427-1434, 2001.

[2] European IST project: *"Photonic Integrated Circuits using photonic Crystal Optics"*, 1/3/2000-28/2/2003.

[3] H. De Neve, *"Ontwerp en realisatie van Licht Emitterende Diodes op basis van het Micro-caviteitseffect"*, Ph. D. Thesis, Ghent University, Ghent, Belgium, 1997.

[4] *camfr.sourceforge.net*

[5] H.C. Casey, D.D. Sell and K.W. Wecht, "Concentration-dependence of absorption-coefficient for n-type and p-type GaAs between 1.3 and 1.6 eV", *J. Appl. Phys.,* vol. 46(1), pp. 250-257, 1975.

[6] R. Bockstaele, *"Resonant Cavity Light Emitting Diode Based Parallel Interconnections"*, Ph. D. Thesis, Ghent University, Ghent, Belgium, 2001.

[7] K. Ghawana, D. Delbeke, I. Christiaens, S. Verstuyft and R. Baets " Heterogeneous integration with BCB applied to GA-RCLEDs", to be submitted to *SPIE Photonics Fabrication Europe 2002*, Brugge, Belgium, 28 October - 1 November 2002.

[8] K. Streubel, N. Linder, R. Wirth and A. Jaeger, "High brightness AlGaInP light-emitting diodes", *IEEE J. Sel. Top. Quantum Electron.,* vol. 8(2), pp. 321-332, 2002.

8

Conclusion and Perspectives

THE need for highly efficient LEDs has been emphasized in the introduction of this thesis. A broad range of applications, ranging from illumination towards communication over indication signs, demands for high efficiency sources, and more in particular for high brightness sources. The silent revolution of their efficiency during the last decades and their variety of assets (longevity, modulation speed, color control, etc.) make LEDs most suitable for these applications. Moreover, LEDs serve already now as the standard light source in several commercial applications.

However, the state-of-the art efficiency is not satisfactory, and, to penetrate a broader market segment, the efficiency has to be increased. One of the limiting factors is the extraction efficiency. Photons are generated inside a high refractive index material. Due to Snell's law of total internal reflection, a large fraction of the photons can not escape this high refractive index material.

The Optoelectronics Industry Development Association (OIDA) [1], launched in March 2001 a Technology Roadmap for LEDs, which intends to identify the technologies required to exploit market opportunities [1]. The fourth recommendation of the long term research issues concerns light extraction and reads as follows:

"The group felt a need to focus on light extraction. Due to the high refractive index of the LED material a large fraction of the generated light is trapped inside the LED structure. Research to overcome this might include developing transparent substrates, reflective contacts, photonic lattices and VCSELs as well as other novel concepts such as new substrates and novel device architectures. It was felt that the

[1] OIDA is a North American industry association representing 50 members, including both large and small companies (e.g. Intel, Lucent, LumiLeds, OSRAM) and universities (e.g. UCLA). OIDA's mission is to promote the global expansion of the optoelectronics industry and technological applications. It conducts industry workshops to assess international market trends and technology roadmaps (www.oida.org).

development of first principles, modelling for light extraction, as well as complete lighting systems should also be investigated.

The development of modelling capabilities and the identification of new methods for light extraction should be explored in the first year. Extensive computer modelling as well as experimentation should be carried out in the first three years to identify efficient means of light extraction from existing devices as well as novel device ideas. Use of these new or existing techniques/device structures in system demonstrations should be achieved in the five year time frame."

This recommendation reflects exactly what has been done during this research work. The main achievements and conclusion are summarised in the third paragraph. Some perspectives and opportunities set in by our research, finish this chapter and this thesis. We first summarise some milestones achieved by other research groups in the (r)evolution of extraction efficiency of LEDs during this research period.

8.1 Evolution of (extraction) efficiency of LEDs (1998-2001)

At the beginning of this research work, by the end of 1997, RCLED devices with an overall efficiency of 22.4% emitting at 980 nm were available. The concept of planar RCLEDs have been further elaborated and led in 1999 to a device with a differential external efficiency of 27% [2] and in 2002 to a device with an external efficiency of 28% [3], both devices with oxidised DBR. The extraction efficiency of these devices is ±30%.

32% multiple side extraction efficiency was reported in Standard LEDs with transparent substrate in 1996 [4]. Replacing the cubic shape by an inverted truncated pyramid led in 1999 to a device with world record external efficiencies of 60.9% [5]. These devices, capable to deliver high optical powers are most suitable as sources for general illumination or solid state lighting [6]. However, for plenty of applications, the overall optical power is a matter of little account. In telecommunication applications, for example, the coupling efficiency of the source into a fibre is directly related with the radiance of the source. Moreover, the small surface of the junction in comparison with the extraction surface indicates an inefficient use of the active surface and is detrimental for scaling. These characteristics do also exclude their use in high density two-dimensional arrays. Planar devices with low dimensions and single side extraction are needed for these applications.

A planar device that enhances the extraction efficiency by altering the path of the photons by use of a tapered waveguide section was presented in 1999 [7]. A wall-plug efficiency of 30% was reported for devices emitting at 980 nm in 2000 [8]. Extraction is single sided but the taper sections need to be quite large and the injected region takes up only 2% of the total extraction surface, which can be unfavorable for scaling and coupling.

The path of the photons can also be altered in an uncontrolled way by roughening an interface of the planar device. Elaboration of this idea in 1998 by Windisch *et al.* gave rise to thin film devices with $\eta_{ext} \approx 46\%$ for $\lambda = 870$ nm in 2000 [9].

Again we can remark that the active region spans a rather small fraction of the extraction surface: one third of the light is extracted in the roughened region around the mesa, while the injected area occupies only one tenth of the total emitting surface.

8.2 Overview of the accomplished work and conclusion

8.2.1 GA-RCLED: Novel design idea for high-efficiency LED. Principle and main assets

The Grating-Assisted Resonant-Cavity Light-Emitting Diode or GA-RCLED is a novel device idea, for the first time reported in this research work. Rigneault *et al.* published independently, an analogous conceptual idea, with special attention for thin film devices in 1999 [10].

Simplistically spoken, the idea of the GA-RCLED is to let spontaneous emission happen in a planar microcavity. Doing so, the optical power is concentrated in several discrete modes. Modes that have a propagation constant that is larger than the vacuum wave vector can not escape the cavity by the extraction interface (top or/and bottom) and are lost unless their photon momentum is changed. This can be accomplished by a periodic shallow grating with appropriate Bragg vectors integrated in one of the interfaces of the cavity: the propagation of the guided modes will be broken and they are diffracted towards the outside media. The device is essentially planar, the extraction is single sided and the area of extraction of the light and of electrical injection coincidence or the available surface is efficiently used. Guided mode extraction can be enhanced in a limited NA (15° cone) around the surface normal direction, benefitting the radiance of the device.

At the beginning of this work, research on the integration of gratings, or more specifically on the integration of photonic crystals, in microcavities focused on the use of these crystals in their photonic bandgap regime [11]. The guided mode is then annihilated. The grating needs to be etched through the active layer. This can result in large non-radiative recombination rates and jeopardises any prospect of high extraction efficiency.

Two groups introduced in 1999 a variant on the GA-RCLED: a microcavity with a 2-D periodic corrugation at the periphery of the LED's active area to extract the guided light reaching the edge of the device. Boroditsky *et al.* reported a 6-fold enhancement of the efficiency, but did not cite absolute efficiencies [12]. Rattier *et al.* predicts a supplementary extraction of 10% as worst case scenario [3], [13]. In comparison with the GA-RCLED, there is a decoupling of the vertical and in-plane issues: it essentially adds new channels of extraction avoiding degradation of existing ones. In the GA-RCLED, vertical and horizontal design issues are entangled. An ill designed GA-RCLED can affect existing extraction channels, resulting in a decrease of efficiency in comparison with gratingless RCLEDs. However, the GA-RCLED has more degrees of freedom concerning its dimensions than the device

with a 2-D periodic corrugation at the periphery of the LED. For small injection diameters, the efficient use of available space decreases in case of the latter device. Due to the finite absorption length of the guided mode in the cavity, a limit is also posed on its maximal diameter (injection diameter $< \pm 100$ to 200 μm). The GA-RCLED has a maximal efficient use of available space independently on the diameter of the device. Moreover, diffraction of the guided mode starts at its origin, cancelling the upper limit on diameter size.

8.2.2 Numerical rigorous analysis tool and computer modelling

We have detailed the electromagnetic analysis that have been developed in the framework of this research to calculate the radiation of an electric dipole located inside a grating structure. The analysis is based on the Rigorous Coupled-Wave Analysis (RCWA) to calculate diffraction of 2-D diffractive structures. The model has been implemented. We are now able to numerically calculate the optical behavior in three dimensions of dipole emission in a periodically corrugated layer structure.

We have used the model to study the behavior of bottom-emitting GA-RCLEDs with periodically modulated top mirror and DBR bottom mirror. Extraction efficiencies up to 40% are predicted. This confirms the enhanced efficiency to be obtained with the proposed new concept of the GA-RCLED. The modelling tool could also point out the drastic influence of ill designed GA-RCLEDs: a deviation of several percents of the parameter values from the optimal values can result in a fall back of the extraction efficiency.

8.2.3 Prototyping

The modelling tool was used to determine the parameter values of the GA-RCLED in view of an optimised extraction efficiency. GA-RCLEDs have been fabricated according to this design.

A holographical process has been developed to realise 2-D gratings. In contrary to the sequential e-beam definition, this process defines the grating in a single step. The processing of a GA-RCLED is as such straightforward and at low cost, adequate to be used in mass-fabrication.

Characterisation of the fabricated GA-RCLED gives evidence of guided mode extraction. A GA-RCLED with a second order triangular lattice grating resulted in an external efficiency of 15.1%. Removing the substrate and providing an ARC can increase this efficiency to 27%. Taking into account the internal efficiency of 79%, this external efficiency corresponds with an extraction efficiency of 35%. The small deviation from the theoretically predicted extraction efficiency is due to a small cavity detuning, which is the delicate point of the GA-RCLED.

8.2.4 Conclusion

A new conceptual idea for highly efficient LEDs has been proposed and specified. A tool to analyse the device has been developed. The idea has been elaborated for a specific configuration: a bottom emitting device with metallic/semiconductor grating top mirror and DBR bottom mirror. Theoretical analysis of the device predicts an extraction efficiency enhancement of 62%. First prototyping gives evidence of guided mode extraction, and at the same time points out the drawback of the concept: the appropriate behavior of the component can take a turn for the worse when small deviations of the optimal cavity parameters are present. A GA-RCLED with a second order triangular lattice grating resulted in an external efficiency of 15.1%, without susbstrate thinning and ARC.

8.3 Perspectives

The concept of dipole radiation into grating structures has been detailed and predicts an increased extraction efficiency and more specifically an increased radiance in comparison with emission into planar stratified layers. A modelling tool to analyse the radiation quantitatively has been set up. This work has focussed attention on the specific structure of a bottom emitting GA-RCLED with metallic/semiconductor grating top mirror and DBR bottom mirror. However, other configurations can be studied with the modelling tool, definitely resulting in high efficiency and high brightness devices. Two examples are given.

The RCLED of [3] can be used as starting point. The bottom mirror is an oxidised DBR, resulting in a smaller effective cavity thickness and a reduction of the power fraction lost through the leaky modes. The device is top emitting: a semiconductor grating will accomplish guided light diffraction, in which case increased metallic absorptions in metallic gratings is avoided.

A second configuration, on which research started only recently, is the thin film GaAs GA-RCLED. This substrate-less LED has been discussed shortly in Chapter 7. First simulations point out that due to the absence of DBR leaky modes and due to the lower metallic absorptions the extraction efficiency can be at least higher than 50%.

The concept and modelling tool for dipole radiation into grating structures have been worked out. Future research can specify the general issues, set up in this work, into concrete device configurations with a high extraction efficiency. These essentially planar devices with a single sided extraction, an efficient use of available surface and enhanced radiance are excellent candidates to be used in applications where light needs to be focussed to a small spot or in high density two-dimensional arrays.

References

[1] OIDA/DOE report, "The Promise of Solid State Lighting for General Illumination", *http://www.eren.doe.gov/buildings/documents/pdfs/oida_led−oled_rpt.pdf*, Optoelectronics Industry Development Association, Washington, DC, March 2001.

[2] J.J. Wierer, D.A. Kellogg and N. Holonyak, "Tunnel contact junction native-oxide aperture and mirror vertical-cavity surface-emitting lasers and resonant-cavity light-emitting diodes", *Appl. Phys. Lett.,* vol. 74(7), pp. 926-928, 1999.

[3] M. Rattier, H. Benisty, R.P. Stanley, J.F. Carlin, R. Houdré, U. Oesterle, C.J.M. Smith, C. Weisbuch and T.F. Krauss, "Toward ultrahigh-efficiency aluminum oxide microcavity light-emitting diodes: guided mode extraction by photonic crystals", *IEEE J. Sel. Top. Quantum Electron.,* vol. 8(2), pp. 238-247, 2002.

[4] F.A. Kish, D.A. Vanderwater, D.C. Defevere, D.A. Steigerwald, G.E. Hofler, K.G. Park and F.M. Steranka, "Highly reliable and efficient semiconductor wafer-bonded AlGaInP/GaP light-emitting diodes", *Electron. Lett.,* vol. 32(2), pp. 132-134, 1996.

[5] M.O. Holcomb, M.R. Krames, G.E. Hofler, C. Carter-Coman, E. Chen, P. Grillot, K. Park, N.F. Gardner, J.-W. Huang, J. Posselt, D. Collins, S.A. Stockman, G. M. Craford, F.A. Kish, I.-H. Tan, T.S. Tan, C.P. Kocot and M. Hueschen, "High-power truncated-inverted-pyramid $(Al_xGa_{1-x})_{0.5}In_{0.5}P$ light-emitting diodes exhibiting $> 50\%$ external quantum efficiency", *Appl. Phys. Lett.,* vol. 75(16), pp. 2365-2367, 1999.

[6] D.A. Steigerwald, J.C. Bhat, D. Collins, R.M. Fletcher, M.O. Holcomb, M.J. Ludowise, P.S. Martin and S.L. Rudaz, "Illumination with solid state lighting technology", *IEEE J. Sel. Top. Quantum Electron.,* vol. 8(2), pp. 310-320, 2002.

[7] W. Schmid, F. Eberhard, M. Schauler, M. Grabherr, R. King, M. Miller, E. Deichsel, G. Stareev, U. Martin, R. Jäger, J. Joos, R. Michalzik and K.J. Ebeling, " Infrared light-emitting diodes with radial outcoupling taper for high extraction efficiency", *Light-Emitting Diodes: research, manufacturing and applications III, Proc. SPIE,* vol. 3621, pp. 198-205, 1999.

[8] W. Schmid, F. Eberhard, R. Jäger, R. King, M. Miller, J. Joos and K.J. Ebeling, " 45% Quantum Efficiency Light-Emitting Diodes with Radial Outcoupling Taper", *Light-Emitting Diodes: research, manufacturing and applications IV, Proc. SPIE,* vol. 3938, pp. 90-97, 2000.

[9] R. Windisch, M. Kuijk, B. Dutta, A. Knobloch, P. Kiesel, G.H. Dölher, G. Borghs and P. Heremans, "Non-Resonant Cavity Light-Emiotting Diodes", in *Light-Emitting Diodes: Research, Manufacturing, and Applications IV, Proc. SPIE,* vol. 3938, pp. 71-76, 2000.

[10] H. Rigneault, F. Lemarchand, A. Sentenac and H. Giovannini, "Extraction of light from source located inside waveguide grating structures", *Opt. Lett.,* vol. 24(3), pp. 148-150, 1999.

[11] S. Fan, P.R. Villeneuve, J.D. Joannopoulos and E.F. Schubert, " High Extraction Efficiency of Spontaneous Emission from Slabs of Photonic Crystals", *Phys. Rev. Lett,* vol. 78(17), pp. 3294-3297, 1997.

[12] M. Boroditsky, T.F. Krauss, R. Coccioli, R. Vrijen, R. Bhat and E. Yablonovitch, "Light extraction from optically pumped light-emitting diode by thin-slab photonic crystal", *Appl. Phys. Lett.,* vol. 75(8), pp. 1036-1038, 1999.

[13] M. Rattier, H. Benisty and C. Weisbuch, "Photonic crystal extractor", in *Electromagnetic Crystal Structures: Proceedings of Workshop on Photonic and Electromagnetic Crystal Structures III (PECS3), 9-14 June 2001, St. Andrews, United Kingdom,* T.F. Krauss (Ed.), 2001.